ABSTRACT

Title of Dissertation:	NONLINEAER NUMERICAL SIMULATION STUDY AND REGIONAL-SCALE SEISMIC RESILIENCE ASSESSMENT OF DEFICIENT WOOD-FRAME STRUCTURES RETROFITTED WITH SELF-CENTERING VISCOELASTIC DAMPERS
	Stephen Eskandari, Doctor of Philosophy, 2025
Dissertation directed by:	Professor Yunfeng Zhang Department of Civil and Environmental Engineering, University of Maryland, College Park

Timber structures are among the most favorite types for constructing low- to mid-rise buildings. Many older wood-frame buildings were not designed to meet the current seismic provisions, and are considered as wood-frame buildings with soft story deficiency. Such residential buildings with three- and four-story are particularly common in the United States.

Recent advancements in seismic design have led to the development of various innovative seismic protection strategies. Notably, the concept of damage-free self-centering systems has garnered significant interest. This approach incorporates a recentering element to restore the structure to its original position and employs fuse devices for energy dissipation, ensuring that the primary structural system remains undamaged during design basis earthquakes.

In this study, new types of retrofitting systems have been developed to overcome the soft-story issue in code-deficient light-frame wood structures. The existing timber soft-story building has been retrofitted using three different systems. In the first phase, the nonlinear seismic behavior of the original unretrofitted building was studied. Then, the existing building has been retrofitted with wood structural panel (WSP) system. In the third phase, the retrofitted building in the previous

step was retrofitted on its ground story only with the proposed novel self-centering viscoelastic damper (SCVD) system. Finally, in the next phase, the original unretrofitted wood building has been seismically retrofitted with the state-of-the-art Y-type braced self-centering viscous damper eccentrically braced frame (Y-SCVD-EBF) system providing high lateral stiffness to the deficient wood framed building. The energy dissipation of the developed systems is mainly provided by fluid viscous damper (VD), and TPAD (Trapezoid Plate Added Damping) acts as the backup fuse device. While the system recentering capability is enabled by utilizing preloaded disc springs.

The load-displacement behavior of the proposed self-centering viscoelastic damper (SCVD) systems was analytically derived, and their seismic performance was assessed through nonlinear numerical static and dynamic analyses of the prototype buildings exposed to far-field (FF) ground motions (GMs).

A Python-based framework was used to conduct an intensity-based regional seismic resilience assessment of wood framed soft-story buildings retrofitted with Y-SCVD-EBF systems. The seismic damage and loss assessment follows the FEMA P-58 methodology, with the resilience metrics visualized using a digital twin model in Geographical Information System (GIS) software. As a case study, the regional seismic resilience of over 2,000 wood-frame residential buildings retrofitted with Y-SCVD-EBF systems was studied in San Francisco.

NONLINEAER NUMERICAL SIMULATION STUDY AND REGIONAL-SCALE SEISMIC RESILIENCE ASSESSMENT OF DEFICIENT WOOD-FRAME STRUCTURES RETROFITTED WITH SELF-CENTERING VISCOELASTIC DAMPERS

by

Stephen Eskandari

Dissertation submitted to the Faculty of the Graduate School of the
University of Maryland, College Park, in partial fulfillment
of the requirements for the degree of
Doctor of Philosophy
2025

Advisory Committee:
Professor Yunfeng Zhang, Chair
Professor Chung C. Fu
Professor Sung W. Lee
Associate Professor Allison C. Reilly
Assistant Professor Shuna Ni

Dedication

to my supportive mother, to whom I owe all my successes,

and to the soul of my father.

Acknowledgments

I would like to deeply appreciate the knowledge, professional experience, and guidance of my advisor, Professor Yunfeng Zhang, throughout my doctorate degree, whose indispensable support and advice have been crucial to be successful in my research. I am profoundly grateful for being his student and for the wealth of knowledge and exceptional experiences I have gained across multiple fields of study.

I would like to extend my sincere appreciations to the members of my dissertation committee, Professors Chung C. Fu, Sung W. Lee, Allison C. Reilly, and Shuna Ni for their valuable contributions to my research and their insightful comments.

I express my deep gratitude to the Department of Civil and Environmental Engineering and the Graduate School at the University of Maryland for providing me with the wonderful opportunity to pursue my Ph.D. degree.

Furthermore, I greatly appreciate all the favors that my friend, Pooya Rezvan, a recent civil engineering doctorate graduate from the University of Maryland, did whose invaluable assistance in developing my models for this research was an immense help. Working with him has been a truly rewarding experience, and I deeply appreciate his friendship, encouragement, and support during the program.

I owe my deepest gratitude to my mother, who has always supported me. I will never forget her incredible encouragement during my doctorate program. I am also thankful to my two sisters for their constant support and encouragement. I feel incredibly blessed to have them all in my life and am deeply grateful for their great support.

Finally, I am greatly appreciative of the many professors, friends, colleagues and family members who have encouraged me and supported my efforts, helping to guide me on the path to success.

Stephen (Amir) Eskandari

March 2025

Table of Contents

Dedication ii
Acknowledgments iii
Table of Contents v
List of Tables ix
List of Figures x
List of Abbreviations xvi
Chapter 1 : Introduction 1
1.1 Background 1
1.2 Research Objectives 2
1.3 Dissertation Organization 5
Chapter 2 : Literature Review 8
2.1 Seismic Behavior of Light-Frame Wood Buildings 8
2.2 Self-Centering Eccentrically Braced Frame (SCEBF) Systems 12
2.3 Regional Seismic Resilience Assessment 22
Chapter 3 : Nonlinear Seismic Analysis and Performance Study of Soft-Story Wood Framed Structures Retrofitted with Wood Structural Panel (WSP) 28
3.1 Seismic Behavior of the System 28
3.2 Analytical Load-Displacement Relationships of Timber Structures 30
3.3 Finite Element Modeling 31
3.4 Prototype Light-Frame Wood Building 34
3.5 Numerical Modeling for Response History Analysis 37
3.6 Eigenvalue and Nonlinear Static Analyses 38
3.7 Nonlinear Dynamic Analysis 40
3.7.1 Original Timber Structure 41
3.7.2 Original Timber Structure Retrofitted with WSP 42
3.7.2 Comparison between the Original and the WSP-Retrofitted Prototypes 43
3.8 Summary 45

Chapter 4 : Nonlinear Seismic Analysis and Performance Study of Soft-Story Wood Framed Structures Retrofitted with Self-Centering Viscoelastic Damper (SCVD) Systems on the First Story only 47
4.1 Seismic Behavior of the System 48
4.2 Analytical Formulations of the SCVD System 49
4.2.1 Self-Centering Viscoelastic Damper (SCVD) Module Frame without the Fuse Device 50
4.2.2 Self-Centering Viscoelastic Damper (SCVD) Module Frame with the TPAD Fuse Device 59
4.3 Design of SCVD Retrofitting Systems 64
4.4 SCVD Module Frame Specifications 65
4.5 Numerical Modeling 67
4.6 SCVD-Retrofitted Prototype Building 70
4.7 Eigenvalue and Nonlinear Static Analyses 70
4.8 Nonlinear Response History Analysis 72
4.9 Results and Discussions 73
4.10 Structural Demands of a Typical Case 76
4.11 Summary 78
Chapter 5 : Nonlinear Seismic Analysis and Performance Study of Soft-Story Wood Framed Structures Retrofitted with Y-type Braced Self-Centering Viscous Damper Eccentrically Braced Frame (Y-SCVD-EBF) Systems 81
5.1 Seismic Behavior of the System 81
5.2 Analytical Formulation of the Y-SCVD-EBF System 83
5.2.1 Y-SCVD-EBF Module without the Fuse Device 84
5.2.2 Y-SCVD-EBF Module with the TPAD Fuse Device 87
5.3 Design of Y-SCVD-EBF Modular Systems 88
5.4 Y-SCVD-EBF Module Specifications 89
5.5 Finite Element Modeling 91
5.6 Prototype Wood Framed Building Retrofitted with Y-SCVD-EBF System 92

5.7 Eigenvalue and Nonlinear Static Analyses ... 93

5.8 Nonlinear Dynamic Analysis ... 95

5.9 Results and Discussions ... 96

5.10 Structural Response of a Typical Case ... 100

5.11 Summary ... 104

Chapter 6 : Regional Seismic Resilience Assessment of Residential Light-Frame Wood Buildings with Soft Stories with the Seismic Retrofit in San Francisco Municipal Area ... 107

6.1 Description of the Python-Based Framework ... 108

6.2 Obtaining the Building Inventory ... 110

6.3 Obtaining the Seismic Design Parameters of the Region ... 110

6.4 Obtaining the Numerical MDOF Lumped-Mass Model ... 110

6.5 Response History Analysis and Engineering Demand Parameters ... 116

6.6 Defining Seismically Vulnerable Components ... 118

6.7 Seismic Resilience Assessment ... 119

6.7.1 Collapse Condition ... 120

6.7.2 Irreparability Condition ... 121

6.7.3 Damage and Loss Assessment ... 121

6.8 Obtaining the Outputs of the Analysis ... 122

6.9 Case Study: Regional Seismic Resilience Assessment of Retrofitted Soft-Story Residential Light-Frame Wood Buildings in San Francisco ... 122

6.9.1 Building Components ... 124

6.9.2 Numerical Modeling of Buildings for Regional Seismic Resilience Assessment ... 125

6.9.3 Damage and Loss Assessment ... 127

6.9.4 Results ... 127

6.10 Summary ... 153

Chapter 7 : Summary, Conclusion, and Future Research ... 156

7.1 Summary ... 156

7.2 Conclusion ... 157

7.2.1 Light Wood Framed Buildings Retrofitted with Wood Structural Panel (WSP) ... 157
7.2.2 Light Wood Framed Buildings Retrofitted with Self-Centering Viscoelastic Damper (SCVD) System on the Ground Story Only ... 158
7.2.3 Light Wood Framed Buildings Retrofitted with Y-type Braced Self-Centering Viscous Damper Eccentrically Braced Frame (Y-SCVD-EBF) System ... 159
7.2.4 Regional Seismic Resilience Assessment of Multi-Family Residential Wood Framed Soft-Story Buildings Retrofitted with Self-Centering Viscous Damper Eccentrically Braced Frame (Y-SCVD-EBF) Modules ... 161
7.3 Future Research ... 162

Appendices ... 164
Appendix A: Specification of the Ground Motion Record Set ... 164

Appendix B: Stiffness and Strength of the Original and WSP-retrofitted Prototypes ... 177

B.1 Original Wood-Frame Prototype ... 177
B.2 WSP-retrofitted Prototype ... 178
Appendix C: Analytical Calculations of the Hysteretic Behavior of the Self-Centering Systems ... 179

C.1 Self-Centering Viscoelastic Damper (SCVD) System ... 179
C.2 Y-type Braced Self-Centering Viscous Damper Eccentrically Braced Frame (Y-SCVD-EBF) System ... 182
Bibliography ... 186

List of Tables

Table 2.1 Components considered in the FEMA P-58 loss assessment (Yi et al. [89]) 24

Table 2.2 Quantity of nonstructural components (You et al. [90]) 25

Table 3.1 Hysteretic Parameters required to create the timber shear wall SAWS model [4]. 31

Table 3.2 Calibrated hardening parameters of Q225 steel for numerical analysis [6] 33

Table 3.3 Wall sheathing length for the prototype wood buildings 37

Table 3.4 Modal properties of the four-story light-frame wood buildings 39

Table 3.5 Statistical data of the maximum IDR of the prototype buildings 44

Table 3.6 Statistical data of the maximum residual IDR of the prototype buildings 45

Table 4.1 Member section size of the SCVD module frame (Unit: mm) 67

Table 4.2 Dimensions of the disc springs in the SCVD module frame (Unit: mm) 67

Table 4.3 Dimensions of the TPAD plate in the SCVD module frame (Unit: mm) 67

Table 4.4 Viscous damper parameters 67

Table 5.1 Member section sizes of the Y-SCVD-EBF module (Unit: mm) 90

Table 5.2 Dimensions of the disc springs in the Y-SCVD-EBF module frame (Unit: mm). 90

Table 5.3 Dimensions of the TPAD plate in the Y-SCVD-EBF module frame (Unit: mm). 91

Table 5.4 Viscous damper parameters 91

Table 6.1 Specifications of the springs in the MDOF lumped mass numerical model 115

Table 6.2 Building demand table (Unit: ft) 118

Table 6.3 Vulnerable components in multi-family residential wood framed buildings 125

List of Figures

Figure 2.1 Prototype D-type SCEBF system with RHD fuse devices: (a) experimental test setup; (b) module configuration; (c) schematics of RHD devices installed to rocking link beam; (d) free-body diagram of RHD devices attached to the rocking link (Tong et al. [56]) 14

Figure 2.2 Schematic view of SCEBF-Y module structure without RHD devices (Keivan and Zhang [57]) 15

Figure 2.3 Configuration of K-type SCEBF module structure: (a) module frame; (b) free body diagram of rocking link beam (Keivan and Zhang [58]) 16

Figure 2.4 Schematics of D-type SCEBF-SRL: (a) elevation view; (b) rocking zone (Rezvan and Zhang [59]) 17

Figure 2.5 Schematics and components of the SCMRF-SRB module (Rezvan and Zhang [52]) 18

Figure 2.6 Conceptual design of a hybrid viscous SMA device (Tang and Lui [68]) 19

Figure 2.7 Configuration of the HSVD: (a) hybrid damper; (b) components of the damper (Nasab and Kim [69]) 20

Figure 2.8 Experimental test setup of viscoelastic damper (Nasab and Kim [69]) 20

Figure 2.9 Schematics of the SCVD system (Yan et al. [60]) 21

Figure 2.10 Hybrid bracing system: (a) schematic of a single story HBF; (b) hysteretic behavior under cyclic dynamic loading (Qiu et al. [70]) 22

Figure 2.11 Map showing the location of SWOF buildings in the city of Los Angeles (Yi et al. [89]) 24

Figure 2.12 Probability density function for regional reinforced masonry structures: (a) Slight damage; (b) Moderate damage; (c) Extensive damage; (d) Complete damage (Lu et al. [91]) ... 26

Figure 2.13 Schematics of the modular self-centering eccentrically braced frame system (Rezvan and Zhang [6]) 27

Figure 3.1 Schematics, and components of the original unretrofitted wood-frame building 29

Figure 3.2 Schematics, and components of the original wood-frame building retrofitted with wood structural panel (WSP) 29

Figure 3.3 Load-displacement behavior of timber shear walls [4] 30

Figure 3.4 2D Numerical wireframe modeling of the original unretrofitted timber structure in OpenSees 32

Figure 3.5 2D Numerical wireframe modeling of the original timber structure retrofitted with WSP in OpenSees 32
Figure 3.6 Calibration of the low-yield Q225 steel based on the material coupon test [6] 33
Figure 3.7 Floor plans of the four-story wood framed prototype building [4]:
(a) First Story; (b) Upper Stories 35
Figure 3.8 Elevation views of the four-story wood framed prototype building [4]:
(a) East view; (b) South view; (c) West view; (d) North view 35
Figure 3.9 Isometric views of the four-story wood framed prototype building [4]:
(a) Northwest view; (b) Northeast view; (c) Southwest view; (d) Southeast view 36
Figure 3.10 Existing wall sheathing in the original building [4]: (a) First Story; (b) Upper Stories 36
Figure 3.11 Modal shapes of the four-story light-frame wood prototype buildings:
(a) Original unretrofitted; (b) WSP-retrofitted 38
Figure 3.12 Pushover curve of the wood-frame prototype: (a) unretrofitted; (b) WSP-retrofitted 40
Figure 3.13 Maximum IDR of the unretrofitted wood building under 0.0002 DBE.................... 41
Figure 3.14 Maximum residual IDR of the unretrofitted wood building under 0.0002DBE....... 42
Figure 3.15 Maximum IDR of the WSP-retrofitted wood building under 0.06DBE.................... 42
Figure 3.16 Maximum residual IDR of the WSP-retrofitted wood building under 0.06DBE...... 43
Figure 3.17 Vertical profile of the IDR of the four-story prototype light-frame timber structures with 16th and 84th percentile values of the peak responses: (a) Original unretrofitted prototype under GM-07 and 0.0002DBE; (b) WSP-retrofitted prototype under GM-05 and 0.06DBE 44
Figure 4.1 Schematics, and components of the SCVD module installed on the first story only.........48
Figure 4.2 Components of the SCVD device.. 49
Figure 4.3 Configuration of the TPAD.. 49
Figure 4.4 Schematic load-displacement relationship of self-centering systems without the displacement-dependent fuse device (e.g. TPAD) [6].. 50
Figure 4.5 Hysteresis response of a viscous damper (VD) [60] 51
Figure 4.6 Schematic flag-shaped load-displacement behavior of a SCVD system without a backup fuse device (e.g. TPAD) [60] 52

Figure 4.7 Free body diagram of the vertical link beam without the fuse device:
(a) Before gap-opening; (b) After gap-opening 54
Figure 4.8 Geometry of a single disc spring and types of stacking [6] 56
Figure 4.9 Force-deflection curves of disc springs [6] 58
Figure 4.10 Schematic flag-shaped load-displacement behavior of the developed self-centering systems with the displacement-dependent damping device (e.g. TPAD) [6] 60
Figure 4.11 Schematic flag-shaped load-displacement behavior of a SCVD system with a back-up fuse device (e.g. TPAD) [60] 61
Figure 4.12 Free body diagram of the SCVD system with the fuse device (i.e. TPAD) 63
Figure 4.13 2D Numerical wireframe modeling of the WSP-retrofitted prototype timber structure retrofitted with SCVD module on the ground story only in OpenSees 68
Figure 4.14 2D Numerical wireframe modeling of the SCVD device in OpenSees 69
Figure 4.15 Modal shapes of the four-story soft-story light-frame wood prototype building retrofitted with SCVD module on the first story only 71
Figure 4.16 First floor pushover curve of the four-story soft-story light-frame wood frame prototype building retrofitted with SCVD module on the first story only 72
Figure 4.17 Maximum IDR responses in the wood building retrofitted with SCVD on the ground story only under $0.45\mathrm{DBE}$ 74
Figure 4.18 Maximum residual IDR in the wood building retrofitted with SCVD on the ground story only under $0.45DBE$ 75
Figure 4.19 Vertical profile of the IDR of the SCVD-retrofitted prototype buildings with 16th and 84th percentile values of the peak responses under $0.45\mathrm{DBE}$: (a) Without the TPAD fuse device under GM-19; (b) With the TPAD fuse device under GM-11 76
Figure 4.20 IDR history of the ground story in the SCVD-retrofitted prototype building under GM-11 at $0.45DBE$ 77
Figure 4.21 Hysteresis behavior of the ground story in the SCVD-retrofitted prototype under GM-11 at $0.45DBE$ 78
Figure 5.1 Schematic, and components of the Y-SCVD-EBF module 82
Figure 5.2 Schematic of link beam and SCVD at the time of gap-opening in the
Y-SCVD-EBF system 83
Figure 5.3 2D Numerical wireframe modeling of the Y-SCVD-EBF system in OpenSees 92

Figure 5.4 Elevation view of the original unretrofitted wood framed building retrofitted on all stories with the Y-SCVD-EBF module: (a) Y-SCVD-EBF steel retrofitting module; (b) Original unretrofitted timber structure 93
Figure 5.5 Modal shapes of the four-story Y-SCVD-EBF steel frame prototype building 94
Figure 5.6 Pushover curve of the four-story Y-SCVD-EBF steel framed prototype building............95
Figure 5.7 Maximum IDR response of the Y-SCVD-EBF prototype building under DBE 96
Figure 5.8 Maximum IDR response of the Y-SCVD-EBF prototype building under MCE_R....... 97
Figure 5.9 Vertical profile of the maximum IDR of the Y-SCVD-EBF prototype with 16th and 84th percentile values of the peak responses at GM-16 and under: (a) DBE; (b) MCE_R............ 98
Figure 5.10 Maximum deflection ratio ($smaxh0'$) of the sets of disc springs of the Y-SCVD-EBF prototype building under DBE 99
Figure 5.11 Maximum deflection ratio ($smaxh0'$) of the sets of disc springs of the Y-SCVD-EBF prototype building under MCE_R 100
Figure 5.12 Drift response history of the first story of the Y-SCVD-EBF prototype at GM-16 under DBE (TPAD is not used in the system) 101
Figure 5.13 Hysteretic loop of the first story of the Y-SCVD-EBF prototype at GM-16 under DBE (TPAD is not used in the system) 102
Figure 5.14 Drift response history of the first story of the Y-SCVD-EBF prototype at GM-16 under DBE (TPAD is utilized in the system)........ 103
Figure 5.15 Hysteretic loop of the first story of the Y-SCVD-EBF prototype at GM-16 under DBE (TPAD is utilized in the system)........ 104
Figure 6.1 Sequential steps of the framework for regional seismic resilience assessment of the Y-SCVD-EBF-retrofitted wood framed buildings........ 109
Figure 6.2 Flag-shaped load-displacement behavior of typical self-centering modular bracing panels [6]........ 111
Figure 6.3 MDOF lumped-mass shear building model of the Y-SCVD-EBF retrofitting module 112
Figure 6.4 Load-displacement behavior of the springs in the MDOF lumped mass model 113
Figure 6.5 Simplified process of damage and loss evaluation following FEMA P-58 [6]......... 120
Figure 6.6 Distribution of multi-family residential buildings with soft story in San Francisco: (A) Histogram of the story numbers; (B) Histogram of the plan area 124

Figure 6.7 Generating the lumped-mass shear building model of the Y-SCVD-EBF systems.. 126
Figure 6.8 Cumulative distribution function (CDF) of the regional normalized repair cost (NRC) 128
Figure 6.9 Cumulative distribution function (CDF) of the regional normalized repair time (NRT) considering parallel working procedure........ 129
Figure 6.10 Cumulative distribution function (CDF) of the regional normalized repair time (NRT) considering serial working procedure 129
Figure 6.11 Regional mean value of NRC with one standard deviation at different intensity levels 130
Figure 6.12 Regional mean value of NRT with one standard deviation at different intensity levels (Parallel working procedure) 130
Figure 6.13 Regional mean value of NRT with one standard deviation at different intensity levels (Serial working procedure) 131
Figure 6.14 Regional mean contribution of the components to the mean repair cost 133
Figure 6.15 Regional mean contribution of the components to the mean repair time........ 133
Figure 6.16 Contribution of the structural and nonstructural components to the regional mean repair cost with one standard deviation at different intensity levels........ 134
Figure 6.17 Contribution of the structural and nonstructural components to the regional mean repair time with one standard deviation at different intensity levels........ 134
Figure 6.18 Contribution of components to the regional mean repair cost at three different intensity levels 135
Figure 6.19 Contribution of components to the regional mean repair time at three different intensity levels 136
Figure 6.20 Normalized mean repair cost (NRC) of Y-SCVD-EBF retrofitted wood framed buildings in ArcGIS Pro: (a) IM-01; (b) IM-05; (c) IM-09........ 138
Figure 6.21 Normalized mean repair time (NRT- parallel working procedure) of Y-SCVD-EBF retrofitted wood framed buildings in ArcGIS Pro: (a) IM-01; (b) IM-05; (c) IM-09........ 139
Figure 6.22 Normalized mean repair time (NRT- serial working procedure) of Y-SCVD-EBF retrofitted wood framed buildings in ArcGIS Pro: (a) IM-01; (b) IM-05; (c) IM-09........ 141

Figure 6.23 Three-dimensional digital twin model of Y-SCVD-EBF retrofitted wood framed buildings symbolized based on normalized mean repair cost (NRC):
(a) IM-01; (b) IM-05; (c) IM-09 142
Figure 6.24 Three-dimensional digital twin model of Y-SCVD-EBF retrofitted wood framed buildings symbolized based on normalized mean repair time (NRT-parallel working procedure):
(a) IM-01; (b) IM-05; (c) IM-09 144
Figure 6.25 Three-dimensional digital twin model of Y-SCVD-EBF retrofitted wood framed buildings symbolized based on normalized mean repair time (NRT-serial working procedure):
(a) IM-01; (b) IM-05; (c) IM-09 145
Figure 6.26 Cumulative distribution function (CDF) of normalized mean repair cost (NRC) of typical wood framed residential buildings at different intensities: (a) 3-story; (b) 4-story 146
Figure 6.27 Normalized repair cost (NRC) at different intensity levels for typical buildings:
(a) 3-story, (b) 4-story 147
Figure 6.28 Normalized repair time (NRT) at different intensity levels for typical buildings considering Parallel working procedure: (a) 3-story, (b) 4-story 148
Figure 6.29 Normalized repair time (NRT) at different intensity levels for typical buildings considering Sequential working procedure: (a) 3-story, (b) 4-story 148
Figure 6.30 Story contribution of a typical 3-story multi-family residential building to the mean repair cost 149
Figure 6.31 Story contribution of a typical 4-story multi-family residential building to the mean repair cost 150
Figure 6.32 Contribution of the components of a typical three-story retrofitted wood framed residential building to the mean repair cost at different IMs 151
Figure 6.33 Contribution of the components of a typical four-story retrofitted wood framed residential building to the mean repair cost at different IMs 151
Figure 6.34 Contribution of the components of a typical three-story retrofitted wood framed residential building to the mean repair time at different IMs 152
Figure 6.35 Contribution of the components of a typical four-story retrofitted wood framed residential building to the mean repair time at different IMs 152

List of Abbreviations

Abbreviation	Meaning
DBE	Design Basis Earthquake
EBF	Eccentrically Braced Frame
EDP	Engineering Demand Parameter
FE	Frequent Earthquake
FEM	Finite Element Model
FF	Far-Field
IDR	Inter-Story Drift Ratio
MCE_R	Risk-Targeted Maximum Considered Earthquake
MDOF	Multi-Degree-of-Freedom
NDA	Nonlinear Dynamic Analysis
NLTH	Non-Linear Time History
NRC	Normalized Repair Cost
NRT	Normalized Repair Time
PGA	Peak Ground Acceleration
PIR	Probability of Irreparability
RHA	Response History Analysis
SAWS	Seismic Analysis of Wood-frame Structures
SCEBF	Self-Centering Eccentrically Braced Frame
SCVD	Self-Centering Viscoelastic Damper
SFRS	Seismic Force Resisting System
TPAD	Trapezoidal Plate Adding Damper
WSP	Wood Structural Panel
Y-SCVD-EBF	Y-type braced Self-Centering Viscous Damper Eccentrically Braced Frame

Chapter 1 : Introduction

1.1 Background

Light-frame wood structures have gained attentions for the construction of low to mid-rise buildings because of their high speed of construction, availability, and cost-effectiveness. In such buildings, timber shear walls provide the lateral force resisting system [1]. Many older timber-frame buildings are not following the modern seismic codes, and are considered as wood-frame buildings with soft stories [2]. There are considerable number of these multi-family three- and four-story buildings in California including in San Francisco Municipal Area [3]. Although such buildings are not seismically adequate in all their stories according to the current seismic provisions, the first story is much "softer" due to more openings such as the existence of doors of parking garages, or store windows. These buildings are seismically vulnerable due to inadequate strength and stiffness of their seismic force resisting system (SFRS) [4].

Light-frame timber structures have a relatively well seismic performance. This is because the seismic forces applied on a building are proportional to the weight of the structure, and such buildings are comparatively light and they have high strength-to-weight ratios. However, modeling the seismic behavior of wood-frame structures is extremely complicated due to the complexity of their load paths. Typical light-frame wood buildings are constructed of numerous framing elements and sub-assemblies, including walls and floor diaphragms, interconnected by dowel-type connectors [2].

Large inter-story drift at the soft story level is the main problem of a soft-story building during a moderate to intense earthquake. In such buildings, upper stories behave as a rigid body. The rigid body behavior of the upper stories causes severe structural damage because the most of the ground motion energy absorbed by the soft story causing soft-story collapse mechanism. Moreover, mechanical properties (stiffness, and strength) of the SFRS at each story can change due to the material degradation. It is estimated that more than 4,000 buildings with soft story exist in San Francisco alone which are prone to severe damage and even collapse during moderate to severe earthquakes [5]. Therefore, retrofitting these buildings is necessary to prevent a huge deadly human disaster [4].

To develop seismic-resilient load-resisting systems that minimize post-earthquake structural repair and reduce functional loss, high-performance self-centering systems have gained significant interest from researchers in recent years [6]. The primary objective of employing these systems is to reduce residual drift in buildings and confine seismic-induced damages to replaceable fuse devices. Therefore, the main structural system is designed to sustain no or minimal damage during a design basis earthquake. In most self-centering systems, characterized by a flag-shaped hysteresis loop, post-tensioned components or pre-compressed springs are utilized to provide the required restoring forces. Additionally, various types of dampers may be employed for energy dissipation.

1.2 Research Objectives

The first goal of this research is to retrofit the existing light-frame wood buildings with soft stories with wood structural panel (WSP) on all the stories. Such panels can be easily installed over the existing walls and they increase the seismic strength and stiffness of the structure.

The second goal is to develop new types of retrofitting systems which can be installed only on the ground story of an existing code deficient wood-frame building to strengthen the soft story seismically against near frequent earthquake (FE) intensities. The self-centering viscoelastic damper (SCVD) retrofitting systems consist of two sets of pre-compressed disc springs, fluid viscous damper (VD), and TPAD (Trapezoidal Plate Added Damping) which are connected to the bottom of a link beam. The preloading of such springs can be performed by prestressing equipment. It is worth noting that such retrofitting systems consist of displacement dependent (i.e. TPAD fuse) as well as velocity-dependent (i.e. viscous damper) energy dissipation devices which their energy dissipation performance is studied in a single system utilizing the two.

Retrofitting the entire building according to the current seismic codes is the next purpose of this research which was performed by installing Y-type braced self-centering viscous damper eccentrically braced frame (Y-SCVD-EBF) systems on all the stories. Such systems can be prefabricated, transported to the building site, and connected to the existing frame members. The ability to achieve the required strength and energy dissipation capacity only by adjusting the number of disc springs and/or the initial pre-compression level, combined with appropriately choosing the viscous damper, and sizing the fuse plates, makes this system particularly advantageous for seismic retrofit applications. Then, the seismic behavior of the entirely-retrofitted building was studied under design basis earthquake, and risk-targeted maximum considered earthquake. In such systems, the disc springs are employed as the self-centering (SC) elements, while fluid viscous damper (VD) and TPAD act as the sources of energy dissipation capacity. Self-centering systems are generally used to minimize the residual drift in structures after an earthquake by bringing the structure back to its initial position. While energy dissipation devices are only responsible for dissipating the seismic energy through the fluid damper viscosity, and flexural yielding of fuse plates.

Resilience is characterized as a measure of a system's robustness, redundancy, resourcefulness, and rapidity [7]. The implementation of innovative high-performance Y-SCVD-EBF systems can significantly improve the resilience metrics of buildings. Such systems can be used in any new building required to be highly resilient that must always operate. They can also be used to improve the resilience metrics of code deficient structures by reducing the repair time and repair cost, enhancing system robustness, and minimizing the residual drift associated with self-centering behavior. Wood frame residential buildings are one of those that should be essentially highly resilient. By retrofitting the code deficient light-frame wood buildings with high-performance portable Y-SCVD-EBF systems, those buildings would become highly resilient. Therefore, utilizing such a retrofitting system for improving the seismic performance of multi-family wood framed buildings, would enhance the regional resilience which is the motivation of the final goal of this research.

The last objective of this study was to conduct a regional resilience evaluation of light-frame wood buildings with soft story located in San Francisco that have been retrofitted with the proposed portable self-centering systems. The goal was to design a seamless methodology within the Python programming language, comprising multiple sequential procedures to depict the seismic losses of these structures visually. These steps entail the acquisition of seismic design parameters, generating of lumped mass models, conducting response history analyses (RHAs), obtaining engineering demand parameters (EDPs), estimating the quantities of both structural and nonstructural components, conducting damage and loss assessments, and visualizing resilience metrics. To efficiently conduct numerous RHAs, a simplified multi-degree-of-freedom (MDOF) shear building model, representative of self-centering systems, was recommended. For a quantitative exploration of seismic resilience metrics, an intensity-based probabilistic assessment of damage and loss was undertaken utilizing the FEMA P-58 methodology [8], recognized as a state-of-the-art component-level approach for probabilistic seismic damage and loss assessment in buildings. The total loss was computed by aggregating the losses of individual components within the building based on EDPs derived from RHAs. The probabilistic loss assessment employs the Monte Carlo simulation method to generate a large number of realizations, each representing a single random combination of potential values of uncertain factors and corresponding to a plausible performance outcome. Subsequently, resilience metrics for each building at each intensity measure (IM) was compiled into a data table and a shape file containing geographic information and resilience metrics for visualization in a geographic information system (GIS) software such as ArcGIS Pro, corresponding to each ground shaking intensity has been generated.

1.3 Dissertation Organization

This dissertation presents a comprehensive nonlinear numerical simulation study and a regional seismic resilience assessment of deficient wood framed structures retrofitted with self-centering viscoelastic dampers. The work is organized into seven chapters as follows:

- Chapter 1 presents the background, motivations, and objectives of the study, along with an overview of the dissertation's organization.
- Chapter 2 provides a review of previous research on light-frame wood structures, the development of self-centering eccentrically braced frame systems with various self-centering and damping mechanisms. Additionally, it discusses prior studies on the regional resilience assessment of buildings.

- Chapter 3 outlines the nonlinear numerical simulation study of the existing unretrofitted timber structure. A 4-story prototype light-frame wood building with soft stories was considered, and its seismic performance was then studied through nonlinear static and dynamic analysis. Additionally, wood structural panel (WSP) is used to retrofit all the stories, and the nonlinear seismic performance of the retrofitted building is studied. This type of retrofit is the main way to retrofit the upper stories; however, the first story is partially retrofitted with WSP. The seismic performance of the original and WSP-retrofitted building is then compared.
- Chapter 4 describes the nonlinear seismic performance study of the WSP-retrofitted wood structure retrofitted only on its ground story with the proposed self-centering viscoelastic damper (SCVD) system. A prototype retrofitting system is designed and its seismic responses are studied through nonlinear numerical static and dynamic analyses.
- Chapter 5 studies the nonlinear seismic behavior of the original light-frame timber building entirely retrofitted with the novel Y-type braced self-centering viscous damper eccentrically braced frame (Y-SCVD-EBF) systems. A prototype retrofitting system is designed and its seismic behavior is investigated through numerical static and dynamic analyses.
- Chapter 6 defines the computational workflow for an intensity-based regional seismic resilience assessment of Y-SCVD-EBF buildings. The regional seismic resilience of over two-thousands wood-frame residential buildings retrofitted with these systems was assessed for the San Francisco area.

- Chapter 7 summarizes the research findings, outlines the key conclusions, and offers suggestions for future study.

Chapter 2 : Literature Review

Previous studies on the seismic performance of light-frame wood buildings are initially discussed in this chapter. Following this, past research on the development of self-centering systems including self-centering eccentrically braced frames (SCEBFs) as a seismic force-resisting system is reviewed. The chapter concludes with a review of studies focused on the regional seismic damage and loss assessment of structures.

2.1 Seismic Behavior of Light-Frame Wood Buildings

Mid-rise light-frame wood buildings have become prevalent in areas prone to high seismic activities. The substantial deformation capacity intrinsic to wood elements and their associated joint connections, such as framing-to-framing and sheathing-to-framing connections, has demonstrated good structural performance when confronted with substantial seismic forces [9-11].

Light-frame wood buildings exhibit favorable performance owing in part to their high strength-to-weight ratios relative to structures constructed from other materials [2]. Similar to other light-weight structural systems, light-frame timber buildings take advantage of relatively low seismic lateral loads imposed upon them [12-14].

In light-frame wood constructions, the conventional mechanism for resisting lateral forces is established through wood shear walls. Early endeavors to replicate the hysteretic response of timber shear walls via numerical modeling were undertaken by Dolan [15], and Kasal and Xu [16]. Their findings indicated that the load capacity, stiffness, and ductility of timber shear walls are primarily dictated by the connections between sheathing and framing elements. Additionally, Benedetti et al. [1] showed that shear bracket connections and sheathing-to-framing connections control the structural seismic responses and failure mode.

Folz and Filiatrault [17] introduced a simplified numerical model designed to show the hysteretic behavior of an individual timber shear wall, which can be applied in the analysis of multi-story structures. Their numerical model formulation was integrated into the CASHEW software [18] using the SAWS (seismic analysis of wood-frame structures) constitutive model [17].

Folz and Filiatrault [19] also conducted an assessment of the accuracy of the SAWS model, offering a comparison between the numerical model and a full-scale experimental test conducted on a two-story wood-framed house. The numerical model showed proficiency in replicating the relative displacement observed in experimental trials.

Pei and van de Lindt [20] created a shear-bending formulation for light-frame timber structures that effectively replicates the global experimental behavior of timber wall systems. They found that in buildings with three or more stories, cumulative uplift and out-of-plane rotation of the horizontal diaphragm are critical factors to consider. Moreover, the response of stacked shear walls in a building differs from that of a single isolated wall.

Pei and van de Lindt [21] compared the seismic response of a six-story light-frame timber building using a numerical simulation based on their coupled shear-bending formulation [20] with experimental results. The simulation slightly underestimated inter-story displacement, and it did not fully capture the building's torsional behavior.

Pang et al. [2] extended the bi-dimensional shear wall model introduced by Christovasilis and Filiatrault [22] and Pang and Shirazi [23]. The model defines the floor diaphragm with 12 degrees of freedom, accounting for both in-plane and out-of-plane flexibilities. Moreover, it effectively captures the collapse mechanism of light-frame wood buildings.

Di Gangi et al. [24] developed a detailed model for single timber shear walls, incorporating each sheathing-to-framing connection, timber frame elements, and sheathing board. They used this model in a parametric study to assess the variables impacting the shear capacity of shear walls.

A detailed finite element modeling strategy was created by Kuai et al. [25] in order to examine the different deformation behaviors of timber walls. They concluded that this method could accurately replicate the experimentally observed local responses. Other efforts to create a detailed model of high-strength timber shear walls [26] and simplified models considering vertical loads and bending moments [27] were made on individual wall elements and did not include all connections or components. The extension of these models to entire building analysis is still in progress [25].

The number of U.S.-based initiatives conducting full-scale testing on light-frame wood buildings have experienced a notable surge since the late 1990s, attributable in part to the CUREE-Caltech Project [28,29] and projects affiliated with the National Science Foundation (NSF) George E. Brown Jr. Network for Earthquake Engineering Simulation (NEES) [3].

As part of the framework of the NEES-Wood Project, Filiatrault et al. [30] performed full-scale tri-axial tests on a two-story townhouse utilizing the twin shake tables located at the State University of New York at Buffalo. This structure was designed in accordance with the 1988 Uniform Building Code (UBC) [31,32]. They concluded that, in the context of light-frame wood buildings typical of the 1980s to 1990s in California, only moderate damage ensued during a seismic event at the DBE level, whereas substantial and economically burdensome damage occurred under conditions simulating the MCE_R level [3].

Mosalam and Mahin [33] tested a three-story apartment building with a tuck-under garage as part of the CUREE-Caltech wood-frame project. They concluded that these buildings are susceptible to torsional response and soft-story collapse.

Seim et al. [34] conducted a comprehensive study on oriented strand boards (OSBs) and gypsum fiber boards (GFBs) as sheathing materials for timber shear walls. They tested different light-frame wall elements and sheathing-to-framing connections with various layouts under cyclic and monotonic loading. Their findings show that timber-framed walls with OSB or GFB boards have similar cyclic responses in terms of energy dissipation and deformation capacity.

To address the seismic vulnerability of wood-frame buildings deemed at risk, van de Lindt et al. [35] and Bahmani et al. [36] performed validation studies of the FEMA P807 retrofit guideline and devised a Performance-Based Seismic Retrofit (PBSR) methodology. This validation process involved a series of comprehensive shake table experiments conducted on a four-story wood-frame building as part of the NEES-Soft project. Two distinct retrofit methodologies were employed for the four-story wood-frame structure. The first methodology, outlined in the FEMA P-807 Guideline [37], was developed by the Applied Technology Council (ATC) and subsequently published as Federal Emergency Management Agency (FEMA) Report P-807 [37]. The second approach, developed within the framework of the NEES-Soft project, entailed the Performance-Based Seismic Retrofit (PBSR) involves a technique that separates building deformation resulting from translation and torsion during the design phase [4,38].

The Federal Emergency Management Agency (FEMA) commissioned the Applied Technology Council (ATC) to develop guidelines (FEMA P-807 [37]) for retrofitting weak first-story wood-frame buildings vulnerable to collapse during earthquakes. These guidelines propose cost-effective retrofit approaches focusing on the first story, reducing the need for occupants to relocate during construction. By setting limits on retrofit strength and stiffness and considering nonstructural walls, the guidelines aim to prevent structural damage. They employ surrogate models to assess retrofit performance probabilistically, offering a wider range of retrofitting options. The default performance level, termed the 'Onset of Strength Loss' (OSL), is determined by inter-story drift limits. FEMA P-807 [37] categorizes systems based on ductility levels, providing specific criteria for low and high ductility systems [3].

2.2 Self-Centering Eccentrically Braced Frame (SCEBF) Systems

Eccentrically braced frames (EBFs) which are widely used as the structural seismic load resisting systems, consist of columns, beams, link beam, and bracings. In order to study the residual deformation of such frames after an earthquake, researchers performed experimental and numerical studies on EBFs equipped with self-centering systems.

Developing self-centering seismic resistant systems employing damping devices, such as fuse devices, in order to dissipate seismic energy from ground motion has gained interests in the last two decades. They are of structural engineers' interests because of their capability to control the residual deformation [39-43]. This approach aims for the main structural system to sustain minimal to no damage during design basis earthquake (DBE). Nonetheless, under risk-targeted maximum considered earthquake (MCE_R), yielding may occur in frame members or supplementary damping elements (e.g., pre-compressed disc springs), although without permitting fracture. Conventional ductile structures may exhibit large residual deformations following a severe seismic event, potentially raising concerns about occupant safety, impeding structural response to subsequent aftershocks, and substantially inflating the costs associated with post-seismic repair or replacement. A characteristic feature of self-centering systems is the presence of a flag-shaped hysteresis loop, facilitating minimal residual structural deformation upon unloading [6].

Researchers investigated various mechanisms for providing the restoring force in self-centering systems including post-tensioning cables, shape memory alloys, ring springs, and disc springs [44-51]. There has been an increasing focus on the using of ring springs and disc springs to generate the restoring force in self-centering systems [52]. Fang et al. [53] introduced a self-centering device utilizing preloaded disc springs intended for application in braced frames. Through a full-scale test, they demonstrated that the device could offer adequate ductility for the frame, sustaining inter-story drift ratios of up to 4%. Wang and Wang [54] recommended employing stacked coned disc springs. Their study investigated the asymmetric hysteric behavior of stacked disc springs and the frictional energy resulting from sliding between the surfaces of the discs.

Cheng et al. [55] incorporated the self-centering concept into the connection between the link beam and adjacent beams using post-tensioned (PT) strands. They tested the full-scale system under cyclic tests which was a one-story one-span eccentrically braced frame. The results showed that the frame sustained no damage during testing, with only minimal residual drifts.

Replaceable hysteretic damper (RHD) fuse devices' seismic behavior has attracted much attention because of their proper energy dissipation capacity. These fuses are typically made of low-yield steel material. They absorb seismic energy, get damaged, and can be quickly replaced after the earthquake. Tong et al. [56] conducted an experimental and analytical investigation on a full-scale D-type self-centering eccentrically braced frame (SCEBF-D) system with RHD fuse devices. They concluded that, after cyclic loading up to a 2.5% drift ratio, the stiffness, strength, recentering capability, and energy dissipation of the SCEBF systems with the replaceable RHD fuse devices were approximately identical to the original structure. Additionally, the damage was limited to the fuse devices only in the SCEBF systems. Figure 2.1 shows the test setup and the rocking link configuration.

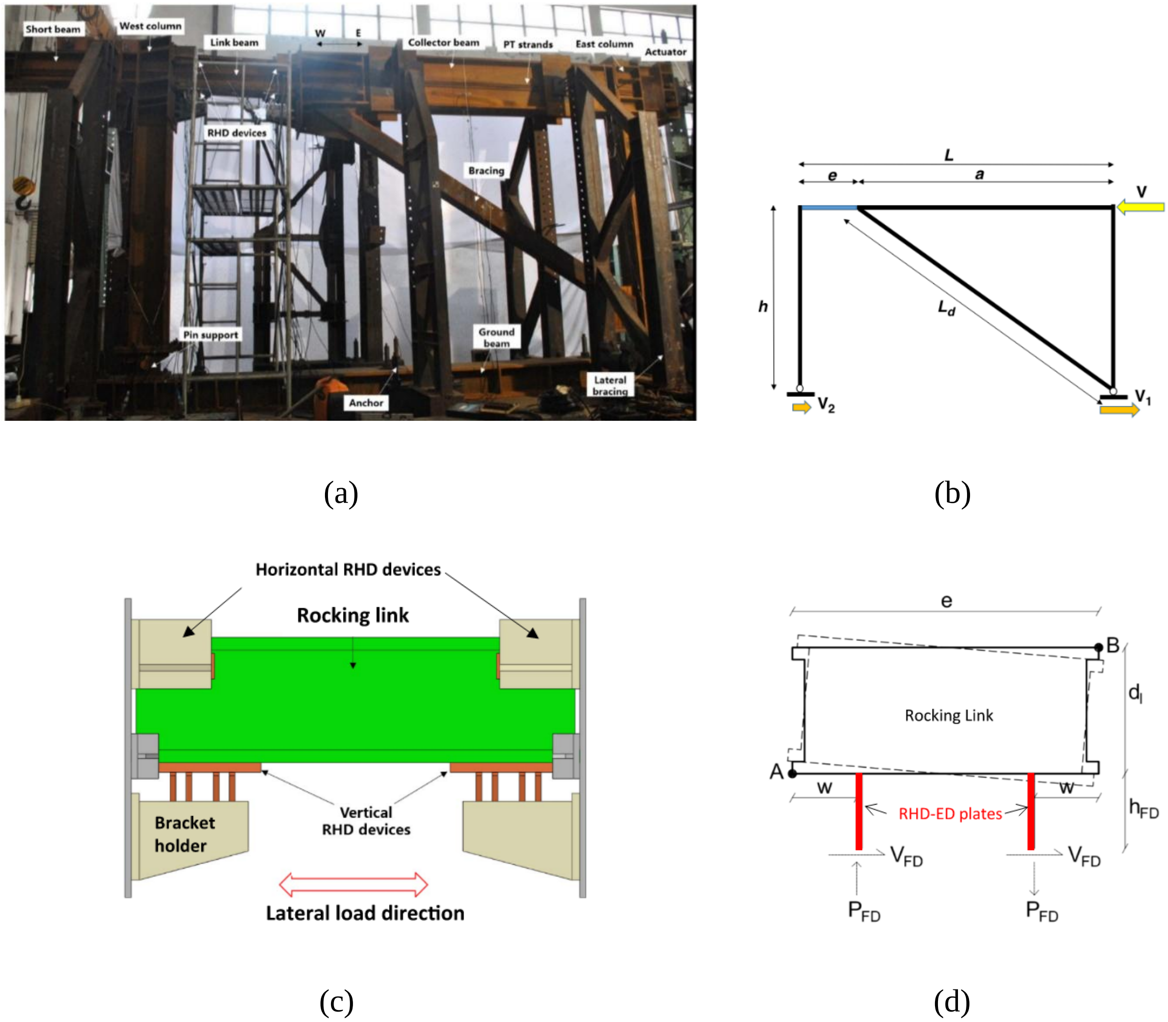

Figure 2.1 Prototype D-type SCEBF system with RHD fuse devices: (a) experimental test setup; (b) module configuration; (c) schematics of RHD devices installed to rocking link beam; (d) free-body diagram of RHD devices attached to the rocking link (Tong et al. [56])

Keivan and Zhang [57] conducted numerical and analytical studies on the nonlinear seismic performance of a three-story Y-type self-centering eccentrically braced frame (SCEBF-Y) structure using RHD fuses. Their system included a gap between the free end of the rocking link beam and the support beam to allow for vertical gap-opening. The structure was subjected to ground motion records scaled to represent seismic design levels in Los Angeles. Their findings indicated that the primary structural members remained elastic due to the implementation of RHD devices, while PT strands facilitated the recentering of the structure. Figure 2.2 shows the schematic view of the module structure without the RHD devices.

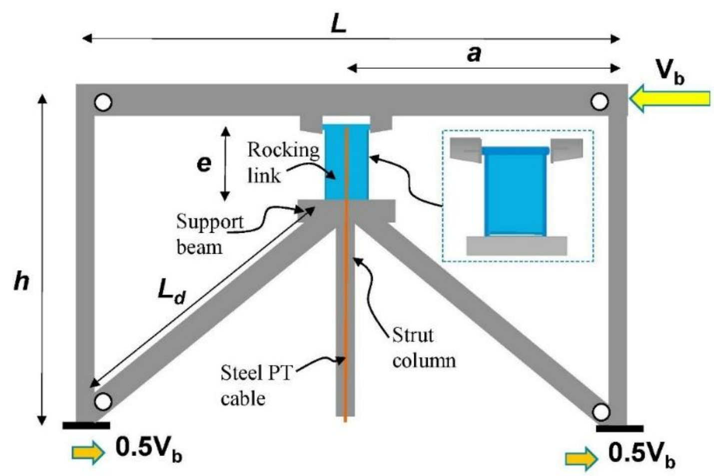

Figure 2.2 Schematic view of SCEBF-Y module structure without RHD devices (Keivan and Zhang [57])

Keivan and Zhang [58] analyzed the seismic performance of a three-story D-type and a four-story K-type self-centering eccentrically braced frame (SCEBF-K) structure using response history analysis (RHA). Their findings indicated that SCEBF buildings can be designed to achieve stiffness and ductility levels comparable to conventional eccentrically braced frames (CEBFs). Figure 2.3 illustrates the module frame configuration of K-type SCEBF structure.

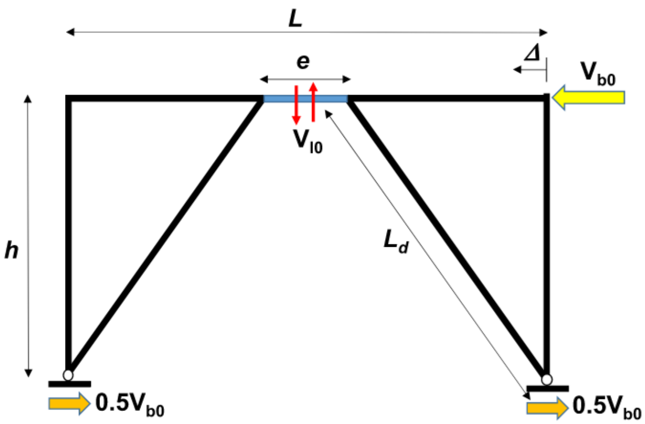

(a)

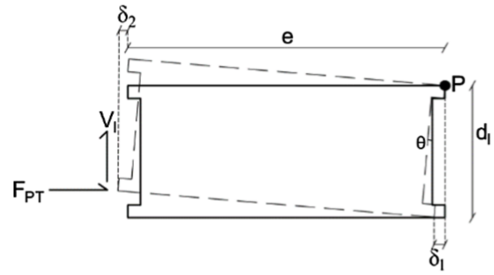

(b)

Figure 2.3 Configuration of K-type SCEBF module structure: (a) module frame; (b) free body diagram of rocking link beam (Keivan and Zhang [58])

Rezvan and Zhang [59] investigated the seismic behavior of the D-type self-centering eccentrically braced frame with a sliding rocking link beam (SCEBF-SRL) through nonlinear static and dynamic analysis of three- and six-story prototype buildings. PT steel-stranded cables and RHD were used as the recentering and energy dissipation devices, respectively. Their nonlinear dynamic analysis (NDA) results show that the ensemble median of the maximum inter-story drift ratios (IDRs) for both prototypes was below 1.4% at the DBE level, and under 2.0% at the MCE_R level. They also concluded that both buildings fully recentered at the MCE_R level, with negligible residual drifts of less than 0.01%. Figure 2.4 shows the elevation view of the structure, and the rocking zone in the system.

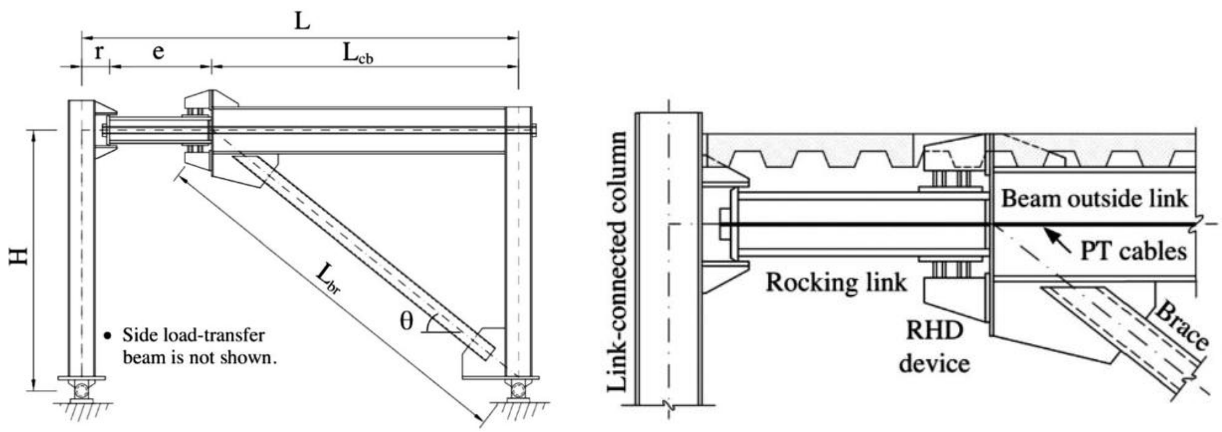

(a) (b)

Figure 2.4 Schematics of D-type SCEBF-SRL: (a) elevation view; (b) rocking zone (Rezvan and Zhang [59])

Rezvan and Zhang [52] performed a nonlinear numerical study of the self-centering moment-resisting frames with sliding rocking beams (SCMRF-SRB). In their proposed system, the restoring force was provided by two sets of preloaded disc springs, and RHD were responsible for energy dissipation. The results of their nonlinear dynamic analyses of the three-story prototype building located in downtown Seattle illustrated that the structure showed the expected seismic performance criteria in terms of recentering behavior, and IDR at DBE. Figure 2.5 demonstrates the SCMRF-SRB module schematics and components.

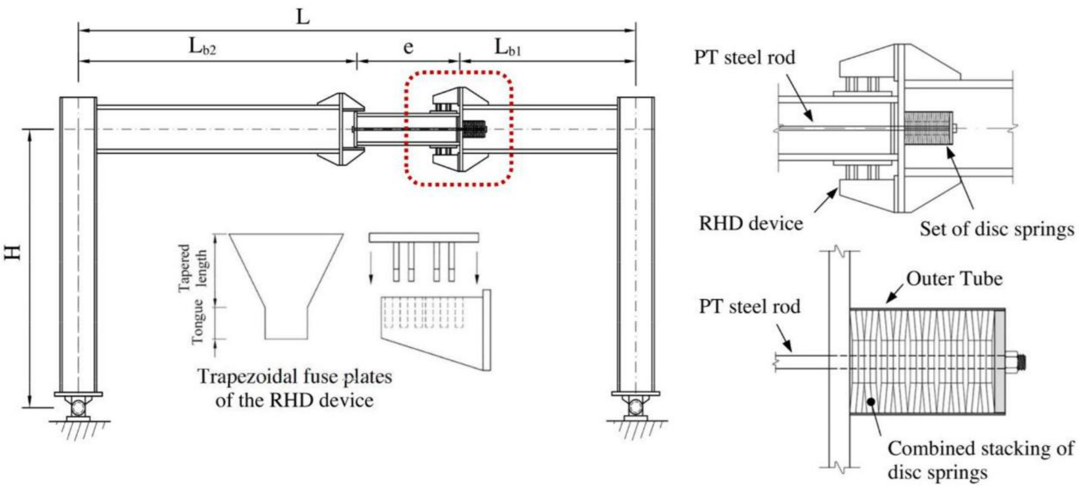

Figure 2.5 Schematics and components of the SCMRF-SRB module (Rezvan and Zhang [52])

Self-centering structures with displacement-based energy dissipation mechanisms face a trade-off between restoring force and energy absorption [60]. While friction [61,62] or material yielding [63,64] dissipates energy during an earthquake, they also weaken the structure's ability to return to its original position. This is because the forces needed for energy dissipation must be lower than the restoring force (prestressing of PT cables or precompression of disc springs). This leads to insufficient energy dissipation under a high frequency excitation [60]. As a result, the structure may deform excessively [65] increasing the risk of collapse which makes self-centering structures less appealing because the damage to drift-sensitive components like walls and pipes is challenging to repair [60].

Such structures often experience higher peak absolute floor accelerations compared to conventional structures with similar base shear due to the reduced energy dissipation and the sudden transitions of the flag-shaped behavior [66]. These accelerations are a major contributor to non-structural failures within the building, leading to injuries, fatalities, and damage to contents [67]. To address this issue, self-centering velocity-dependent energy dissipation mechanisms, like self-centering viscous dampers (SCVDs), can be employed to enhance energy absorption without compromising self-centering capability [60].

Tang and Lui [68] proposed and examined a hybrid recentering energy dissipation device that combines the recentering and energy dissipation capabilities. The hybrid shape memory alloy (SMA) recentering viscous fluid (RCVF) energy dissipation device, connects the apex of a chevron brace to an adjoining beam using two sets of SMA wires arranged in series on each side, with a viscous fluid damper placed in parallel to the SMA wires. The viscous damper was utilized because, as a velocity-dependent energy dissipation device, it does not oppose the recentering force. They conducted comparative studies on some single-story shear frames and four-story steel frames to investigate the performance of the proposed device. They concluded that the hybrid device makes the frames experiencing significantly reduced peak top story displacements and residual story drifts. Their proposed hybrid viscous device is shown in Figure 2.6.

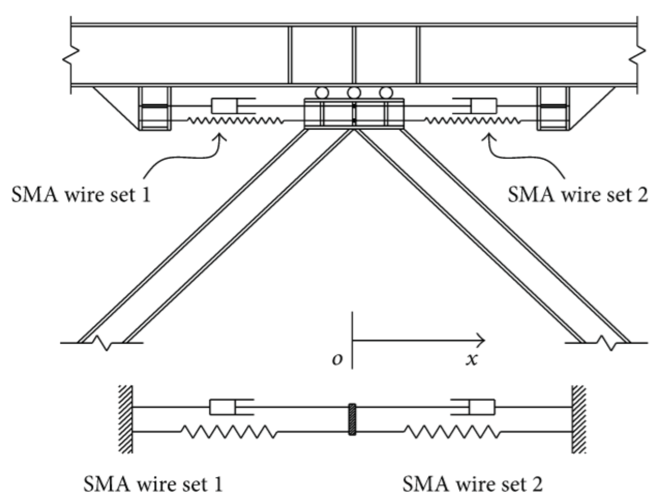

Figure 2.6 Conceptual design of a hybrid viscous SMA device (Tang and Lui [68])

Nasab and Kim [69] proposed a hybrid steel slit–viscoelastic damper (HSVD) to improve the structural seismic performance. They performed experimental studies to validate the analytical model, and to understand the viscoelastic and the hybrid damper behavior. They investigated seismic performance of a three-story moment-resisting frame, before and after retrofitting with steel slit dampers and HSVDs. Fragility analysis showed that adding a viscoelastic component to the steel slit damper significantly enhanced the seismic performance. They also found that the capacity and demand diagram procedure is effective for the preliminary design of hybrid dampers to achieve specific performance targets. Figure 2.7 shows the configuration of the HSVD, and Figure 2.8 shows the experimental test setup.

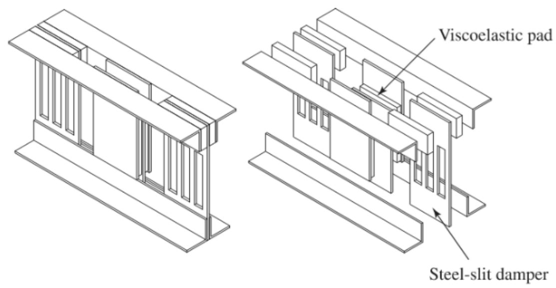

(a) (b)

Figure 2.7 Configuration of the HSVD: (a) hybrid damper; (b) components of the damper (Nasab and Kim [69])

Figure 2.8 Experimental test setup of viscoelastic damper (Nasab and Kim [69])

Yan et al. [60] developed a self-centering viscous damper (SCVD) system in order to enhance the structural seismic resiliency. The proposed damper showed significant flexibility in load resistance, deformability, and velocity-dependent energy dissipation. Their experimental studies demonstrated flag-shaped hysteretic behavior, minimal strength degradation, and reliable energy dissipation, achieving a maximum equivalent viscous damping of 38.33% at high frequencies. Their results showed that the self-centering mechanism was fully effective by the end of loading. A system-level analysis compared the SCVD's performance with buckling-restrained and conventional self-centering braced frames, illustrated the SCVD's superior control over peak and residual deformation, as well as peak floor acceleration. Figure 2.9 shows the schematics of the SCVD device.

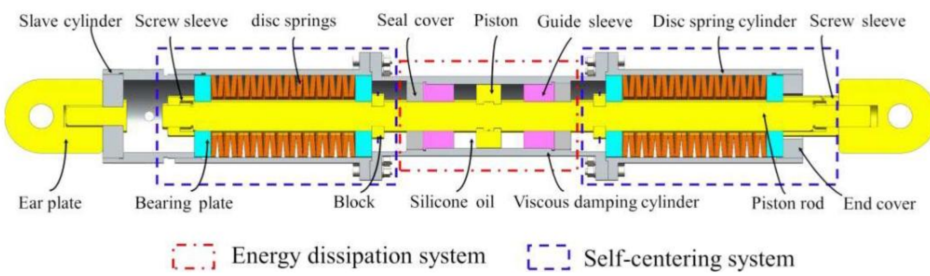

Figure 2.9 Schematics of the SCVD system (Yan et al. [60])

Qiu et al. [70] applied the performance-based plastic design (PBPD) method to hybrid braced frames (HBFs) with self-centering braces (SCBs) and fluid viscous damping braces (FVDBs). Combining SCBs with FVDBs in parallel presents a promising seismic-resistance approach, as it effectively controls peak deformation, peak acceleration, peak base shear, and minimizes residual deformation. The PBPD method begins by selecting target drift and yield mechanism, then derives the design base shear utilizing the energy equivalent concept. A critical step involves obtaining constant-ductility spectra for equivalent single-degree-of-freedom systems through non-linear time history (NLTH) analysis, and incorporating regression functions into the PBPD process. The NLTH analysis results confirmed that the frames met the performance targets, showing the robustness of the design method. This method could also be applicable to other hybrid systems with displacement- and velocity-dependent damping braces. The hybrid bracing system is illustrated in Figure 2.10.

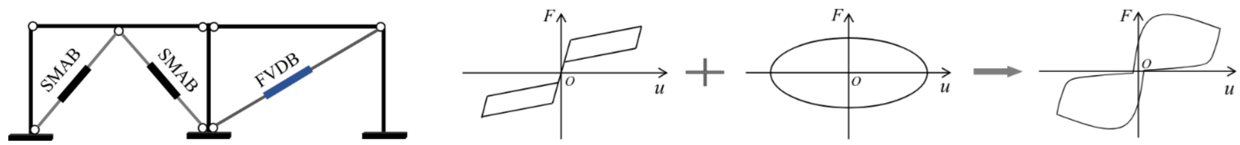

(a) (b)

Figure 2.10 Hybrid bracing system: (a) schematic of a single story HBF; (b) hysteretic behavior under cyclic dynamic loading (Qiu et al. [70])

2.3 Regional Seismic Resilience Assessment

The primary goal of self-centering systems is to enhance the resilience of a structure by mitigating seismic losses incurred by the building following an earthquake. Seismic loss estimation has been investigated for various types of self-centering systems ([6,71,72]).

One of the prominent approaches for regional loss estimation has been developed through the HAZUS program [73-75]. This program offers data, standards, and tools designed to assess regional risk associated with various natural hazards [76]. It utilizes the capacity response spectrum method and models buildings as single-degree-of-freedom (SDOF) systems [77-80].

The FEMA P-58 methodology stands as the modern approach for component-level probabilistic seismic damage and loss assessment of buildings by considering the maximum structural responses from response history analysis (RHA) as the engineering demand parameters (EDPs) [8,81]. This methodology comprises of four distinct analyses: hazard analysis, structural analysis, damage analysis, and loss analysis [82]. According to the component fragility curves, and related consequences provided by FEMA P-58, the damage and loss evaluation is conducted by aggregating the damage to both structural and nonstructural components within each story [8, 83,84]. The utilization of the FEMA P-58 methodology for seismic loss assessment at a regional scale presents a notable challenge due to the extensive computational time needed for conducting numerous RHAs to obtain EDPs, and the lack of information in order to assemble buildings' performance models [81,85]. Achieving an optimal balance between reliability, practicality, and computational efficiency in defining the refinement level of the numerical model depends on the available computational resources [86].

Efficient acquisition of EDPs for numerous buildings at a city scale can be achieved with reasonable accuracy through the adaptation of multi-story concentrated-mass shear models. Lu and Guan [87] introduced a method for generating lumped-mass models of conventional structures in a city scale using simplified pinching hysteretic behavior in order to perform a nonlinear RHA. Additionally, Lu et al. [88] developed an open-source framework for regional earthquake loss estimation utilizing the building inventory of the region and conducting nonlinear RHA employing simplified MDOF shear building models in San Francisco.

Yi et al. [89] performed a multi-scale cost-benefit analysis of the Los Angeles soft-story ordinance for wood-frame residential buildings. They employed the FEMA P-58 seismic loss assessment methodology [8] to compute building-specific loss functions on archetype buildings representing various structural characteristics affected by the ordinance. Cost-benefit ratio is determined by dividing retrofit cost by earthquake-induced loss reduction. They concluded that the probability of achieving a desirable cost-benefit ratio within a 50-year period is roughly 0.9.

Figure 2.11 illustrates the location of soft, weak, and open front (SWOF) buildings in Los Angeles. FEMA P-58 loss assessment component information is summarized in Table 2.1.

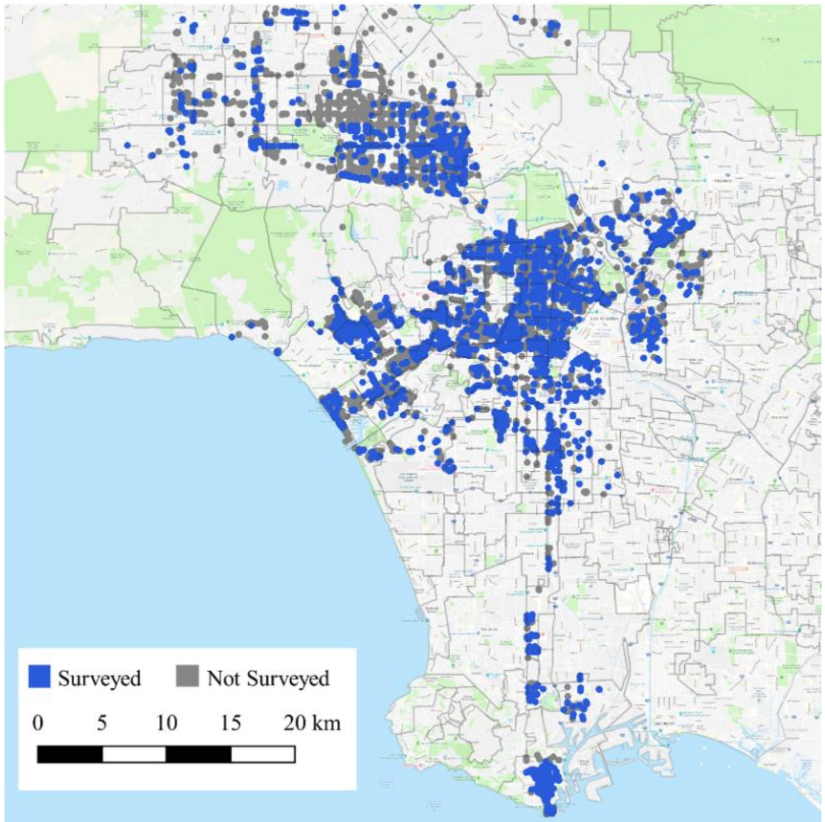

Figure 2.11 Map showing the location of SWOF buildings in the city of Los Angeles (Yi et al. [89])

Table 2.1 Components considered in the FEMA P-58 loss assessment (Yi et al. [89])

Component Name	Fragility Unit	Demand Parameter	Direction
Light framed wood lateral walls	100 SF	Story Drift Ratio	Directional
Steel Column Base Plates	1 EA	Story Drift Ratio	Directional
Welded Steel Moment Connection	1 EA	Story Drift Ratio	Directional
Prefabricated steel stair no seismic joint	1 EA	Story Drift Ratio	Directional
Potable Water Piping	1000 LF	Peak Floor Acceleration	Non-directional
Heating Water Piping	1000 LF	Peak Floor Acceleration	Non-directional
Heating Water Pipe Bracing	1000 LF	Peak Floor Acceleration	Non-directional
Sanitary Waste Piping	1000 LF	Peak Floor Acceleration	Non-directional
HVAC Ducting	1000 LF	Peak Floor Acceleration	Non-directional
Fire Sprinkler Water Piping	1000 LF	Peak Floor Acceleration	Non-directional
Fire Sprinkler Drop	100 EA	Peak Floor Acceleration	Non-directional
Low Voltage Switchgear	1 EA	Peak Floor Acceleration	Non-directional
Wall Partition, Wood Stud	100 LF	Story Drift Ratio	Directional
Clay tile roof	100 SF	Peak Floor Acceleration	Non-directional

You et al. [90] studied the probabilistic seismic performance of a 20-story cross-laminated timber coupled-wall (CLT-CW) structure, focusing on economic loss, downtime, and resilience index. They developed a model for incremental dynamic analysis using 30 pairs of ground motion records, reflecting the seismicity of Vancouver, Canada. They performed intensity-based and time-based loss assessments following the FEMA P-58 methodology [8] to estimate seismic loss probability distributions. Seismic resilience indices at various intensities were also calculated. They concluded that coupling beams contribute the most to repair costs, but their replaceability and energy dissipation capabilities enhance the building's efficiency and resilience, validating the CLT-CW system's effectiveness. Table 2.2 illustrates the total quantity of each nonstructural component.

Table 2.2 Quantity of nonstructural components (You et al. [90])

Pact fragility no.	Name	Performance group quantity	Unit	Dispersion	Direction	Floor
B2022.001	Curtain walls	58.61	30 SF	0.6	1	All
B2022.001	Curtain walls	58.61	30 SF	0.6	2	All
B3011.011	Concrete tile roof	37.51	100 SF	0.9	—	Roof
C1011.011a	Wall partition	14.06	100 LF	0.3	1	All
C1011.011a	Wall partition	14.06	100 LF	0.3	2	All
C2011.001a	Stairs	1.41	1 EA	0.1	1	All
C2011.001a	Stairs	1.41	1 EA	0.1	2	All
C3011.001a	Wall finishes	4.47	100 LF	0.4	1	All
C3011.001a	Wall finishes	4.47	100 LF	0.4	2	All
D2021.011a	Potable water piping	1.24	1000 LF	0.4	—	All
D3041.011a	HVAC ducting	0.58	1000 LF	0.6	—	All
D3041.031a	HVAC drops/diffusers	9.37	10 EA	0.4	—	All
D3041.041a	Variable air volume box	4.68	10 EA	0	—	All
D4011.021a	Fire sprinkler water piping	2.57	1000 LF	0.1	—	All
D4011.031a	Fire sprinkler drop	1.40	100 EA	0.1	—	All
D5011.011a	Transformer	11.70	1 EA	0.5	—	1
D5012.021a	Low voltage switchgear	0.04	225 AP	0.3	—	All
D5012.031a	Distribution panel	3.05	1 EA	0.2	—	1
D1014.011	Traction elevator	7.97	1 EA	0.8	—	1

EA: each; SF: square feet; LF: linear foot; HVAC: heating, ventilation, and air conditioning; AP: ampere.

Lu et al. [91] performed a regional seismic damage assessment of reinforced masonry structures by performing an RHA utilizing a MDOF shear building model. They investigated the damage of almost 200 buildings located at a university campus in China. Figure 2.12 illustrates the probability density function for each damage state across the regional reinforced masonry buildings.

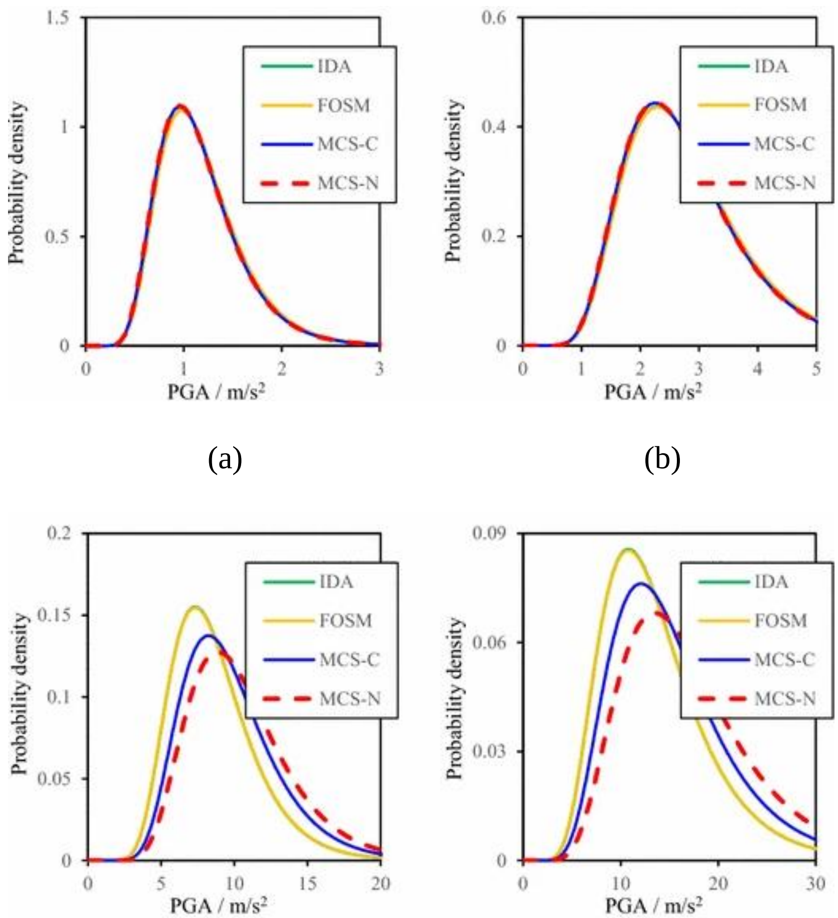

(a) (b) (c) (d)

Figure 2.12 Probability density function for regional reinforced masonry structures: (a) Slight damage; (b) Moderate damage; (c) Extensive damage; (d) Complete damage (Lu et al. [91])

Rezvan and Zhang [6] developed a procedure to conduct a regional intensity-based seismic resilience assessment of a structural system. They reported the results (e.g. repair cost, repair time, and probability of irreparability) at different intensities and in different contexts. They performed a regional seismic resilience assessment of self-centering eccentrically braced frames (SCEBFs) by conducting a probabilistic intensity-based damage and loss assessment of school buildings in San Francisco using FEMA P-58 procedure [8]. In their study, they simulated the flag-shaped hysteresis behavior of the SCEBF systems by using a spring model. Their results show that at smaller intensities, nonstructural components contribute the most to the regional seismic losses, and irreparable damages are negligible. They concluded that structural components do not contribute to the losses, and the replacement of fuse devices might be necessary only at very large IDRs. It was also shown that the proportional contribution of each nonstructural component to the overall loss of nonstructural elements varies depending on the intensity. For certain components, their relative contribution increases as intensity rises, while for others, the contribution decreases. Additionally, some components, like variable air volume systems, have a minimal impact on seismic losses. Figure 2.13 illustrates their proposed SCEBF system.

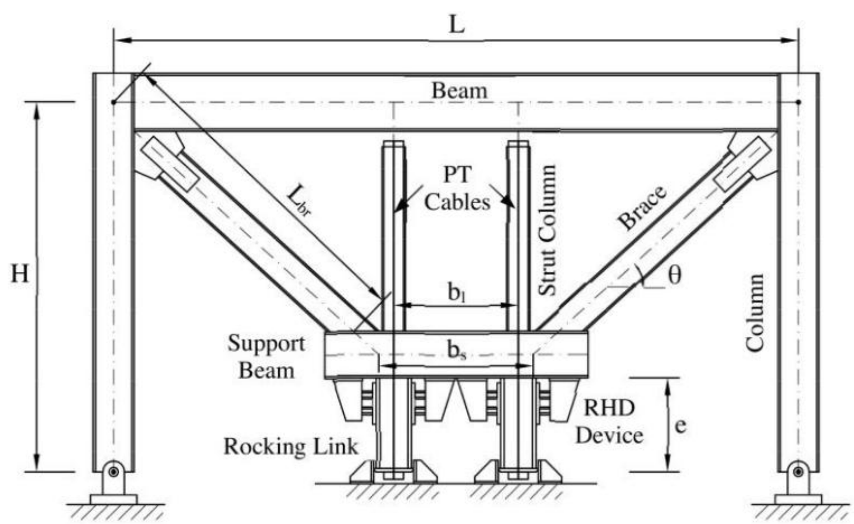

Figure 2.13 Schematics of the modular self-centering eccentrically braced frame system

(Rezvan and Zhang [6])

Chapter 3 : Nonlinear Seismic Analysis and Performance Study of Soft-Story Wood Framed Structures Retrofitted with Wood Structural Panel (WSP)

In this chapter, the nonlinear seismic performance of soft-story light-frame timber structures has been studied. The original unretrofitted structure then has been seismically strengthened with wood structural panels (WSPs) and the seismic behavior of the retrofitted structure has been investigated as well. The nonlinear seismic behavior of both structures has been studied through static and dynamic analysis of the four-story prototype wood building under far-field ground motions.

3.1 Seismic Behavior of the System

Figure 3.1 shows the prototype unretrofitted light-frame wood building. The original timber structure consists of the original wood-frame including the timber columns, beams, and wood shear walls sheathed with HWS (horizontal wood siding) and GWB (gypsum wall board). In the retrofitted structure, the building has been seismically strengthened with WSP (wood structural panel) on all the four stories; however, retrofitting the first story with WSP is limited due to unavailability of existing timber shear walls because of existence of more openings. Figure 3.2 illustrates the WSP-retrofitted building. As illustrated, in a typical wood framed structure, the lateral resistance is provided by timber shear walls and the wood floor deck at each level. In order to study the seismic behavior of the light-frame wood structures in the numerical finite element model, SAWS springs were used to simulate the hysteretic behavior of the wood-frame lateral load resisting system. In the models, the story height, and bay width are considered as $\mathrm{H} = 3150$ mm, and $\mathrm{W} = 5830$ mm, respectively.

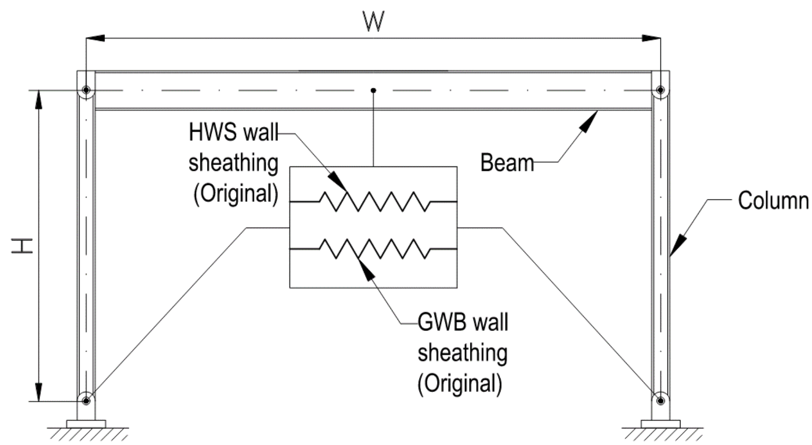

Figure 3.1 Schematics, and components of the original unretrofitted wood-frame building

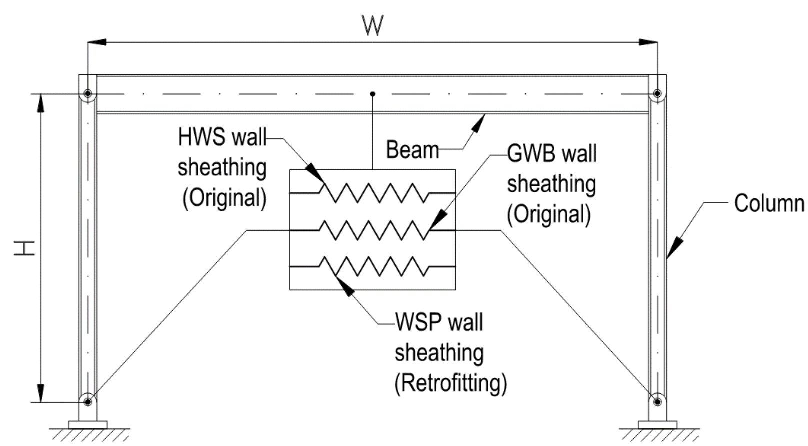

Figure 3.2 Schematics, and components of the original wood-frame building retrofitted with wood structural panel (WSP)

3.2 Analytical Load-Displacement Relationships of Timber Structures

Folz and Filiatrault [92] investigated the analytical load-displacement relationships of timber shear walls. They studied the structural behavior of timber wall sheathings (e.g. HWS, GWB, and WSP). Figure 3.3 presents the load-displacement behavior of timber shear walls representing the popular ten-parameter hysteretic spring for sheathed wood shear walls used in numerical modeling of wood-frame structures.

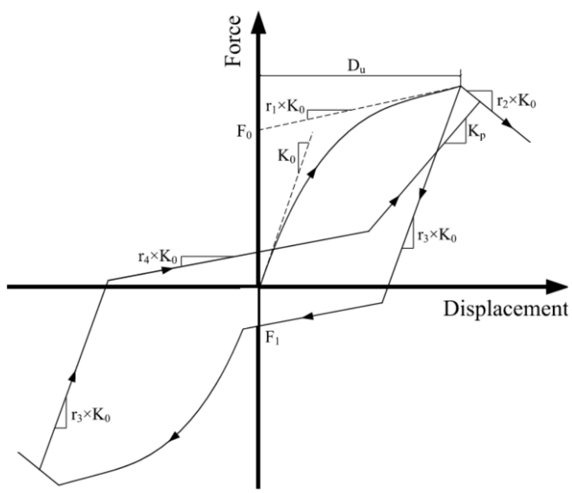

Figure 3.3 Load-displacement behavior of timber shear walls [4]

Table 3.1 summarizes the ten parameter values of the SAWS model required in the FE OpenSees software [93]. As can be observed, WSP stiffness and strength are highly dependent on the nailing pattern. Denser nail schedule procedure may be followed in order to have a stiffer and stronger element. SAWS model parameters are defined as follows [93]:

K_0: Initial stiffness of the shear wall spring element ($K_0 > 0$).
F_0: Intercept strength of the shear wall spring element for the asymptotic line to the envelope curve ($F_0 > F_1 > 0$).
F_1: Intercept strength of the spring element for the pinching branch of the hysteretic curve ($F_1 > 0$).
r_1: Stiffness ratio of the asymptotic line to the spring element envelope curve. The slope of this line is r_1K_0 ($0 < r_1 < 1.0$).
r_2: Stiffness ratio of the descending branch of the spring element envelope curve. The slope of this line is r_2K_0 ($r_2 < 0$).
r_3: Stiffness ratio of the unloading branch off the spring element envelope curve. The slope of this line is r_3K_0 ($r_3 > 1.0$).
r_4: Stiffness ratio of the pinching branch for the spring element. The slope of this line is r_4K_0 ($r_4 > 0$).

D_u: Spring element displacement at ultimate load ($D_u > 0$).
α: Stiffness degradation parameter for the shear wall spring element (α > 0).
β: Stiffness degradation parameter for the spring element (β > 0).

Table 3.1 Hysteretic Parameters required to create the timber shear wall SAWS model* [4]

Type of lateral force resisting element		Fastener spacing, mm (in.)	K_0, N/mm/m (lb./in./ft)	F_0, N/m (lb./ft)	F_1, N/m (lb./ft)	r_1	r_2	r_3	r_4	D_u, mm (in.)	α	β
Existing SFRS	**HWS** [(a)]	406 (16)	85 (148)	657 (45)	248 (17)	0.095	-0.95	1.01	0.035	206 (8.1)	0.45	1.06
	GWB [(b)]	406 (16)	259 (450)	1459 (100)	95 (6.5)	0.023	-0.04	1.01	0.01	28 (1.1)	0.8	1.1
Retrofit SFRS	**Wood Shear Wall** [(c)] **(Wood Structural Panel)**	51/305 (2/12)	2431 (4232)	29026 (1989)	3605 (247)	0.03	-0.073	1.01	0.033	50 (1.97)	0.76	1.24
		76/305 (3/12)	2176 (3787)	18635 (1277)	2481 (170)	0.032	-0.06	1.01	0.023	48 (1.9)	0.71	1.29
		102/305 (4/12)	1740 (3028)	14680 (1006)	2131 (146)	0.026	-0.056	1.01	0.022	47 (1.85)	0.76	1.29
		153/305 (6/12)	1355 (2359)	9850 (675)	1328 (91)	0.025	-0.049	1.01	0.019	47 (1.84)	0.71	1.29
		305/305 (12/12) [(d)]	416 (724)	3026 (207)	407 (27.9)	0.025	-0.049	1.01	0.019	47 (1.84)	0.71	1.29

* The parameters are based on 305 mm (1 ft) length of the sheathing.

(a) 19×184 mm (0.75×7.25 in.) horizontal wood siding fastened to vertical wall stud with two 8d common nails.

(b) 12.7 mm (0.5 in.) gypsum wall board fastened with #6 bugle head coarse threaded drywall screws.

(c) 12 mm (15/32 in.) thick sheathing-rated plywood fastened with 10d common nails.

(d) 9.5 mm (3/8 in.) thick sheathing-rated plywood fastened with 6d common nails.

3.3 Finite Element Modeling

2D wireframe numerical models, which were created in the FE software OpenSees [93], include all structural components and nonlinear behaviors. Schematic views of the numerical model of the original unretrofitted timber light-frame building, and the WSP-retrofitted wood framed structure are shown in Figure 3.4 and Figure 3.5, respectively. In these FE numerical models, lateral resistance is provided by wood shear walls only which are simulated using SAWS springs.

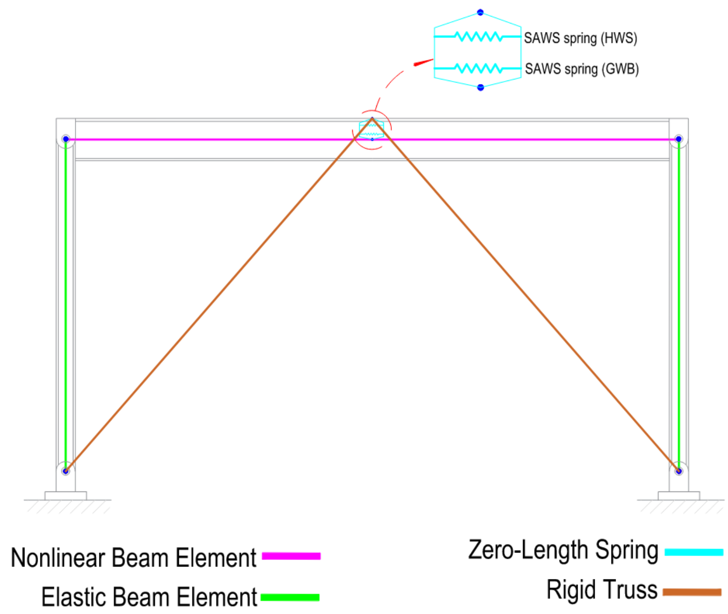

Figure 3.4 2D Numerical wireframe modeling of the original unretrofitted timber structure in OpenSees

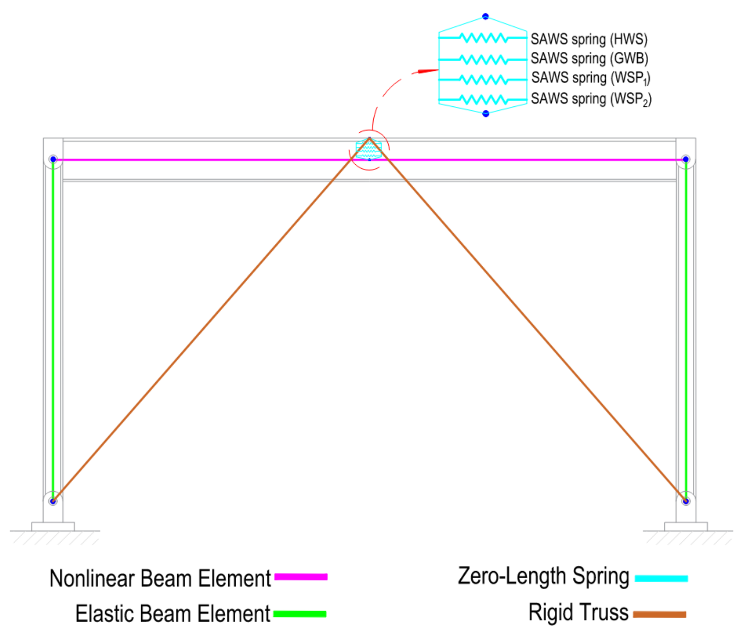

Figure 3.5 2D Numerical wireframe modeling of the original timber structure retrofitted with WSP in OpenSees

In the numerical models developed, “Steel02” material from the OpenSees [93] library with isotropic hardening parameters was used for all structural steel members, and the hardening parameters of Q225 low yield (Q225LY) steel were calibrated based on the material coupon test data as shown in Figure 3.6. The calibrated hardening parameters are illustrated in Table 3.2 [6].

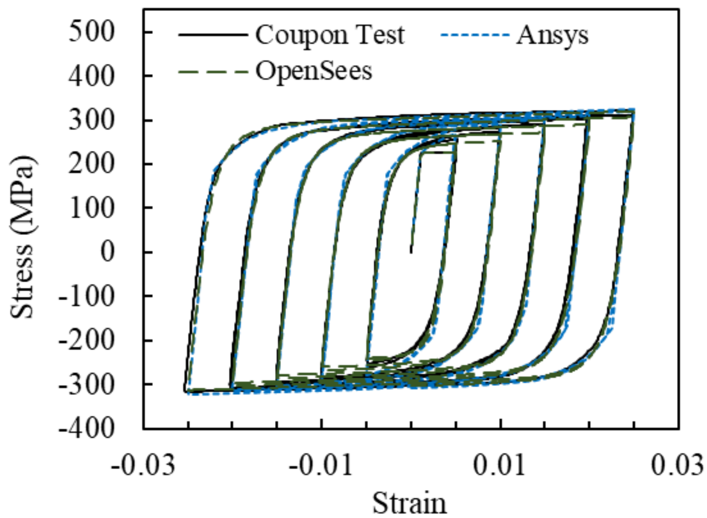

Figure 3.6 Calibration of the low-yield Q225 steel based on the material coupon test [6]

Table 3.2 Calibrated hardening parameters of Q225 steel for numerical analysis [6]

<table>
<tr><td colspan="10">ANSYS</td></tr>
<tr><td colspan="2" rowspan="2">Chaboche hardening</td><td>C_1 (MPa)</td><td>g_1</td><td>C_2 (MPa)</td><td>g_2</td><td colspan="2" rowspan="2">Isotropic hardening</td><td>F_y (MPa)</td><td>b</td></tr>
<tr><td>2,000</td><td>340</td><td>800</td><td>10</td><td>225</td><td>50</td></tr>
<tr><td colspan="10">OpenSees (Steel02)</td></tr>
<tr><td>F_y (MPa)</td><td>E (MPa)</td><td>b</td><td>R_0</td><td>cR_1</td><td>cR_2</td><td>a_1</td><td>a_2</td><td>a_3</td><td>a_4</td></tr>
<tr><td>225</td><td>2.0E+05</td><td>0.003</td><td>17</td><td>0.85</td><td>0.15</td><td>0.03</td><td>1.0</td><td>0.03</td><td>1.0</td></tr>
</table>

In the original unretrofitted timber structure, the main column frame members were modeled using “ElasticBeamColumn” elements with the moment released at both ends. Floor beam elements were modeled using “NonlinearBeamColumn” element. The floor beam and columns were connected using simple connection by introducing an intermediate zero-length spring with flexible material used in the rotation simulating pinned connection. In order to simulate the hysteretic behavior of sheathed timber shear walls, two zero-length springs with “SAWS uniaxialMaterial” were utilized in parallel to represent existing HWS and GWB wall sheathings. In the model, top ends of the columns were assigned equal horizontal degree-of-freedom (DOF).

For the second case where the original timber structure is retrofitted with wood structural panels (WSPs), the unretrofitted case model has been seismically strengthened with zero-length springs added in parallel to the existing sheathed wood shear walls (HWS, and GWB) in order to take the plywood retrofitting panels into consideration.

3.4 Prototype Light-Frame Wood Building

In order to investigate the seismic behavior of the light-frame timber structures, a prototype four-story building located in downtown San Francisco was designed and its nonlinear seismic behavior was studied [4]. Floor plans, elevation views, and isometric views of the building are shown in Figure 3.7 through Figure 3.9.

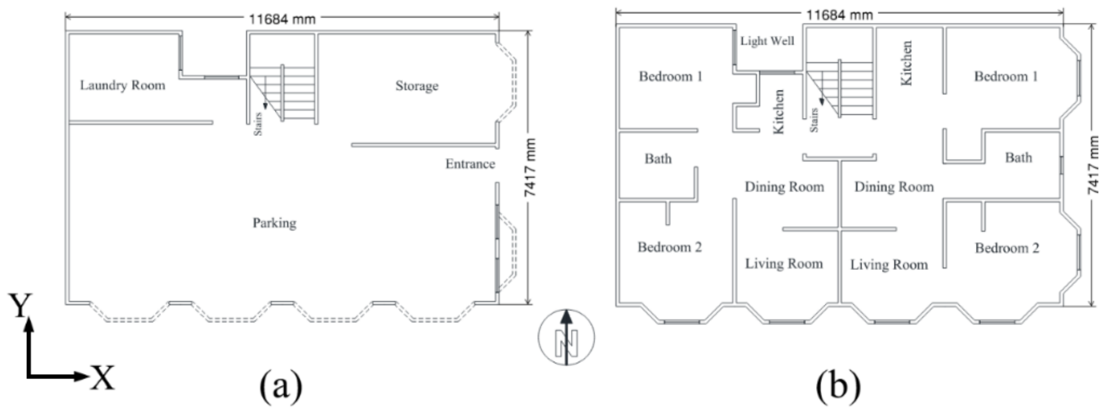

Figure 3.7 Floor plans of the four-story wood framed prototype building [4]:

(a) First Story; (b) Upper Stories

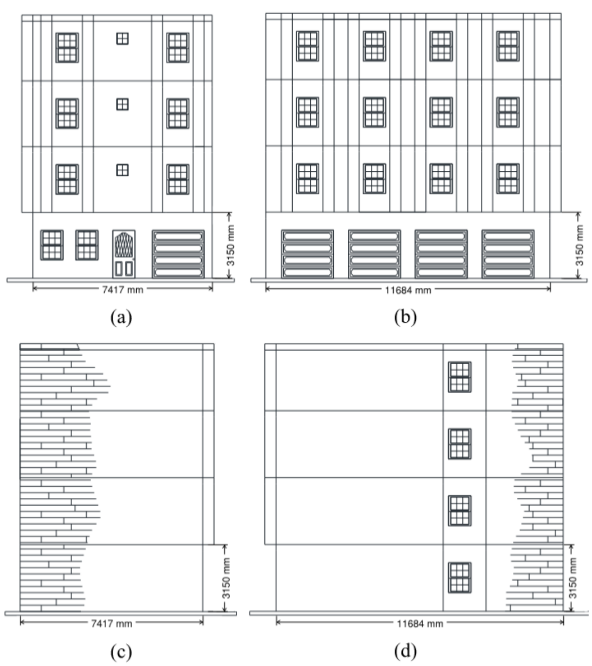

Figure 3.8 Elevation views of the four-story wood framed prototype building [4]:

(a) East view; (b) South view; (c) West view; (d) North view

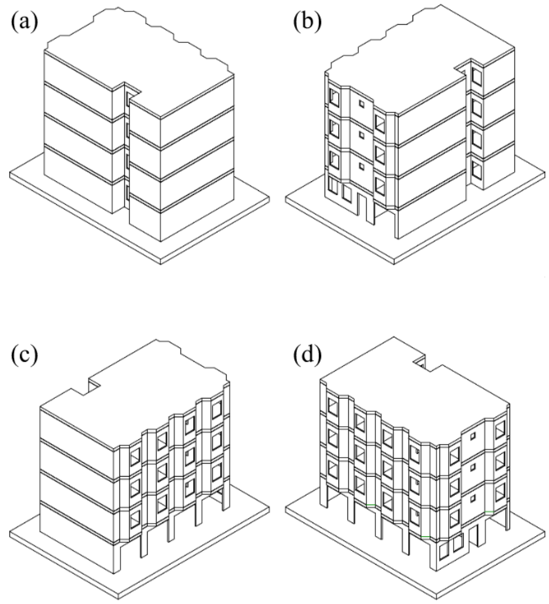

Figure 3.9 Isometric views of the four-story wood framed prototype building [4]:

(a) Northwest view; (b) Northeast view; (c) Southwest view; (d) Southeast view

The prototype building is located in San Francisco. The total seismic mass of the four-story timber building is 48,000 kg, and original wall sheathing includes HWS, and GWB [4]. The existing SFRS of the building is shown in Figure 3.10.

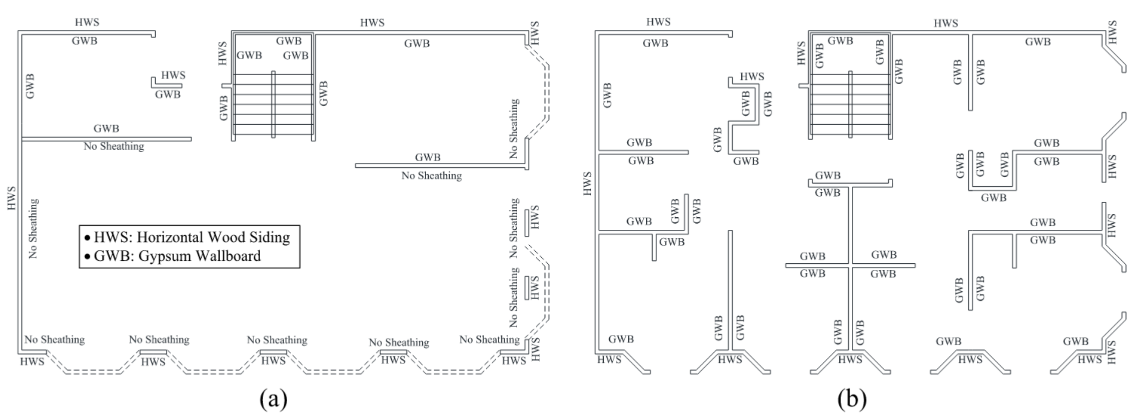

Figure 3.10 Existing wall sheathing in the original building [4]: (a) First Story; (b) Upper Stories

3.5 Numerical Modeling for Response History Analysis

To study the nonlinear seismic performance of timber structures, the four-story prototype wood building shown in Figure 3.7 through Figure 3.10 was considered for numerical analysis. For the prototype structure, a 2D frame consisting of timber shear walls, and one lean-on-column with lumped nodal seismic masses were modeled in the OpenSees FE software [93].

Hysteretic modeling of light-frame wood buildings gained a considerable popularity among research community as the development of the seismic analysis of wood-frame structure (SAWS) model [4]. The structural behavior of timber shear walls with sheathing (e.g. HWS, GWB, and WSP) was modeled in the OpenSees software [93] using a well-known ten-parameter hysteretic model developed by Folz and Filiatrault [92]. Table 3.3 shows the length of wall sheathing for each floor of the prototype timber structures.

Table 3.3 Wall sheathing length for the prototype wood buildings

Floor	Existing SFRS Length (m)		Retrofitting SFRS Length (m)			
	HWS	**GWB**	**WSP (305/305)**	**WSP (153/305)**	**WSP (76/305)**	**WSP (51/305)**
1	25.69	11.45	-	-	-	2.4
2	14.78	27.08	-	-	2.8	2×2.8
3	14.78	27.08	-	3.05	2×3.05	-
4	14.78	27.08	2.2	2×2.2	-	-

3.6 Eigenvalue and Nonlinear Static Analyses

The modal shapes and modal properties of the two prototypes are illustrated in Figure 3.11, and Table 3.4, respectively. The natural period of the original and WSP-retrofitted four-story light-frame timber structure is 0.762 sec and 0.488 sec, respectively. Larger initial stiffness of the retrofitted building leads to the shorter natural period.

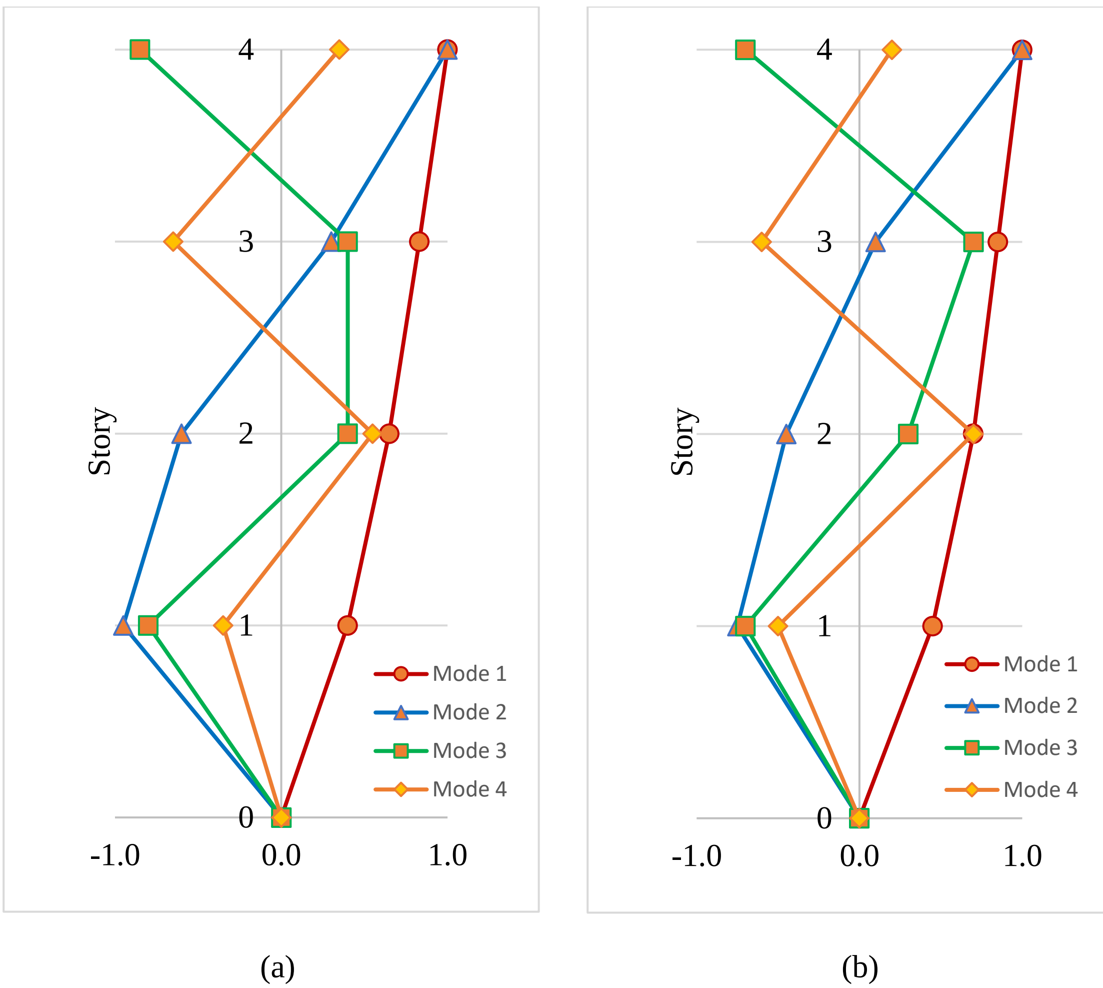

Figure 3.11 Modal shapes of the four-story light-frame wood prototype buildings:

(a) Original unretrofitted; (b) WSP-retrofitted

Table 3.4 Modal properties of the four-story light-frame wood buildings

Mode	**Original unretrofitted**	**WSP-retrofitted**
	Natural Period (sec.)	Natural Period (sec.)
1	0.762	0.488
2	0.254	0.164
3	0.162	0.105
4	0.131	0.077

To perform nonlinear static analysis, a load profile conforming to the first mode shape of the structure (a nearly inverted triangular-shaped load profile) was applied to the nodes of the lean-on-column. The structure was pushed to 0.06% of the roof drift ratio, -0.06% of the roof drift ratio, then unloaded for the original case, and it was pushed to 0.3% of the roof drift ratio, -0.3% of the roof drift ratio, then unloaded for the retrofitted case. The pushover curves of the unretrofitted prototype wood frame structure, and the original structure retrofitted with WSP are illustrated in Figure 3.12.

As shown in Figure 3.12, the WSP-retrofitted building shows higher elastic limit than that of the unretrofitted counterpart as it was retrofitted with the plywood retrofitting panels. The initial stiffness of the retrofitted building is larger than the original. The original and retrofitted structures are different in terms of residual drift, and energy dissipation. It is worth noting that both structures are not fully recentered because there is no self-centering mechanism provided in the two prototypes.

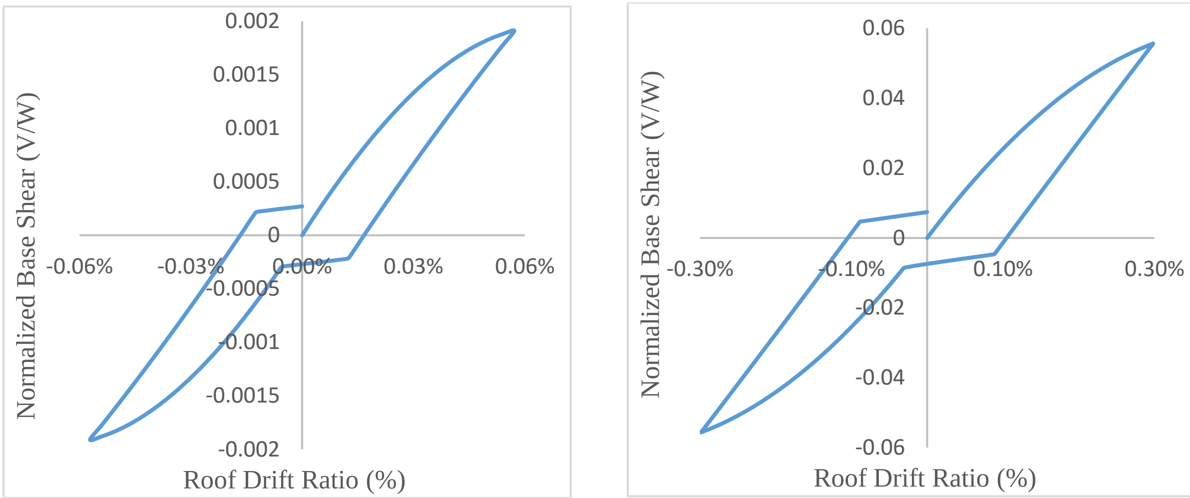

(a) (b)

Figure 3.12 Pushover curve of the wood-frame prototype: (a) unretrofitted; (b) WSP-retrofitted

3.7 Nonlinear Dynamic Analysis

In order to investigate the nonlinear seismic performance of the prototype light-frame timber structures subjected to seismic excitations, non-linear time history (NLTH) analysis was performed at different intensity levels. The Far-field (FF) suite of ground motions from the FEMA P695 [94] database was adopted in this research. The dataset comprises twenty-two pairs of ground motion components (a total of forty-four horizontal ground motions) recorded at sites located at a distance of at least 10 km from the fault rupture. One ground motion from each component pair was randomly selected for the NLTH analysis in order to reduce the computation time. Appendix A includes all the specifications and acceleration history of the ground motions. The nonlinear seismic responses of the two prototype buildings are thoroughly presented and discussed in the subsequent section.

3.7.1 Original Timber Structure

Figure 3.13 illustrates the maximum inter-story drift ratio (IDR) responses of the four-story unretrofitted wood prototype exposed to the twenty-two Far-field (FF) records.

The original unretrofitted building can survive under all the 22 ground motions (GMs) when exposed to 0.0002DBE. Although, it collapses under 1, and 4 ground motions (GMs) when the intensities are 0.0003DBE and 0.001DBE, respectively. Additionally, the ensemble median value of the maximum IDRs at the 0.0002DBE level is 0.04%. Maximum response refers to the maximum value of the peak responses among all stories.

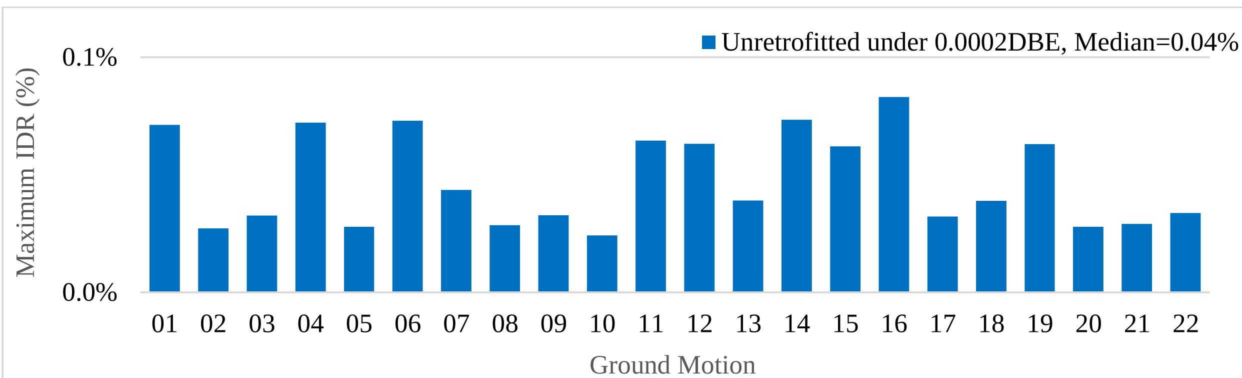

Figure 3.13 Maximum IDR of the unretrofitted wood building under 0.0002 DBE

The maximum residual IDRs of the original prototype timber structure at the 0.0002DBE level is shown in Figure 3.14. The median value of the maximum residual IDRs at this level is 0.02%.

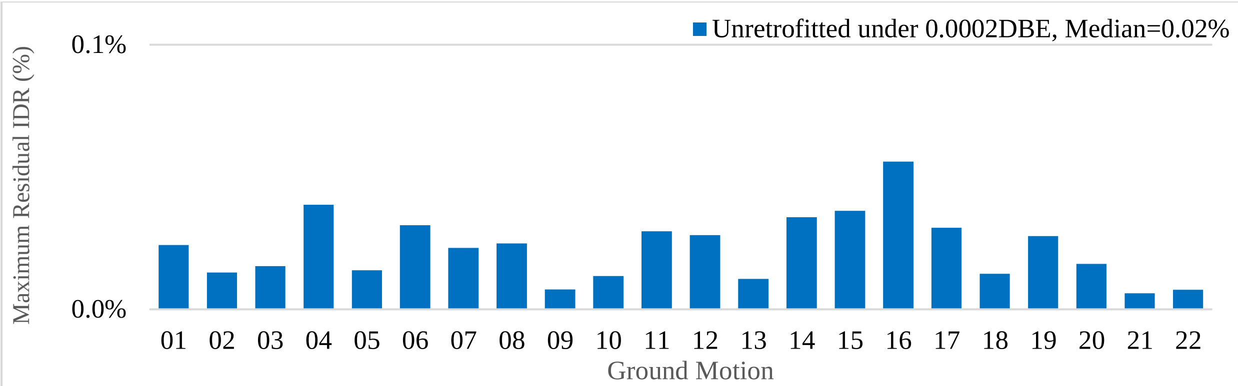

Figure 3.14 Maximum residual IDR of the unretrofitted wood building under 0.0002DBE

3.7.2 Original Timber Structure Retrofitted with WSP

Figure 3.15 demonstrates the maximum inter-story drift ratio (IDR) responses of the four-story original timber structure retrofitted with WSP under the FF record set.

The WSP-retrofitted building can survive under all the 22 ground motions (GMs) when exposed to 0.06DBE. Although, it collapses only under one ground motion (GM) when exposed to 0.07DBE, and 0.1DBE. The ensemble median value of the maximum IDRs at the 0.06DBE level is 0.18%.

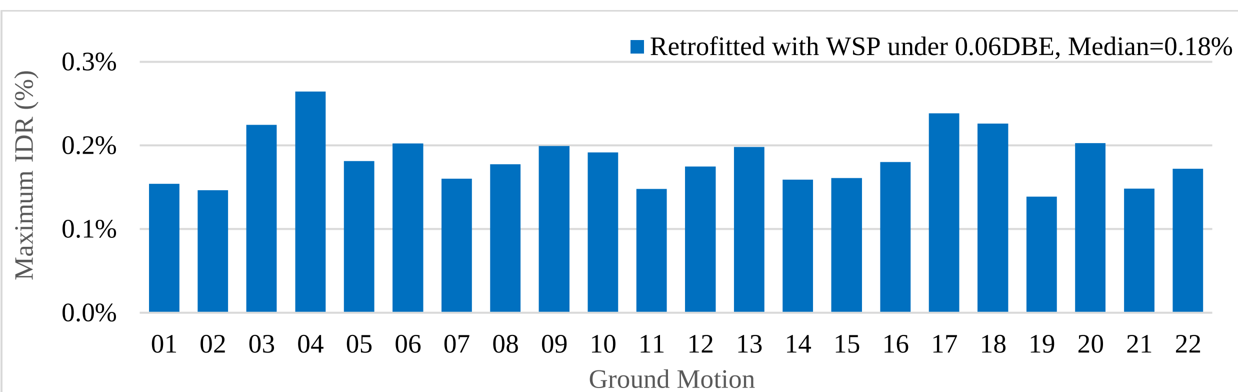

Figure 3.15 Maximum IDR of the WSP-retrofitted wood building under 0.06DBE

The maximum residual IDRs of the original prototype timber structure retrofitted with WSP at the 0.06DBE level is shown in Figure 3.16. The median value of the maximum residual IDRs at this level is 0.1%.

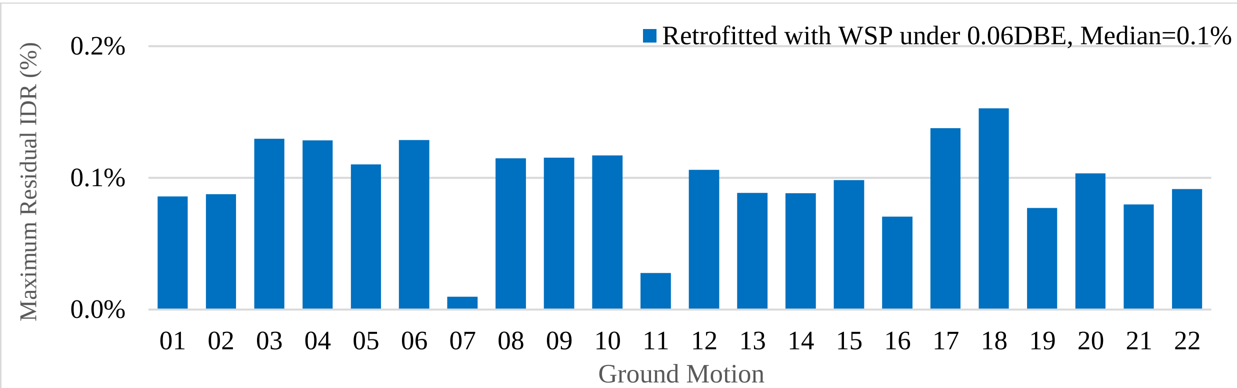

Figure 3.16 Maximum residual IDR of the WSP-retrofitted wood building under 0.06DBE

3.7.2 Comparison between the Original and the WSP-Retrofitted Prototypes

The vertical profile of the IDR of the unretrofitted four-story prototype light-frame wood structure as well as the WSP-retrofitted counterpart subjected to GM-07, and GM-05, respectively corresponding to the ensemble median of the maximum drift responses of the prototype buildings, with 16^{th} and 84^{th} percentile values are shown in Figure 3.17. In both the original and WSP-retrofitted wood buildings, the maximum drift responses occur on the first story at the related intensities. The peak drifts of both the prototype buildings considering quantile values, are more scattered at the ground story; and the dispersions are comparable at the upper stories.

The statistical data of the structural seismic responses of the prototype wood buildings are illustrated in Table 3.5 and Table 3.6. In conclusion, WSP-retrofitted prototype timber building showed much better seismic performance in terms of drift control, and restraining residual drift compared to the unretrofitted counterpart.

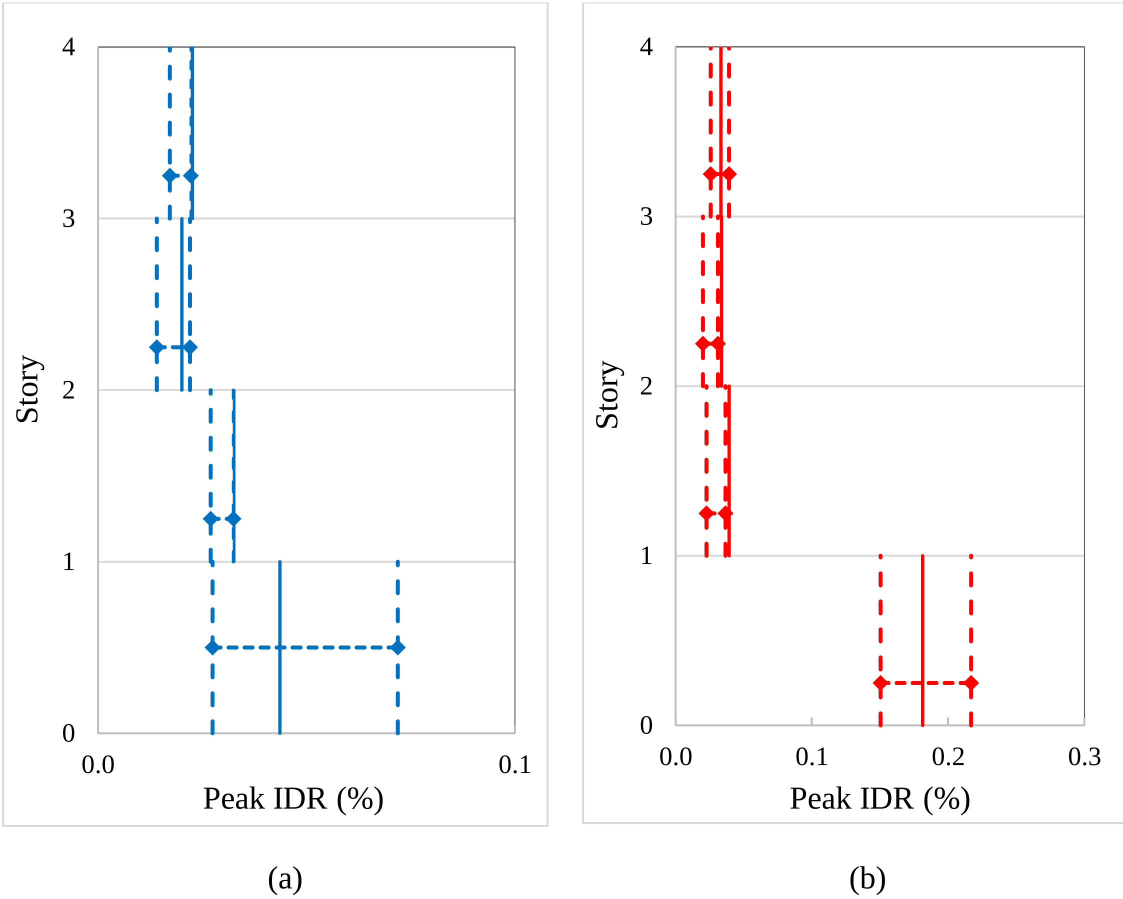

Figure 3.17 Vertical profile of the IDR of the four-story prototype light-frame timber structures with 16th and 84th percentile values of the peak responses: (a) Original unretrofitted prototype under GM-07 and 0.0002DBE; (b) WSP-retrofitted prototype under GM-05 and 0.06DBE

Table 3.5 Statistical data of the maximum IDR of the prototype buildings

Record set	Original unretrofitted under 0.0002DBE			WSP-retrofitted under 0.06DBE		
	Mean	COV	Median	Mean	COV	Median
	Four-story light frame timber structure					
Far-field (FF)	0.05%	41.59%	0.04%	0.18%	17.96%	0.18%

Table 3.6 Statistical data of the maximum residual IDR of the prototype buildings

Record set	Original unretrofitted under 0.0002DBE			WSP-retrofitted under 0.06DBE		
	Mean	COV	Median	Mean	COV	Median
	Four-story light frame timber structure					
Far-field (FF)	0.02%	53.93%	0.02%	0.10%	34.12%	0.10%

3.8 Summary

This chapter presented an analysis of the nonlinear seismic behavior of light-frame wood structures with soft stories. Planar wireframe Finite Element (FE) models were developed to evaluate the seismic performance of these wood-frame buildings. The study focused on both the original unretrofitted timber structure and a retrofitted prototype enhanced with wood structural panels (WSPs), utilizing nonlinear static and dynamic analyses on four-story prototypes. The following key conclusions were drawn:

- The ensemble median value of the maximum inter-story drift ratios (IDRs) for the original unretrofitted light-frame wood building is less than 0.05% at the 0.0002 DBE level under the Far-field (FF) record set, with the maximum residual IDR observed at 0.02% for the same intensity level.
- For the WSP-retrofitted prototype building, the ensemble median value of the maximum IDRs is less than 0.2% at the 0.06 DBE level under the FF record set, while the structure shows a maximum residual IDR of 0.1% at the same intensity level.
- In both the unretrofitted and WSP-retrofitted wood-frame prototypes, the maximum drift responses occur in the first story at the studied intensity levels, due to the limited availability of lateral walls. Although the original prototype is considered a soft-story

structure at all levels, the first story is significantly softer than the upper stories due to the presence of more and larger-sized openings, such as windows, storefronts, and garage doors, resulting in fewer timber lateral walls available to resist seismic loads. Moreover, peak drifts, considering quantile values, are more widely dispersed at the ground story, while the dispersions at the upper stories are comparable for both the cases studied.

- The WSP-retrofitted prototype exhibited improved seismic performance in terms of controlling drift and minimizing residual drift. This retrofitting method proves to be practical, cost-effective, and easy to implement, as the new plywood sheathing can be installed directly over the existing timber walls. Therefore, retrofitting with WSP minimizes the interference of retrofit elements with openings and occupied areas in the building. These panels can also be replaced for non-structural walls.
- Although the WSP retrofitting method provides considerable benefits for the upper stories due to the availability of existing walls at these levels, it proves to be ineffective for the ground story. Therefore, alternative retrofitting procedures must be implemented to strengthen the ground story exclusively, which will be addressed in the following chapter.

Chapter 4 : Nonlinear Seismic Analysis and Performance Study of Soft-Story Wood Framed Structures Retrofitted with Self-Centering Viscoelastic Damper (SCVD) Systems on the First Story only

In this chapter, a novel self-centering viscoelastic damper (SCVD) system is introduced. In order to overcome the problem using self-centering systems along with displacement-dependent energy dissipation mechanisms, a velocity-dependent energy dissipation system is proposed in this research. Velocity-based energy dissipation devices are of interest because in such damper systems, maximum load occurs where the displacement is zero, while in displacement-based damper devices, maximum load occurs at the largest story drift. Therefore, velocity-dependent dampers impose much less demand to the story shear compared to the displacement-dependent counterparts.

Analytical and numerical investigations are made to study the nonlinear seismic performance of light-frame wood buildings with soft stories retrofitted with such viscoelastic damper systems on their first story only. In these retrofitting systems, preloaded disc springs are utilized as the recentering devices, viscous damper is used as the primary element to dissipate seismic energy, and replaceable trapezoidal plate added damping (TPAD) fuse device which is considered as a displacement-dependent energy dissipation device is employed as the secondary or backup element to dissipate the energy.

A four-story soft-story prototype light-frame timber structure has been designed and its seismic behavior is studied through nonlinear numerical simulation. The prototype structure in this chapter is considered as the WSP-retrofitted wood building in chapter 3. It should be noted that the WSP-retrofitted prototype in the last chapter is basically the original unretrofitted timber structure retrofitted with WSP plywood installed over the existing timber shear walls. Therefore, the WSP-retrofitted building is still very soft on its ground story because of much less availability of the existing timber shear walls due to more and larger-sized openings at this level.

4.1 Seismic Behavior of the System

The prototype structure which is a four-story soft-story wood building has been retrofitted on upper stories, and partially retrofitted on the first story with wood structural panels (WSPs) in the last phase as shown in Figure 3.2. Figure 4.1 shows the newly developed SCVD retrofitting system utilized on the ground story only. The retrofitting system is a steel framed module consisting of one steel vertical link beam, and the SCVD device. The SCVD device includes two sets of pre-compressed disc springs, a viscous damper, and a TPAD fuse as demonstrated in Figure 4.2. Hydraulic rams can be used in order to pre-compress the discs. Figure 4.3 shows the configuration of the TPAD.

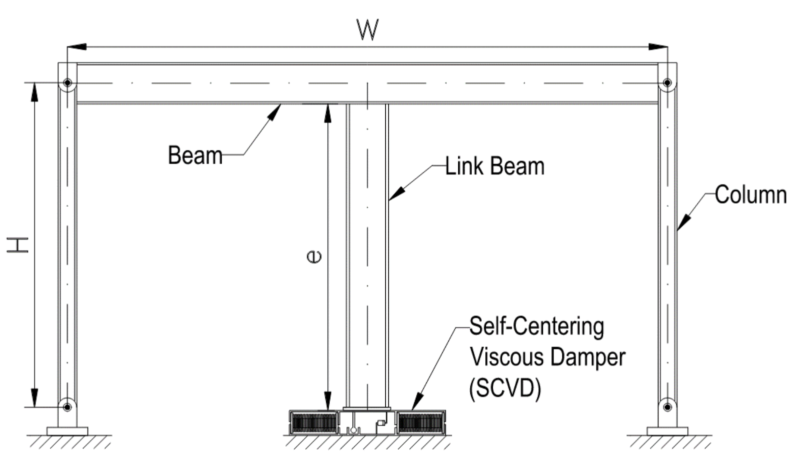

Figure 4.1 Schematics, and components of the SCVD module installed on the first story only

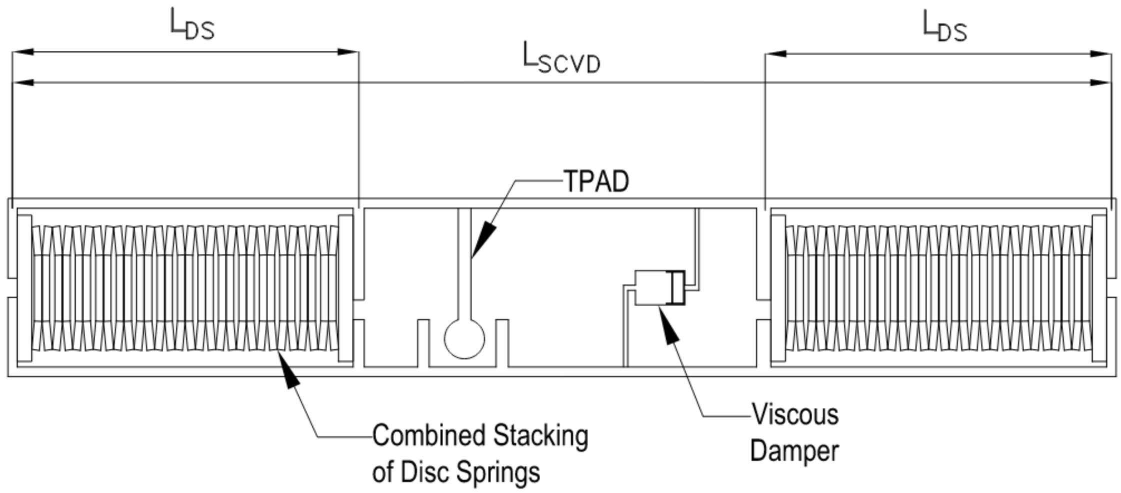

Figure 4.2 Components of the SCVD device

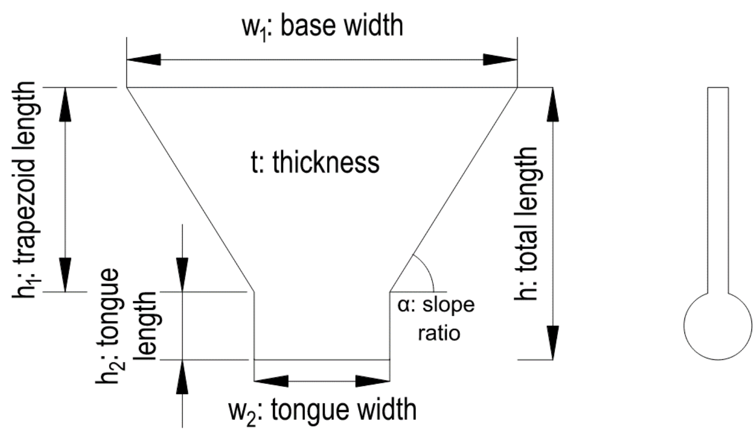

Figure 4.3 Configuration of the TPAD

4.2 Analytical Formulations of the SCVD System

In this section, the analytical load-displacement relationships of an SCVD module frame retrofitting the ground story of the four-story prototype soft-story light-frame wood building shown in Figure 4.1, are discussed. The analytical formulations of the module frame without the fuse device are discussed first, and then the contribution of the TPAD to the total response of the module will be presented next.

4.2.1 Self-Centering Viscoelastic Damper (SCVD) Module Frame without the Fuse Device

The schematic analytical load-displacement hysteresis curve for the proposed self-centering (SC) systems without a fuse is depicted in Figure 4.4 [6]. To characterize the inelastic response behavior of a self-centering module, three key parameters are required: (1) initial stiffness, K_1; (2) base shear at gap-opening, V_0; and (3) post-gap-opening stiffness, K_{PGO}. The initial stiffness of the proposed self-centering system, K_1, depends on the main wood-frame section sizes and lengths as well as the steel frame section dimensions and overall geometry of the frame. The base shear at gap-opening, V_0, is a function of the pre-compression force in the self-centering damper box enclosure, which is generated by preloaded disc springs. The post-gap-opening stiffness, K_{PGO}, is provided by the elastic deformation of the disc springs. This stiffness can be modified by adjusting the size and number of the discs or arranging them in series or parallel configurations.

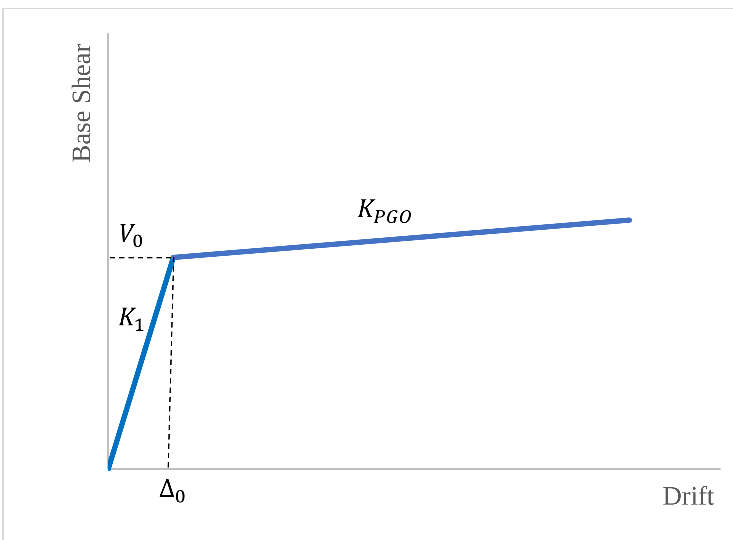

Figure 4.4 Schematic load-displacement relationship of self-centering systems without the displacement-dependent fuse device (e.g. TPAD) [6]

The effect of using a velocity-dependent energy dissipation mechanism (i.e. viscous damper) in the SCVD modular frame can be observed when the hysteretic response is studied in a time-dependent (i.e. time history) analysis. Figure 4.5 and Figure 4.6 illustrate the hysteretic behavior of a viscous damper (VD), and a self-centering viscoelastic damper (SCVD) system without a fuse device [60].

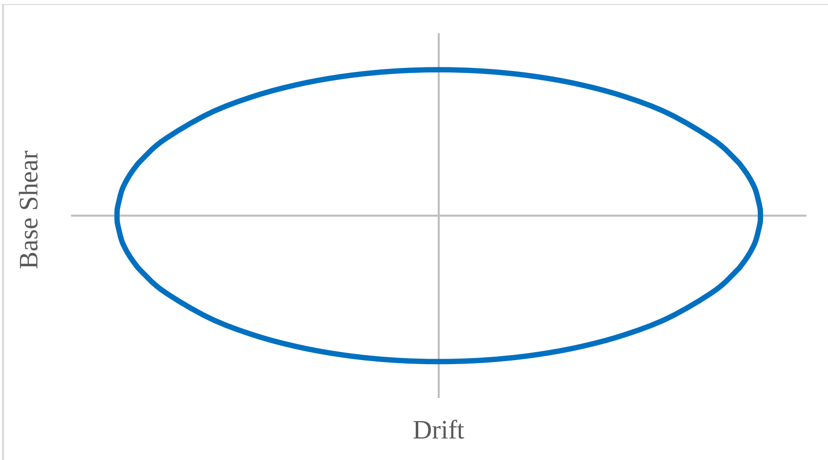

Figure 4.5 Hysteresis response of a viscous damper (VD) [60]

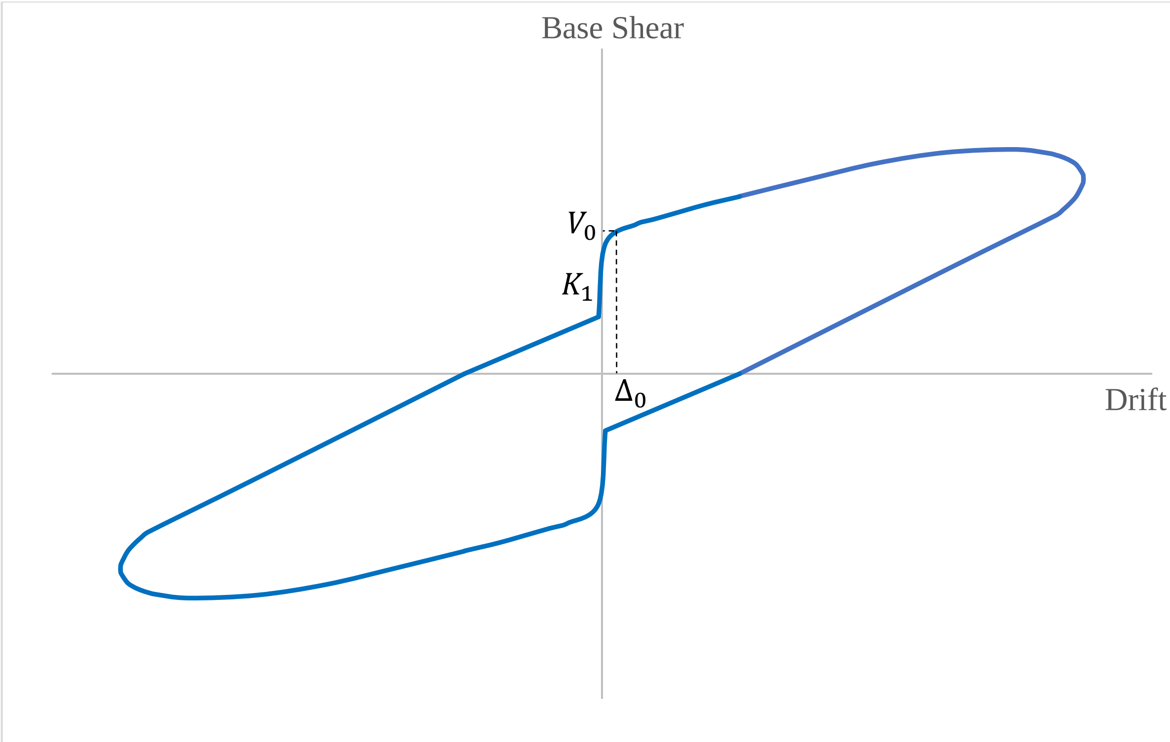

Figure 4.6 Schematic flag-shaped load-displacement behavior of a SCVD system without a backup fuse device (e.g. TPAD) [60]

According to Figure 4.1 , $H, W,$ and e denote the frame height, bay width, and vertical link beam length, respectively. In the following formulations: I_b, and I_{lb} express the moment of inertia of the beam, and link beam, respectively. A_b, and A_{lb} show the cross-sectional area of the beam, and link beam, and A_b^w, and A_{lb}^w represent the web cross-sectional area of the beam, and link beam. w_{SCVD}, and t_{SCVD} denote the height and plate thickness of the SCVD box enclosure, respectively. E and G are Young's modulus and shear modulus of steel. In this study, existing structural wood seismic force resisting system (SFRS) includes HWS (horizontal wood siding), and GWB (gypsum wall board). These two zero-length spring elements are parallel in the OpenSees Finite Element (FE) model which were retrofitted with WSP (wood structural panel) system. Their hysteretic behaviors are all simulated by employing the related SAWS model ($K_{SAWS} = K_{HWS} + K_{GWB} + K_{WSP}$).

Before the gap-opening, the initial stiffness of the SCVD module, K_1 is due to the frame's elastic stiffness and can be expressed using Equation (4.1).

$$\mathrm{K}_1 = \left(\frac{1}{\mathrm{K_a}} + \frac{1}{\mathrm{K_f}} + \frac{1}{\mathrm{K_s}}\right)^{-1} \tag{4.1}$$

Where $\mathrm{K_a}$, $\mathrm{K_f}$ and $\mathrm{K_s}$ denote the frame lateral stiffness due to the contribution of axial, flexural, and shear deformation of the frame members, respectively, and are developed based on the principle of virtual work. The lateral stiffness due to the axial deformation of the frame members, $\mathrm{K_a}$ would be calculated using Equations (4.2) and (4.3).

$$\mathrm{K_a} = \left(\frac{1}{\mathrm{K_0^a}} + \frac{1}{\mathrm{K_{lb}^a}} + \frac{1}{\mathrm{K_{SAWS}^a}}\right)^{-1} \tag{4.2}$$

$$\mathrm{K_a} \approx \left(\frac{\mathrm{e}^3}{\mathrm{EA_{lb}}W^2} + \frac{1}{\mathrm{K_{SAWS}^a}}\right)^{-1} \tag{4.3}$$

Where $\mathrm{K_0^a}$, $\mathrm{K_{lb}^a}$ and $\mathrm{K_{SAWS}^a}$ represent the frame lateral stiffness due to the contribution of the axial deformation of the self-centering (SC) damper enclosure, link beam, and wood shear walls (SAWS), respectively. The lateral stiffness due to the frame flexural deformations, $\mathrm{K_f}$, would be obtained using Equations (4.4) and (4.5).

$$\mathrm{K_f} = \left(\frac{1}{\mathrm{K_0^f}} + \frac{1}{\mathrm{K_{lb}^f}} + \frac{1}{\mathrm{K_{SAWS}^f}}\right)^{-1} \tag{4.4}$$

$$\mathrm{K_f} \approx \left(\frac{\mathrm{e}^3}{3E\mathrm{I_{lb}}} + \frac{1}{\mathrm{K_{SAWS}^f}}\right)^{-1} \tag{4.5}$$

Where K_0^f, K_{lb}^f and K_{SAWS}^f denote the frame lateral stiffness due to the contribution of the flexural deformation of the SC damper enclosure, link beam, and timber shear studs (SWAS), respectively. The frame lateral stiffness due to the frame shear deformations, K_s, can be formulated using Equations (4.6) and (4.7).

$$K_s = \left(\frac{1}{K_0^s} + \frac{1}{K_{lb}^s} + \frac{1}{K_{SAWS}^s}\right)^{-1} \tag{4.6}$$

$$K_s \approx \left(\frac{e}{GA_{lb}^w} + \frac{1}{K_{SAWS}^s}\right)^{-1} \tag{4.7}$$

Where K_0^s, K_{lb}^s and K_{SAWS}^s depict the frame lateral stiffness due to the shear deformation of the SC damper enclosure, link beam, and timber shear walls (SAWS), respectively. The free-body diagram of the link beam is shown in Figure 4.7.

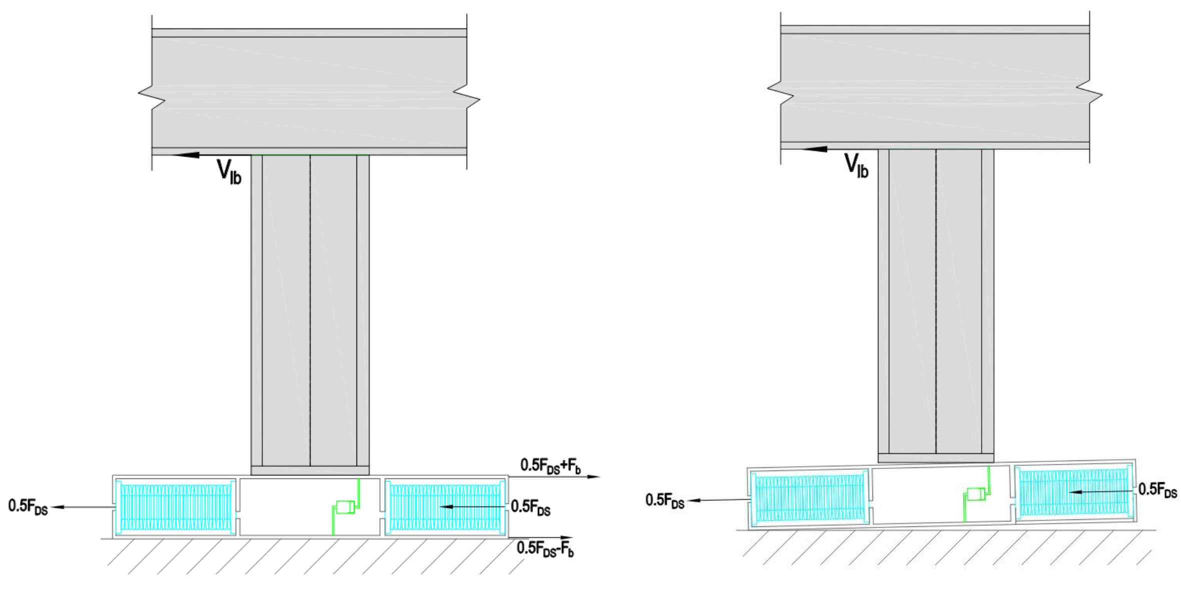

Figure 4.7 Free body diagram of the vertical link beam without the fuse device:

(a) Before gap-opening; (b) After gap-opening

The pre-loading force of the two sets of disc springs resist the bending moment, $V_{lb}e$, due to the horizontal force, V_{lb}, before gap-opening. Once the tensile action in either top or bottom end of the SCVD box reaches the pre-compression force due to the pre-loading of the disc springs, the corresponding side of the SCVD box loses contact and gap-opening occurs. The beam shear, V_{lb}, the story shear of the frame at gap-opening, V_0, and the corresponding story drift, Δ_0, can be expressed using Equations (4.8) and (4.9).

$$V_0 = V_{lb} = \frac{(F_{DS})(\frac{w_{SCVD} + t_{SCVD}}{2})}{e} = \frac{(F_{DS})(\frac{w'_{SCVD}}{2})}{e} \tag{4.8}$$

$$\Delta_0 = \frac{V_0}{K_1} \tag{4.9}$$

Where F_{DS} is the total axial force in the disc springs due to the pre-loading, and $w'_{SCVD} = w_{SCVD} + t_{SCVD}$ is the total height of the self-centering viscous damper box. After gap-opening, the stiffness of the frame, K_{PGO}, is provided primarily by the disc springs and would be calculated using Equations (4.10) and (4.11) . In these relationships, K_{SC} is the lateral stiffness due to the contribution of the disc springs, and K_D is the equivalent stiffness of two sets of disc springs. The geometry of a single disc spring and stacking types are shown in Figure 4.8 [6].

$$K_{PGO} = \left(\frac{1}{K_{SC}} + \frac{1}{K_1}\right)^{-1} \tag{4.10}$$

$$K_{PGO} \approx K_{SC} = K_D(\frac{w'_{SCVD}}{2e})^2 \tag{4.11}$$

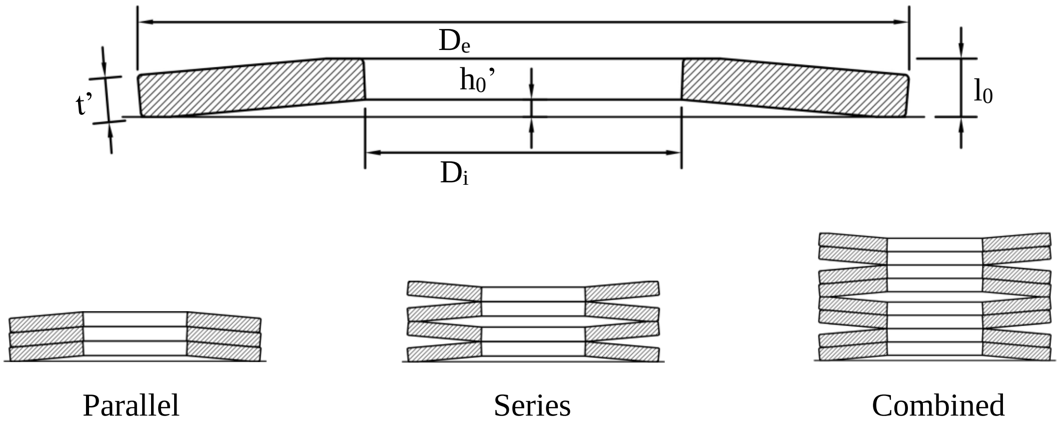

Figure 4.8 Geometry of a single disc spring and types of stacking [6]

Equation (4.12) shows the relationship between the axial compressive force of a single disc spring, $\mathrm{F(s)}$, and its elastic deflection, s [6].

$$\mathrm{F(s)} = \frac{4\mathrm{E}}{1-\mu^2}\frac{\mathrm{t}'^4}{\mathrm{K_1 D_e^2}}\mathrm{K_4^2}\frac{\mathrm{S}}{\mathrm{t}'}[\mathrm{K_4^2}\left(\frac{\mathrm{h}_0'}{\mathrm{t}'}-\frac{\mathrm{S}}{\mathrm{t}'}\right)\left(\frac{\mathrm{h}_0'}{\mathrm{t}'}-\frac{\mathrm{S}}{2\mathrm{t}'}\right)+1] \tag{4.12}$$

In this equation, E represents Young’s modulus of the disc spring material, μ denotes Poisson’s ratio, $\mathrm{t}' \approx 0.94\mathrm{t}$ is the reduced thickness (for discs where t > 6 mm), and $\mathrm{h}_0' = \mathrm{l}_0 - \mathrm{t}'$ is the free height (i.e. maximum deflection capacity) of the disc spring. Additionally, t and $\mathrm{h}_0 = \mathrm{l}_0 - \mathrm{t}$ represent the nominal thickness and nominal free height of the disc spring, respectively. Other parameters are calculated based on Equations (4.13) through (4.17) [6].

$$\delta = \frac{\mathrm{D_e}}{\mathrm{D_i}} \tag{4.13}$$

$$\mathrm{K_1} = \frac{1}{\pi}\cdot\frac{[\frac{\delta-1}{\delta}]^2}{\frac{\delta+1}{\delta-1}-\frac{2}{\ln\delta}} \tag{4.14}$$

$$K_4 = \sqrt{-\frac{C_1}{2} + \sqrt{(\frac{C_1}{2})^2 + C_2}} \tag{4.15}$$

$$C_1 = \frac{(\frac{t'}{t})^2}{\left(\frac{1}{4}.\frac{l_0}{t} - \frac{t'}{t} + \frac{3}{4}\right).(\frac{5}{8}.\frac{l_0}{t} - \frac{t'}{t} + \frac{3}{8})} \tag{4.16}$$

$$C_2 = \frac{C_1}{(\frac{t'}{t})^3}[\frac{5}{32}\left(\frac{l_0}{t} - 1\right)^2 + 1] \tag{4.17}$$

Figure 4.9 illustrates the force-deflection curves of single disc springs with varying $\frac{h_0}{t}$ ratios. The vertical axis represents the ratio of the force in the disc spring, F, to the force at the flattened position, $F_c(s = h'_0)$. As shown, the curvature of these curves is significantly influenced by the $\frac{h_0}{t}$ ratio; as this ratio increases, the force-deflection relationship becomes increasingly quadratic. According to DIN EN 16983 [95], disc springs are classified into three series A, B, and C, based on this ratio. For series A, with $\frac{h_0}{t} < 0.4$, stiffness remains nearly linear. In this study, all disc springs used were from this category, allowing for the assumption of linear stiffness in analytical formulations [6].

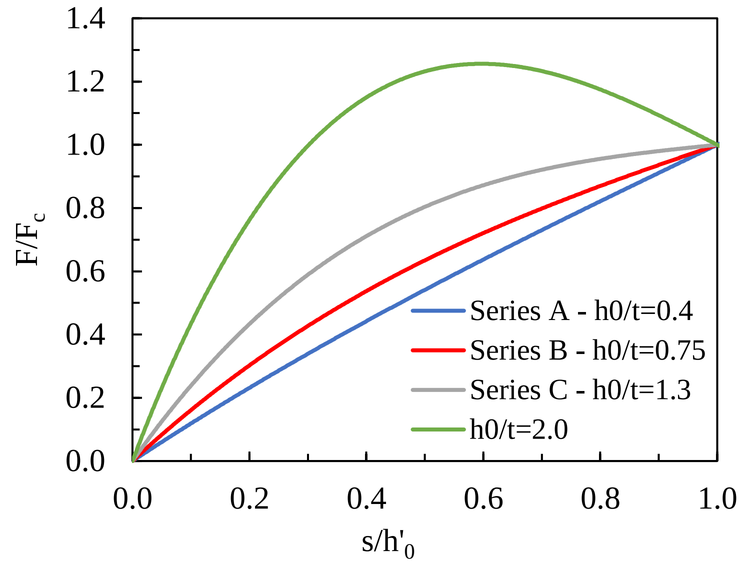

Figure 4.9 Force-deflection curves of disc springs [6]

For a given disc size, the stiffness and load-bearing capacity can be enhanced by stacking the discs in parallel. Additionally, stacking discs in series allows for achieving the desired deflection capacity. Consequently, by employing a combination of parallel and series stacking, both the targeted resistance and deformation capacity can be attained [6]. The elastic stiffness of the single disc spring, K_S, with $\frac{h_0}{t} < 0.4$ can be calculated approximately by Equation (4.18) [6].

$$K_S \approx \frac{4E}{1-\mu^2} \cdot \frac{t'^3}{K_1 D_e^2} \cdot K_4^2 . h_0' \tag{4.18}$$

The equivalent stiffness for two sets of disc springs in a combined stacking arrangement can be calculated using Equation (4.19), where K_{DS} represents the equivalent stiffness of each set of disc springs [6].

$$K_D \approx \frac{2n_p}{n_s} . K_S = 2K_{DS} \tag{4.19}$$

In this context, n_p denotes the number of disc springs in parallel stacking, while n_s indicates the number of groups of discs arranged in series within each set of combined stacking. It is advisable to limit the design to approximately 75% of the total deformation capacity of the disc spring set ($s \approx 0.75h_0'$) as larger deflections may lead to deviations from analytical predictions, accompanied by a progressive increase in force [6].

It is important to note that the relative motion between disc springs in parallel stacking, as well as between the disc springs and the top/bottom connection plates, generates a frictional force that contributes to the system energy dissipation. However, given the low coefficient of friction between these surfaces (0.005-0.05) [95,96], this effect is minimal relative to the system's overall energy dissipation and is therefore not considered in this study [6].

4.2.2 Self-Centering Viscoelastic Damper (SCVD) Module Frame with the TPAD Fuse Device

TPAD as the seismic fuse device is the backup source of energy dissipation in the proposed SCVD retrofitting system. The schematic analytical load-displacement relationship characterizing the flag-shaped hysteresis curve of the proposed self-centering (SC) system with the displacement-dependent replaceable damping device (i.e. TPAD) is shown in Figure 4.10 [6] which is a combination of the frame without TPAD (Figure 4.4) and a mechanism frame with the fuse device only. The required parameters needed to characterize the inelastic response behavior of the self-centering module are: (1) initial stiffness, K_1; (2) base shear at gap-opening, V_0; (3) stiffness after gap-opening, K_2; (4) system strength, V_y; (5) post-yield stiffness, K_3.

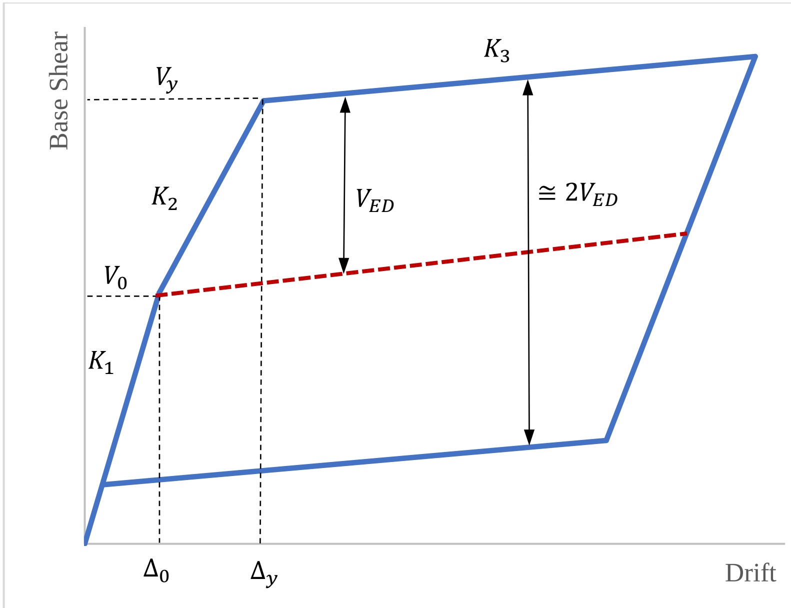

Figure 4.10 Schematic flag-shaped load-displacement behavior of the developed self-centering systems with the displacement-dependent damping device (e.g. TPAD) [6]

The initial stiffness is a function of the timber shear walls and the retrofitting steel frame (i.e. SCVD box enclosure, and link beam dimensions). The base shear at gap-opening, V_0, is a function of the pre-compression force in the SCVD box, which is generated by preloading the disc springs. Once gap-opening happens, the initial stiffness reduces to the secondary stiffness, K_2. The secondary stiffness is basically provided by the elastic stiffness of the fuse device and the disc springs. Once TPAD yielding starts, the stiffness decreases gradually until the fuse reaches its full plastic capacity. The system strength, V_y, is calculated by summing up the base shear at gap-opening, V_0, and the additional system strength provided by the fuse device, V_{ED}. The post-yield stiffness is provided by the axial stiffness of the self-centering element. Therefore, it can be adjusted by changing the number and/or the size and/or the series/ parallel configurations of the disc springs.

Studying the effects of a viscous damper (VD) mechanism in the self-centering (SC) system should be performed in a time-dependent (i.e. time history) analysis. The hysteretic response of a self-centering viscous damper (SCVD) system with a backup fuse is illustrated in Figure 4.11 [60].

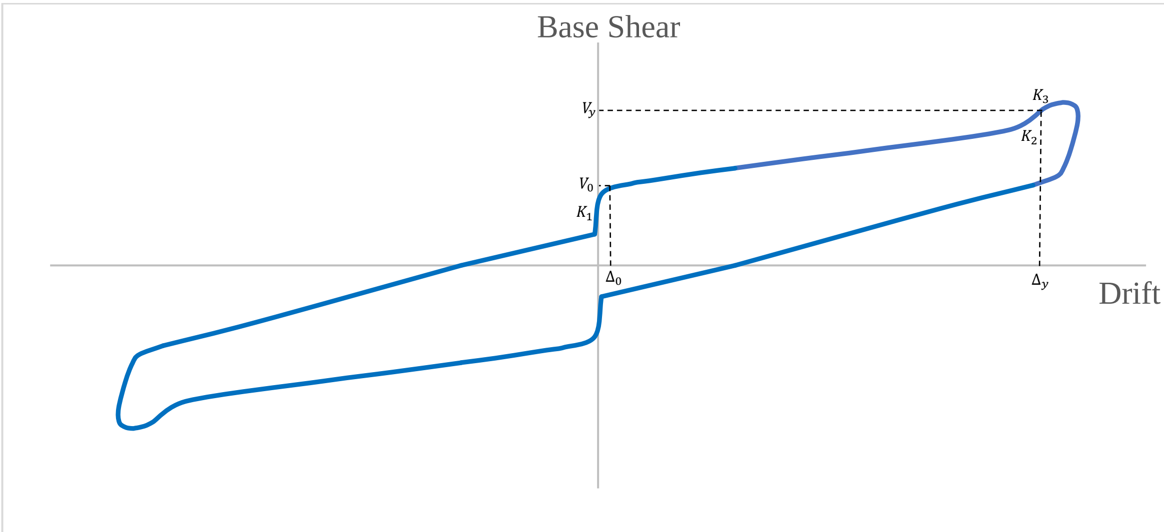

Figure 4.11 Schematic flag-shaped load-displacement behavior of a SCVD system with a back-up fuse device (e.g. TPAD) [60]

Initial stiffness, and base shear at gap-opening increase negligibly by adding TPAD to the self-centering (SC) module frame. The secondary stiffness, K_2, which is basically provided by the elastic stiffness of the fuse plate and disc springs can be calculated using Equation (4.20) [6].

$$\mathrm{K}_2 = (\frac{1}{\mathrm{K}_{\mathrm{ED}} + \mathrm{K}_{\mathrm{SC}}} + \frac{1}{\mathrm{K}_1})^{-1} \tag{4.20}$$

In the above equation, K_{ED} is the TPAD contribution to the lateral stiffness after gap-opening (i.e. TPAD elastic lateral stiffness) which is calculated using Equation (4.21) [97].

$$\mathrm{K}_{ED} = \frac{\mathrm{NE}w_1 t^3}{6h^3} \tag{4.21}$$

Where N is the number of TPAD plates, E is the TPAD plate's young modulus, w_1 is the TPAD top width, t is the TPAD thickness, and h is the TPAD height as illustrated in Figure 4.3. The TPAD yielding force, $V_{y,TPAD}$, is derived based on the plastic moment of its top section, $M_{p,TPAD}$, calculated using Equation (4.22). In this relationship, $F_{y,TPAD}$ is the TPAD plate's yield stress [97].

$$V_{y,TPAD} = \frac{NM_{p,TPAD}}{h} = \frac{Nw_1 t^2 F_{y,TPAD}}{4h} \tag{4.22}$$

The free-body diagram of the self-centering viscoelastic damper (SCVD) with TPAD is shown in Figure 4.12. As the lateral load increases, the bottom surface of the TPAD tends to get closer to the restraints. Once the TPAD bottom surface touches the adjacent walls, it will be triggered and with increasing the lateral load to the structure, load to the TPAD bottom surface increases until it yields. After yielding starts, the stiffness decreases gradually until the TPAD reaches its plastic moment, $M_{p,TPAD}$. This has been simplified to a bilinear elastoplastic behavior in the analytical derivation. The system strength, V_y, can be calculated by summing up the base shear at gap-opening, V_0, and the additional strength by the fuse device, V_{ED}, as expressed in Equations (4.23) and (4.24). Additionally, Δ_y is the displacement corresponding to the system strength which is calculated using Equation (4.25).

$$V_y = V_0 + V_{ED} \tag{4.23}$$

$$V_{ED} = V_{y,TPAD} \tag{4.24}$$

$$\Delta_y = \Delta_0 + \frac{V_{ED}}{K_2} \tag{4.25}$$

After plastic hinges in TPAD have been formed, the lateral stiffness drops considerably. Although the post-yield stiffness, K_3, is basically provided by the elastic stiffness of the disc springs, the linear hardening of TPAD also contributes negligibly per Equations (4.26) and (4.27) [6].

$$K_3 = \left(\frac{1}{K_{ED}^{H} + K_{SC}} + \frac{1}{K_1}\right)^{-1} \tag{4.26}$$

$$K_{ED}^{H} = \alpha_{sh} K_{ED} \tag{4.27}$$

In this equation, K_{ED}^{H} is the lateral stiffness provided by the linear hardening of the fuse trapezoidal plate, and α_{sh} is the strain hardening ratio of the fuse plate material. As demonstrated in Figure 4.10, without considering the effect of fuse hardening, the flag height of the hysteretic response is almost twice the strength provided by the TPAD ($h_{flag} \approx 2V_{ED}$) [6].

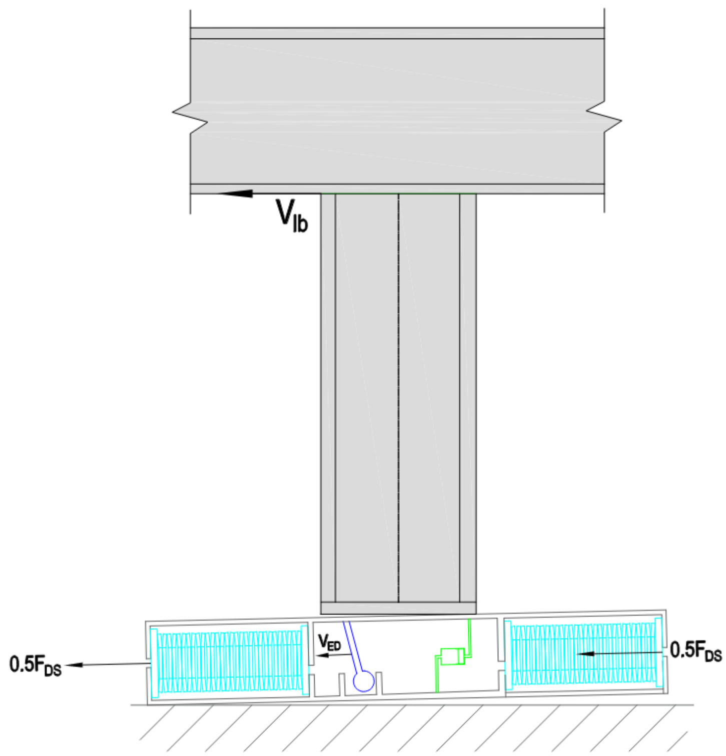

Figure 4.12 Free body diagram of the SCVD system with the fuse device (i.e. TPAD)

In all the aforementioned systems, the viscous damper (VD) acts as the primary mechanism to dissipate the seismic energy. The fundamental equation that describes the behavior of fluid viscous damper (VD) can be expressed as in Equation (4.28) [98].

$$\mathrm{F}_V = \mathrm{C}\mathrm{V}^{\alpha} \tag{4.28}$$

Where F_V is the output damper force, C is the damping constant, V is the induced velocity, and α is the damping exponent depending on the fluid viscosity properties. For seismic applications in buildings, values of α may be less than or equal to 1. With α = 1.0, the device is called a linear viscous damper and with α < 1.0, non-linear viscous damper properties are achieved which is effective in minimizing high velocity shocks. The non-linear damper can give a larger damping force [99].

4.3 Design of SCVD Retrofitting Systems

Following events can be considered critical for a typical SCVD retrofitting system in a light-frame wood building: (1) gap-opening in the vertical link beam; (2) yielding of the TPAD fuse; (3) yielding of wood-frame members; (4) yielding of the SCVD box enclosure; (5) strength degradation due to fracture of the fuse device, flattening of the disc springs or fracture of SCVD box enclosure.

The SCVD system retrofitting the ground story only has been designed based on the gap-opening force and stiffness required in the ground story compared to the second story considering the story shear ratio between the two stories. Such modular frames are appealing to seismic retrofit of existing timber structures as they can be fabricated in shop, transferred to the site, and connected to the existing structure. ASCE 7-22 [100] needs to be used to calculate the design story shear for each story in order to estimate the gap-opening force required to retrofit.

In a self-centering system with the displacement-dependent fuse only as the energy dissipation device, the system strength can be calculated by determining the gap-opening force and TPAD based on the required energy dissipation ratio, β_E, which is defined as the ratio of the energy dissipated by the fuse device to the system strength and can be estimated using Equation (4.29) [6].

$$\beta_E \cong \frac{V_{ED}}{V_y} = \frac{V_{ED}}{V_0 + V_{ED}} \tag{4.29}$$

In the self-centering systems without any fuse device, β_E equals to zero. In order to guarantee the satisfactory self-centering performance of a system under static loading, it is usually recommended to assume $\beta_E \leq 50\%$ [6].

As discussed in the last section, the friction force increases the story strength; although, it is recommended not to consider this additional strength to design the disc springs and the TPAD fuse because this extra strength is inconsiderable at small drifts. Once the size and number of parallel disc springs based on the required gap-opening force have been defined, the number of series disc springs based on the required deflection capacity was determined.

4.4 SCVD Module Frame Specifications

In this section, the properties of the SCVD module frame are presented. The length of existing and retrofitting timber shear wall sheathing in the WSP-retrofitted prototype is demonstrated in Table 3.3. In this chapter, the WSP-retrofitted building is retrofitted on its ground story only with the SCVD modular frame. Retrofitting with WSP in the last phase was performed based on the available timber shear walls at each level of the building, and because of much less availability of existing shear walls on the first floor compared to upper stories due to more openings, the structure was retrofitted partially with WSP at the first level.

Table 4.1 summarizes the geometries of the SCVD steel framed module in which d, $\mathrm{b_f}$, $\mathrm{t_f}$ and $\mathrm{t_w}$ represent the total depth, flange width, flange thickness, and web thickness of the structural steel section, respectively. Table 4.2 and Table 4.3 illustrate the disc spring, and TPAD geometrical properties, and finally, viscous damper's parameters are demonstrated in Table 4.4. In these tables, $\mathrm{D_e}$, $\mathrm{D_i}$, $\mathrm{L_0}$, t, $\mathrm{n_p}$, and $\mathrm{n_s}$ are the disc springs outer diameter, inner diameter, height, thickness, and number of springs in parallel, and series, respectively. Additionally, $\mathrm{w_1}$, $\mathrm{w_2}$, $\mathrm{h_1}$, h and t are the TPAD base width, tongue width, trapezoid length, total length, and thickness, and $\mathrm{c_d}$, and α are damping constant, and damping exponent, respectively. In the model, the story height, span length, and link beam length are $\mathrm{H} = 3150\ \mathrm{mm}$, $\mathrm{W} = 5830\ \mathrm{mm}$, and $\mathrm{e} = 2915\ \mathrm{mm}$.

In this model, the vertical link beam is a wide-flange section. The link beam and the SCVD box enclosure are made of Grade A992 steel. Two sets of combined stacking disc springs preloaded to 15% of their total deflection capacity were used in the model. Each set contains three disc-springs in parallel stacking and fourteen in series stacking. It should be noted that the width of the TPAD plate changes linearly, and the total length is the summation of trapezoidal length and tongue length. The TPAD plate is made of low-yield steel Q225LY with the yield stress of 225 MPa. "Steel-02" material with isotropic hardening parameters in Table 3.2 was used in the OpenSees model for the TPAD fuse device [6]. All the structural steel used in the model is "Steel-02" material.

Table 4.1 Member section size of the SCVD module frame (Unit: mm)

Member	Section	d	t_w	b_f	t_f	Length
Vertical Link Beam	W	700	6	320	12	e=2915

Table 4.2 Dimensions of the disc springs in the SCVD module frame (Unit: mm)

D_e	D_i	l_0	t	n_p	n_s
250	102	18	10	3	14

Table 4.3 Dimensions of the TPAD plate in the SCVD module frame (Unit: mm)

w_1	w_2	h_1	h	t	gap
360	120	200	250	25	6

Table 4.4 Viscous damper parameters

c_d (N.s/mm)	α
9290	0.5266

4.5 Numerical Modeling

The numerical model of the original timber structure retrofitted with WSP in the FE software OpenSees [93] is shown in Figure 3.5. Figure 4.13 illustrates the numerical model of the SCVD module frame retrofitting the ground story only of the four-story prototype WSP-retrofitted building. This is a planar schematic view of the wireframe model showing the vertical link beam, self-centering viscoelastic damper, TPAD, and the damper box enclosure.

As shown in Figure 4.13, in the self-centering viscoelastic damper (SCVD) modular frame, the vertical link beam was modeled using “NonlinearBeamColumn” element. Top end of the link beam was assigned the same node as the middle node of the floor beam. Top of SCVD box enclosure and bottom of link beam were assigned the same horizontal degree of freedom (DOF). The main column frame members were modeled using “ElasticBeamColumn” elements with the moment released at both ends. Floor beam elements were modeled using “NonlinearBeamColumn” element. The floor beam and columns were connected using simple connection by introducing an intermediate zero-length spring with flexible material used in the rotation simulating pinned connection.

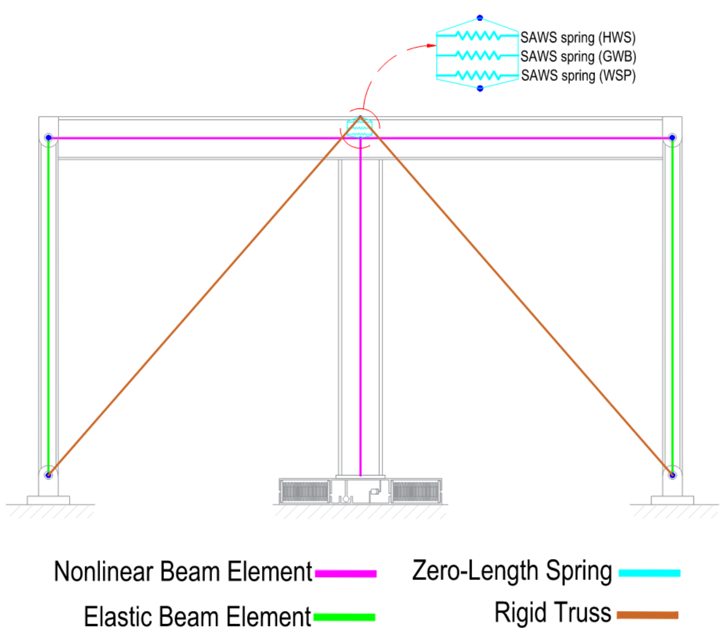

Figure 4.13 2D Numerical wireframe modeling of the WSP-retrofitted prototype timber structure retrofitted with SCVD module on the ground story only in OpenSees

In the self-centering viscoelastic damper (SCVD), “NonlinearBeamColumn” element with distributed plasticity was used for the damper box enclosure, and TPAD fuse as shown in Figure 4.14. Multiple elements with different cross-sections were employed in series connections for modeling the varying cross-section of the TPAD plate. The “twoNodeLink” spring element was employed to model the disc springs. Additionally, “initStrain” material along with “ElasticPPGap” material was used in order to model the compression-only behavior of the disc springs and apply the preload. The “twoNodeLink” flexible spring with an initial gap representing the deformation capacity of the sets of the disc springs was utilized to model the deflection capacity of the sets of disc springs.

In order to model the viscous damper, a zero-length spring with viscous material was used. A gap between the TPAD and the adjacent walls on each side inside the viscoelastic damper was created using a “twoNodeLink” spring with an “ElasticPPGap” material. The damper box is fixed to the ground node in the middle using a rigid zero-length spring.

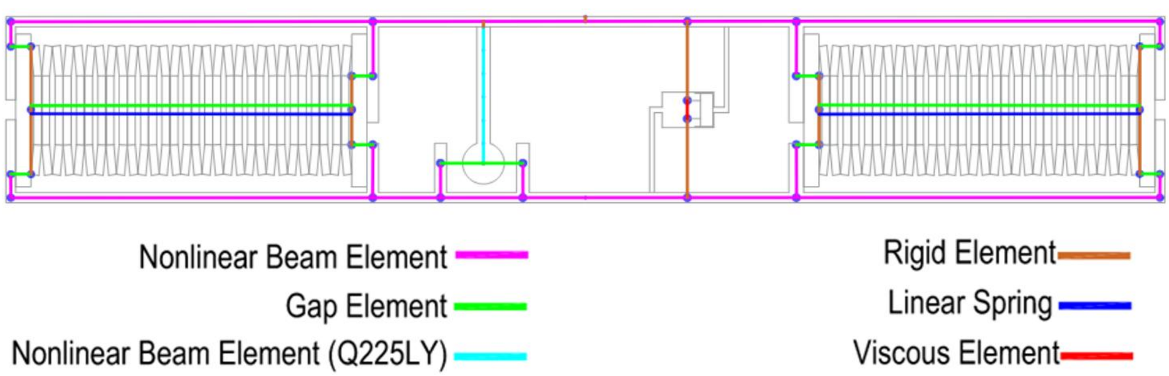

Figure 4.14 2D Numerical wireframe modeling of the SCVD device in OpenSees

4.6 SCVD-Retrofitted Prototype Building

The seismic performance of the prototype four-story soft-story light-frame wood building retrofitted with the novel SCVD module frame on the ground story only located in downtown San Francisco was investigated through nonlinear static and dynamic analyses. The prototype building was designed and its floor plans, elevation views, and isometric views are illustrated in Figure 3.7 through Figure 3.9 [4]. The ASCE 7-22 [100] provisions were used to design the structure. The seismic Design Category D for the prototype located in San Francisco is considered. The total seismic mass of the four-story timber building is 48,000 kg.

Existing seismic force resisting system (SFRS) is shown in Figure 3.10. Original wall sheathing includes HWS, and GWB, and WSP retrofitting panels were used to strengthen the entire building in the last phase. One modular SCVD frame was considered along each direction on the first story of the code-deficient wood frame building to strengthen the existing lateral load-resisting system. Using SCVD module system in order to retrofit the first story only is proper because the first story has not been adequately retrofitted with WSP in the last step due to less availability of the existing timber shear walls at this level.

4.7 Eigenvalue and Nonlinear Static Analyses

Figure 4.15 illustrates the mode shapes of the retrofitted prototype building. The modal periods are 0.395 sec, 0.151 sec, 0.101 sec, and 0.076 sec among which the first mode dominates. An approximately inverted triangular-shaped load profile conforming to the first mode shape was applied to the nodes of the lean-on-column in order to conduct the nonlinear static analysis. For this purpose, the structure was pushed to 2.0% of the roof drift ratio and unloaded. The pushover curve of the SCVD-retrofitted prototype is shown in Figure 4.16. It should be noted that the effect of velocity-dependent energy dissipation device (i.e. viscous damper) is not observed in the nonlinear static analysis.

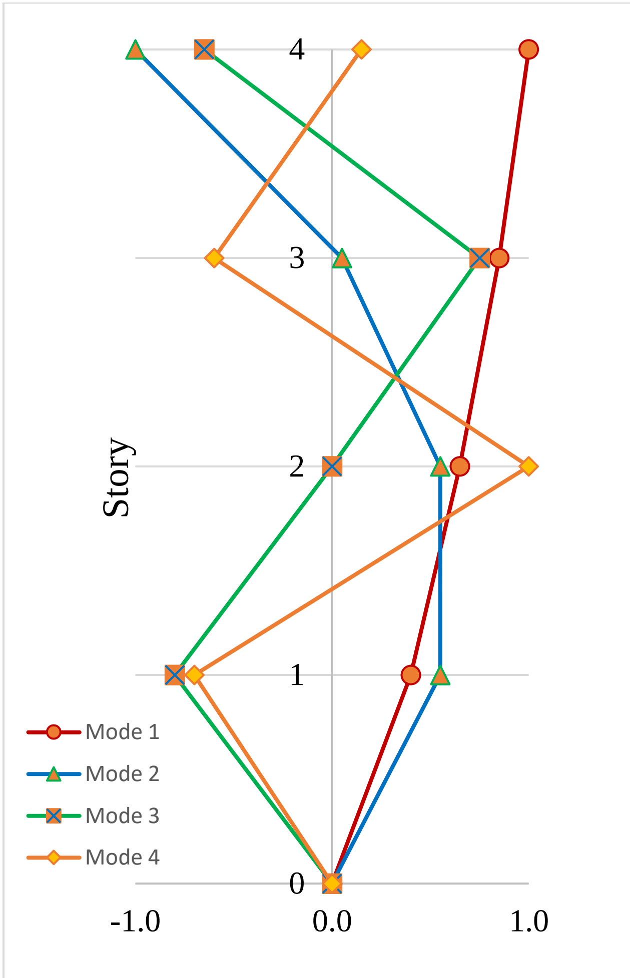

Figure 4.15 Modal shapes of the four-story soft-story light-frame wood prototype building retrofitted with SCVD module on the first story only

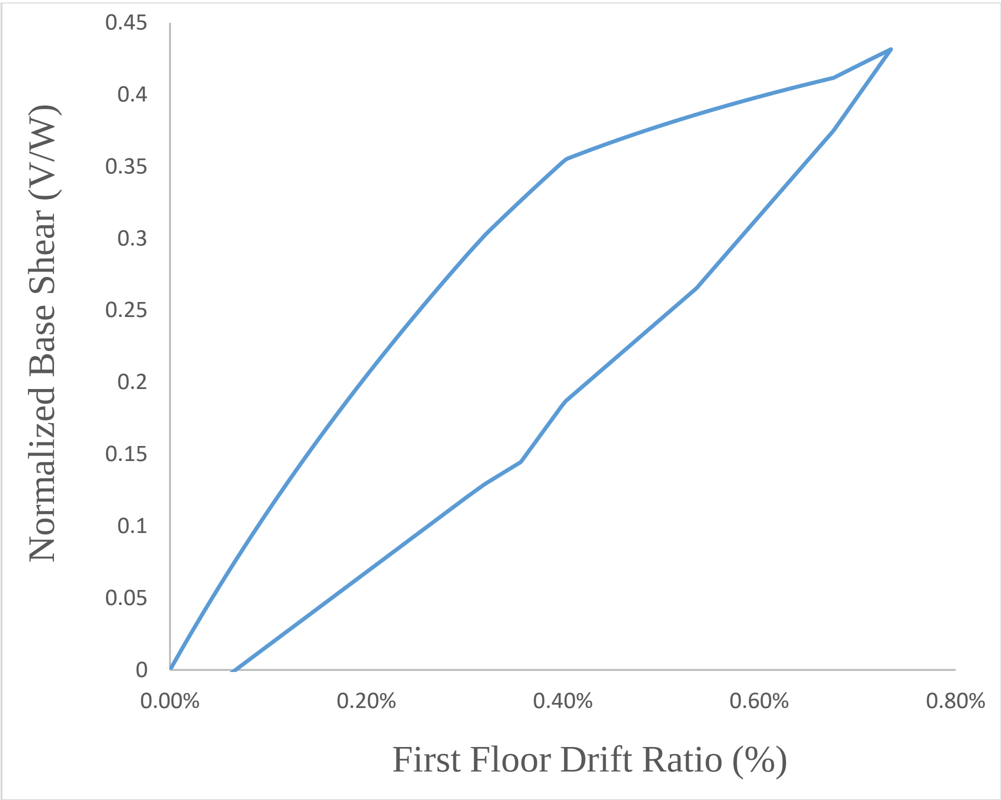

Figure 4.16 First floor pushover curve of the four-story soft-story light-frame wood frame prototype building retrofitted with SCVD module on the first story only (viscous damper contribution is not observed)

4.8 Nonlinear Response History Analysis

The seismic behavior of the SCVD-retrofitted building was assessed through nonlinear response history analysis (RHA). The far-field (FF) record set of ground motions was considered according to FEMA P695 [94] which includes twenty-two component pairs and forty-four horizontal ground motion records. All the details of the ground motions are included in Appendix A of this dissertation. A total of twenty-two horizontal ground motion records (one ground motion from each component pair) was chosen for the nonlinear time-history (NLTH) numerical analysis. Newmark method was used for the analysis considering β=0.25 and γ=0.5. Rayleigh damping with a 5% viscous damping ratio was utilized for the system damping. The nonlinear springs, rigid elements, and gap elements that may cause damping leakage were excluded from the classical Rayleigh damping [6].

4.9 Results and Discussions

In this section, the results of the nonlinear RHA of the WSP-retrofitted prototype building retrofitted on its ground story only with the proposed novel SCVD system subjected to the ground motions of the Far-field (FF) record set are presented. The ground story only-retrofitted building can survive under all the ground motions (GMs) in case the intensity is set to $0.45\mathrm{DBE}$. The building failed under one ground motion only when subjected to $0.5\mathrm{DBE}$. In earthquake engineering, this level is considered as the frequent earthquake (FE) intensity. Furthermore, the structure collapsed under 2, and 15 GMs when exposed to $0.6\mathrm{DBE}$, and DBE levels, respectively.

The maximum value of the peak responses among all the four stories is considered as the maximum response. The maximum inter-story drift ratio (IDR) responses of the retrofitted building with and without the TPAD fuse device are shown in Figure 4.17 with an ensemble median value of 0.43%, and 0.47% at the $0.45\mathrm{DBE}$ level, respectively, and the maximum IDR is more than 1.0% only under one ground motion at this level of intensity which can be because of the yielding of the timber shear walls and large inelastic deformation in the link beam.

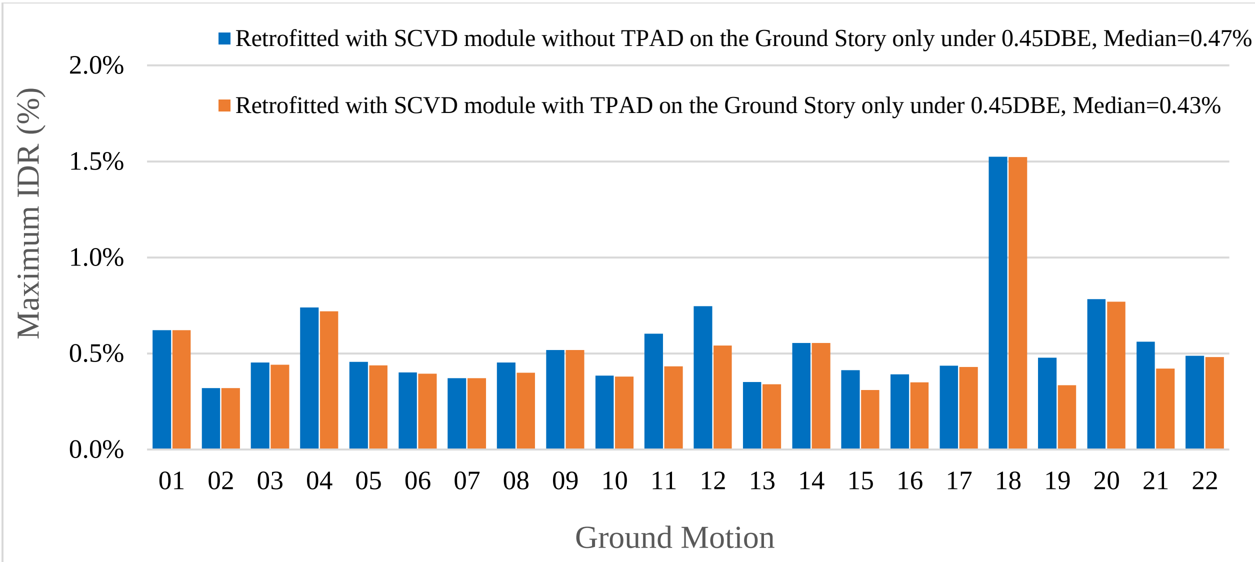

Figure 4.17 Maximum IDR responses in the wood building retrofitted with SCVD on the ground story only under 0.45DBE

The maximum residual IDR of the retrofitted building is illustrated in Figure 4.18. The median values of the maximum residual IDRs with and without TPAD are 0.17%, and 0.22%, respectively. These numbers show that the SCVD-retrofitted prototype performs satisfactorily under almost the frequent earthquake (FE) intensity in terms of recentering behavior, and constraining the maximum IDR responses.

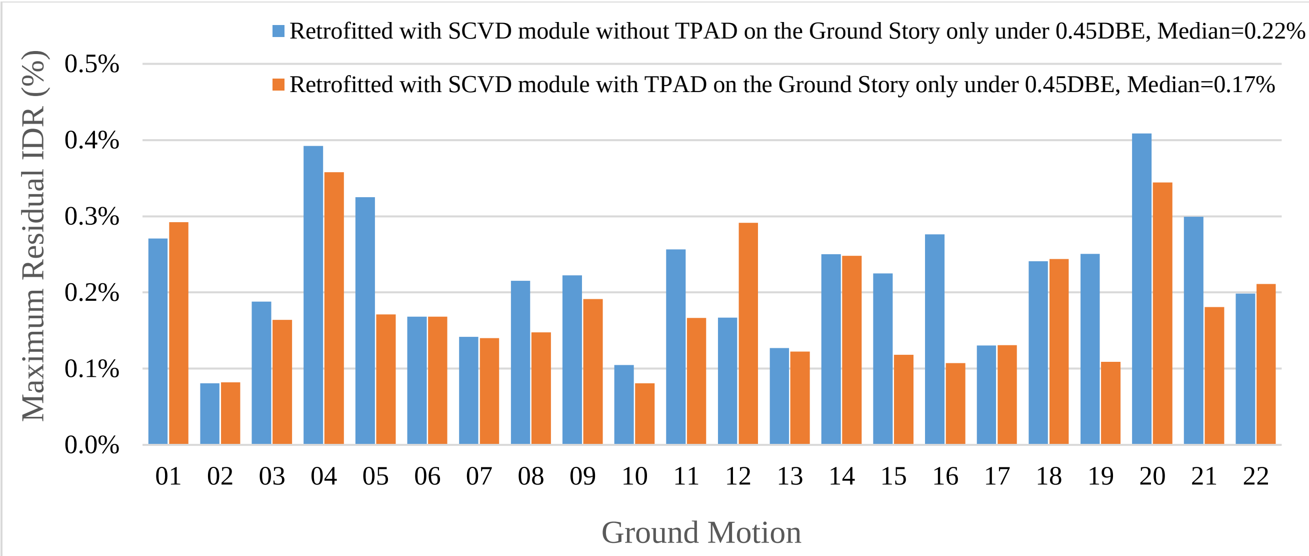

Figure 4.18 Maximum residual IDR in the wood building retrofitted with SCVD on the ground story only under $0.45DBE$

The vertical profile of the IDR responses of the first-story-only retrofitted prototypes without and with the fuse device subjected to the ground motions GM-19, and GM-11, respectively corresponding to the median of the maximum drift responses of the prototypes along with 16th and 84th percentile values of the peak drifts are presented in Figure 4.19. According to the figure, the peak drifts, when considering quantile values, exhibit greater dispersion at the upper stories, while the ground story shows a narrower dispersion. This effect is more apparent in the retrofitted case that includes the TPAD fuse device.

In the SCVD-retrofitted prototype without the fuse plate, the maximum peak inter-story drift ratio (IDR) occurs at the roof level, while the minimum peak IDR is observed approximately at the ground story. However, in the retrofitted prototype with the fuse device, the maximum peak IDR occurs at the second story, while the minimum peak IDR remains at the ground story.

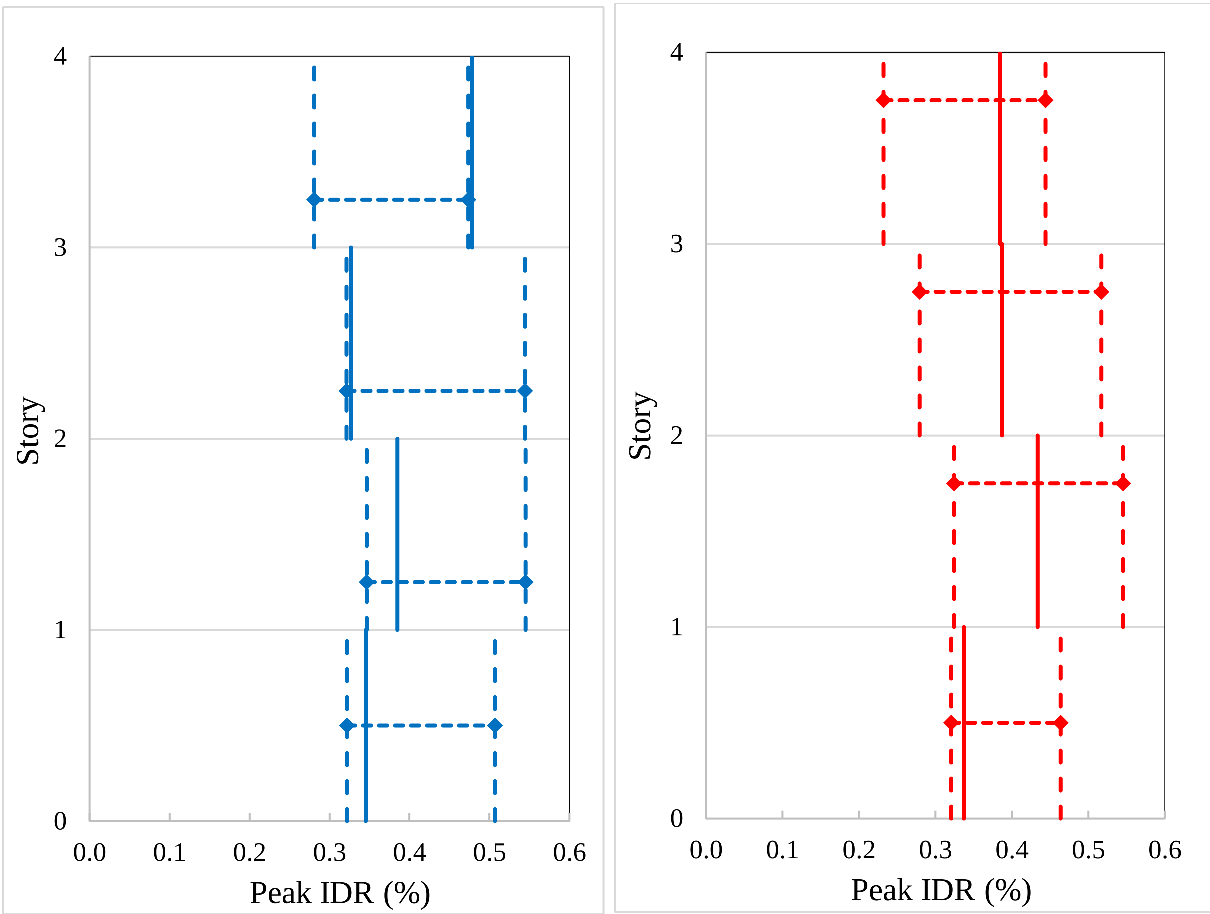

(a) (b)

Figure 4.19 Vertical profile of the IDR of the SCVD-retrofitted prototype buildings with 16th and 84th percentile values of the peak responses under 0.45DBE: (a) Without the TPAD fuse device under GM-19; (b) With the TPAD fuse device under GM-11

4.10 Structural Demands of a Typical Case

The structural responses of the SCVD-retrofitted with TPAD prototype building under a typical ground motion are presented in this section. For this purpose, the structural responses of the ground story subjected to GM-11 are shown at the 0.45DBE level. This is the ground motion under which the structure has shown the same maximum IDR as the mean value. Figure 4.20 shows the first story drift response history with the peak response value of 0.34%. The story demonstrates an acceptable recentering performance with the residual IDR value of 0.009%. Figure 4.21 illustrates the hysteresis behavior of the ground story in the prototype four-story wood framed SCVD-retrofitted building.

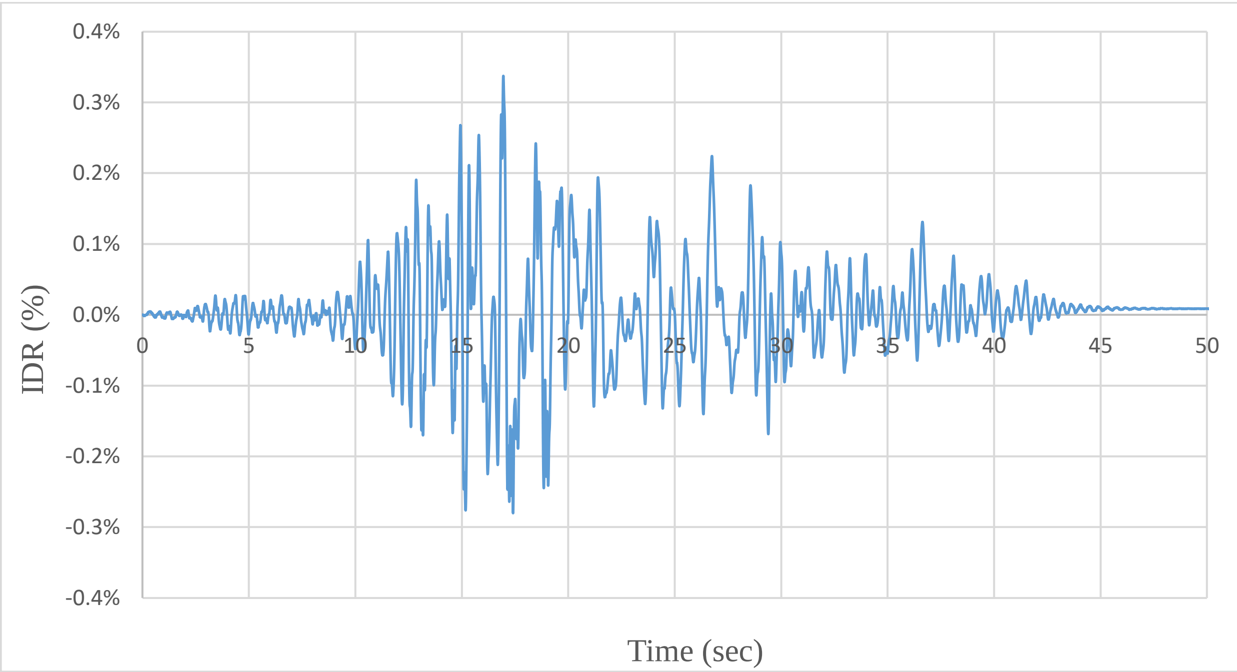

Figure 4.20 IDR history of the ground story in the SCVD-retrofitted prototype building under GM-11 at $0.45DBE$

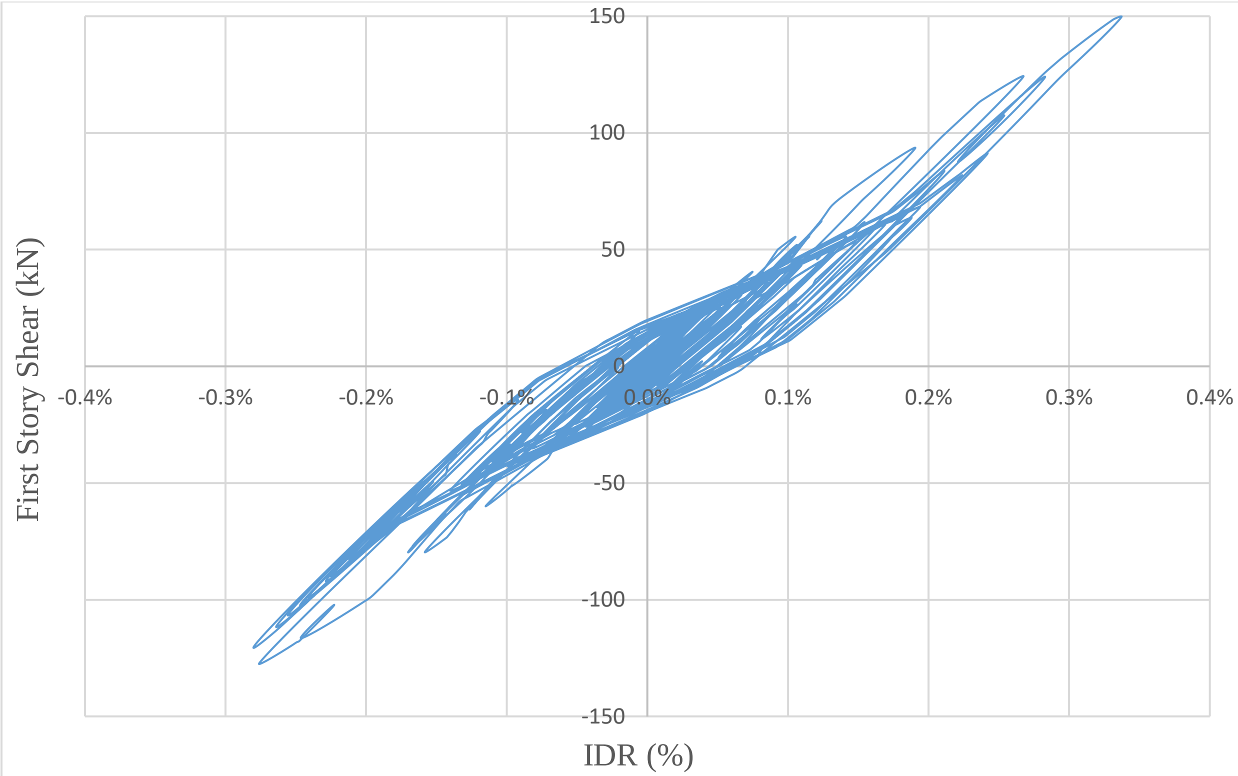

Figure 4.21 Hysteresis behavior of the ground story in the SCVD-retrofitted prototype under GM-11 at $0.45DBE$

4.11 Summary

In this chapter, nonlinear seismic behavior of a WSP-retrofitted prototype light-frame wood building retrofitted on its ground story only with the self-centering viscoelastic damper (SCVD) modular frame was studied through analytical and numerical investigations. The analytical relationships of the system key properties were derived based on the system's behavior. A four-story soft-story prototype light-frame timber structure was designed originally and was retrofitted with WSP in the previous phase. The seismic performance of the WSP-retrofitted prototype retrofitted at the ground story level with the novel SCVD module was assessed through nonlinear numerical static and dynamic analyses. According to the results of the nonlinear numerical study of the SCVD-retrofitted prototype structure, the following conclusions can be drawn:

- The ensemble median value of the maximum IDRs for the SCVD-retrofitted prototype without TPAD is less than 0.5% at the 0.45DBE level under the far-field (FF) record set, with the maximum residual IDR less than 0.25% for the same intensity level.
- The ensemble median value of the maximum IDRs, and the maximum residual IDR for the SCVD-retrofitted prototype with TPAD is less than 0.45%, and less than 0.2%, respectively at the 0.45DBE level under the far-field (FF) record set.
- The peak drifts, considering quantile values, are more widely dispersed at the upper stories, while the dispersion at the ground story is narrower. This is more apparent in the retrofitted case incorporating the TPAD fuse device.
- In the SCVD-retrofitted prototype without considering the fuse plate, the maximum value of the peak IDR takes place at the roof level while the minimum value occurred at the ground story approximately. In the retrofitted prototype with the fuse device, the maximum value of the peak IDR occurred at the second story while the minimum value takes place at the ground-story level. This conclusion is based on the results from the ground motions (GMs) their maximum IDR values are the same as the ensemble median of the maximum IDR of all the record set for each case.
- The SCVD retrofitting systems can be designed in order to retrofit the ground story only of a soft-story wood frame building in order to achieve an improved seismic performance under almost the frequent earthquake (FE) intensity in terms of inter-story drift ratio (IDR), recentering behavior, energy dissipation, and the response of the existing wood lateral wall framing. This retrofitting method proves to be cost-effective, and easy to implement, as the

new retrofitting system can be installed at the ground story only without any disruption to the upper stories of the existing building.

Chapter 5 : Nonlinear Seismic Analysis and Performance Study of Soft-Story Wood Framed Structures Retrofitted with Y-type Braced Self-Centering Viscous Damper Eccentrically Braced Frame (Y-SCVD-EBF) Systems

In this chapter, the nonlinear seismic performance of Y-type braced self-centering viscous damper eccentrically braced frame (Y-SCVD-EBF) modules has been studied. For this purpose, the original code-deficient prototype wood building has been retrofitted entirely with the novel Y-SCVD-EBF retrofitting system in order to comply with current seismic provisions. Then, the retrofitted structure has been undergone the nonlinear static and dynamic seismic loadings. Analytical relationships of a typical light-frame soft-story wood framed structure retrofitted with the proposed Y-SCVD-EBF module have been derived. It should be noted that the existing timber shear walls have not been considered in this seismic analysis as the lateral stiffness and strength of the new retrofitting steel frame are much greater than those of the existing wood seismic force resisting system (SFRS). Nonlinear response history analyses (RHA) have been conducted on the four-story retrofitted prototype building to investigate the seismic behavior of the developed system.

5.1 Seismic Behavior of the System

The schematic and components of the Y-SCVD-EBF module inserted into the code-deficient wood frame building is shown in Figure 5.1. The connection between the diagonal braces to the beam-to-column joints is considered as simple; however, the other end of the braces is fixed to the support beam. Recentering capability of the system is provided by the two sets of pre-loaded disc springs inside the self-centering viscoelastic damper box enclosure. Seismic energy is dissipated primarily by the viscous damper while TPAD is utilized as the backup source of energy dissipation dissipating the energy through the flexural yielding mechanism. Both devices are inside the self-centering viscoelastic damper box enclosure. The components of the SCVD device and TPAD are shown in Figure 4.2 and Figure 4.3, respectively. The schematic of the system at the time of gap opening is illustrated in Figure 5.2.

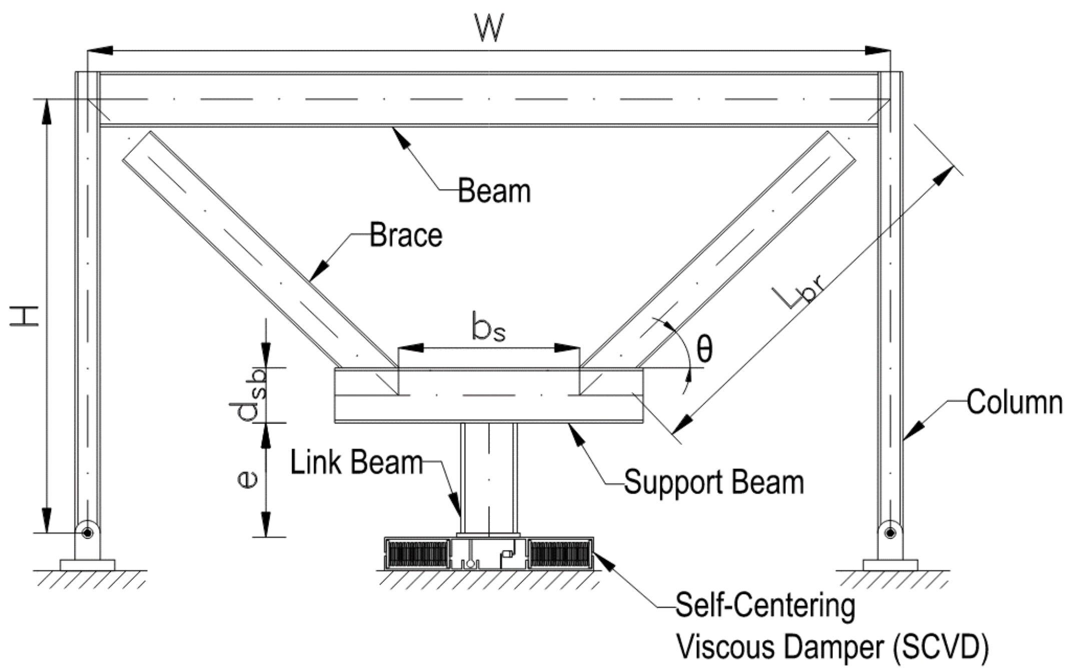

Figure 5.1 Schematic, and components of the Y-SCVD-EBF module

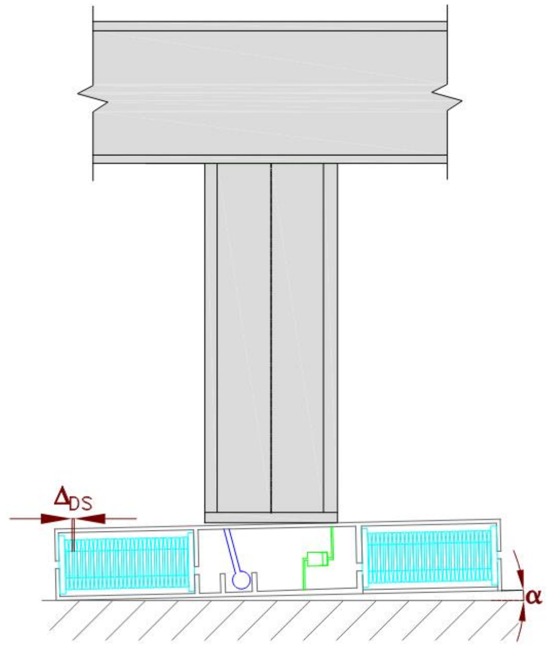

Figure 5.2 Schematic of link beam and SCVD at the time of gap-opening in the Y-SCVD-EBF system

5.2 Analytical Formulation of the Y-SCVD-EBF System

In this section, the analytical relationships of the load-displacement behavior of the proposed Y-SCVD-EBF system shown in Figure 5.1 have been presented. The behavior of the retrofitting system without the fuse device is studied first, and then the effects of adding a TPAD to the system are investigated afterwards. The hysteresis behavior of the two systems is shown in Figure 4.4, and Figure 4.10, representing the bilinear elastic, and the flag-shaped curve, respectively, where the effects of the velocity-dependent energy dissipation device (i.e. viscous damper) is not considered in the system. The load-displacement behavior of the aforementioned systems with the viscous damper is shown in Figure 4.6, and Figure 4.11, respectively.

5.2.1 Y-SCVD-EBF Module without the Fuse Device

Figure 4.4 illustrates the load-displacement behavior of a self-centering system without the fuse device. The following parameters are required to characterize the bilinear elastic hysteresis of a bare module frame: (1) initial stiffness, K_1; (2) base shear at gap-opening, V_0; (3) post-gap-opening stiffness, K_{PGO}.

According to Figure 5.1, $H, W, L_{br}, e,$ and b_s represent the frame height, span length, brace length, vertical link beam length, and the horizontal distance between the working points of the braces on the centerline of the support beam. In the following equations: I_{br}, I_{lb}, and I_{sb} express the moment of inertia of the braces, vertical link beam, and support beam, respectively. A_{br}, A_{cl}, A_{fb}, and A_{sb} show the cross-sectional area of the braces, columns, floor beam, and support beam, and A^{w}_{lb}, A^{w}_{sb}, and A^{w}_{br} represent the web cross-sectional area of the link beam, support beam, and braces. The height and thickness of the self-centering viscous damper box are expressed as w_{SCVD}, and t_{SCVD}, respectively. Additionally, E and G are Young's modulus and shear modulus of steel. The stiffness of the existing wood shear walls of the building is much less compared to that of the steel-frame retrofitting system. Therefore, in this chapter, existing Seismic Force Resisting System (SFRS) components of the wood-frame prototype, which are HWS, and GWB, are not considered in the analyses. The parameters required in the analyses are defined in Equations (5.1) through (5.3).

$$L'_{br} = L_{br}/(2\sin\theta) \tag{5.1}$$

$$\gamma_1 = 0.5\cos\theta + (H/W)\sin\theta \tag{5.2}$$

$$\gamma_2 = (H/W)\cos\theta - 0.5\sin\theta \tag{5.3}$$

The initial stiffness of the Y-SCVD-EBF module frame before the gap-opening, K_1, results from the elastic stiffness of the frame and can be obtained using Equation (5.4).

$$K_1 = \left(\frac{1}{K_a} + \frac{1}{K_f} + \frac{1}{K_s}\right)^{-1} \tag{5.4}$$

Where K_a, K_f and K_s denote the lateral stiffness of the frame due to the axial, flexural, and shear deformation of the frame members, respectively, and are developed based on the principal of virtual work. The lateral stiffness due to the axial deformation of the members, K_a, can be calculated using Equations (5.5) through (5.9).

$$K_a = \left(\frac{1}{K_0^a} + \frac{1}{K_{br}^a} + \frac{1}{K_{cl}^a} + \frac{1}{K_{fb}^a} + \frac{1}{K_{sb}^a}\right)^{-1} \tag{5.5}$$

$$K_{br}^a = \frac{EA_{br}}{2L_{br}\gamma_l^2} \tag{5.6}$$

$$K_{cl}^a = \left(\frac{EA_{cl}}{2H}\right)\left(\frac{W}{H}\right)^2 \tag{5.7}$$

$$K_{fb}^a = \frac{4EA_{fb}}{W} \tag{5.8}$$

$$K_{sb}^a = \frac{4EA_{sb}}{b_s} \tag{5.9}$$

Where $K_0^a, K_{br}^a, K_{cl}^a, K_{fb}^a$ and K_{sb}^a denote the frame lateral stiffness due to the axial deformation of the self-centering damper box enclosure, braces, columns, floor beam, and support beam, respectively. The lateral stiffness due to the flexural deformations, K_f, would be calculated using Equations (5.10) through (5.13).

$$K_f = \left(\frac{1}{K_0^f} + \frac{1}{K_{lb}^f} + \frac{1}{K_{br}^f} + \frac{1}{K_{sb}^f}\right)^{-1} \tag{5.10}$$

$$K_{lb}^f = \frac{3EI_{lb}}{e^3} \tag{5.11}$$

$$K_{br}^f = \frac{3EI_{br}}{2L_{br}^3\gamma_2^2} \tag{5.12}$$

$$K_{sb}^f = \frac{EI_{sb}}{2}\left\{\frac{b_s}{2}\left[(\gamma_2 L'_{br})^2 + \frac{b_s^2}{12}\left(\frac{H}{W}\right)^2 + \gamma_2 L'_{br}\frac{Hb_s}{2W}\right]\right\}^{-1} \tag{5.13}$$

Where $K_0^f, K_{lb}^f, K_{br}^f$ and K_{sb}^f express the frame lateral stiffness due to the flexural deformation of the self-centering damper box enclosure, link beam, braces, and support beam, respectively. The frame lateral stiffness due to the shear deformations, K_s, is calculated using Equations (5.14) through (5.17).

$$K_s = \left(\frac{1}{K_0^s} + \frac{1}{K_{lb}^s} + \frac{1}{K_{br}^s} + \frac{1}{K_{sb}^s}\right)^{-1} \tag{5.14}$$

$$K_{lb}^s = \frac{GA_{lb}^w}{e} \tag{5.15}$$

$$K_{br}^s = \frac{GA_{br}^w}{2L_{br}{\gamma_2}^2} \tag{5.16}$$

$$K_{sb}^s = \left(\frac{GA_{sb}^w}{b}\right)\left(\frac{W}{H}\right)^2 \tag{5.17}$$

Where $K_0^s, K_{lb}^s, K_{br}^s$ and K_{sb}^s represent the frame lateral stiffness due to the shear deformation of the self-centering damper box enclosure, link beam, braces, and support beam, respectively. The free-body diagram of the SCVD and the vertical link beam is shown in Figure 4.7. The story shear of the frame at gap- opening, V_0, the corresponding story drift, Δ_0, the stiffness of the frame after gap-opening, K_{PGO}, the axial compressive force of a single disc spring, $F(s)$, the elastic stiffness of a single disc spring, K_S, and the equivalent stiffness of the two sets of disc springs in combined stacking, K_D, can be calculated using Equations (4.8) through (4.19). Figure 4.8 and Figure 4.9 show the geometry of a single disc spring and types of stacking, and force-deflection curve of disc springs.

5.2.2 Y-SCVD-EBF Module with the TPAD Fuse Device

TPAD as the displacement-dependent energy dissipation fuse device is the backup source of seismic energy dissipation in the proposed Y-SCVD-EBF system. The flag-shaped hysteresis curve of the Y-SCVD-EBF module which is shown in Figure 4.10 is the combination of the bare frame without the fuse and a mechanism frame with TPAD only.

The key parameters required to characterize the inelastic response behavior of the Y-SCVD-EBF module with TPAD are: (1) initial stiffness, K_1; (2) base shear at gap-opening, V_0; (3) stiffness after gap-opening, K_2; (4) system strength, V_y; (5) post-yield stiffness, K_3. The free-body diagram of the SCVD system with TPAD is shown in Figure 4.12. Adding TPAD to the SCVD module frame increases the initial stiffness, and base shear at gap-opening negligibly. The secondary stiffness, K_2, the contribution of the TPAD to the lateral stiffness after gap-opening, K_{ED}, the additional strength provided by fuse elements, V_{ED}, the system strength, V_y, the displacement corresponding to the system strength, Δ_y, the post-yield stiffness, K_3, the lateral stiffness contributed by the linear hardening of the trapezoidal plate, K_{ED}^{H}, and the output viscous damper force, F_V, can be calculated using Equations (4.20) through (4.28).

5.3 Design of Y-SCVD-EBF Modular Systems

In the Y-SCVD-EBF system, the stress within the frame members (i.e. columns, beam, braces, link beam, and support beam) and the SCVD box enclosure should remain within the elastic limit up to the design basis earthquake (DBE). Yielding must be confined exclusively to the TPAD fuse. However, any reduction in strength due to fracture of frame members or the TPAD should be avoided under the risk-targeted maximum considered earthquake (MCE_R).

Frame members are categorized as "force-controlled" elements and should be designed according to the seismic load combinations specified in ASCE 7-22 [100]. The system's required strength should be supplied by the viscous damper, gap-opening force, and TPAD, and thus these components should be designed to meet the specified design story shear.

Determining the gap-opening force and link beam stiffness is critical in developing Y-SCVD-EBF retrofitting modules. These modular frames are particularly advantageous for seismic retrofitting of existing light timber structures, as they contribute sufficient stiffness and strength to the existing seismic force resisting system (SFRS). For a typical four-story soft-story light-frame wood building in the San Francisco Municipal Area, the required stiffness and strength were calculated based on current seismic provisions, and the retrofitting modular frame was designed accordingly. It is important to note that the stiffness and strength of the existing timber shear walls were not factored into the retrofitting system design because they are much less compared to those of the steel framed retrofitting system.

For a multi-story light-frame wood building retrofitted with the proposed Y-SCVD-EBF steel-frame module, the gap-opening force and link beam for each story should be designed based on the design story shear, as specified by the applicable method in ASCE 7-22 [100]. The gap-opening force for each story is calculated according to its respective story shear and required lateral strength, and the link beam stiffness is calculated based on the related story shear and required stiffness for each story.

The required force from the preloaded disc springs dictates the choice of disc size, number of discs in parallel, and preloading amount. Once these parameters are set to achieve the target force, the number of series groups is determined based on deflection needs, ensuring that: (1) total deformation remains within 75% of the discs deflection capacity at DBE drift demands [95], and (2) the discs avoid reaching a flattened position up to MCE_R drift demands [6].

5.4 Y-SCVD-EBF Module Specifications

The properties of the Y-SCVD-EBF retrofitting module are presented in this section. In this chapter, the original four-story soft-story light-frame wood building is entirely retrofitted with the proposed retrofitting module. Existing seismic force resisting system (SFRS) which are mainly timber shear walls are neglected in the analysis because their stiffness is much less than that of the steel framed retrofitting system.

The Y-SCVD-EBF modular steel frame geometries are summarized in Table 5.1 in which d, $\mathrm{b_f}$, $\mathrm{t_f}$, and $\mathrm{t_w}$ denote the total depth, flange width, flange thickness, and web thickness of the structural steel sections, respectively. Table 5.2 and Table 5.3 show the disc springs, and TPAD geometrical properties. Additionally, Table 5.4 illustrates the viscous damper's parameters. In these tables, $\mathrm{D_e}$, $\mathrm{D_i}$, $\mathrm{L_0}$, t, $\mathrm{n_p}$, and $\mathrm{n_s}$ are the disc springs outer diameter, inner diameter, height, thickness, and number of springs in parallel, and series. The parameters $\mathrm{w_1}$, $\mathrm{w_2}$, $\mathrm{h_1}$, h and t are the TPAD base width, tongue width, trapezoid length, total length, and thickness, respectively, and $\mathrm{c_d}$, and α are the damping constant, and damping exponent.

All the structural steel is made of Grade A992 steel. The TPAD plate is made of low-yield steel Q225LY with the yield stress of 225 MPa. "Steel-02" material with isotropic hardening parameters in Table 3.2 was used in the OpenSees model for TPAD which were calibrated based on the material coupon test data [6]. All the structural steel used in the model is "Steel-02" material.

Table 5.1 Member section sizes of the Y-SCVD-EBF module (Unit: mm)

Member	**Section**	d	t_w	b_f	t_f	**Length**
Column	W	180	14	300	20	H=3150
Beam	W	400	14	300	20	W=5830
Vertical Link Beam	W	410	20	240	30	e=800
Brace	W	300	14	200	15	$L_{br} = 2830$
Support Beam	W	400	14	300	20	$L_{sb} = 2250$

Table 5.2 Dimensions of the disc springs in the Y-SCVD-EBF module frame (Unit: mm)

	D_e	D_i	l_0	t	n_p	n_s
1st Floor	100	41	7.75	5	4	37
2nd Floor	90	46	7	5	4	49
3rd Floor	125	51	9.4	6	2	30
4th Floor	125	51	9.4	6	1	30

Table 5.3 Dimensions of the TPAD plate in the Y-SCVD-EBF module frame (Unit: mm)

w_1	w_2	h_1	h	t	gap
1080	360	100	150	25	16

Table 5.4 Viscous damper parameters

c_d (N.s/mm)	α
9290	0.5266

5.5 Finite Element Modeling

The nonlinear seismic behavior of the four-story soft-story light-frame wood prototype building retrofitted entirely with the novel Y-SCVD-EBF module is numerically modeled as a planar wireframe in the FE software OpenSees [93]. The structural components have been modeled using proper elements reflecting their nonlinear behaviors. Figure 5.3 shows a schematic view of the 2D numerical model of the Y-SCVD-EBF retrofitting module which consists of the columns, beam, Y-bracings, support beam, vertical link beam, and the SCVD box. Modeling details of the self-centering viscoelastic damper is shown in Figure 4.14.

"NonlinearBeamColumn" element with distributed plasticity was used for all frame members. The connections between the beam and the columns, and between the braces and the columns were considered to be pinned by using intermediate zero-length springs connecting the two with flexible material in the rotation direction simulating simple connection. The connection between the braces and the support beam, and the link beam and the support beam were modeled using "twoNodeLink" spring with rigid material in the rotation direction simulating rigid connection. The bottom of link beam and top of SCVD box enclosure were assigned an equal horizontal degree of freedom (DOF) in the FE OpenSees model.

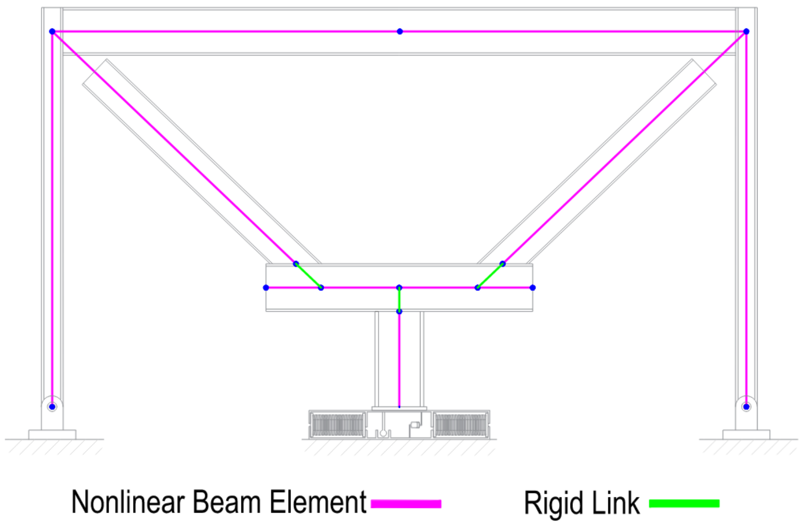

Figure 5.3 2D Numerical wireframe modeling of the Y-SCVD-EBF system in OpenSees

5.6 Prototype Wood Framed Building Retrofitted with Y-SCVD-EBF System

The module frame shown in Figure 5.1 is developed and used to retrofit the original four-story soft-story light-frame wood building. As mentioned in this chapter, the existing SFRS of the wood building is not considered in modeling the structure. Figure 5.4 shows how the original building is retrofitted with the Y-SCVDF-EBF modular system. The original prototype building is illustrated in Figure 3.7 through Figure 3.9.

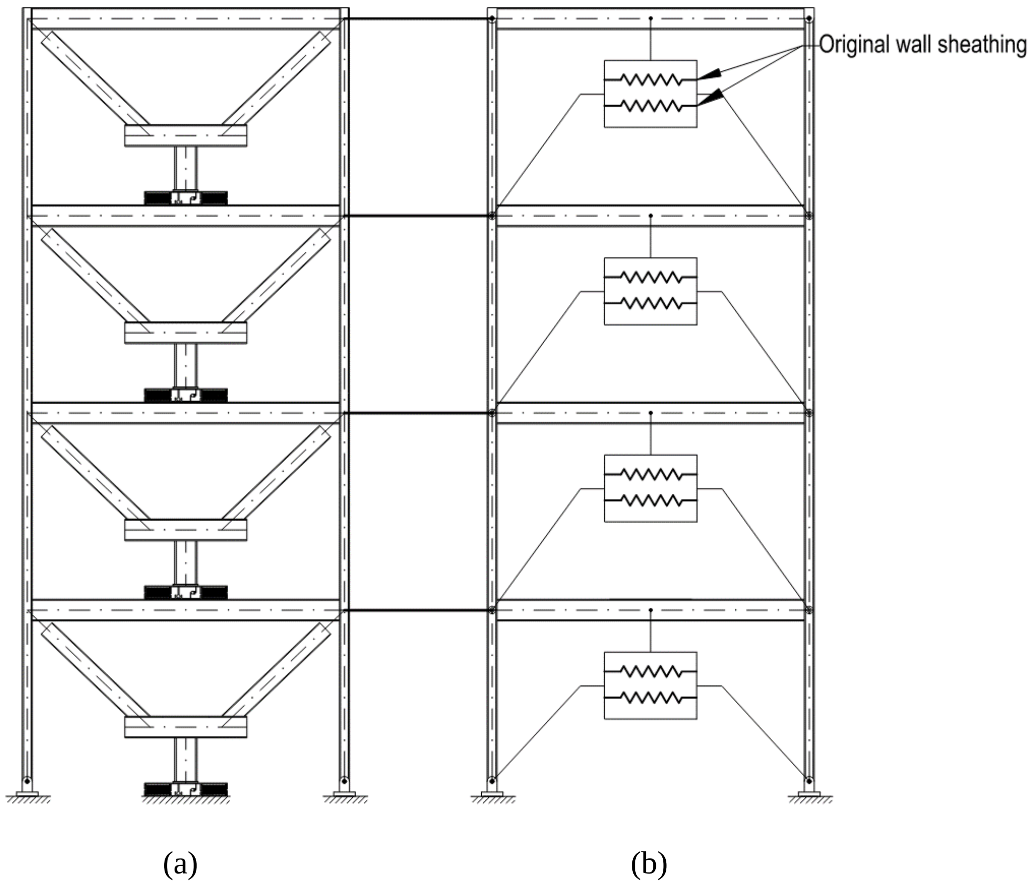

Figure 5.4 Elevation view of the original unretrofitted wood framed building retrofitted on all stories with the Y-SCVD-EBF module: (a) Y-SCVD-EBF steel retrofitting module; (b) Original unretrofitted timber structure

5.7 Eigenvalue and Nonlinear Static Analyses

The natural period of the steel framed prototype was calculated to be 0.216 sec based on the results of the Eigenvalue analysis. The other three modal periods were 0.071 sec, 0.045 sec, and 0.038 sec. Figure 5.5 shows the mode shapes of the retrofitted building. In order to perform the nonlinear static analysis, the structure needs to be exposed to an approximate inverted triangular-shaped load profile which conforms to the structural first mode shape. The loading was applied to the lean-on-column nodes, and the structure was pushed to 2.0% of the roof drift ratio and unloaded. The structure shows a fully recentering behavior as shown in Figure 5.6. Points A, B, C, and D represent the gap-opening point, TPAD activation point, TPAD full yielding point, and TPAD full plastic capacity point, respectively. As mentioned in the last chapter, the effect of velocity-dependent energy dissipation device (i.e. viscous damper) is not observed in the nonlinear static analysis.

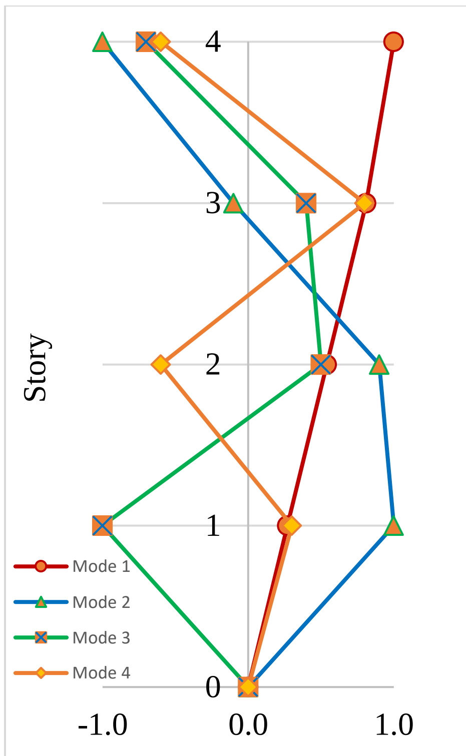

Figure 5.5 Modal shapes of the four-story Y-SCVD-EBF steel frame prototype building

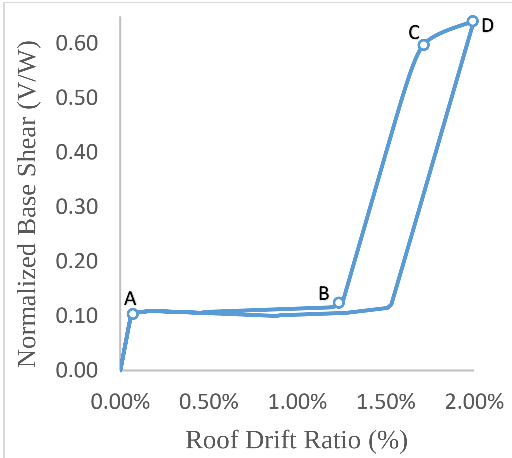

Figure 5.6 Pushover curve of the four-story Y-SCVD-EBF steel framed prototype building (viscous damper contribution is not observed)

5.8 Nonlinear Dynamic Analysis

In order to investigate the nonlinear seismic performance of the retrofitted building under strong ground motions, nonlinear response history analysis (RHA) was conducted at DBE and MCE_R levels. The Far-field (FF) record set of ground motions from the FEMA P695 [94] database was employed in this research consisting of twenty-two component pairs and forty-four horizontal ground motion records from sites located greater than or equal to 10 km from the fault rupture. All the details of the ground motions are included in Appendix A of this dissertation. A total of twenty-two horizontal ground motion records (one ground motion from each component pair) was randomly chosen for nonlinear RHA. Newmark method was used for the nonlinear dynamic analysis considering β=0.25 and γ=0.5. Rayleigh damping with a 5% viscous damping ratio was employed for the system damping. The nonlinear springs, rigid elements, and gap elements which might cause spurious damping force were not considered in the classical Rayleigh damping [6].

5.9 Results and Discussions

The results of the non-linear time-history (NLTH) analysis are presented in this section. The retrofitted structure can withstand under all the ground motions (GMs) at the DBE, and MCE_R intensities. The maximum inter-story drift ratio (IDR) of the prototype structure is presented in Figure 5.7 and Figure 5.8 under DBE, and MCE_R, respectively. Maximum response is considered as the maximum value of the peak responses among all the four stories. In case of no fuse devices in the system, the ensemble median of the maximum IDR responses at the DBE, and MCE_R levels is 0.7% and 1.28%, respectively. However, using the TPAD in the retrofitting module can change the aforementioned values to 0.63%, and 0.78%, respectively. Additionally, the median value of the maximum residual IDR at the two intensity levels is almost zero (~6E-06%).

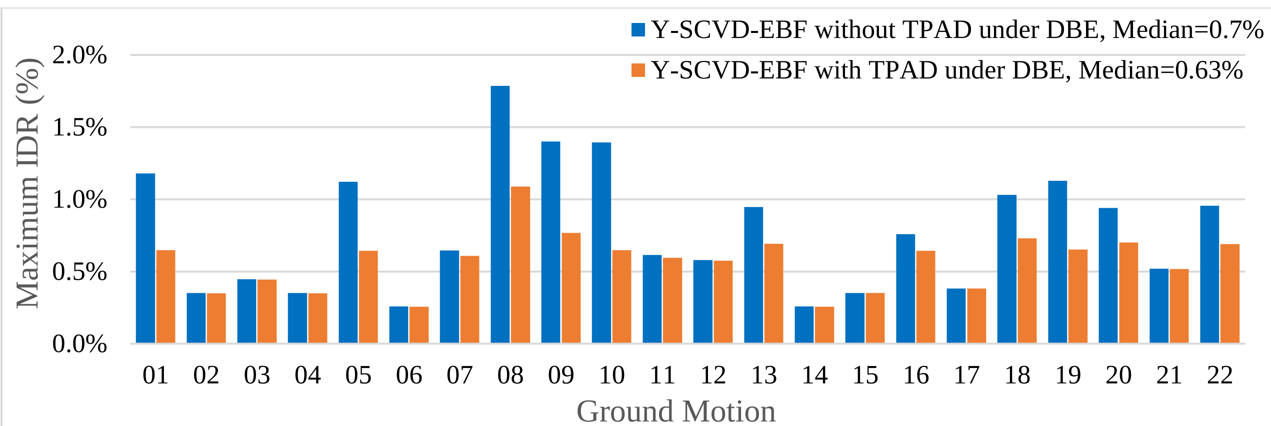

Figure 5.7 Maximum IDR response of the Y-SCVD-EBF prototype building under DBE

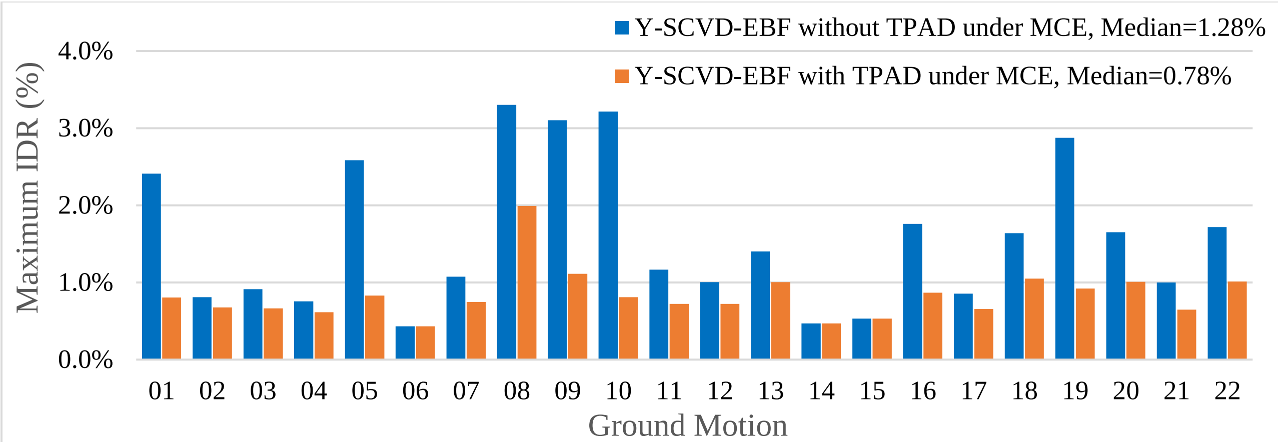

Figure 5.8 Maximum IDR response of the Y-SCVD-EBF prototype building under MCE_R

The vertical profile of the inter-story drift ratios (IDRs) of the prototype buildings subjected to the closest ground motion (GM) to the median of the maximum IDR responses of the retrofitted building with the fuse device under DBE along with 16th and 84th percentile values of the peak drifts are illustrated in Figure 5.9.

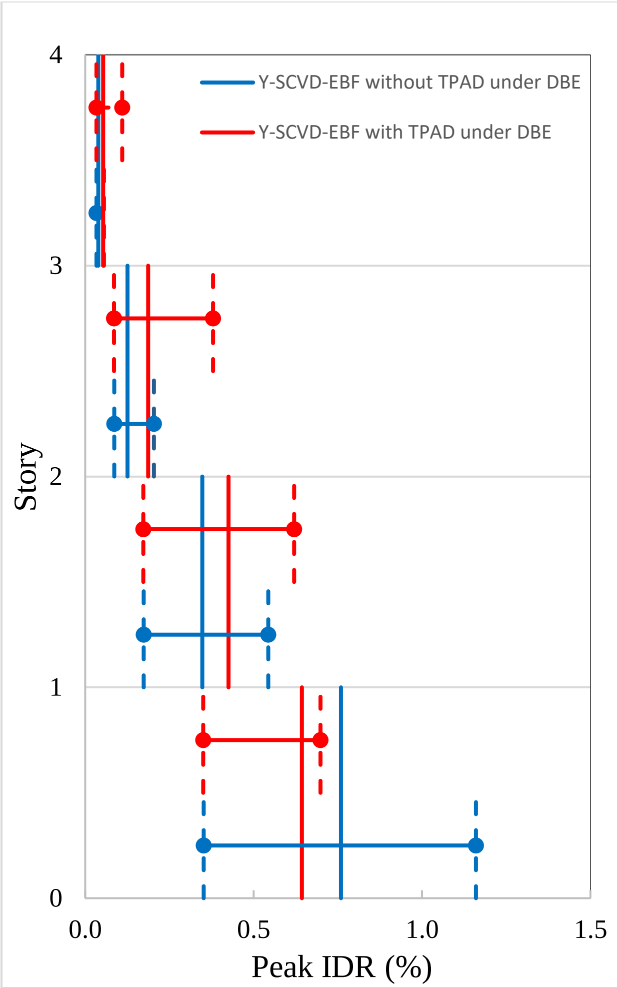

(a)

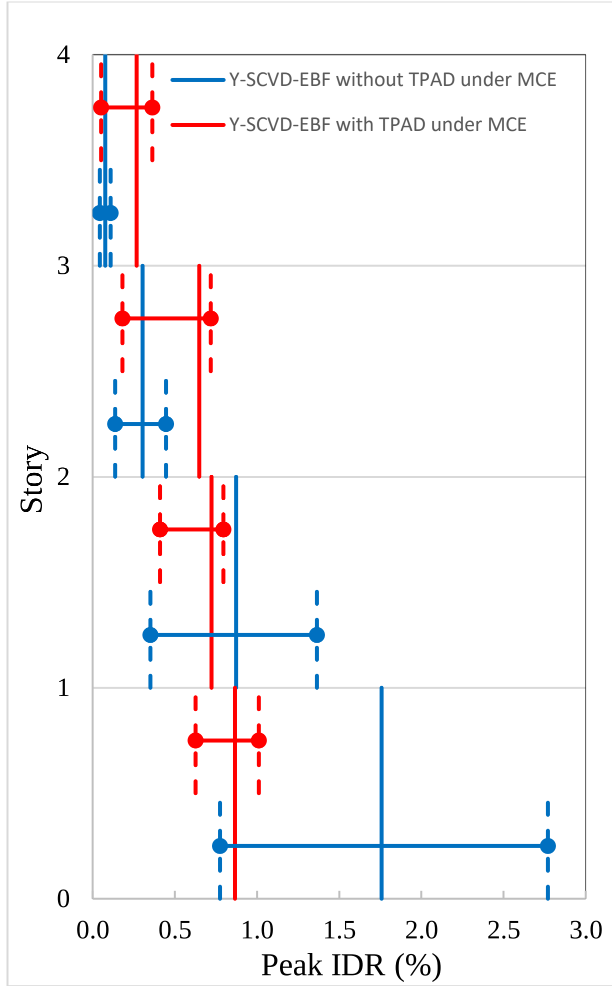

(b)

Figure 5.9 Vertical profile of the maximum IDR of the Y-SCVD-EBF prototype with 16th and 84th percentile values of the peak responses at GM-16 and under: (a) DBE; (b) MCE_R

The maximum deflection ratio of the sets of disc springs ($\frac{s_{max}}{h_0'}$) is illustrated in Figure 5.10 and Figure 5.11. The ensemble median of the maximum deflection ratio responses of the sets of disc springs at the DBE level where TPAD is not used in the retrofitting system is 32.3%. This value is 31.8% where TPAD is employed in the system. These values are both less than the recommended limit value of 75% which are acceptable.

At the MCE_R level, the ensemble median values are 61.7%, and 56.4% in case of without TPAD, and with TPAD, respectively. The disc springs reached their flattened position ($s_{max} = h_0'$) at the MCE_R level under 6 out of 22 ground motions (GMs) in case where TPAD is not used; however, this scenario takes place only under 1 GM where TPAD is utilized in the modular system.

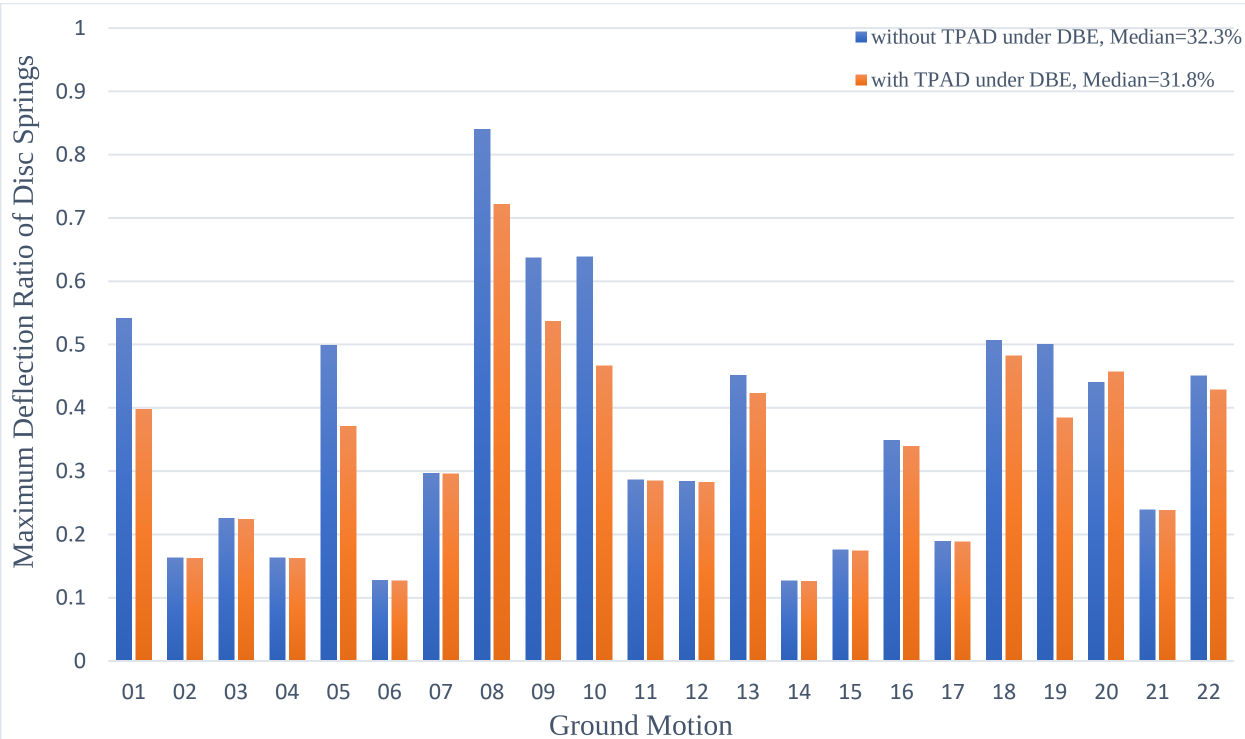

Figure 5.10 Maximum deflection ratio ($\frac{s_{max}}{h_0'}$) of the sets of disc springs of the Y-SCVD-EBF prototype building under DBE

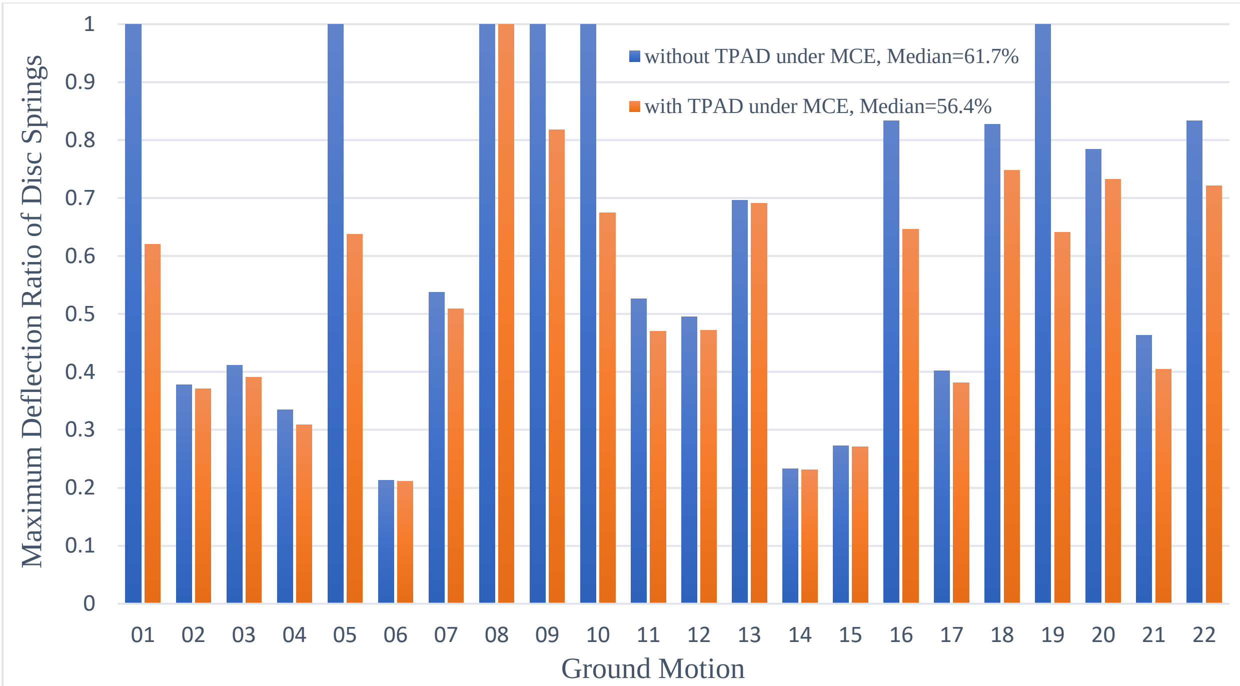

Figure 5.11 Maximum deflection ratio ($\frac{s_{max}}{h_0'}$) of the sets of disc springs of the Y-SCVD-EBF prototype building under MCE_R

In summary, the Y-SCVD-EBF retrofitted prototype structure shows satisfactory design performance in terms of drift control, recentering behavior, disc spring response, and damage control.

5.10 Structural Response of a Typical Case

In this section, the ground motion with the value of the maximum IDR closest to the median of the maximum IDRs in the prototype building is considered, and the structural responses of the first story are presented at the DBE level.

As shown in the story drift response history in Figure 5.12, the peak drift response of the first story is 0.76% where TPAD is not used in the system. The story shows a full recentering behavior with almost zero residual drift. The hysteresis diagram of the story is illustrated in Figure 5.13.

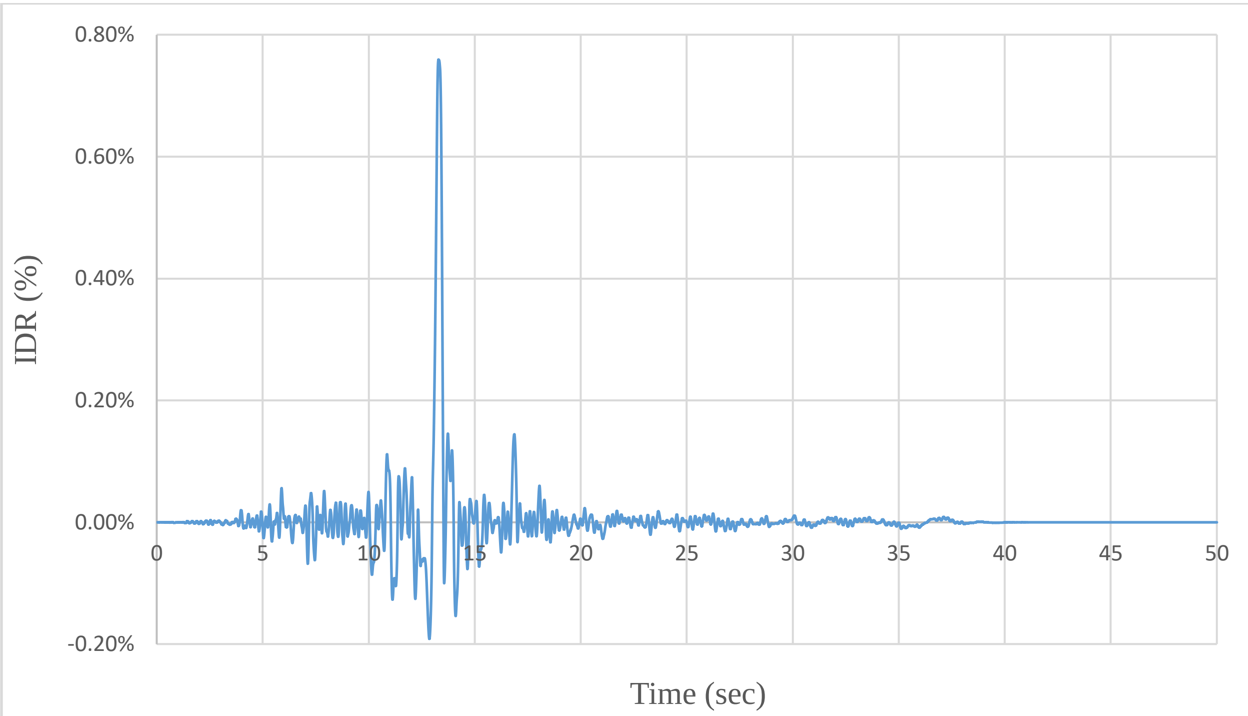

Figure 5.12 Drift response history of the first story of the Y-SCVD-EBF prototype at GM-16 under DBE (TPAD is not used in the system)

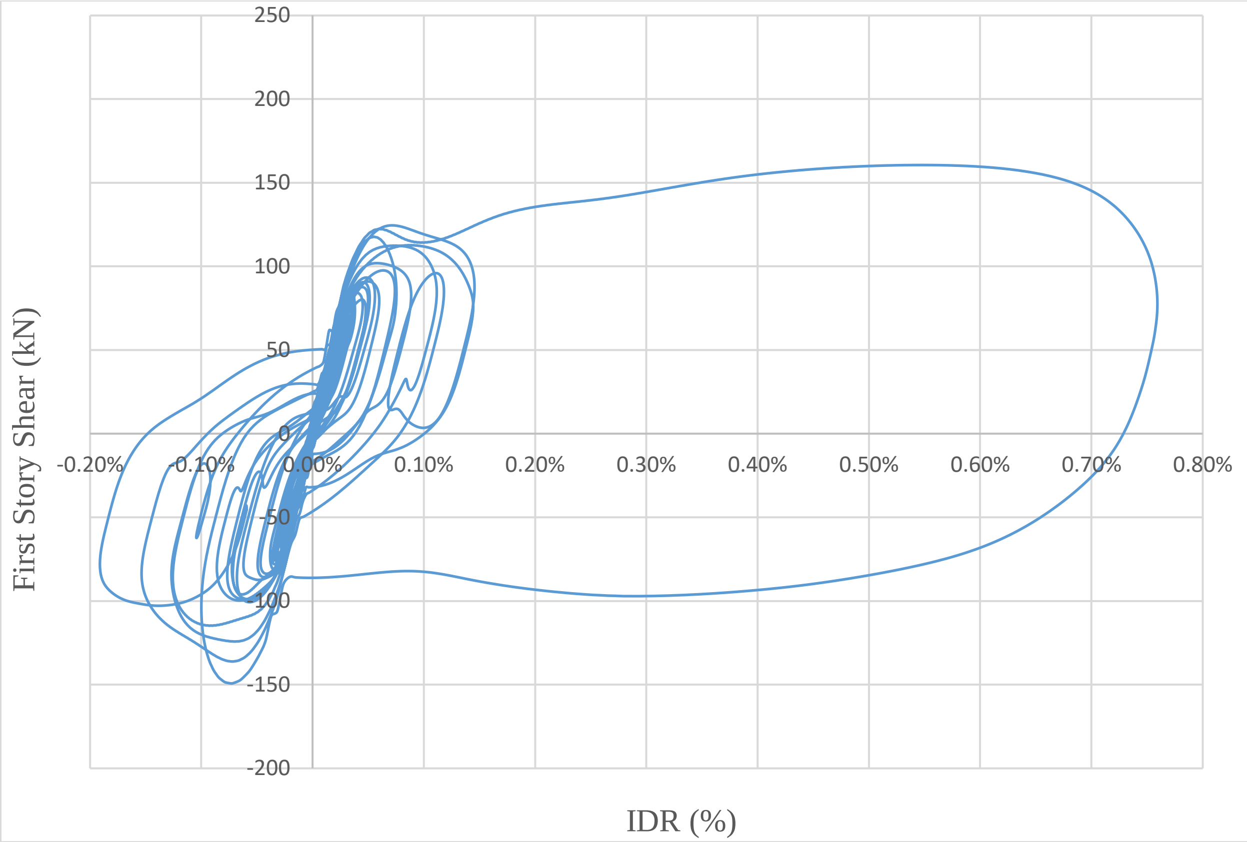

Figure 5.13 Hysteretic loop of the first story of the Y-SCVD-EBF prototype at GM-16 under DBE (TPAD is not used in the system)

According to the story drift response history in Figure 5.14, the story demonstrates a full recentering behavior and the peak drift response of the first story is 0.64% where TPAD is utilized in the system. The hysteresis diagram is shown in Figure 5.15.

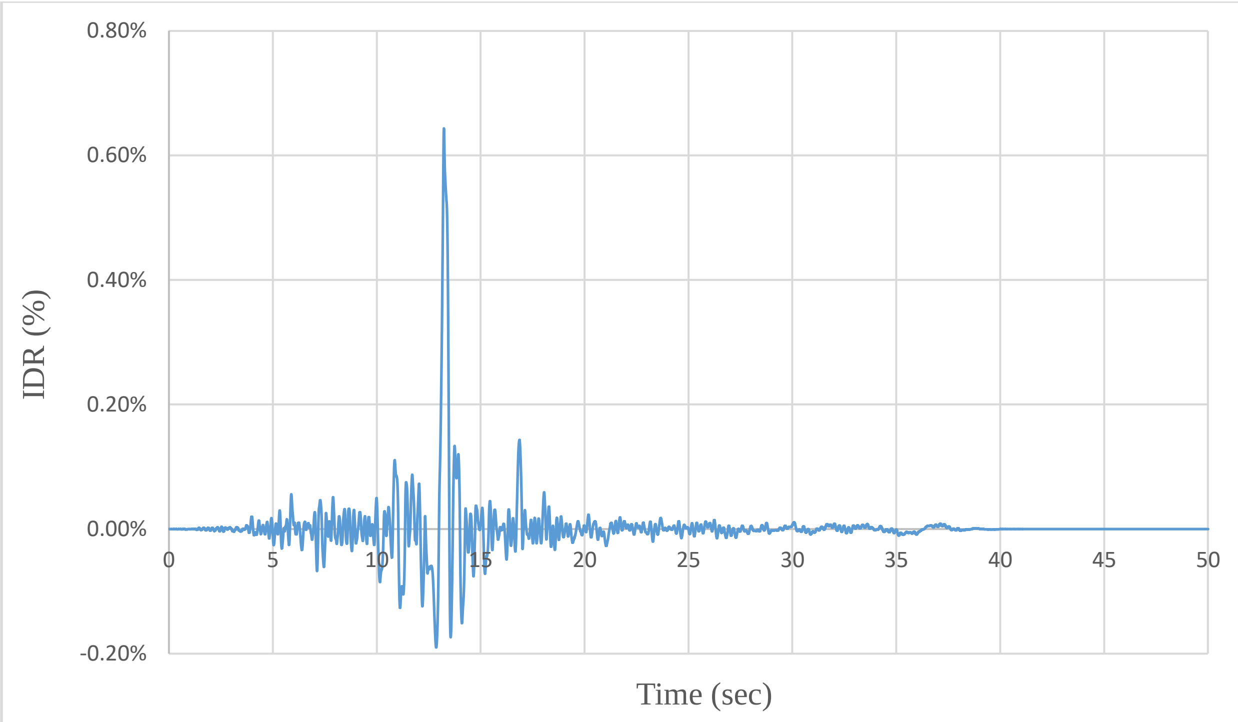

Figure 5.14 Drift response history of the first story of the Y-SCVD-EBF prototype at GM-16 under DBE (TPAD is utilized in the system)

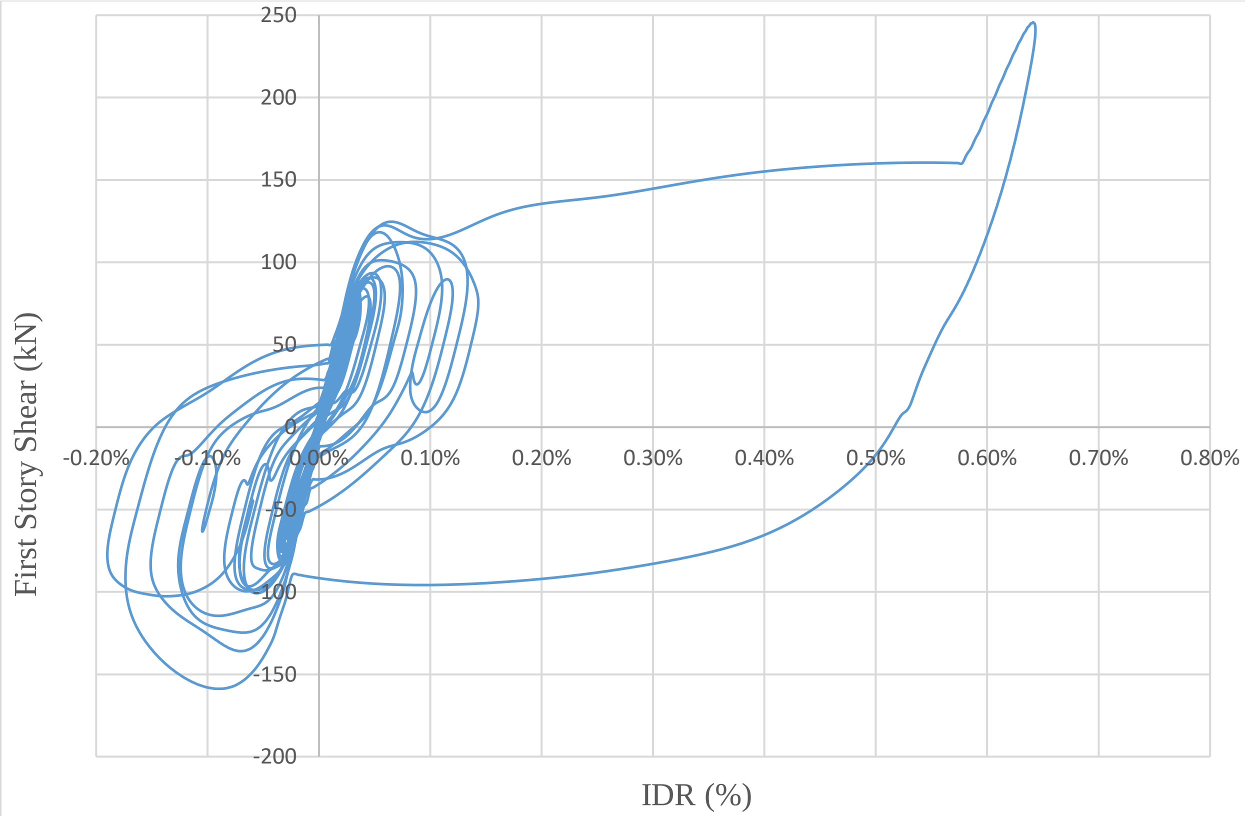

Figure 5.15 Hysteretic loop of the first story of the Y-SCVD-EBF prototype at GM-16 under DBE (TPAD is utilized in the system)

5.11 Summary

In this chapter, nonlinear seismic behavior of the prototype four-story soft-story light-frame wood building retrofitted with the Y-SCVD-EBF modular system was studied under the far-field (FF) record set of ground motions. The analytical relationships predicting the load-displacement behavior of the developed retrofitting system were presented. A two-dimensional wireframe FE model was created in OpenSees to simulate the structural seismic behavior numerically.

The four-story prototype Y-SCVD-EBF retrofitted wood building located in Downtown, San Francisco, was designed and its seismic behavior was investigated by conducting nonlinear static and dynamic analyses. The structural demands of the retrofitted building were investigated under the FF record set. The findings can be summarized as follows:

- The ensemble median of the maximum inter-story drift ratios (IDRs) of the prototype building without the TPAD fuse device was 0.7% and 1.28% at the DBE and MCE_R levels, respectively and the building had almost zero median residual drift at both intensities.
- The ensemble median of the maximum IDRs of the prototype with the TPAD fuse device was 0.63% and 0.78% at the DBE and MCE_R levels, respectively and the building had almost zero median residual drift at the both intensity levels.
- Using TPAD in the retrofitting system reduces the maximum IDR of the ground story by 0.12% at the DBE level considering the prototype under the ground motion with the maximum IDR closest to the median of the maximum IDR of the Far-field (FF) record set. In the case where TPAD is used, the structure shows a greater maximum base shear and more energy being dissipated.
- Utilizing the fuse device in the viscoelastic damper can reduce the peak IDR of the stories with the maximum IDR greater than 0.5%.
- Maximum deformation ratio of the sets of disc springs is affected by the displacement-dependent energy dissipation device. Using TPAD can lower the median of the deformation ratio of the disc springs by 0.5%, and 5.3% at the DBE, and MCE_R levels, respectively. TPAD can also help avoiding the disc springs flattened condition.
- The effects of using the TPAD fuse device in reducing the maximum IDR and deflection ratio of the disc springs are much sensible in case of more intense ground motions (GMs). Using TPAD could reduce the median of the maximum IDR by 0.07% under DBE;

however, employing the fuse device lowered the maximum IDR by 0.5% under MCE_R. Additionally, using the fuse could decrease the ensemble median of the maximum deflection ratio of the disc springs by 0.5%, and 5.3% under DBE, and MCE_R, respectively.

- The retrofitted structure achieved the design satisfactory performance in terms of drift control, recentering behavior, disc spring response, and concentrating damages in the fuse.
- It was concluded that the prototype wood-frame code-deficient building retrofitted with SCVD system on its ground story only shows satisfactory performance up to almost frequent earthquake (FE) intensity, while the counterpart entirely retrofitted with Y-SCVD-EBF system is seismically efficient at DBE, and MCE_R levels. Therefore, if the owner has limited budget and desires to retrofit the existing building so that it can perform well under frequent earthquake intensity, it is recommended that retrofitting the ground story only is taken into consideration; however, if the budget is not of concern, it is suggested that the entire building be retrofitted so that it is seismically adequate up to MCE_R intensity. It should be noted that there are some other differences between the two retrofitting procedures that need to be considered including the construction time, and areas disrupted due to construction which affect residents at different floors of the building.

Chapter 6 : Regional Seismic Resilience Assessment of Residential Light-Frame Wood Buildings with Soft Stories with the Seismic Retrofit in San Francisco Municipal Area

In this section, regional seismic resilience assessment of multi-family residential wood buildings with soft story retrofitted with the novel Y-SCVD-EBF modular system is conducted. FEMA P-58 component-level methodology is used for this purpose [8,83,84]. The framework includes a sequence of steps built in the Python environment and it utilizes different packages. The framework results are generated in the forms of graphs, attribute tables, and vector shapefiles which demonstrate the seismic resilience metrics and building footprints. The vector shapefiles can be imported into a geographical information system (GIS) software to have a visualized presentation of the resilience metrics helping the policy-makers to have a more intelligible quantitative assessment of the regional seismic damages and losses. The steps include obtaining the building information, acquiring seismic design parameters, generating simplified multi-degree-of-freedom (MDOF) numerical models, conducting response history analyses (RHAs), obtaining engineering demand parameters (EDPs), assessing the quantity of nonstructural and structural components, probabilistic seismic damage and loss assessments, and generating the building-specific and regional outputs including a vector shapefile of building prototypes consisting of seismic resilience metrics (repair time, repair cost, and probability of irreparability) [6]. In this research, the seismic resilience assessment of over 2,000 multi-family residential wood-frame buildings retrofitted with the portable Y-type braced self-centering viscous damper eccentrically braced frame (Y-SCVD-EBF) modules in the San Francisco Municipal Area was performed at nine intensity measures (IMs). A simplified multi-degree-of-freedom (MDOF) lumped-mass shear model using nonlinear spring elements was developed as surrogate FE nonlinear models for the prototype buildings in order to simulate the hysteresis behavior of a typical wood framed building equipped with the Y-SCVD-EBF module. The outputs of the building-specific and the regional-level analyses are presented at the end of the chapter.

6.1 Description of the Python-Based Framework

The Python-based model for the regional seismic resilience assessment of residential buildings is outlined in Figure 6.1 consisting of the following sequential steps [6]: (1) compiling a regional building inventory, including details such as location, height, plan area, and footprint; (2) gathering the seismic design parameters of the sites where the buildings are located; (3) developing nonlinear multi-degree-of-freedom (MDOF) lumped-mass shear models for the buildings under investigation; (4) conducting intensity-based response history analysis (RHA) at different intensity levels; (5) processing the results to obtain the required statistical information of engineering demand parameters (EDPs); (6) assessing the quantities of vulnerable structural and nonstructural elements of the buildings; (7) performing probabilistic damage and loss assessments at each intensity to derive resilience metrics; and (8) generating outputs, including graphs, attribute tables, and vector shapefiles. The framework can be adapted to represent different structural systems by modifying the user-defined story-shear hysteresis characteristics. To improve computational efficiency, parallel processing was implemented in the Python framework, allowing to use multi-core CPUs efficiently.

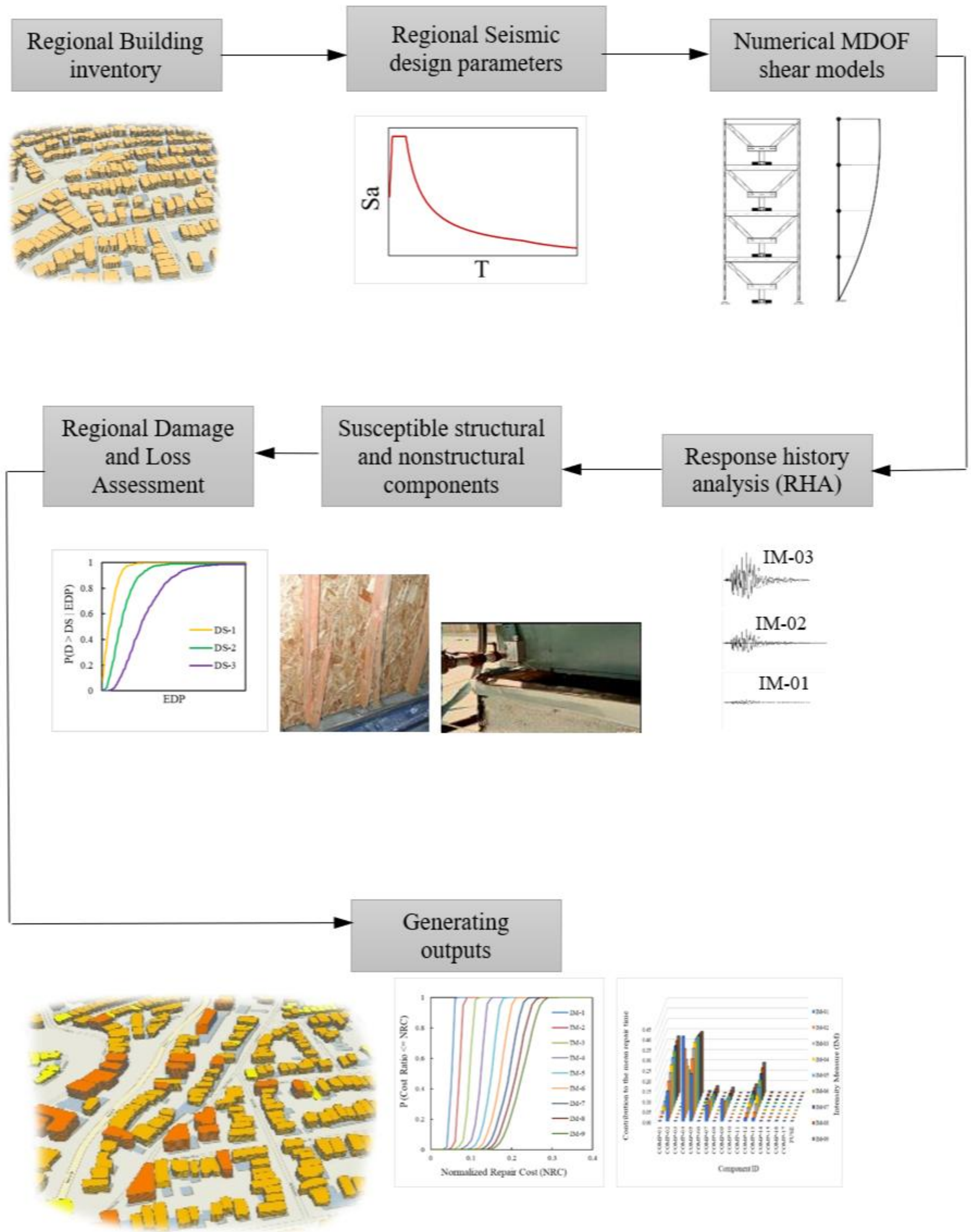

Figure 6.1 Sequential steps of the framework for regional seismic resilience assessment of the Y-SCVD-EBF-retrofitted wood framed buildings

6.2 Obtaining the Building Inventory

The regional seismic resilience assessment framework requires a CSV file as the input, containing basic building information such as location, height, plan area, and footprint, along with the building footprints in the GEOJSON format. If all the required data are available, the CSV file can be used directly as the input of the framework. Alternatively, data can be obtained from sources such as the FEMA Geospatial Resource Center [101]. Additionally, building heights, which may be missing from the shapefiles, can be derived from regional remote sensing data. This involves using the digital surface model (DSM) and digital elevation model (DEM) obtained from processing regional LiDAR point clouds available through the USGS National Map Data Download and Visualization Services [102]. The processed building footprints are then converted to GEOJSON format and stored in a CSV file, along with other required information, using the ArcPy module [103].

6.3 Obtaining the Seismic Design Parameters of the Region

The seismic design parameters (S_{D1}, S_{DS}, T_0, T_S, T_L) specific to each building site are essential for constructing the design response spectrum used to scale ground motions (GMs). These parameters are also critical for determining the building's story shear, which characterizes the nonlinear hysteresis behavior of the stories and helps quantify the structural components. This data can be retrieved as a JSON file directly from the United States Geological Survey (USGS) website [104].

6.4 Obtaining the Numerical MDOF Lumped-Mass Model

In this research, in order to obtain the engineering demand parameters (EDPs) required for damage and loss assessment of the buildings, post-processing the results of nonlinear response history analysis (RHA) using a record set of ground motions (GMs) is required. OpenSeesPy [105] was used to generate the numerical models by running the OpenSees [93] commands in Python. A simplified multi-degree-of-freedom (MDOF) shear building model using nonlinear spring elements simulating the hysteresis behavior of the proposed system was utilized to perform the response history analysis (RHA). Lu and Guan [87] proposed a model conducting a regional seismic analysis using multi-degree-of-freedom (MDOF) shear models. The principles of their model are adopted in this study and the hysteretic behavior of the structural system of interest (i.e. Y-SCVD-EBF) is employed. The flag-shaped load-displacement behavior of a typical self-centering modular bracing panel considering the fuse device and effect of friction force is illustrated Figure 6.2 [6], where K_1 is the initial stiffness, K_2 is the post gap-opening stiffness, K_3 is the post-yielding stiffness, V_0 is the gap-opening force, and V_y is the system capacity. The superscript "fr" illustrates the effect of friction force on gap-opening force and system strength. It is worth noting that this hysteresis curve does not show the effects of using a velocity-dependent energy dissipation device (i.e. viscous damper) in the system. The typical load-displacement behavior of self-centering viscoelastic dampers with a fuse device is shown in Figure 4.11.

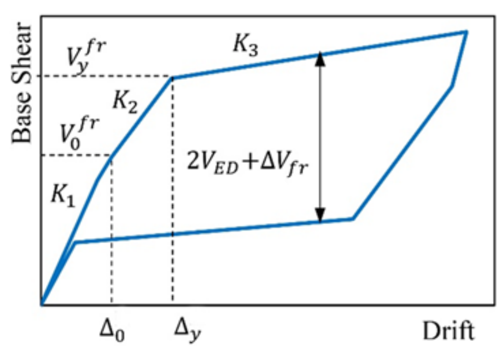

Figure 6.2 Flag-shaped load-displacement behavior of typical self-centering modular bracing panels [6]

Figure 6.3 illustrates the MDOF shear building model of the Y-SCVD-EBF module simulating the load-displacement behavior of the structure. This model is appropriate for performing large-scale regional seismic resilience assessment of buildings where the global responses of the structure (i.e. floor acceleration and velocity, IDR, and residual IDR) are of interest. According to Figure 6.3, concentrated mass is used at the story nodes, and the story stiffness is modeled using a combination of nonlinear springs simulating the hysteresis behavior of the Y-SCVD-EBF system.

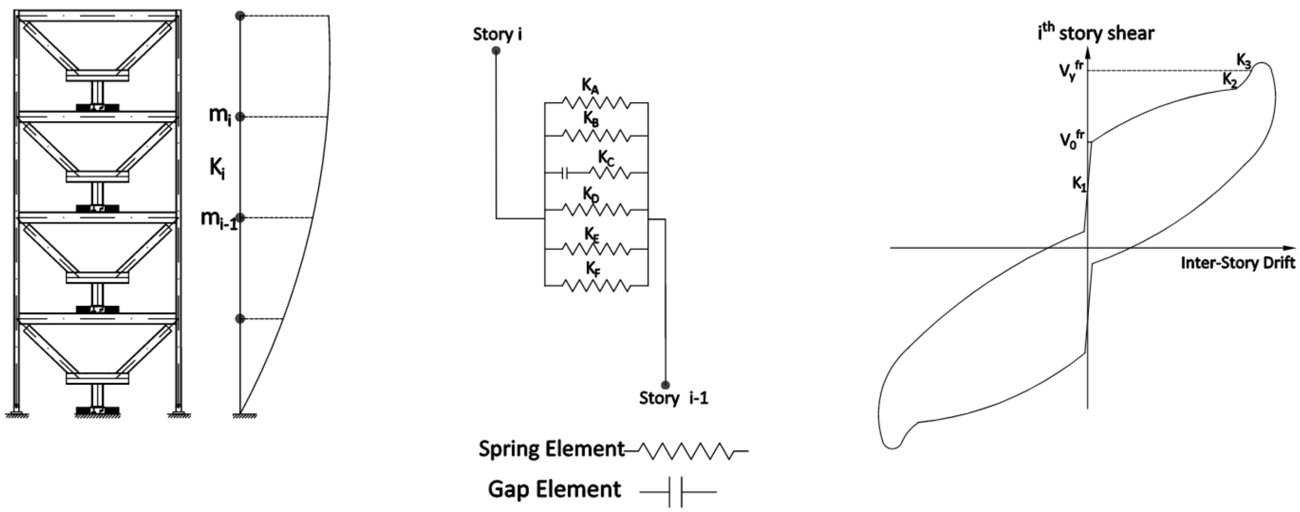

Figure 6.3 MDOF lumped-mass shear building model of the Y-SCVD-EBF retrofitting module

The first five springs in the parallel configuration represent the nonlinear behavior of the retrofitting system as follows: K_A denotes the gap-opening behavior with rigid bilinear elastic material, K_B represents the post-TPAD-yielding stiffness and nonlinear behavior of the disc springs with elastic-linear hardening material, K_C demonstrates the system's strength and energy dissipation by the TPAD fuse device with the Steel-02 material, K_D is the energy dissipation by the friction force with elastic-perfectly plastic material, K_E denotes the energy dissipation by the viscous damper using a zero-length viscous element. In the FE model, the frame members stiffness (K_F) is the story elastic stiffness. The gap element is used in order to simulate the gap between the TPAD fuse device and the adjacent walls so that the fuse is triggered once the structural drift exceeds the gap value as explained in chapter 5. The gap value in this chapter is considered as 2% of the story height. Table 6.1 summarizes the spring model specifications. The spring model simulating the hysteretic behavior of each story is shown in Figure 6.4.

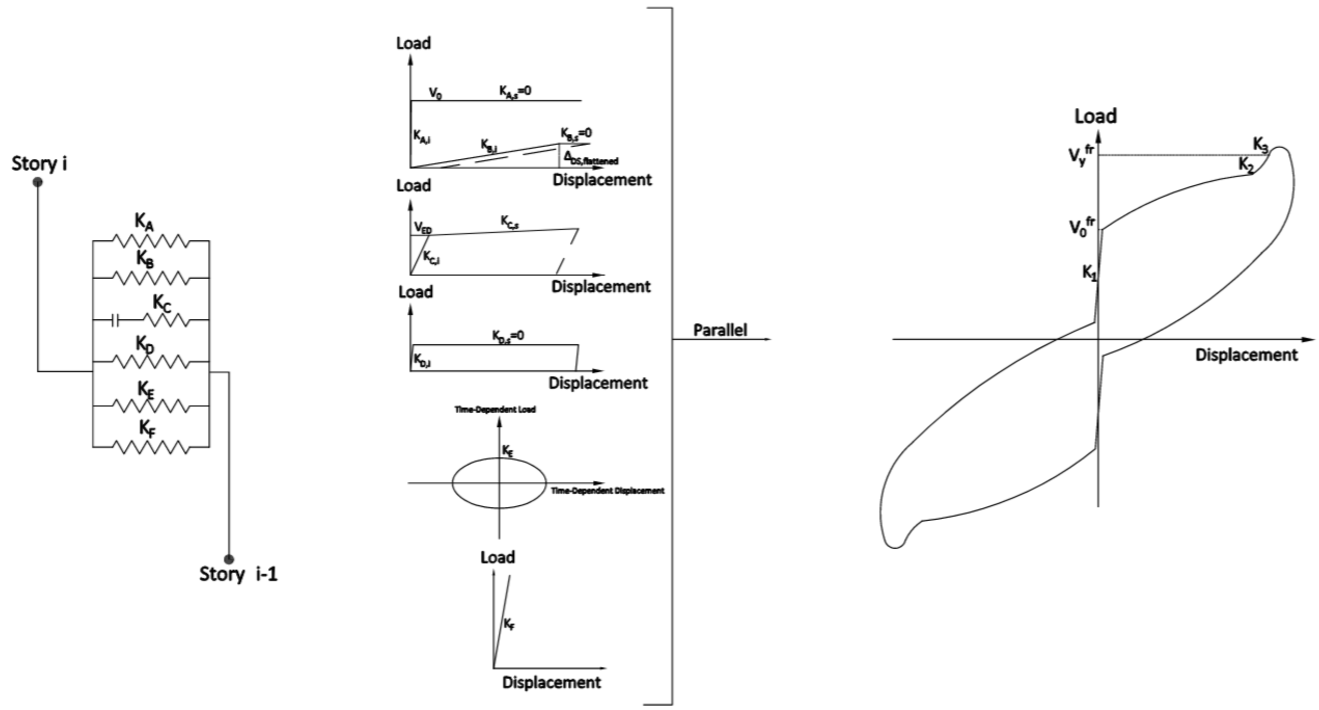

Figure 6.4 Load-displacement behavior of the springs in the MDOF lumped mass model

In Y-SCVD-EBF structures, the restoring force is generated by preloaded disc springs. When these discs undergo flattening, there is a potential for a partial or complete loss of the initial pre-compression force, which may subsequently result in significant residual deformation.

The hysteretic behavior of the Y-SCVD-EBF system is simulated using a nonlinear MDOF spring model. Within this lumped mass shear building model, Spring A is designated to represent the gap-opening behavior, while Spring B characterizes the post-yield stiffness and nonlinear response of the disc spring assemblies. Consequently, the gap-opening force, V_0, and the yielding force of Spring B, $f_{y,B}$, must accurately reflect the effects of the flattened disc springs. In scenarios where the disc spring assemblies become fully flattened, the gap-opening phenomenon ceases, resulting in a zero gap-opening force ($V_0 \approx 0$) meaning the total initial preload loss occurs. These effects are comprehensively incorporated into the numerical model. Within the Python-based model, IDRs are continuously monitored at each time step of the analysis. If the IDRs exceed the drift limit associated with the flattening of the disc springs, denoted as $\delta_{flat,DS}$, the corresponding parameters are subsequently updated to reflect this condition. In the initial step, controlling switches are established to delineate the status of the disc springs, incorporating the necessary actions to be executed accordingly. Drift responses are continuously recorded and evaluated to determine whether they represent the peak values up to the current time at each time step. Upon identification of peak drifts, new parameter values are calculated and subsequently integrated into the model. If the drift response value is the maximum and exceeds $\delta_{flat,DS}$, the loss of gap-opening story shear denoted as V_{loss} is calculated. When $V_{loss} < V_0$, the "partial_loss" switch is activated, and new values for V_0 and $f_{y,B}$ are subsequently determined. Otherwise, the "total_loss" switch is activated, the gap-opening force is set to zero, and a new value for $f_{y,B}$ is calculated. The updated parameters are calculated at the peak drift but are not immediately integrated into the model. To incorporate these parameters, the drift ratios are evaluated, and if the current drift does not correspond to the peak value, the conditions for "partial_loss" and "total_loss" are assessed to determine whether any updated parameters need to be applied [6].

Table 6.1 Specifications of the springs in the MDOF lumped mass numerical model

Spring	K_i	K_s	f_y
A	$15K_1$	0.0	V_0
B	$\left[\frac{K_1K_3}{(K_1-K_3)}-\alpha_{sh}K_{i,C}\right]$	0.0	$V_0+F(s=h_0')\cdot\frac{2e}{w'}$ $\delta_{flat,DS}=\frac{F(s=h_0')\cdot\frac{2e}{w'}}{K_{i,B}}$
C	$\frac{K_1^2(K_2-K_3)}{[(1-\alpha_{sh})(K_1-K_2)(K_1-K_3)]}$	$\alpha_{sh}K_{i,C}$	V_{ED}
D	$f_{y,D}\cdot\frac{V_0}{K_1}$	0.0	$(\alpha_{fr}-1)\cdot(V_0+V_{ED}/2)$
E	0.0	0.0	---
F	K_1	---	---

Estimation of the fundamental period of the buildings in the case study is made using ASCE 7-22 [100] empirical relationships for different structural systems. According to the plan area and the occupancy type, floor seismic mass of the buildings is calculated afterwards. The story mass, m, and initial stiffness, k_0, are distributed uniformly along the structural height [6]. Therefore, the stiffness matrix, [K], and mass matrix , [M], are created and the initial stiffness of the stories is determined as follows [87]:

$$[K]=k_0\begin{bmatrix}2&-1&&&\\-1&2&-1&&\\&-1&\ddots&\ddots&\\&&\ddots&2&-1\\&&&-1&1\end{bmatrix}\tag{6.1}$$

$$[M] = m \begin{bmatrix} 1 & & & & \\ & 1 & & & \\ & & \ddots & & \\ & & & 1 & \\ & & & & 1 \end{bmatrix} = m[I] \tag{6.2}$$

$$k_0 = \lambda \frac{4\pi^2 m}{T_1^2} \tag{6.3}$$

$$\lambda = \left(\frac{[\Phi_1]^T [I] [\Phi_1]}{[\Phi_1]^T [A] [\Phi_1]} \right) \tag{6.4}$$

The first vibration mode shape vector, $[\Phi_1]$, is independent of the constant values of m and k_0, and it can be determined through Eigenvalue analysis by considering m=1 and $k_0 = 1$. The base shear, $V_{y,1}$, is obtained according to ASCE 7-22 [100] provisions and the seismic forces are considered to vary linearly along the structural height. The i-th story shear, $V_{y,i}$, is calculated using the following equations where N represents the total number of stories in the building [6].

$$V_{y,i} = \Theta_i V_{y,1} \tag{6.5}$$

$$\Theta_i = 1 - \frac{i(i-1)}{(N+1)N} \tag{6.6}$$

6.5 Response History Analysis and Engineering Demand Parameters

Once the nonlinear RHA of a building is performed and the median and dispersion of EDPs are obtained, seismic damage and loss of each building at the considered intensity measure, IM, is assessed. The seismic damage and loss of structural and nonstructural components in a building are mainly dependent on the EDPs such as inter-story drift, floor acceleration, floor velocity, and residual drift per FEMA P-58. In this study, eleven pairs of ground motion (GM) records were used for RHA which is sufficient based on the FEMA P-58 database. The GM pairs were chosen from the far-field (FF) record set of the FEMA P695 [94] database. Appendix A includes the specifications and acceleration history of all the GMs. Newmark method with β=0.25 and γ=0.5 was employed for the numerical analysis in this study [6].

The intensity-based seismic damage and loss assessment, following the FEMA P-58 methodology [8], primarily uses the spectral acceleration (S_a) as the intensity measure (IM) parameter. However, previous studies have recommended using peak ground acceleration (PGA) as the IM parameter for regional seismic damage and loss assessments. This recommendation arises from the potential variability in the fundamental periods of buildings, where scaling ground motions based on the spectral acceleration (S_a) might result in significant differences in PGA values [85]. However, both ground motion scaling methods are considered valid options and can be selected based on the analysis requirements [6].

Following the response history analysis (RHA), engineering demand parameters (EDPs) are generated, and by post-processing the results, the median and dispersion of peak inter-story drift, floor acceleration, floor velocity, and residual drift for each story and intensity measure (IM) are calculated. These outputs are stored in a CSV file which is compatible with the Pelicun framework [106], enabling probabilistic damage and loss assessment in accordance with FEMA P-58 [8]. Table 6.2 shows an example of the demand parameters with their median and standard deviation of a building. The demands are recorded in the format x-EDP-x-x, where the first number corresponds to the ground motion intensity ID, the three letters specify the type of demand parameter, and the final two numbers denote the floor location and direction, respectively [6].

Table 6.2 Building demand table (Unit: ft)

EDP*	Median	Lognormal standard deviation
1-PFA-0-1	0.357856	0.37264
1-PFA-1-1	0.445639	0.213847
1-PID-1-1	0.005457	0.179676
1-PFV-0-1	138.164	0.37264
1-PFV-1-1	132.813	0.371926
1-RID-1-1	1.00E-05	3.55E-15
1-PFA-0-2	0.440102	0.475761
1-PFA-1-2	0.404879	0.296528
1-PID-1-2	0.004805	0.206105
1-PFV-0-2	169.918	0.475761
1-PFV-1-2	168.126	0.488918
1-RID-1-2	1.00E-05	3.55E-15

*PFA=Peak Floor Acceleration, PFV=Peak Floor Velocity, PID=Peak Inter-story Drift, RID= Residual Inter-story Drift

6.6 Defining Seismically Vulnerable Components

The location and quantity of the susceptible components to seismic loading need to be determined. All the structural members except for the fuses should remain elastic at the design basis earthquake (DBE) intensity level. At higher seismic intensities, force-controlled structural members may yield, resulting in significant residual drift in the structure. FEMA P-58 suggests that if the residual drift exceeds a specified threshold, the structure is categorized as irreparable, with the repair cost and repair time set equal to the building's replacement cost and replacement time, respectively. Based on the FEMA P-58 database, only fuse elements are typically considered vulnerable to seismic damage. This approach can be extended to the structural system in this case study, with fragility and consequence functions for specific fuse components defined and integrated into the database. The size of fuse elements at each story is determined based on the design story shear and additional requirements for such components. For instance, in the proposed Y-SCVD-EBF module, the TPAD serves as the fuse, requiring its fragility and consequence functions to be specified and added to the database. In this study, the fragility and consequence functions for the TPAD fuse plate have been incorporated into the FEMA P-58 database included in the Pelicun package [6].

6.7 Seismic Resilience Assessment

The probabilistic seismic damage and loss assessment of the buildings in the case study is carried out using Pelicun [106] in OpenSeesPy [105] developed by the NHERI SimCenter. Python with the Pelicun package includes the required tools to perform probabilistic damage and loss evaluations following the FEMA P-58 methodology [8]. All the uncertainties in the assessment are addressed using Monte Carlo simulations. These simulations produce numerous realizations, with each realization representing a unique combination of uncertain variables and corresponding performance outcomes. The overall damage and loss are determined by aggregating them in structural and nonstructural components using fragility curves and consequence functions from the FEMA P-58 database. Repair times are estimated for two scenarios—parallel and serial working procedures—representing the lower and upper practical limits, respectively. Figure 6.5 presents the simplified algorithm employed for assessing the damages and losses occurred in each realization, as implemented by Pelicun which is based on FEMA P-58 [8]. Prior to conducting the damage and loss analysis for each realization, the building must be assessed for collapse and irreparability conditions. If either condition is met, the repair time and repair cost are assigned to the replacement time and replacement cost, respectively, and further damage and loss analysis for the performance groups is skipped [6].

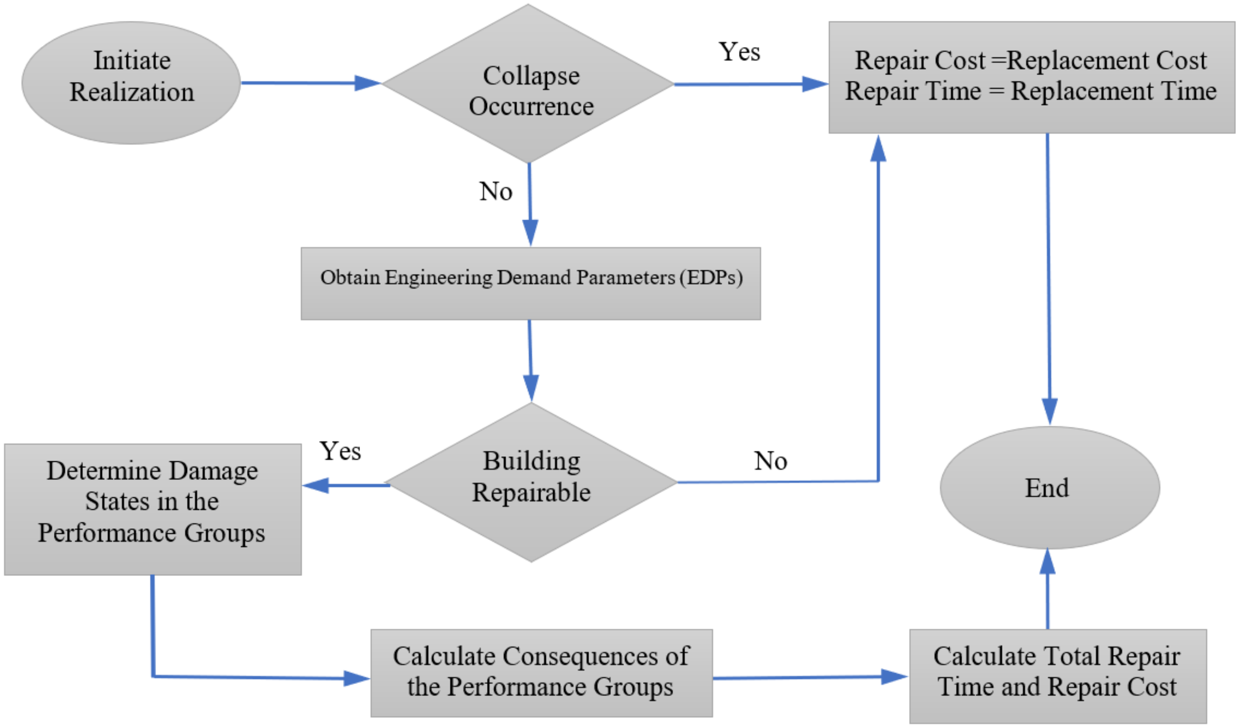

Figure 6.5 Simplified process of damage and loss evaluation following FEMA P-58 [6]

6.7.1 Collapse Condition

The collapse condition is determined using the collapse fragility function specific to the structural system under consideration. This requires defining the median and dispersion of collapse spectral acceleration at the building's fundamental period ($S_a(T)$). Collapse is evaluated by comparing the collapse probability, calculated at the median spectral acceleration of the ground motion suite at the building's natural period, with a randomly generated value between 0 and 100. If the random value exceeds the collapse probability, the building is deemed to collapse.

FEMA P-58 [8] outlines several methods to determine the collapse fragility function, with the median and dispersion of the system's collapse capacity derived using one of these approaches. The target collapse resistance method is incorporated within the framework as a simplified alternative that does not require additional finite element analysis. Using this method, the median collapse capacity, $\hat{S}_a(T)$, can be estimated with Equation (6.7), where $S_{aD}(T)$ represents the design spectral acceleration at the fundamental period. For regular buildings, a dispersion (β) of 0.6 or greater is recommended for the collapse fragility function [6].

$$\hat{S}_a(T) = 4S_{aD}(T) \tag{6.7}$$

6.7.2 Irreparability Condition

If the building does not collapse, it is evaluated for irreparability based on the maximum residual drift and its repair fragility. A random number between 1 and 100 is generated and compared to the probability of irreparability associated with the maximum residual drift ratio. If the random number is greater than this probability, the building is deemed irreparable, and the repair cost and repair time are set equal to the replacement cost and replacement time. FEMA P-58 [8] recommends using a median residual drift ratio of 1.0% and a dispersion value of 0.3 to characterize the repair fragility for irreparable damage [6].

6.7.3 Damage and Loss Assessment

If collapse or irreparable condition does not occur in a given realization, the damage states of the performance groups are assessed. Components that respond to similar EDPs are grouped into performance groups within the same fragility group. The relationships between damage states within a fragility group can be sequential, mutually exclusive, or simultaneous. Additionally, damage states within a performance group can be classified as either correlated or uncorrelated. All the components in the performance group are presumed to undergo the same damage state for correlated damage states. Each damage state in a performance group is linked to consequence functions specifying probabilistic distributions for metrics like repair time and repair cost. The building's total loss is estimated considering the losses from all performance groups for each realization. Performing this process across numerous realizations provides the probabilistic distribution of the building's overall losses [6].

6.8 Obtaining the Outputs of the Analysis

The outcomes of the regional seismic damage and loss assessment are provided in different forms for each intensity measure (IM). By incorporating building footprints and resilience metrics for each IM, several shapefiles are generated along with the attribute tables consisting of the resilience metrics at various IMs. These results can be visualized using GIS software enabling decision-makers to conduct quantitative evaluation of the regional seismic resilience of the specific building asset groups under study. Additionally, damage and loss assessment could be carried out for a specific building and the results can be obtained for further analysis.

6.9 Case Study: Regional Seismic Resilience Assessment of Retrofitted Soft-Story Residential Light-Frame Wood Buildings in San Francisco

Multi-family residential wood-frame buildings with soft stories are prevalent throughout California. In San Francisco, many of these structures do not comply with current seismic code provisions, making them susceptible to damage from moderate to severe earthquakes. Due to their widespread presence and vulnerability, ensuring the resilience of these buildings is crucial, as even a moderate earthquake could cause significant destruction. Recent advancements in seismic design have led to the development of novel protection mechanisms, with self-centering systems gaining significant interest. The Y-SCVD-EBF system offers a portable, modular panel solution that can be integrated into existing wood-frame structures. In this system, pre-compressed disc springs provide the necessary recentering capability. While viscous damper serves as the primary energy dissipation device, functioning as a velocity-dependent damper. Additionally, the trapezoidal plate added damper (TPAD) acts as the secondary or backup, and is a displacement-dependent energy dissipating device. These fuse components are designed for easy replacement following seismic events, enhancing the resilience and reparability of the system.

Self-centering systems can effectively control damage and minimize residual structural deformations after significant earthquakes. As resilience is defined by a system's robustness, redundancy, resourcefulness, and rapidity [7], the use of portable retrofitting panels reduces repair time and enhances overall robustness leading to building resilience improvement. By implementing Y-SCVD-EBF modular panels, buildings can be quickly re-occupied after an earthquake through the immediate replacement of fuse devices, if necessary. This ensures faster recovery and maintains operational continuity with minimal downtime. To quantify the impact of Y-SCVD-EBF retrofitting systems on enhancing the regional seismic resilience of critical wood-frame buildings, the framework was applied to 2,088 soft-story residential buildings in San Francisco incorporating these systems. The live load and the dead load were determined for wood-frame residential buildings accordingly, and applied to the buildings under investigation. The histograms of the story numbers and plan area of the residential buildings considered in this case study are presented in Figure 6.6.

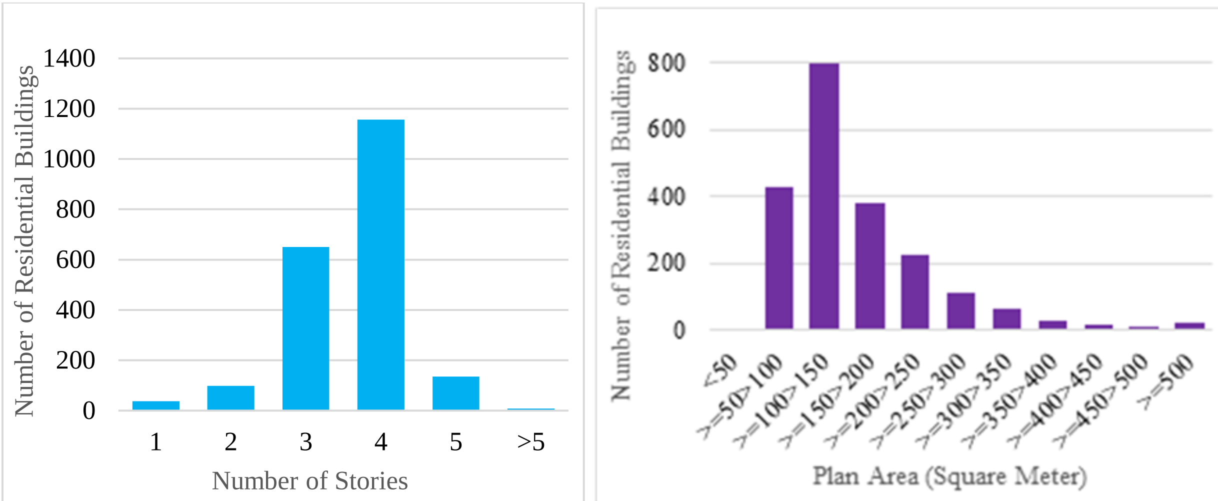

(a) (b)

Figure 6.6 Distribution of multi-family residential buildings with soft story in San Francisco: (a) Histogram of the story numbers; (b) Histogram of the plan area

6.9.1 Building Components

The dimensions of the TPAD fuse and the number of disc springs per story were calculated based on the required design story strength and energy dissipation. Prior to designing these structural components, key practical assumptions were made, informed by analytical relationships [6]. Light framed wood lateral framings are also considered as part of the structural components for wood buildings per FEMA P-58 database [8]. The type and quantity of structural and nonstructural components were determined based on normative data for residential occupancy, story plan area, and the number of stories. Table 6.3 outlines the susceptible components along with their normative quantities and dispersion values. The selection of these components aligns with findings from previous studies on wood-frame buildings [89,90].

Table 6.3 Vulnerable components in multi-family residential wood framed buildings

FEMA P-58 ID	Framework ID	Component	Unit	Normative quantity	Dispersion
B1071.001	COMP-01	Light framed wood lateral walls	ft^2	1.2E-01	0.4
B1071.041	COMP-02	Exterior walls	ft	6.0E-02	0.3
B2022.001	COMP-03	Curtain Walls	ft^2	1.5E-01	0.6
B3011.014	COMP-04	Clay tile roof	ft^2	4.0E-01	0.9
C1011.011a	COMP-05	Wall partition with wood studs	ft	1.2E-01	0.3
C2011.001a	COMP -06	Prefabricated steel stairs	each	1.2E-04	0.1
C3011.001a	COMP-07	Wall partition finishes	ft	3.8E-02	0.4
C3034.001	COMP-08	Independent pendant lighting	each	1.0E-03	0.2
D1014.011	COMP-09	Traction elevator	each	3.4E-05	0.8
D2021.011a	COMP-10	Potable water piping	ft	1.1E-01	0.4
D3041.011a	COMP -11	HVAC ducting	ft	5.0E-02	0.6
D3041.031a	COMP-12	HVAC drops/diffusers	each	8.0E-03	0.4
D3041.041a	COMP-13	Variable air volume box	each	8.0E-03	0.6
D4011.021a	COMP-14	Fire sprinkler water piping	ft	2.2E-01	0.1
D4011.031a	COMP-15	Fire sprinkler drop	each	1.2E-02	0.1
D5011.011a	COMP-16	Transformer	each	5.0E-05	0.5
D5012.031a	COMP-17	Distribution panel	each	1.3E-05	0.2

6.9.2 Numerical Modeling of Buildings for Regional Seismic Resilience Assessment

The process for developing the MDOF lumped-mass shear model for Y-SCVD-EBF modular systems, simulated using a nonlinear spring model, is depicted in Figure 6.7.

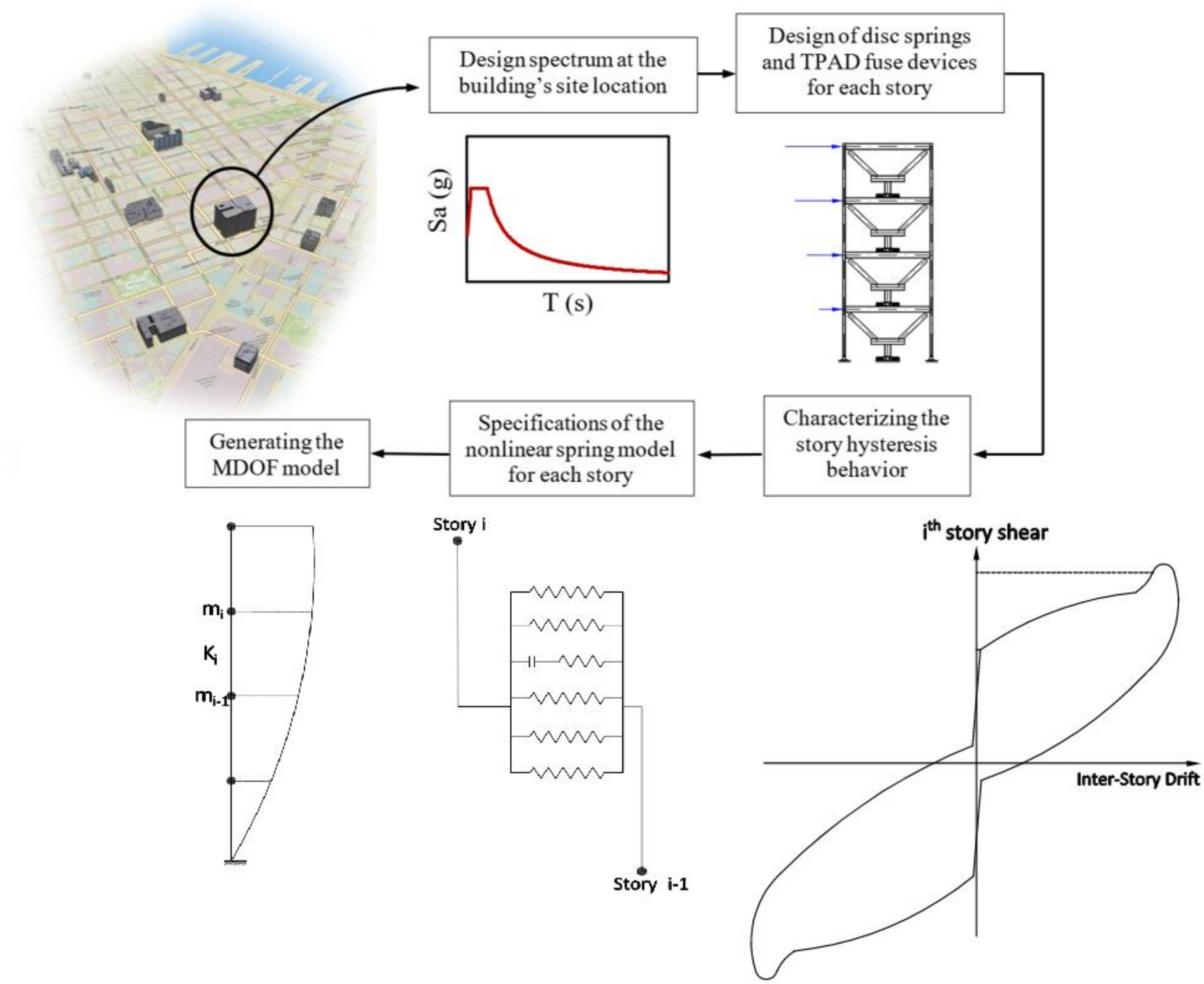

Figure 6.7 Generating the lumped-mass shear building model of the Y-SCVD-EBF systems

The system's energy dissipation capacity, which is characterized by the ratio of the strength contributed by the fuse devices to the total system strength, can be adjusted by modifying the size of the fuse devices and the gap-opening force. Therefore, for a given system strength, various configurations of fuse devices and disc springs can be designed to achieve different energy dissipation ratios [6]. However, since the primary energy dissipation mechanism is provided by the viscous damper and TPAD serves as the backup source in the proposed SCVD system, most of the seismic energy is dissipated through the viscous damper.

6.9.3 Damage and Loss Assessment

The damage and loss assessment were carried out at nine different intensity levels, ranging from $\mathrm{PGA} = 0.2\mathrm{g}$ to $\mathrm{PGA} = 1.0\mathrm{g}$, in $0.1\mathrm{g}$ increments. For each intensity level, 1000 realizations were performed to estimate the probabilistic seismic damage and loss of each building. Given the high performance of the proposed Y-SCVD-EBF retrofitting systems, it is anticipated that excluding collapse scenarios from the analysis will not impact the results. The repair cost and repair time derived from the probabilistic damage and loss assessment were normalized by the building replacement cost (BRC) and building replacement time (BRT), respectively. Since the consequence functions in FEMA P-58 are based on 2011 pricing, the replacement cost was adjusted to align with that period. This study adopted a unit replacement cost of $250 per square foot ($2,690 per square meter), as recommended in FEMA P-58 [8]. Repair time and replacement time are expressed in *worker.days*. The building replacement time was estimated using the relationship $\mathrm{BRT} = \mathrm{BRC} \times \frac{\mathrm{LCP}}{\mathrm{WDC}}$ where the labor cost percentage (LCP) and worker daily cost (WDC) were assumed to be 50% and $680 per *worker.day*, respectively, consistent with FEMA P-58 guidelines [6].

6.9.4 Results

The results of the intensity-based probabilistic regional damage and loss assessment of 2,088 multi-family residential code-deficient wood framed buildings retrofitted with the novel Y-SCVD-EBF modular systems are presented in this section. Cumulative distribution function (CDF) of the regional normalized mean repair cost (NRC), and normalized mean repair time (NRT) considering parallel and serial working procedures are demonstrated in Figure 6.8 to Figure 6.10. It is observed that the regional median NRC and NRT ($\mathrm{CDF} = 0.5$) increase with the intensity level.

It is worth noting that all the damages in this case study are repairable (the probability of irreparability or PIR is zero) because this analysis is performed on code-deficient light wood framed buildings which are retrofitted with high-performance modular systems and since the seismic loads on a structure are proportional to the weight of the building, seismic loads are much less compared to those of other types of structures such as steel framed or reinforced concrete buildings, and the retrofitted structures are seismically adequate. Therefore, the EDPs of interest are limited and no severe damages resulting in irreparable losses occur.

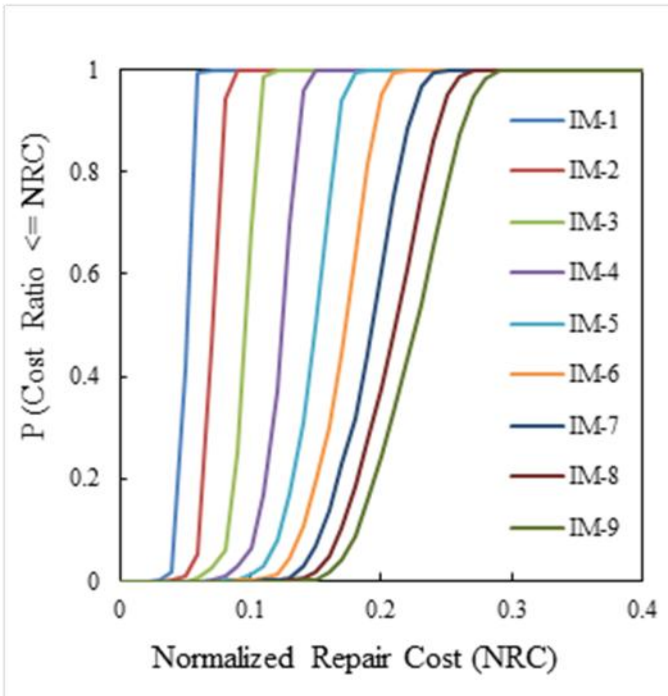

Figure 6.8 Cumulative distribution function (CDF) of the regional normalized repair cost (NRC)

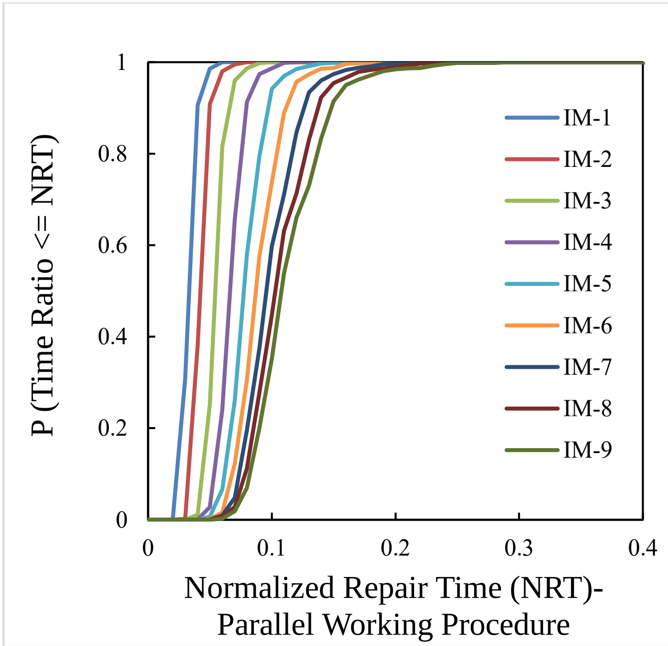

Figure 6.9 Cumulative distribution function (CDF) of the regional normalized repair time (NRT) considering parallel working procedure

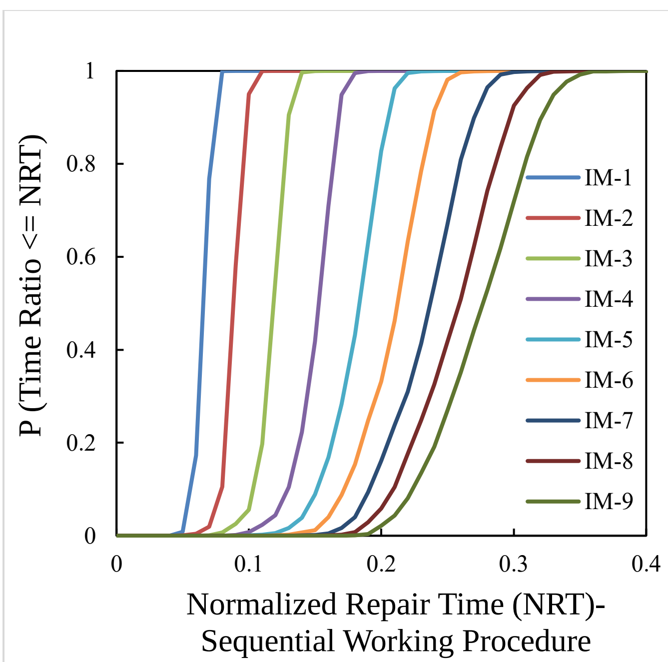

Figure 6.10 Cumulative distribution function (CDF) of the regional normalized repair time (NRT) considering serial working procedure

The regional mean value of the resilience metrics with one standard deviation at different intensity levels are illustrated in Figure 6.11 through Figure 6.13. According to the graphs, normalized repair cost (NRC) and normalized repair time (NRT) increase with the intensity measure (IM). Additionally, parallel working procedure takes much less time than that of the serial approach.

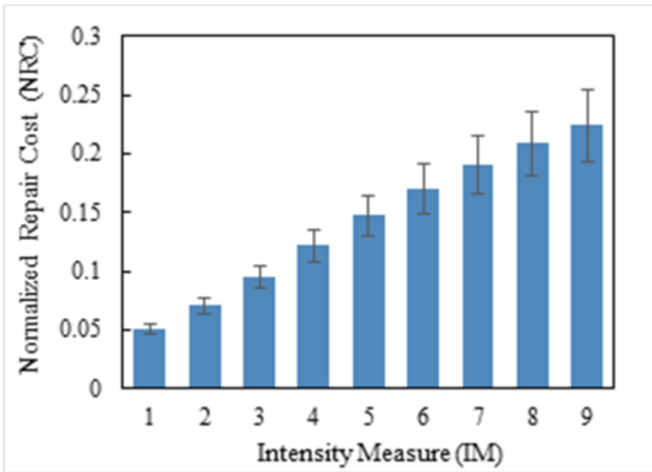

Figure 6.11 Regional mean value of NRC with one standard deviation at different intensity levels

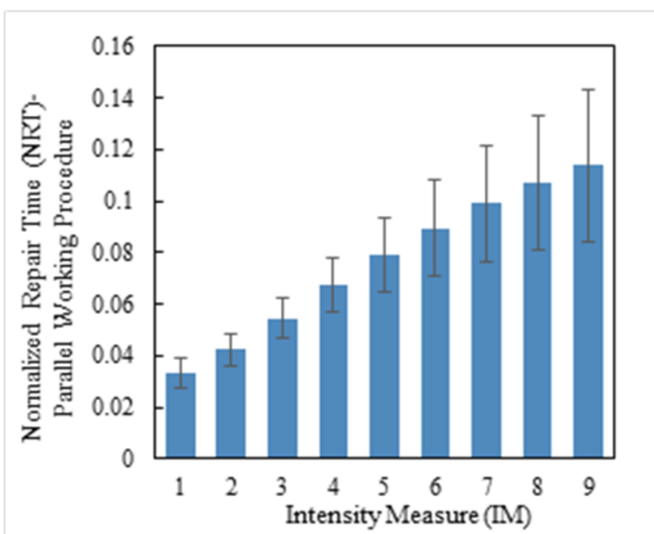

Figure 6.12 Regional mean value of NRT with one standard deviation at different intensity levels

(Parallel working procedure)

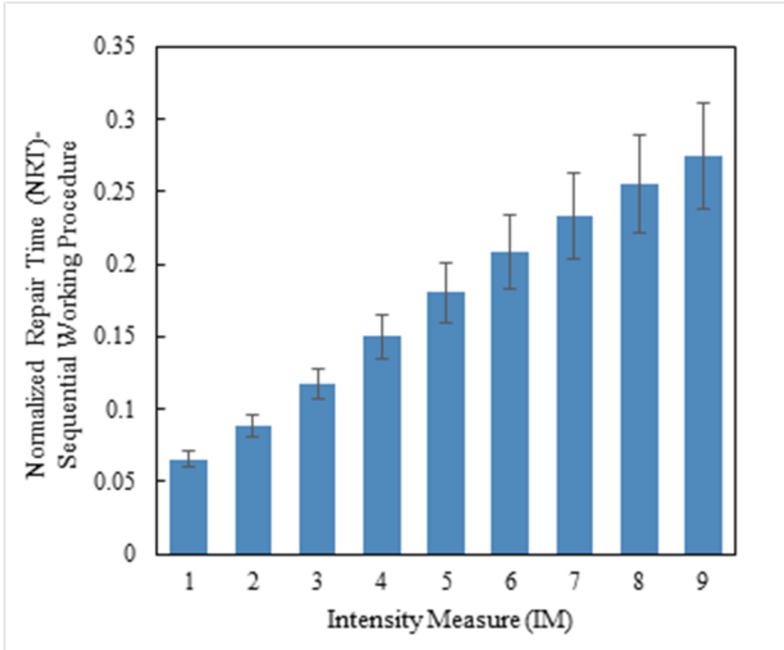

Figure 6.13 Regional mean value of NRT with one standard deviation at different intensity levels (Serial working procedure)

Figure 6.14 and Figure 6.15 illustrate the contribution of building components to the mean repair cost (component repair cost/ total repair cost) and mean repair time (component repair time/ total repair time) in the regional scale, respectively. According to the graphs, COMP-02, COMP-04, and COMP-05 constitute a significant portion of the repair cost and repair time in the regional scale. However, COMP-05 (wall partition with wood studs) is the component with the greatest effect on the regional resilience metrics. Additionally, it is seen that the extent to which individual components contribute to the regional repair cost and repair time varies with the intensity level. As the intensity level increases, components COMP-01 (wood shear walls), COMP-02 (exterior walls), and COMP-13 (variable air volume box) show more contribution to the resilience metrics, although some others including COMP-04 (clay tile roof), COMP-07 (wall partition finishes), and COMP-09 (traction elevator) are conversely proportional to the IMs. As an example, COMP-02 (exterior walls) has around 17% contribution at IM-01, while its share to the mean repair cost increases to about 30% at IM-09. Conversely, COMP-04 (clay tile roof) has approximately contributed 34% and 9% to the repair cost of the region at IM-01, and IM-09, respectively. The results also show that some components such as COMP-03 (curtain walls), COMP-08 (independent pendant lighting), COMP-10 (potable water piping), COMP-11 (HVAC ducting), COMP-15 (fire sprinkler drop), and COMP-17 (distribution panel) do not impact the regional resilience metrics considerably at any intensity.

In this analysis, COMP-01 (wood shear walls) and FUSE (TPAD fuse devices) are considered as the structural components of the buildings studied in the region. FUSE has as an inconsiderable impact on the regional mean repair cost and repair time. The replacement of such fuses is usually required when the IDR is very large leading to a residual drift and building irreparability. Figure 6.16 and Figure 6.17 show the contribution of the structural and nonstructural components to the mean repair cost and repair time in the regional scale with one standard deviation at different intensity levels. The contribution of the structural component (COMP-01) to the regional mean repair cost increases from 0.1% to 4.6% as the intensity increases from IM-01 to and IM-09. These values are 0.1% and 5% for the repair time case, respectively.

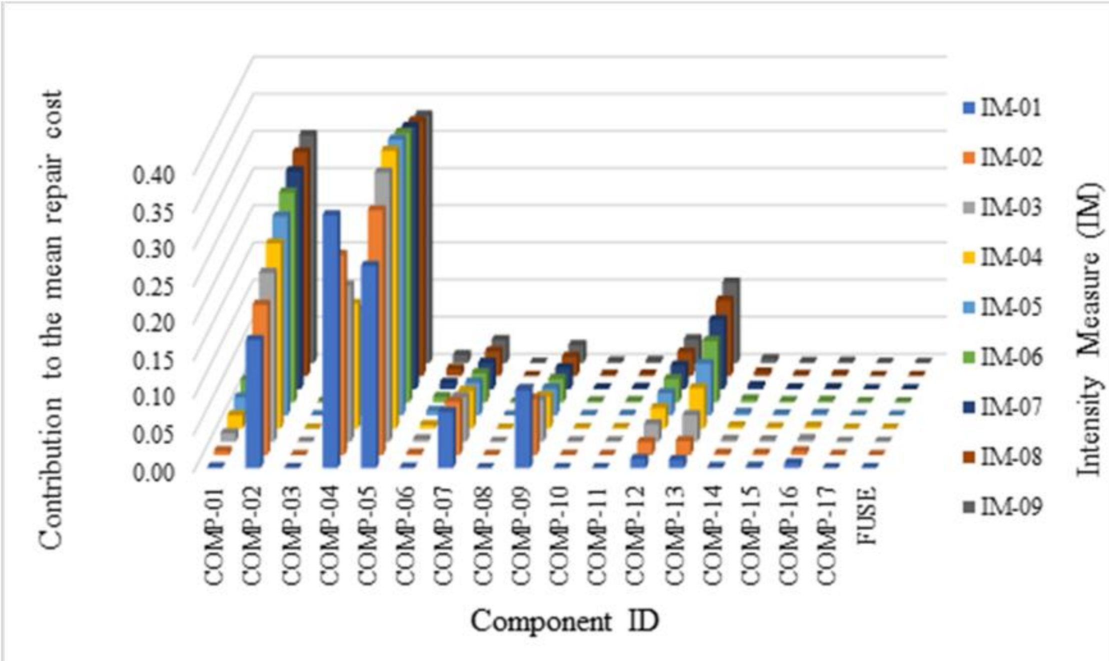

Figure 6.14 Regional mean contribution of the components to the mean repair cost

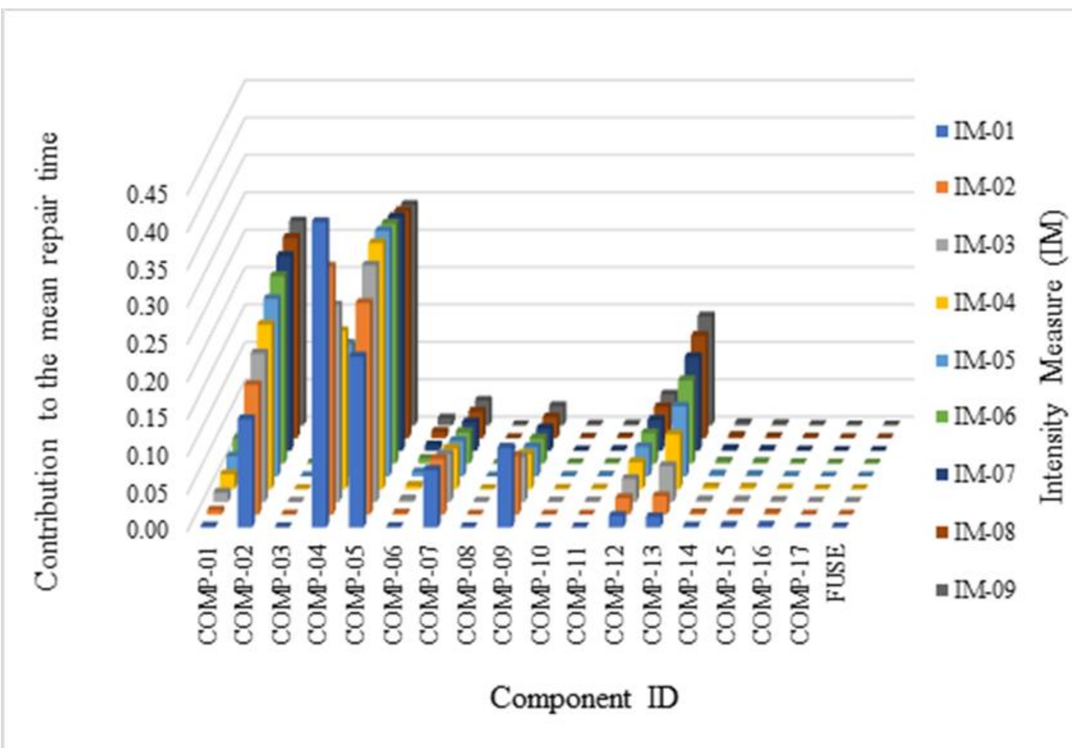

Figure 6.15 Regional mean contribution of the components to the mean repair time

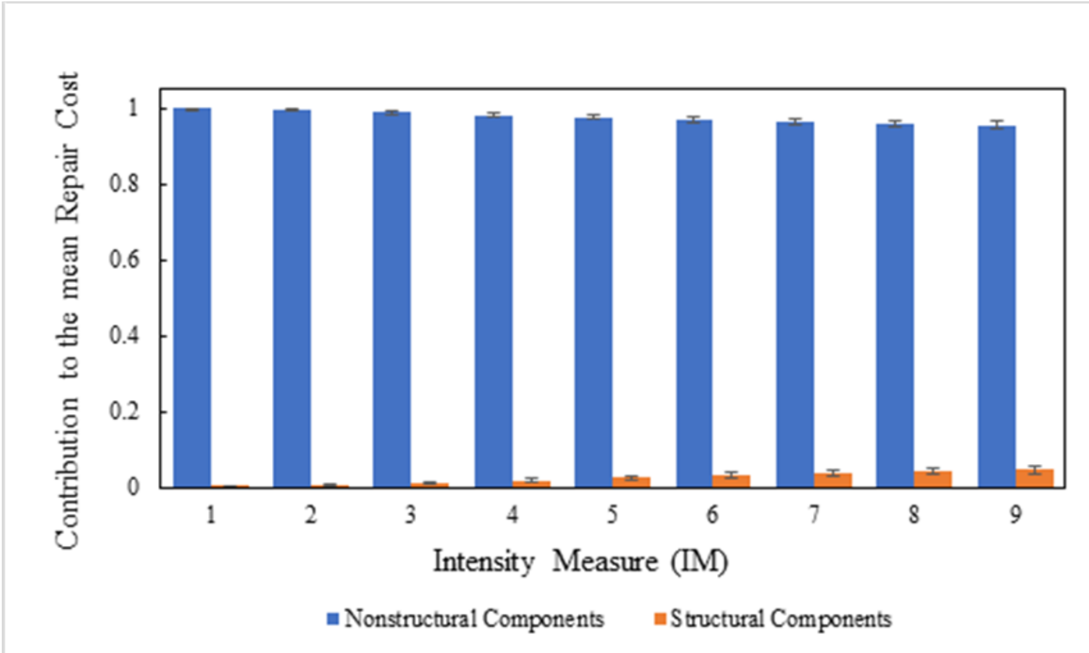

Figure 6.16 Contribution of the structural and nonstructural components to the regional mean repair cost with one standard deviation at different intensity levels

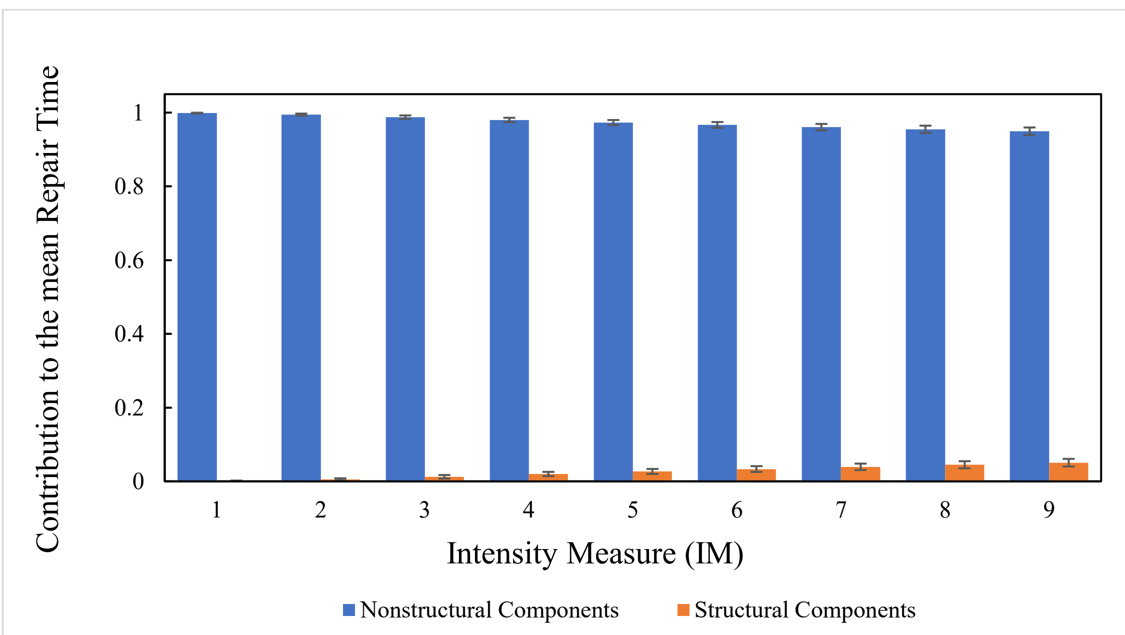

Figure 6.17 Contribution of the structural and nonstructural components to the regional mean repair time with one standard deviation at different intensity levels

Figure 6.18 and Figure 6.19 demonstrate the contribution of the components COMP-01, COMP-02, COMP-04, COMP-05, COMP-07, COMP-09, COMP-12, and COMP-13 to the mean repair cost and repair time in the region at IM-01, IM-05, and IM-09 as the rest of the components have a negligible contribution to the regional resilience metrics. Components COMP-01, COMP-02, COMP-12, and COMP-13 are directly proportional to the intensity level; however, COMP-04, and COMP-07, and COMP-09 are inversely proportional to the IM as with increasing the intensity, their contribution to the mean repair cost and repair time decreases.

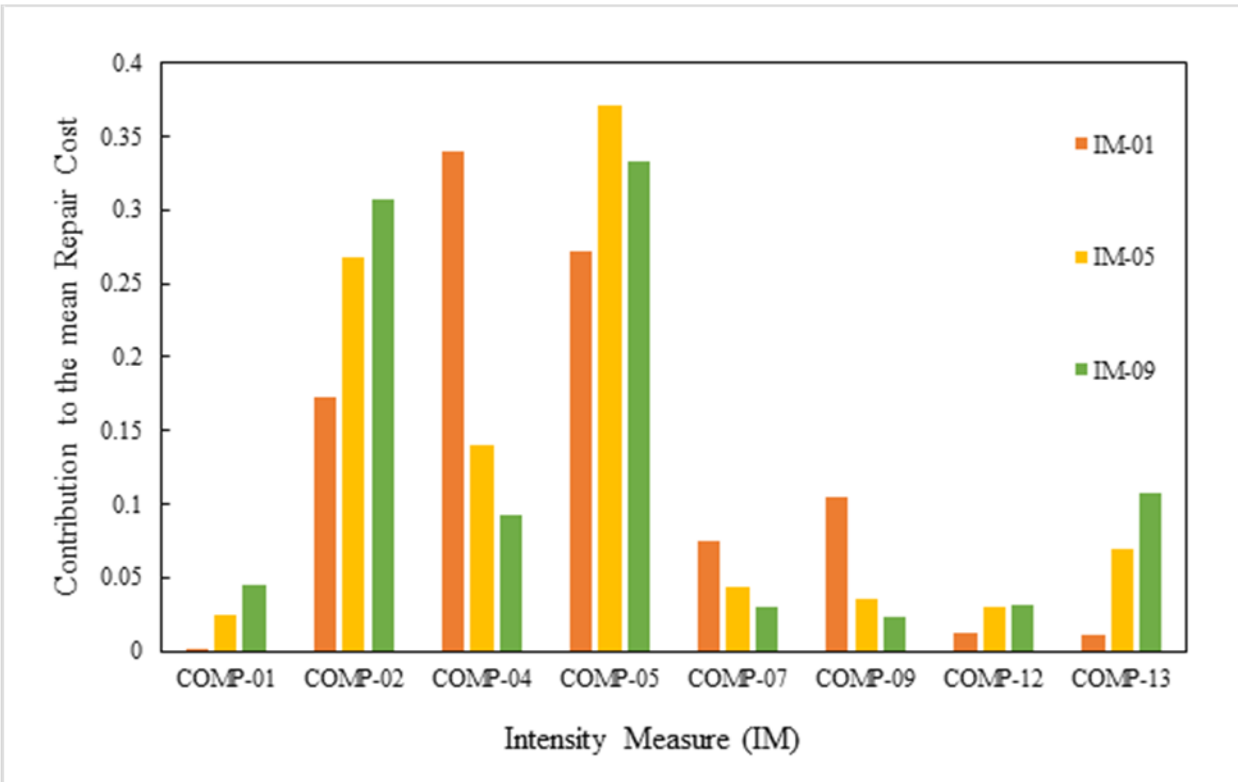

Figure 6.18 Contribution of components to the regional mean repair cost at three different intensity levels

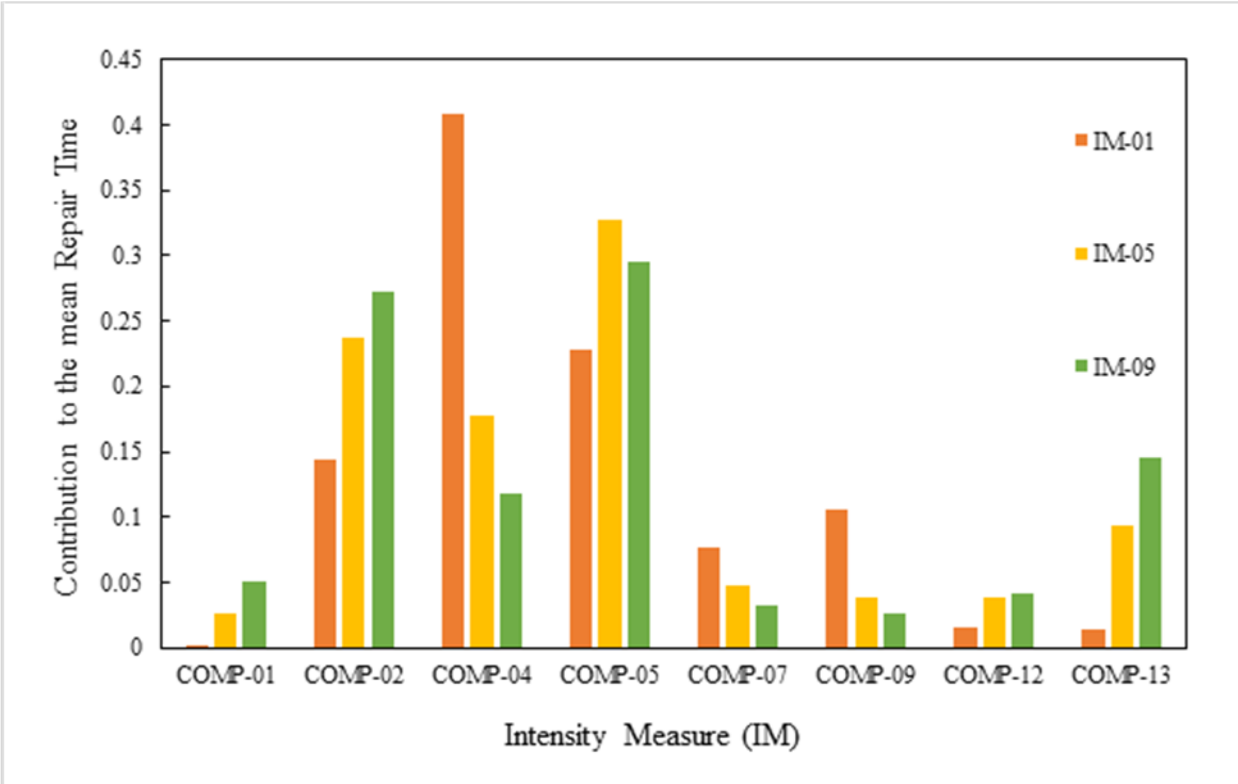

Figure 6.19 Contribution of components to the regional mean repair time at three different intensity levels

In order to enhance the clarity of the analysis results, standard visualizations of the damage and loss assessment for the buildings under investigation in ArcGIS Pro [103] are provided in this section. Figure 6.20 through Figure 6.22 illustrate part of San Francisco and the NRC and NRT (accounting for both parallel and serial working procedures) at IM-01, IM-05, and IM-09 intensity levels. Furthermore, three-dimensional digital twin representations of the buildings, color-coded according to resilience metrics, are presented in Figure 6.23 through Figure 6.25.

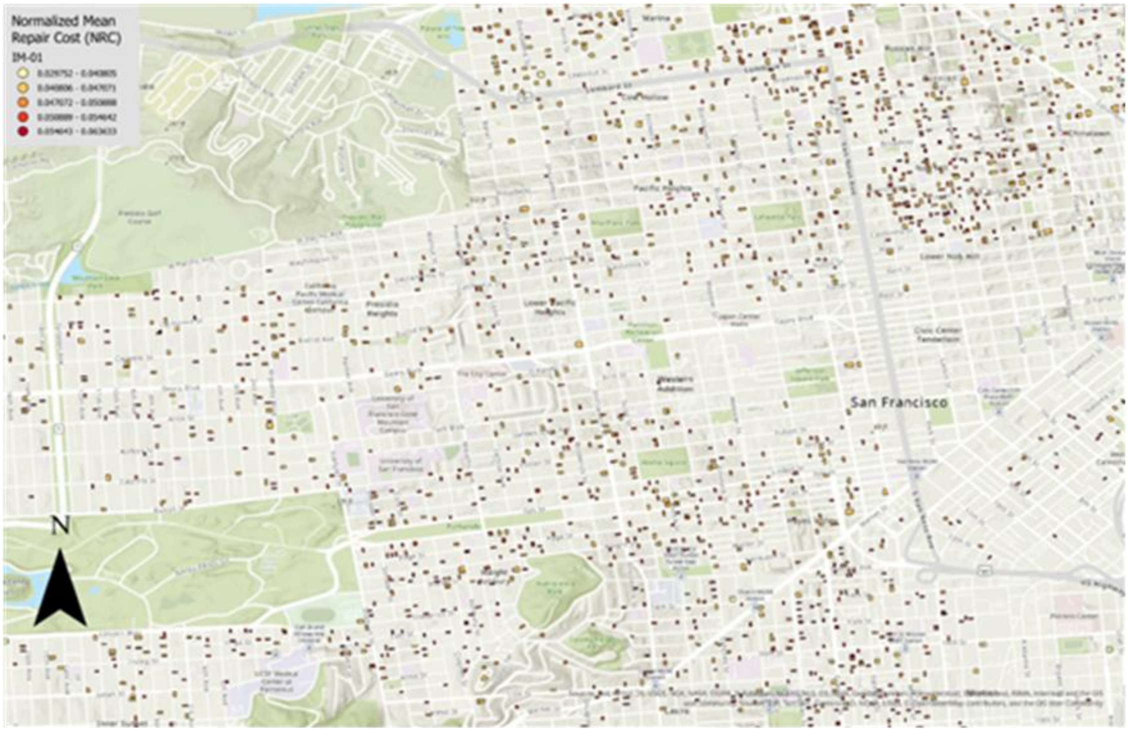
Normalized Mean
Repair Cost (NRC)
IM-01
0.029752 - 0.040805
0.040806 - 0.047071
0.047072 - 0.050888
0.050889 - 0.054642
0.054643 - 0.063633
San Francisco
N

(a)

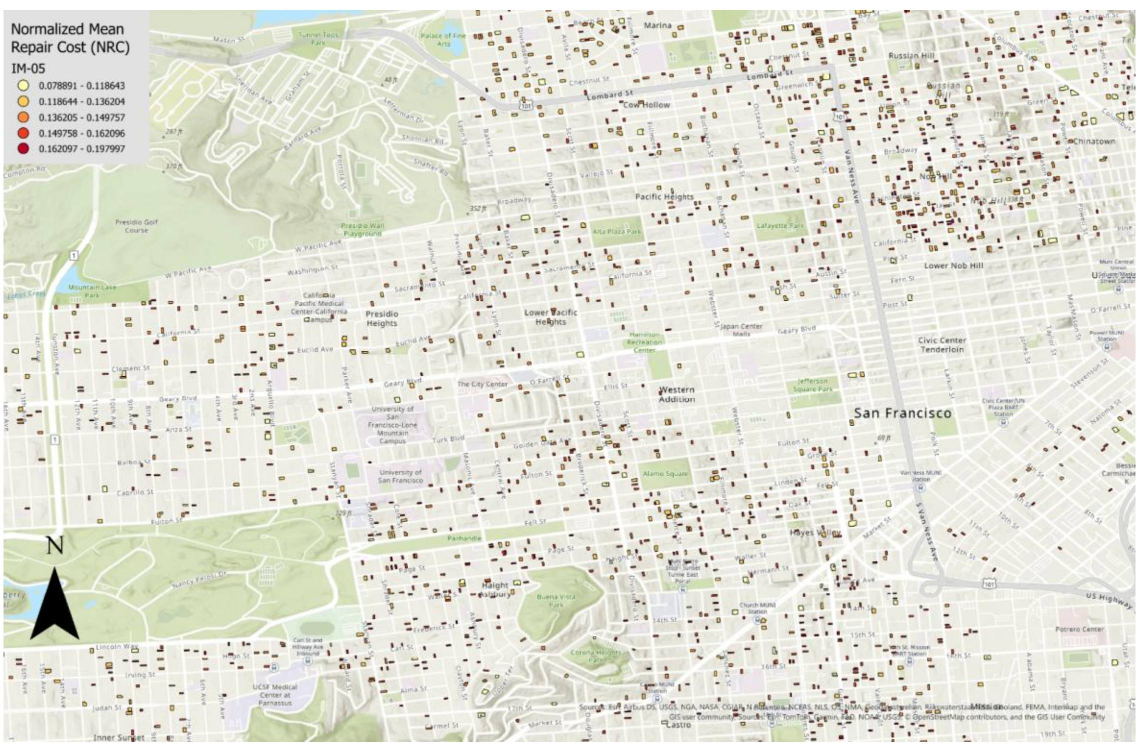
Normalized Mean
Repair Cost (NRC)
IM-05
0.078891 - 0.118643
0.118644 - 0.136204
0.136205 - 0.149757
0.149758 - 0.162096
0.162097 - 0.197997
Marina
Russian Hill
Cow Hollow
Chinatown
Pacific Heights
Nob Hill
Lower Nob Hill
Presidio Heights
Lower Pacific Heights
Civic Center
Tenderloin
Western Addition
San Francisco
Haight Ashbury
Potrero Center
N

(b)

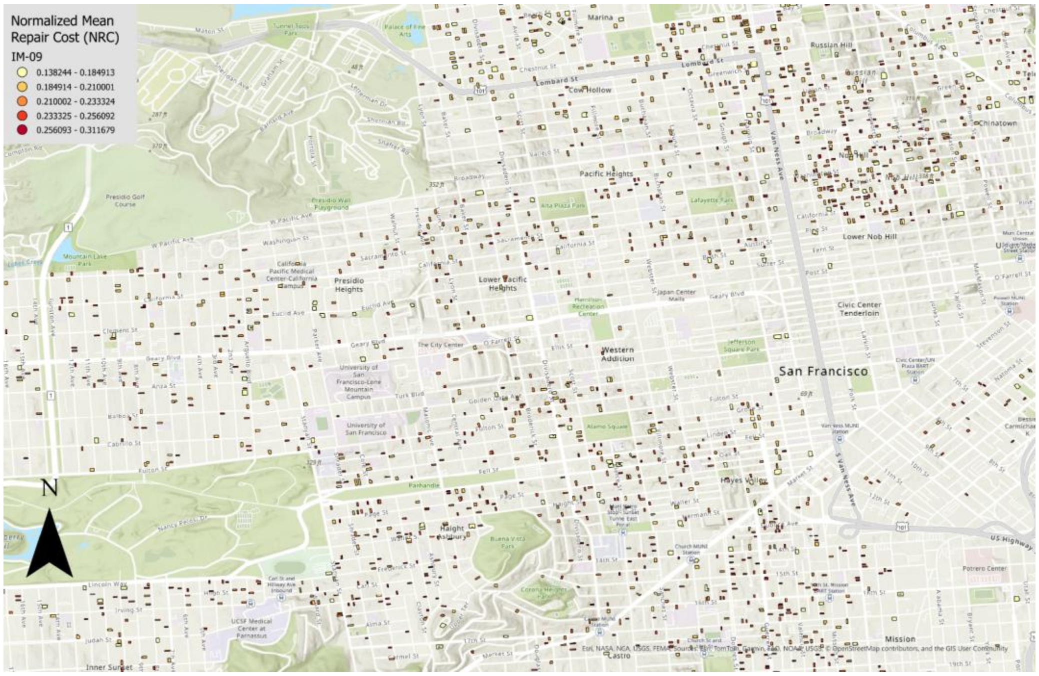

(c)

Figure 6.20 Normalized mean repair cost (NRC) of Y-SCVD-EBF retrofitted wood framed buildings in ArcGIS Pro: (a) IM-01; (b) IM-05; (c) IM-09

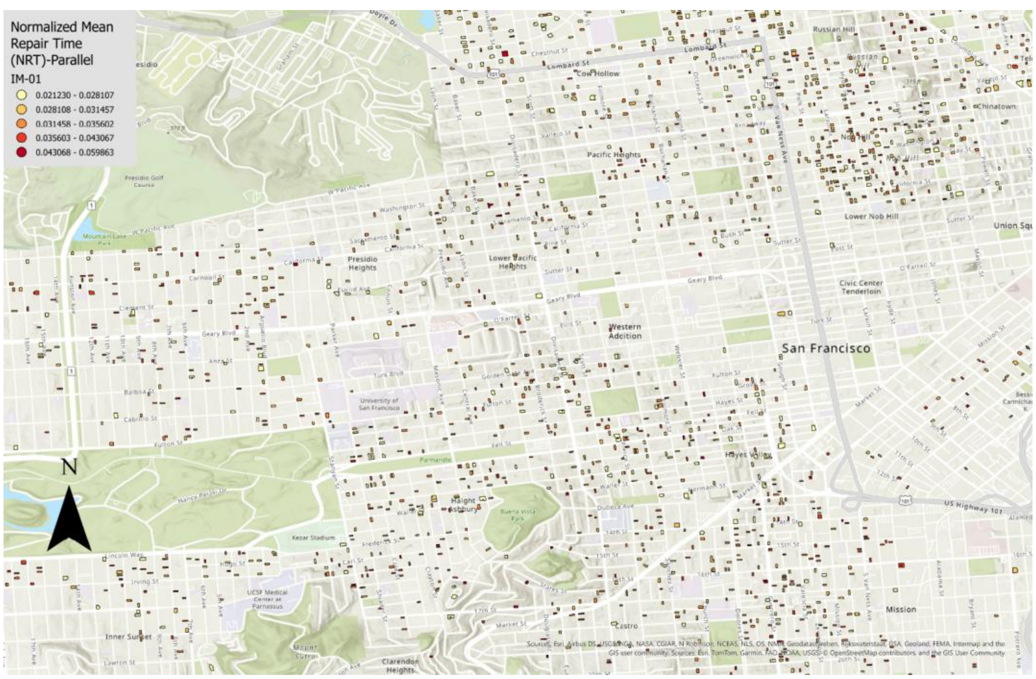

(a)

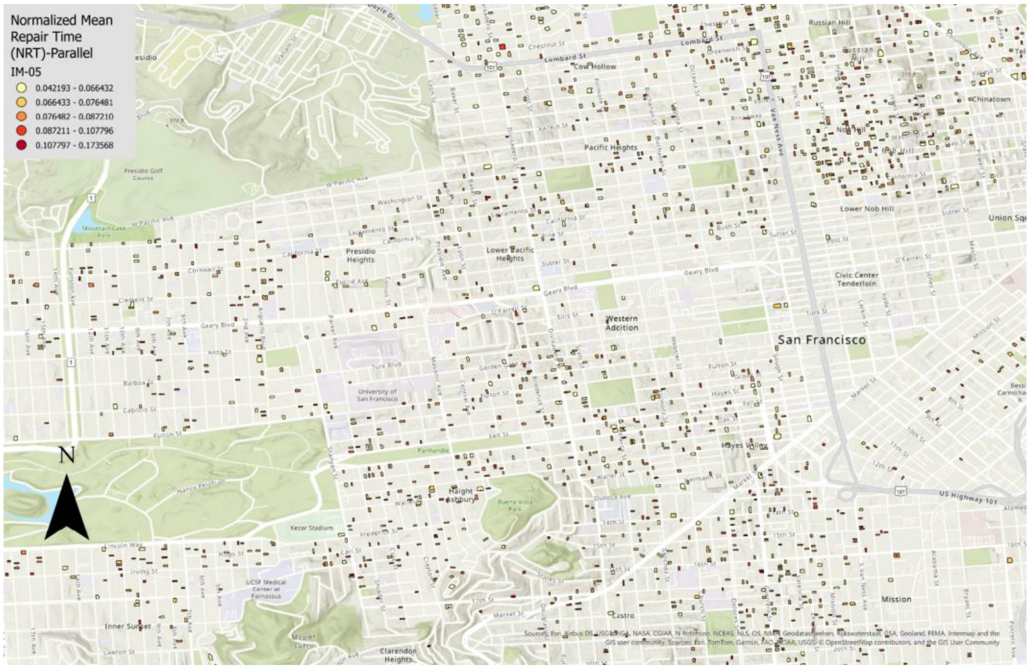

(b)

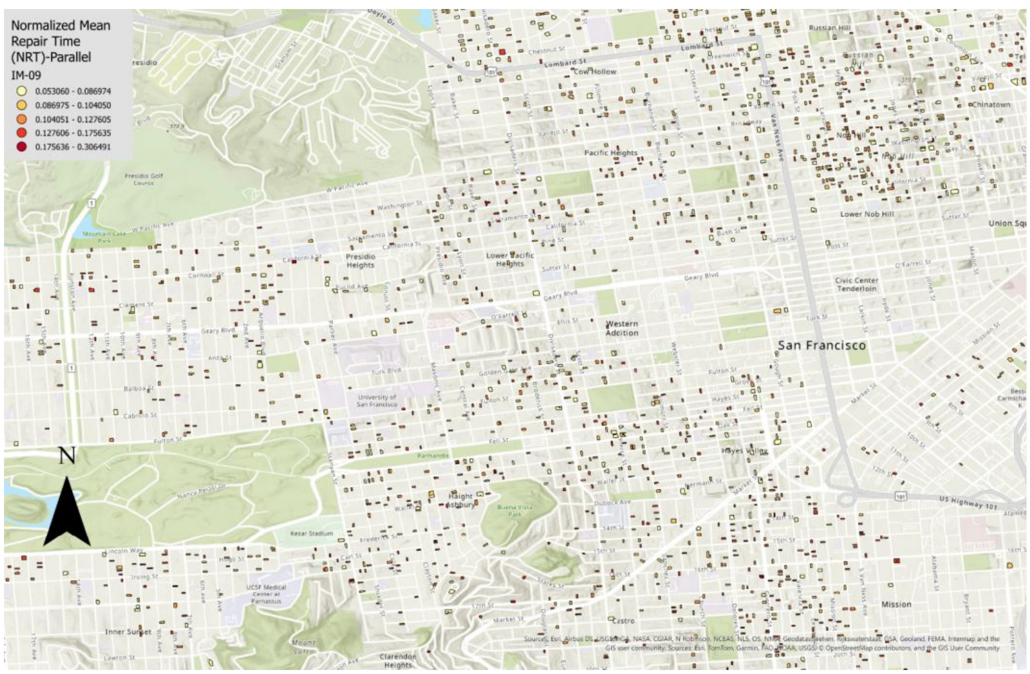

(c)

Figure 6.21 Normalized mean repair time (NRT- parallel working procedure) of Y-SCVD-EBF retrofitted wood framed buildings in ArcGIS Pro: (a) IM-01; (b) IM-05; (c) IM-09

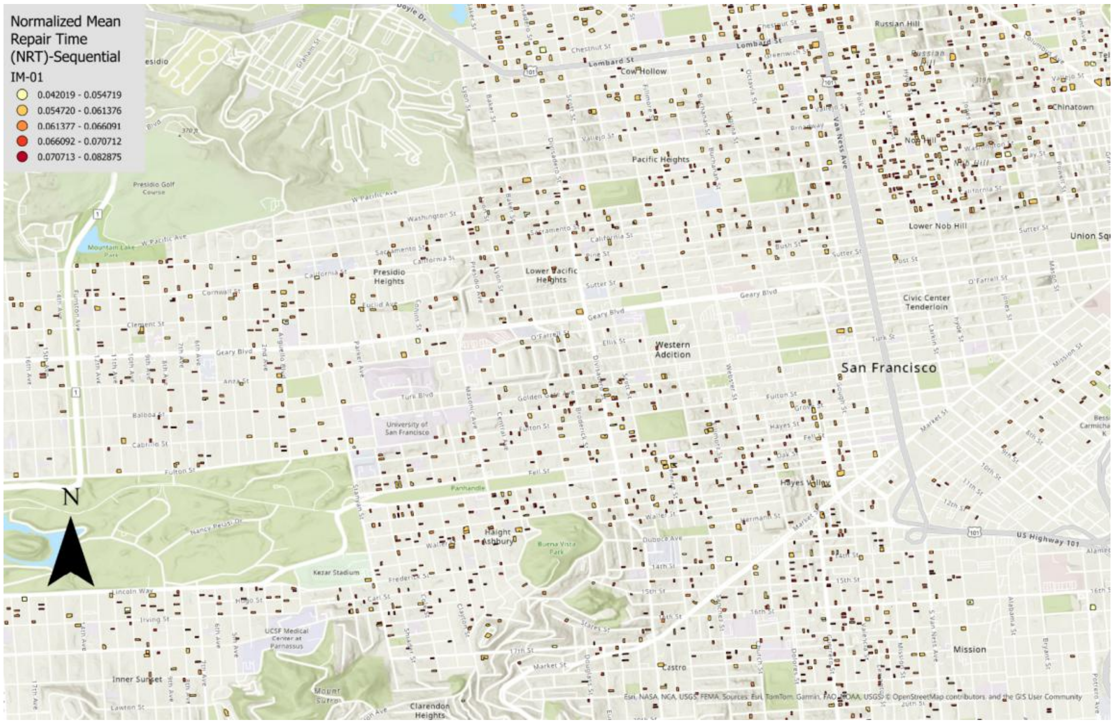
Normalized Mean Repair Time (NRT)-Sequential
IM-01
0.042019 - 0.054719
0.054720 - 0.061376
0.061377 - 0.066091
0.066092 - 0.070712
0.070713 - 0.082875
N
San Francisco
Pacific Heights
Western Addition
Haight Ashbury
Hayes Valley
Mission
Civic Center Tenderloin
Nob Hill
Russian Hill
Chinatown
Cow Hollow
Presidio Heights
Lower Pacific Heights
Lower Nob Hill
Inner Sunset
Castro

(a)

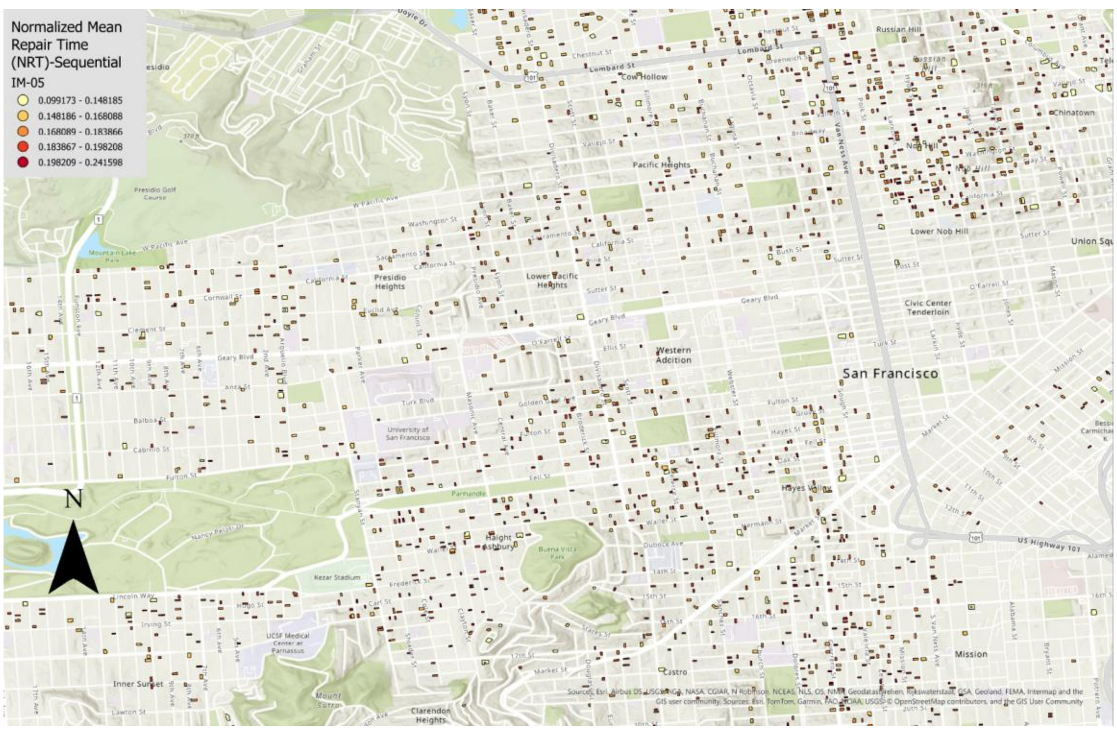
Normalized Mean Repair Time (NRT)-Sequential
IM-05
0.099173 - 0.148185
0.148186 - 0.168088
0.168089 - 0.183866
0.183867 - 0.198208
0.198209 - 0.241598
N
San Francisco
Pacific Heights
Western Addition
Haight Ashbury
Hayes Valley
Mission
Civic Center Tenderloin
Nob Hill
Russian Hill
Chinatown
Cow Hollow
Presidio Heights
Lower Pacific Heights
Lower Nob Hill
Inner Sunset
Castro

(b)

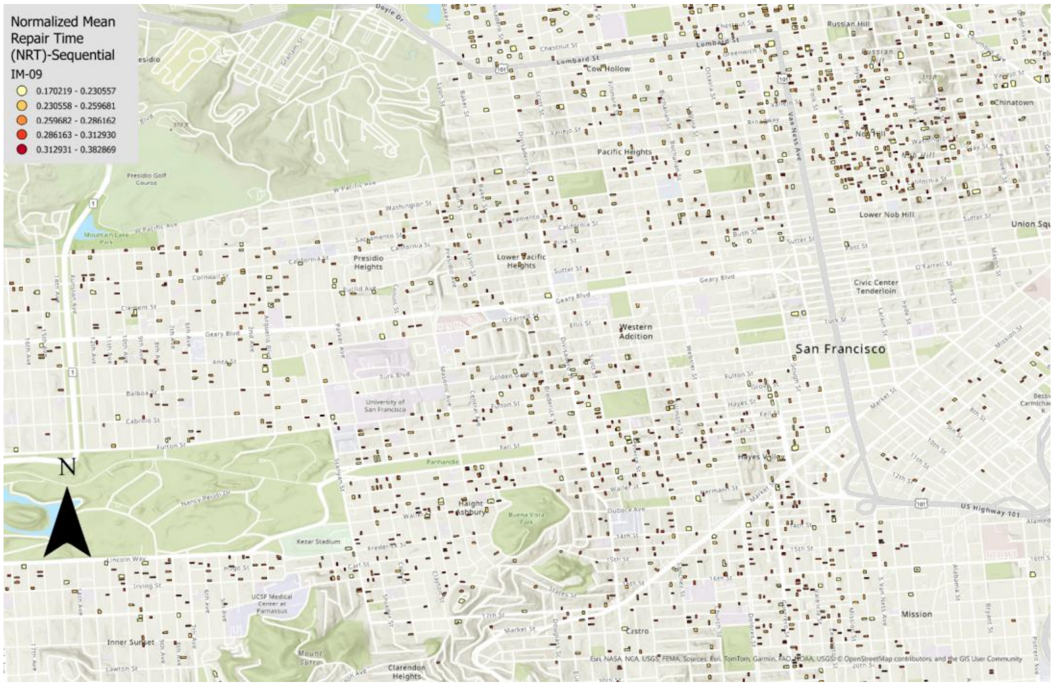

(c)

Figure 6.22 Normalized mean repair time (NRT- serial working procedure) of Y-SCVD-EBF retrofitted wood framed buildings in ArcGIS Pro: (a) IM-01; (b) IM-05; (c) IM-09

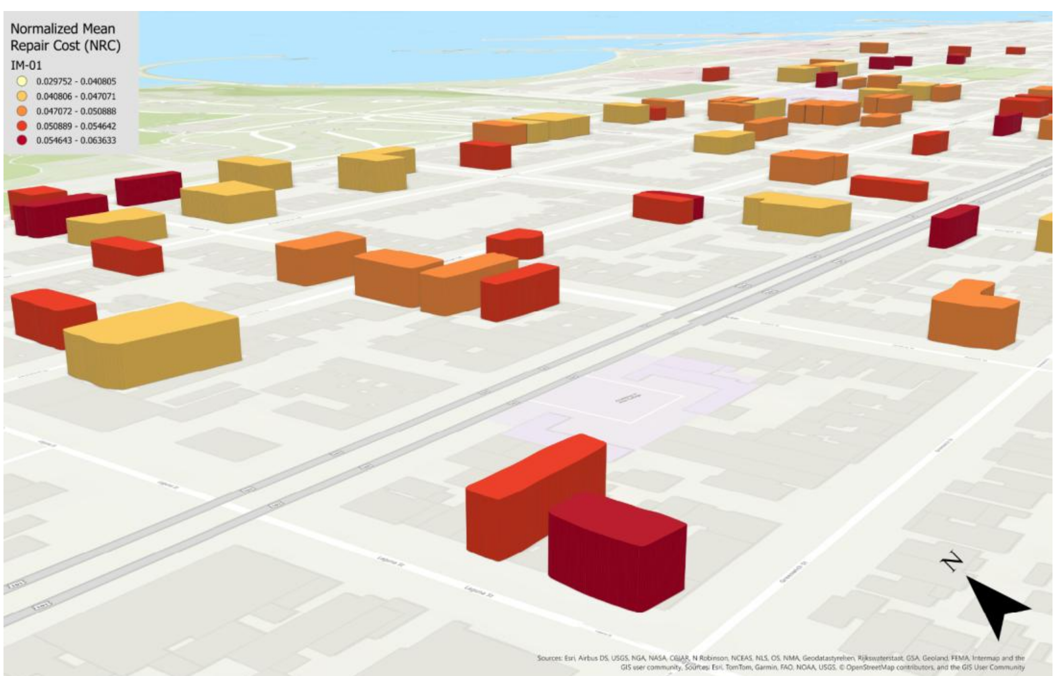

(a)

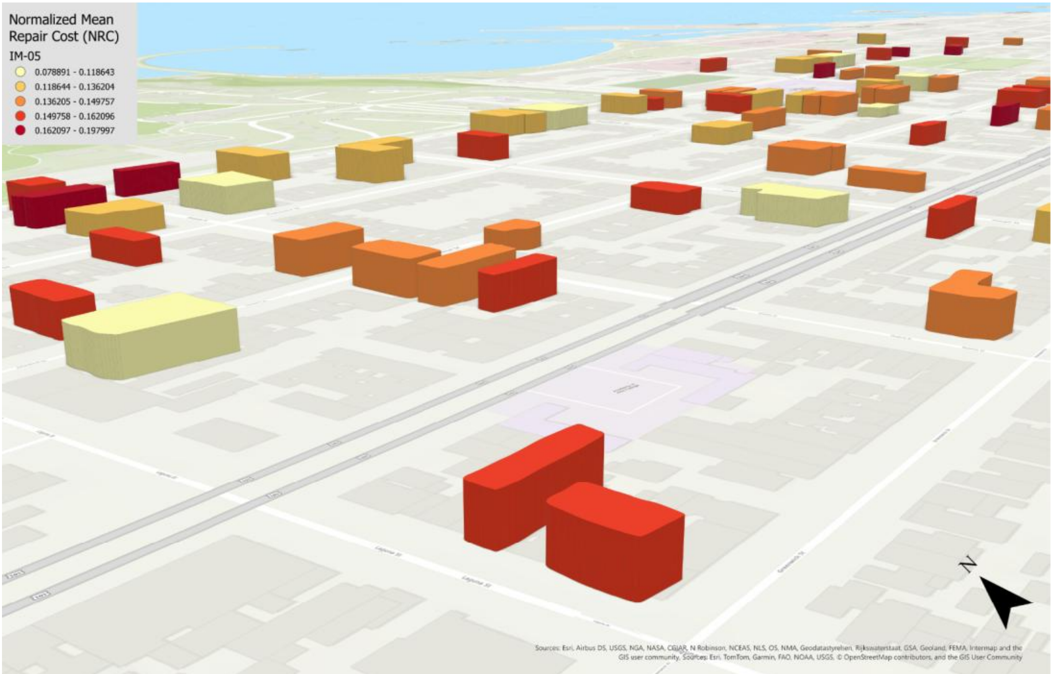

(b)

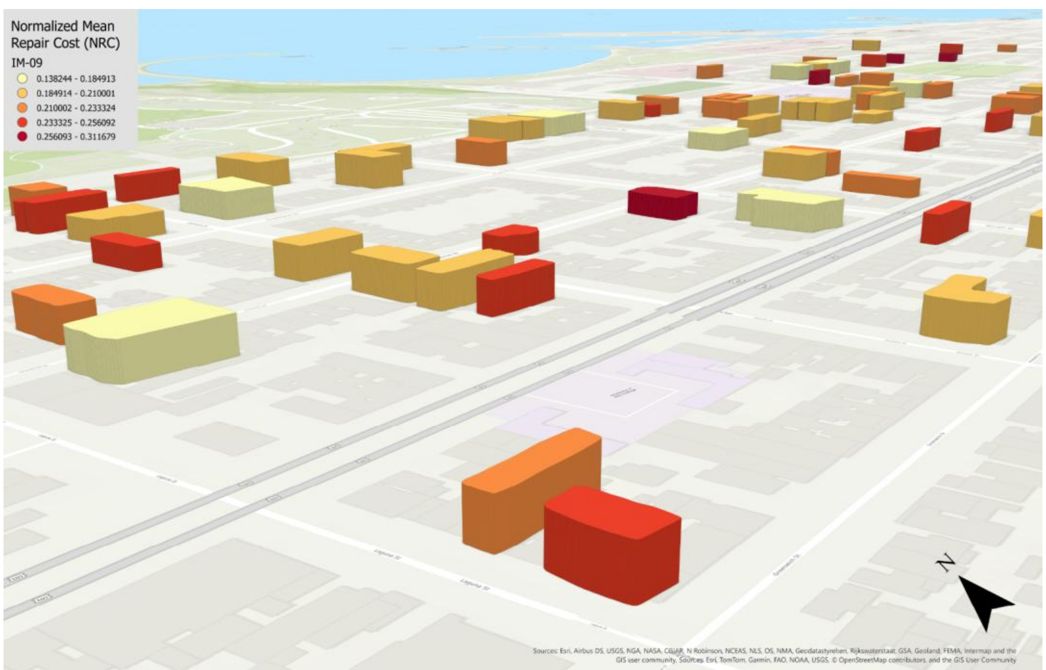

(c)

Figure 6.23 Three-dimensional digital twin model of Y-SCVD-EBF retrofitted wood framed buildings symbolized based on normalized mean repair cost (NRC):

(a) IM-01; (b) IM-05; (c) IM-09

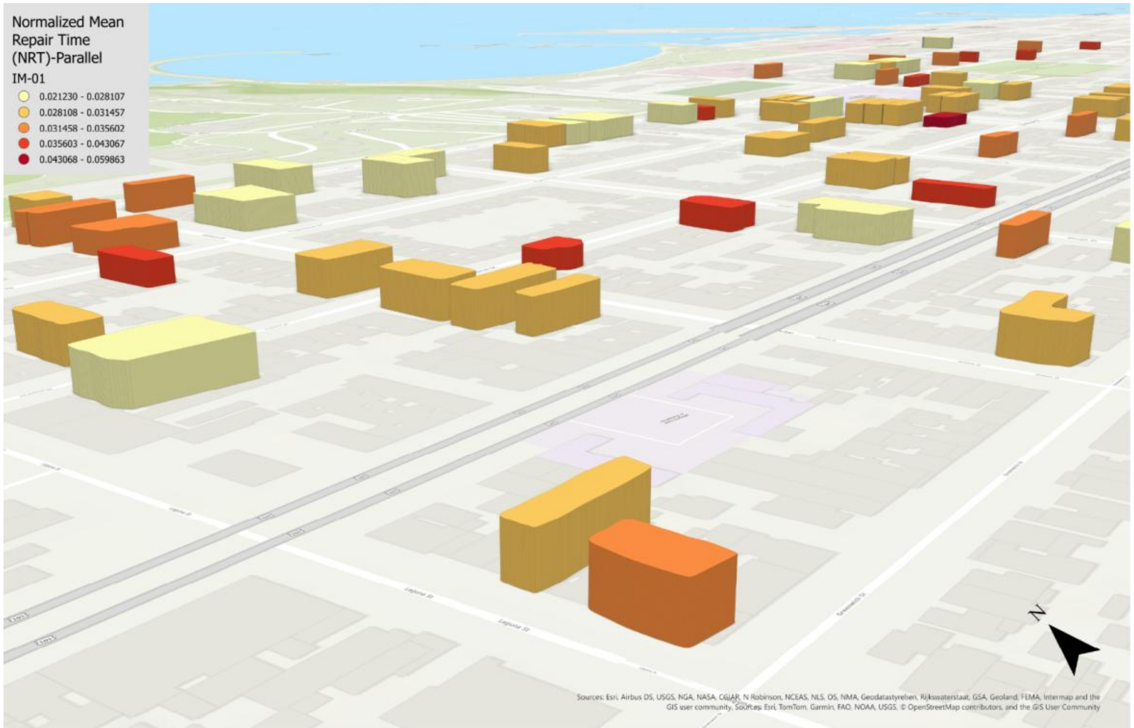
Normalized Mean
Repair Time
(NRT)-Parallel
IM-01
0.021230 - 0.028107
0.028108 - 0.031457
0.031458 - 0.035602
0.035603 - 0.043067
0.043068 - 0.059863
N

(a)

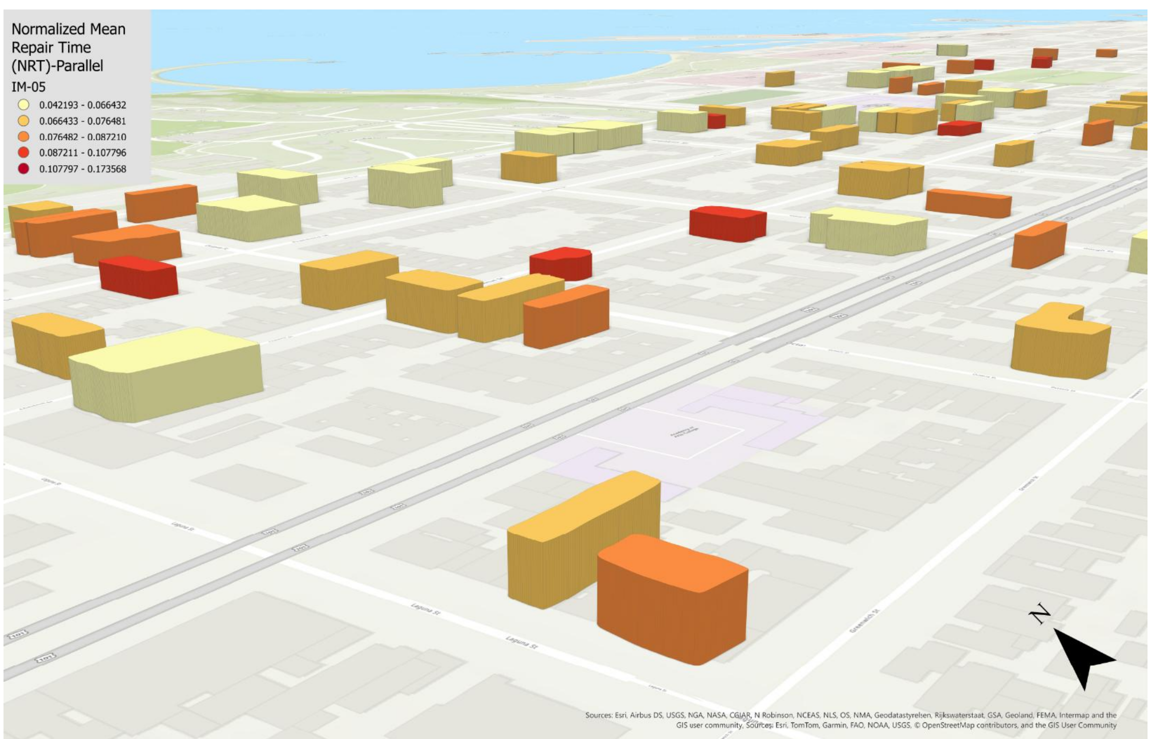
Normalized Mean
Repair Time
(NRT)-Parallel
IM-05
0.042193 - 0.066432
0.066433 - 0.076481
0.076482 - 0.087210
0.087211 - 0.107796
0.107797 - 0.173568
N

(b)

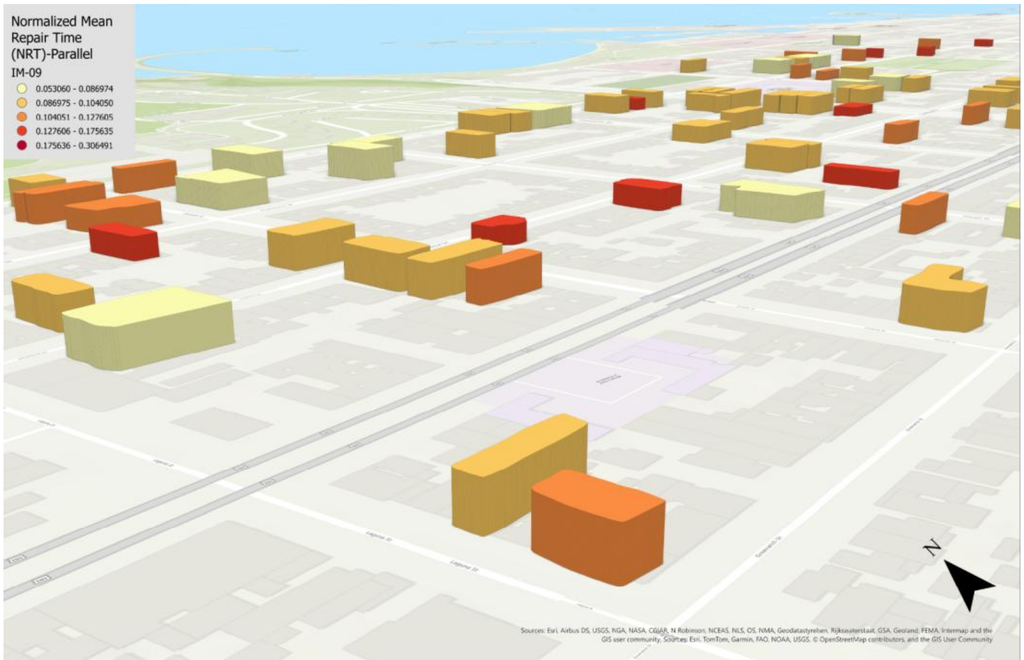

(c)

Figure 6.24 Three-dimensional digital twin model of Y-SCVD-EBF retrofitted wood framed buildings symbolized based on normalized mean repair time (NRT-parallel working procedure): (a) IM-01; (b) IM-05; (c) IM-09

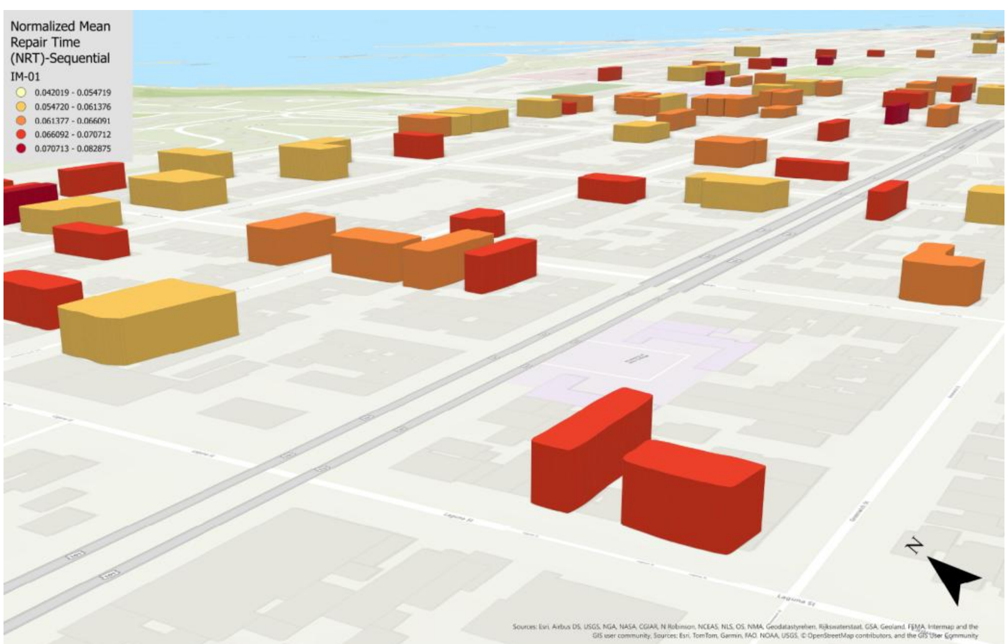

(a)

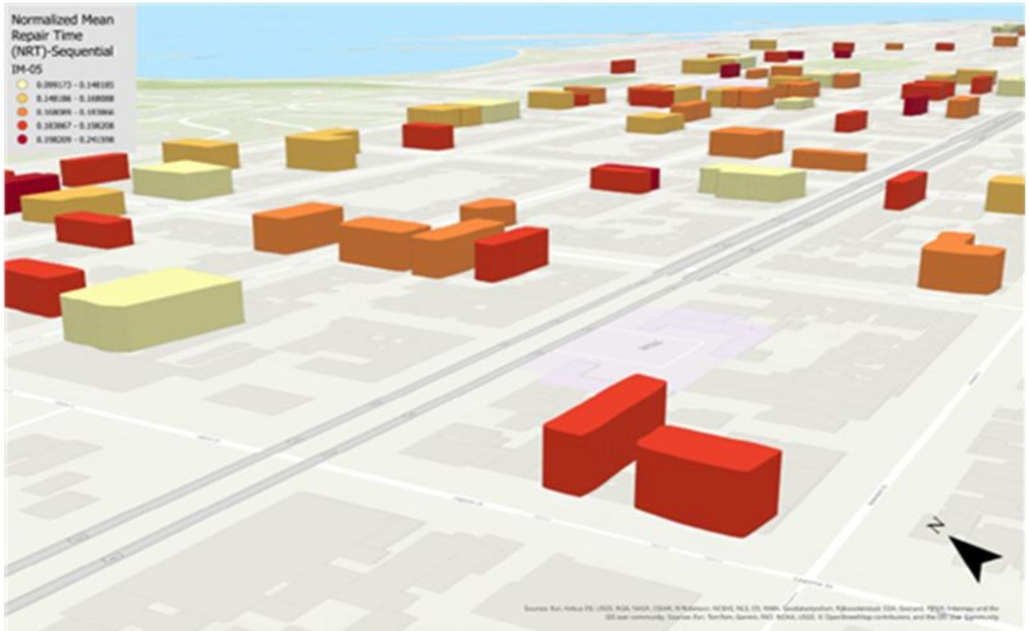

(b)

(c)

Figure 6.25 Three-dimensional digital twin model of Y-SCVD-EBF retrofitted wood framed buildings symbolized based on normalized mean repair time (NRT-serial working procedure): (a) IM-01; (b) IM-05; (c) IM-09

In this section, damage and loss assessment outputs of typical three- and four-story wood-frame multi-family residential buildings retrofitted with the proposed Y-SCVD-EBF modular system is discussed. Three- and four-story buildings are the two most frequent soft-story buildings in San Francisco as illustrated in Figure 6.6. Figure 6.26 shows the CDF of normalized mean repair cost at different intensity levels for the typical buildings. There are no irreparable damages associated with the buildings considered; therefore, the probability of irreparability (PIR) is zero. According to Figure 6.26, the three-story building has a wider CDF graph compared to that of the four-story counterpart.

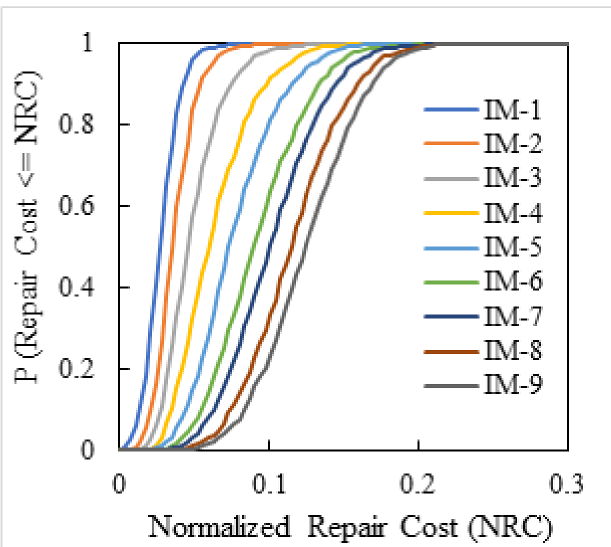

(a)

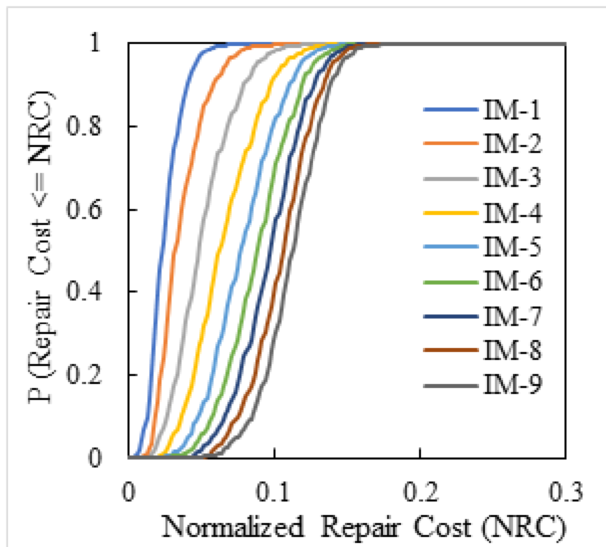

(b)

Figure 6.26 Cumulative distribution function (CDF) of normalized mean repair cost (NRC) of typical wood framed residential buildings at different intensities: (a) 3-story; (b) 4-story

The resilience metrics at different intensity levels for the two buildings are illustrated in Figure 6.27 through Figure 6.29. According to the figures, normalized repair cost (NRC) and normalized repair time (NRT) are directly proportional to the intensity measure (IM) as increasing the intensity levels results in increasing the resilience metrics in the building-specific scale.

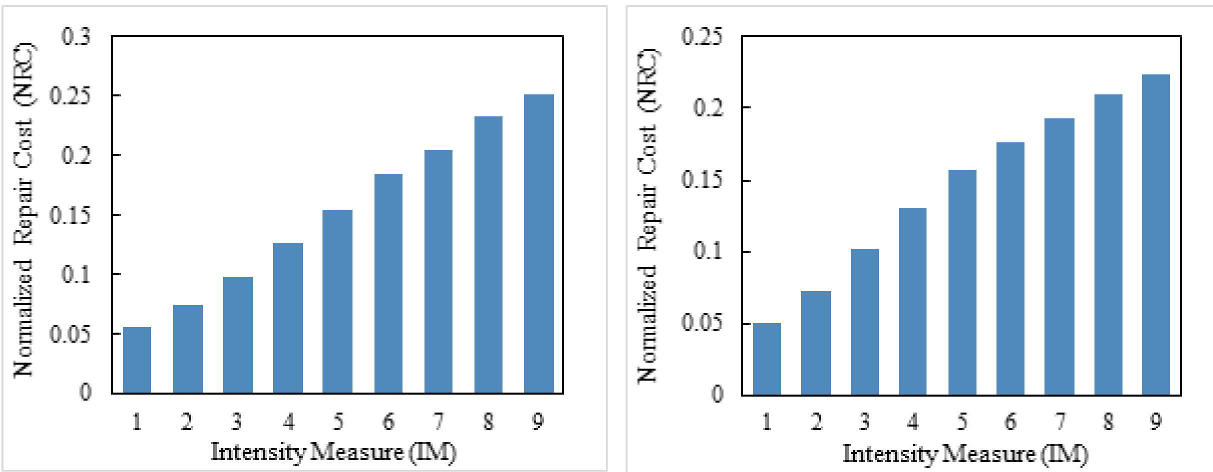

(a) (b)

Figure 6.27 Normalized repair cost (NRC) at different intensity levels for typical buildings: (a) 3-story, (b) 4-story

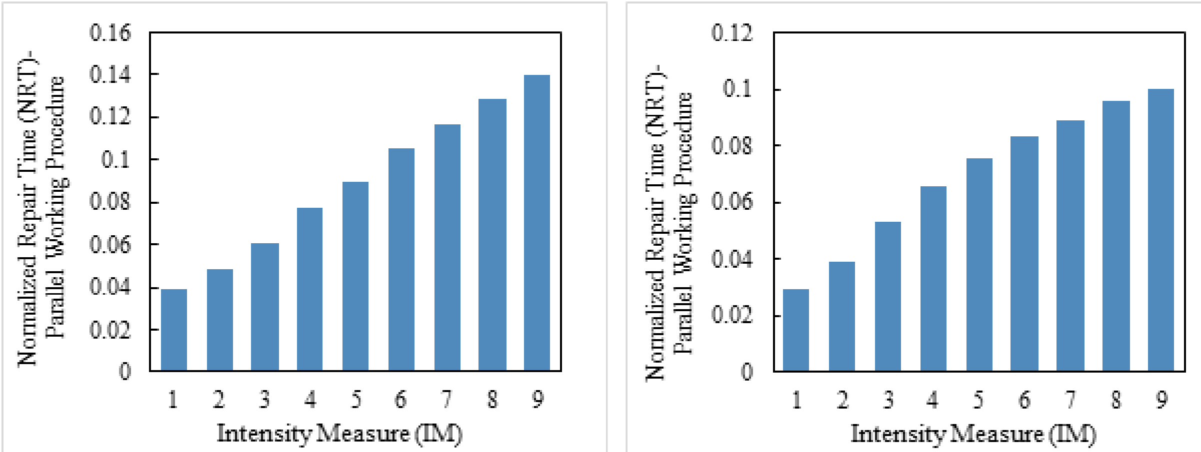

(a) (b)

Figure 6.28 Normalized repair time (NRT) at different intensity levels for typical buildings considering Parallel working procedure: (a) 3-story, (b) 4-story

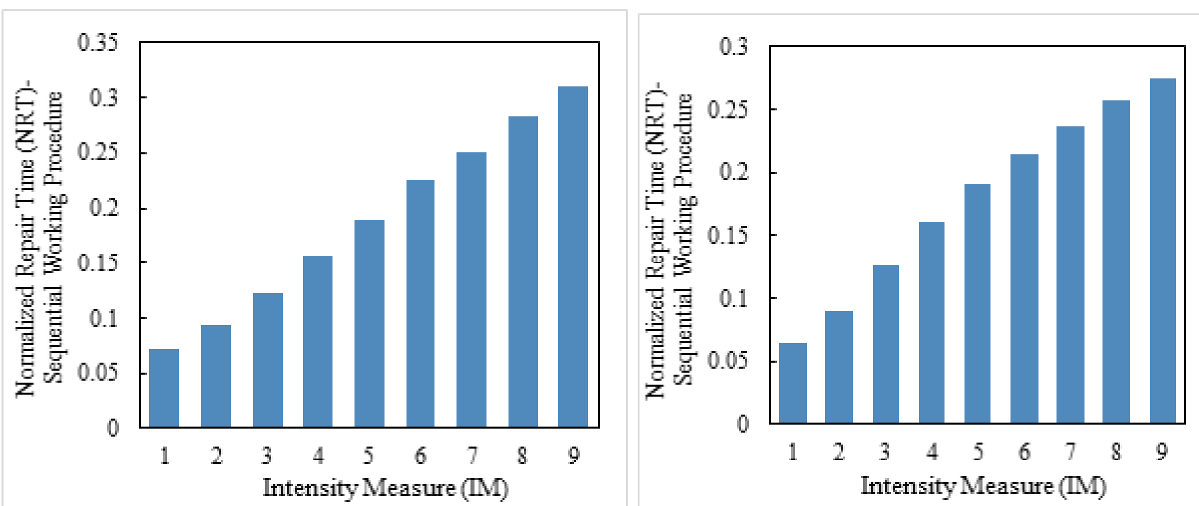

(a) (b)

Figure 6.29 Normalized repair time (NRT) at different intensity levels for typical buildings considering Sequential working procedure: (a) 3-story, (b) 4-story

Figure 6.30 and Figure 6.31 illustrate the proportionate contribution of each floor to the mean repair costs of the building across various intensity measures (IMs). It is observed that the first floor accounts for a larger share of repair costs at lower IMs, primarily because of the loss of the components assigned to this floor only. As seismic intensity increases, other components also contribute, thereby diminishing the relative contribution of the first floor. Nonetheless, the first floor consistently remains the most significant contributor to repair costs across all intensity levels. Additionally, the top story maintains a nearly constant contribution regardless of the intensity measure.

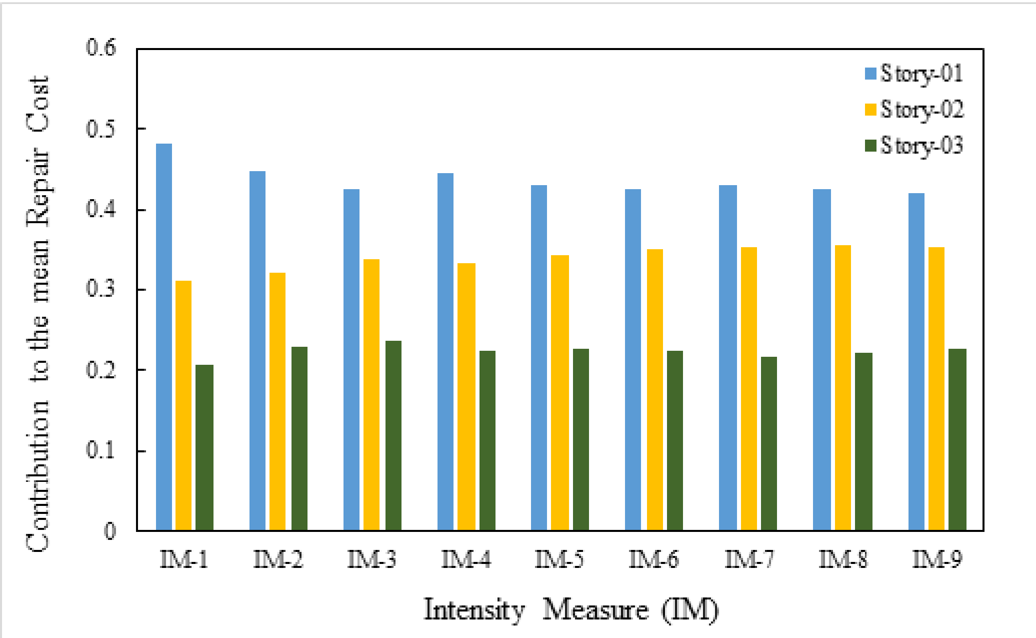

Figure 6.30 Story contribution of a typical 3-story multi-family residential building to the mean repair cost

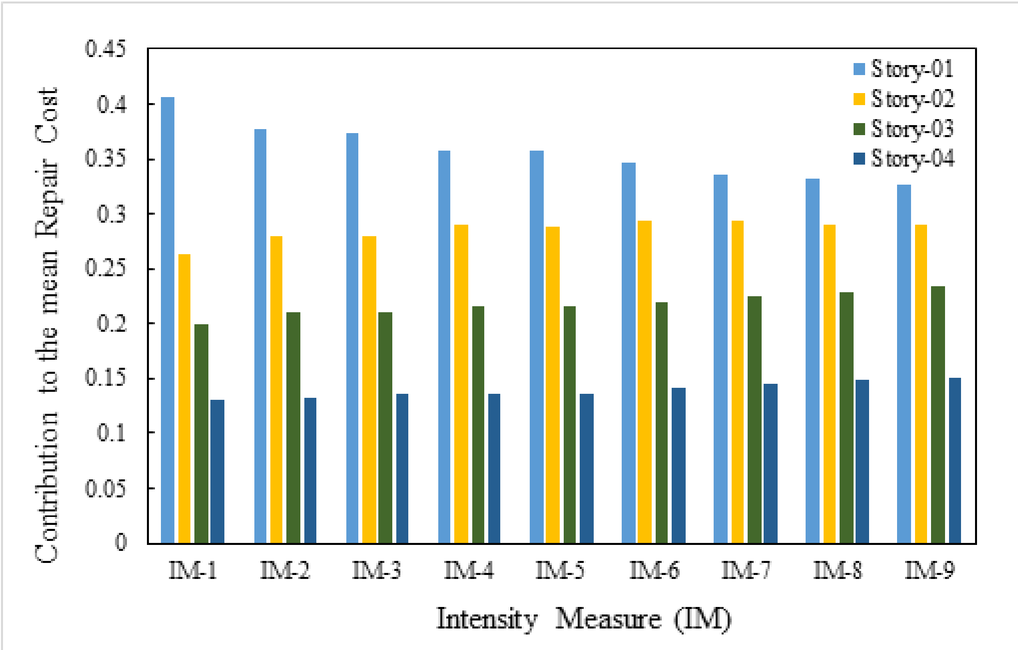

Figure 6.31 Story contribution of a typical 4-story multi-family residential building to the mean repair cost

Figure 6.32 through Figure 6.35 illustrate the contribution of buildings' components to the mean repair cost and mean repair time at three different intensity levels for the two buildings. According to the figures, the structural component (COMP-01) contribution increases as the intensity level increases. The other components, which are nonstructural, have different behaviors as the intensity measure (IM) changes.

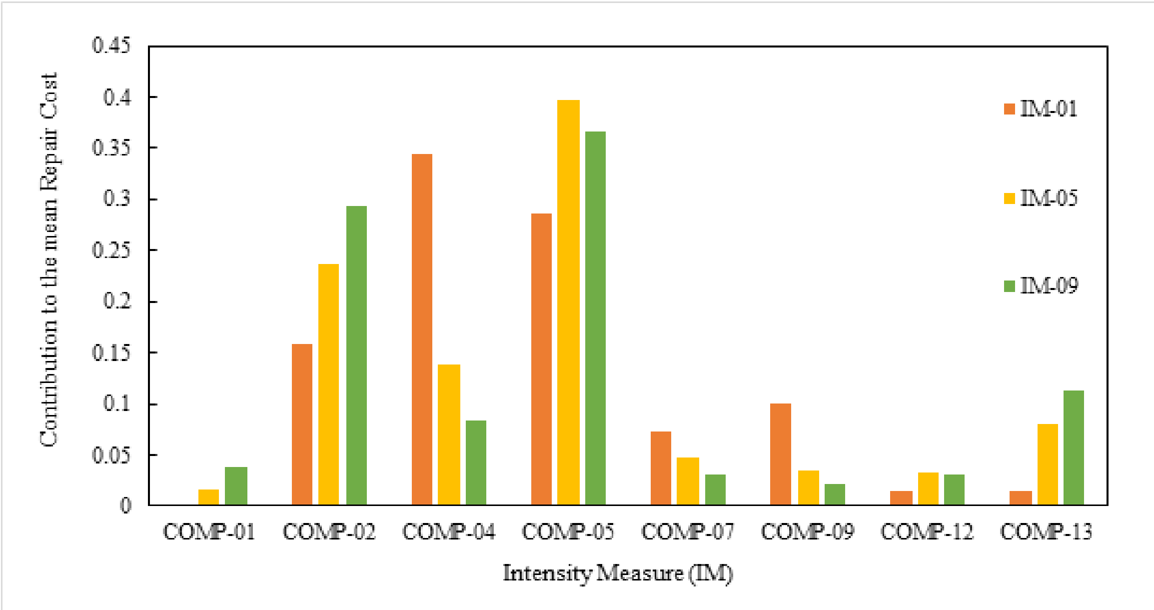

Figure 6.32 Contribution of the components of a typical three-story retrofitted wood framed residential building to the mean repair cost at different IMs

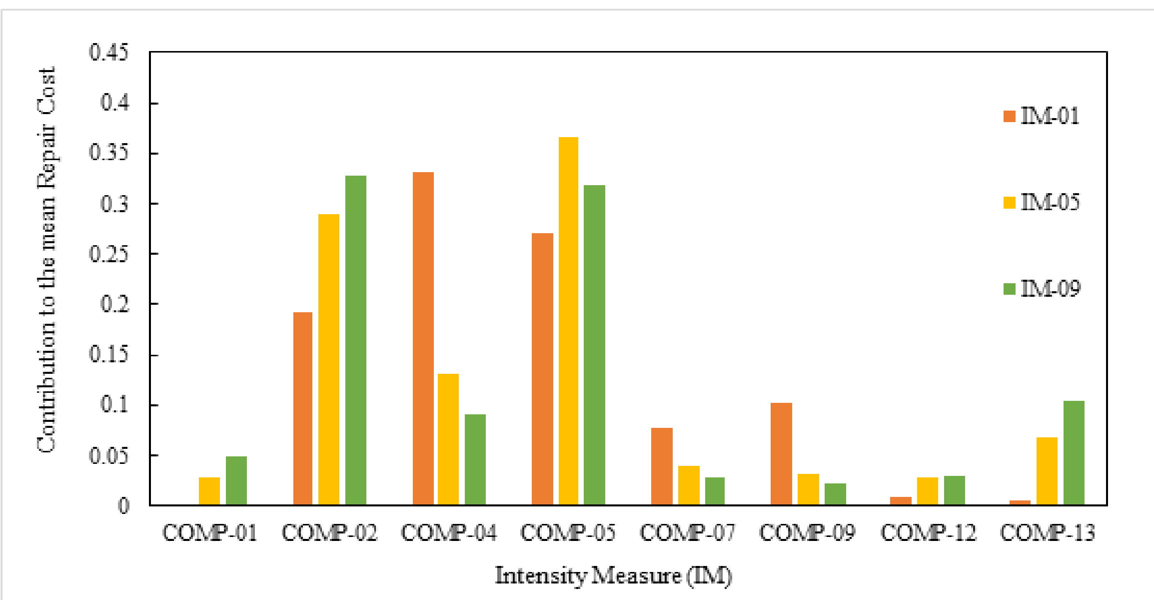

Figure 6.33 Contribution of the components of a typical four-story retrofitted wood framed residential building to the mean repair cost at different IMs

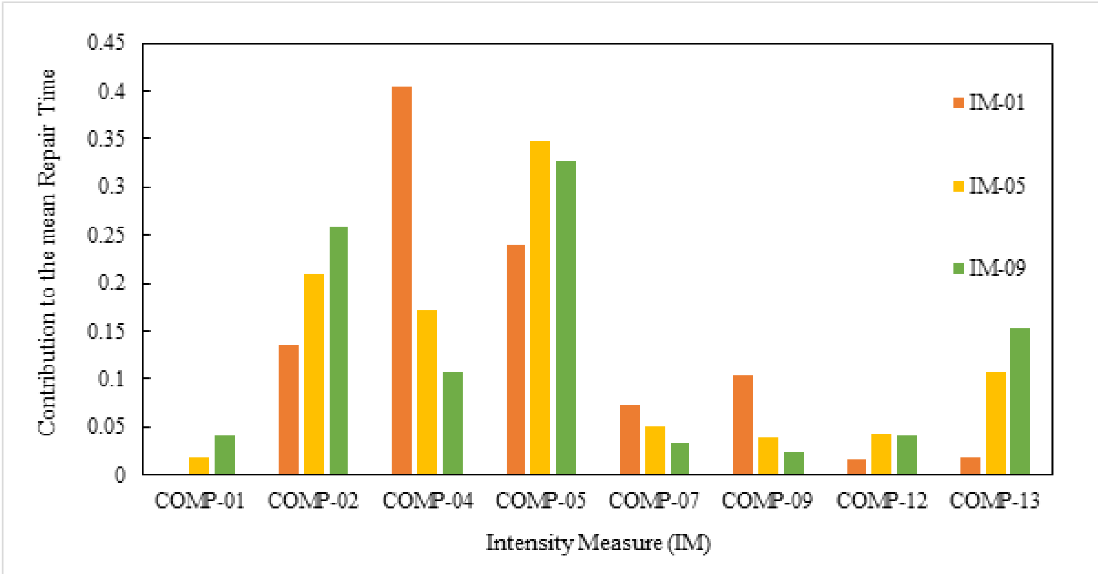

Figure 6.34 Contribution of the components of a typical three-story retrofitted wood framed residential building to the mean repair time at different IMs

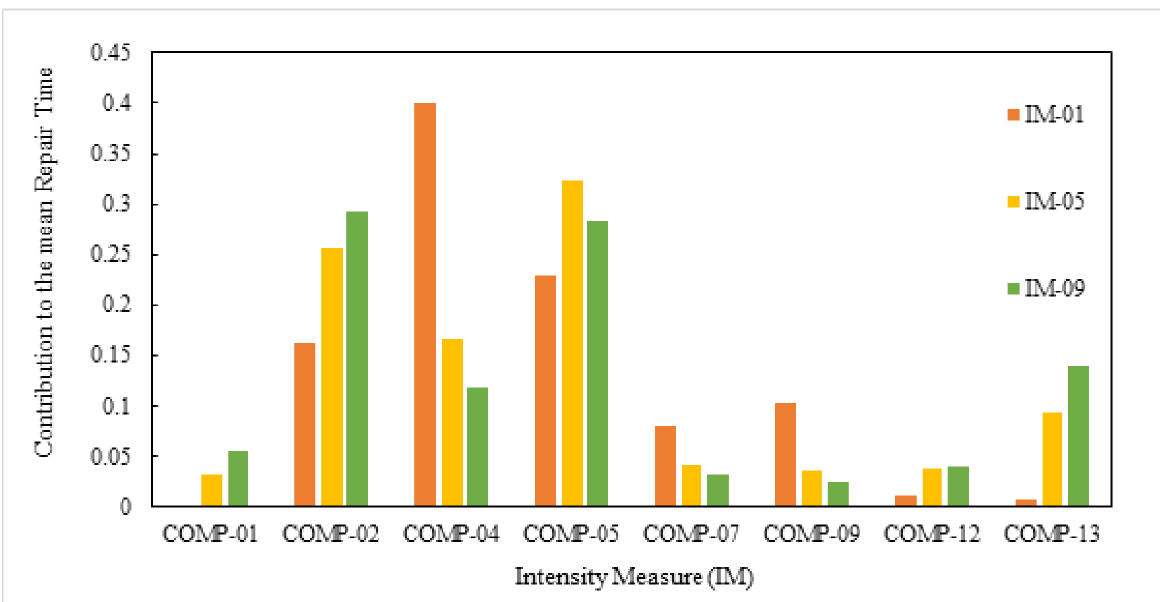

Figure 6.35 Contribution of the components of a typical four-story retrofitted wood framed residential building to the mean repair time at different IMs

6.10 Summary

Intensity-based seismic resilience assessment of wood framed soft-story residential buildings retrofitted with the novel Y-SCVD-EBF modular systems was performed in regional and building-specific scales in this chapter. The digital twin model framework uses Python packages such as OpenSeesPy to conduct RHA, Pelicun to perform probabilistic seismic damage and loss assessment, and ArcPy to visualize the results in two and three dimensions. Over 2,000 light-frame timber structured soft-story multi-family residential buildings in San Francisco Municipal Area were retrofitted and regional seismic resilience assessment was carried out at nine intensities using the component-level FEMA P-58 methodology [8]. In this case study, nonlinear RHAs were performed for the buildings in the region first in order to obtain the EDPs required to conduct the damage and loss assessment. The evaluation was conducted using the Pelicun package in Python-based framework. The findings of this study are summarized as follows:

- At the highest intensity level (PGA = 1.0g), the regional normalized mean repair cost (NRC) is quantified at 22.4%. Of this total loss, over 95% is attributable to the repair costs of nonstructural components, whereas less than 5% pertains to structural components. However, at the lowest intensity measure (PGA = 0.2g), the regional NRC is approximately 5%, with nearly all of this cost associated exclusively with nonstructural component contributions.

- In this study, the probability of irreparability (PIR) is zero across all cases, primarily due to the substantial restoring force and the reduced likelihood of plastic deformation in the preloaded disc springs. Additionally, the buildings are light wood-framed structures with high strength-to-weight ratios, which enhance their seismic resilience. However, they were code deficient and have been retrofitted with the novel Y-SCVD-EBF systems. As a result, the seismic loads imposed on these retrofitted buildings are relatively low and the retrofitted buildings are seismically adequate, preventing severe damages and eliminating the necessity for irreparable repairs or replacements. This combination of robust restoring mechanisms and favorable structural characteristics makes the retrofitted light wood-framed buildings highly seismically favorable.

- Regional seismic losses are predominantly attributed to nonstructural components across all intensity levels. The fuse devices, which are part of the structural components of the proposed retrofitting system, do not contribute to building losses. This is because their replacement is typically required only at very high inter-story drift ratios (IDRs), at which point the building is generally deemed irreparable due to excessively large residual drifts. Therefore, wood shear walls are the sole structural components that contribute to building losses which is not significant.

- The relative contribution of each component to the overall loss varies with seismic intensity. Specifically, for certain elements such as exterior walls, their relative contribution to total losses increases as intensity levels rise. In contrast, other components, including clay tile roofs, demonstrate a decreasing relative contribution with higher intensities.

- Although structural components contribute minimally to repair costs in high-performance self-centering systems, nonstructural elements are critical to the overall seismic losses experienced by a building. Peak floor acceleration is a crucial parameter for determining nonstructural failures. In this case study, TPAD fuse devices were used as the backup damper in the retrofitting system; however, the implementation of viscous dampers as the primary energy dissipation devices was found to be highly effective in further reducing the acceleration responses of the building stories within the developed systems.

Chapter 7 : Summary, Conclusion, and Future Research

In this chapter, the overall scope of the research is first summarized, followed by a discussion of the findings and conclusions pertaining to each area of the research work. The chapter concludes by proposing avenues for future inquiry to address the identified gaps.

7.1 Summary

Light-frame wood buildings with soft stories are widely observed in California, particularly in San Francisco. To improve their seismic performance, this study proposes a set of novel self-centering viscoelastic damper (SCVD) systems. Three distinct retrofit strategies were investigated: (1) a wood structural panel (WSP) retrofit primarily strengthening the upper stories, (2) a self-centering viscoelastic damper (SCVD) system installed at the ground story, and (3) a Y-type braced self-centering viscous damper eccentrically braced frame (Y-SCVD-EBF) module designed to retrofit the entire structure. The nonlinear seismic behavior of a typical code-deficient wood framed soft-story building retrofitted with these systems was then evaluated to determine their effectiveness.

Finally, a Python-based computational framework was employed to simulate and visualize the regional seismic damage and loss assessment of deficient wood-framed residential buildings retrofitted with Y-SCVD-EBF modular systems. The seismic resilience of these upgraded buildings was evaluated by applying this workflow to over 2,000 multi-family residential buildings in the San Francisco Municiapl Area.

7.2 Conclusion

7.2.1 Light Wood Framed Buildings Retrofitted with Wood Structural Panel (WSP)

The nonlinear seismic behavior of light-frame wood buildings with soft stories was studied through static and dynamic analyses of a four-story prototype building. The effects of retrofitting the original building with wood structural panel (WSP) were investigated by performing nonlinear static and dynamic analyses. The results are summarized as follows:

- Under the Far-field (FF) record set at the 0.0002 DBE level, the ensemble median of the maximum inter-story drift ratios (IDRs) for the original, unretrofitted light-frame wood building is below 0.05%, while the median maximum observed residual IDR at the same intensity level is 0.02%. These values for the WSP-retrofitted prototype building at the 0.06 DBE level are below 0.2%, and 0.1%, respectively.
- In both the unretrofitted and WSP-retrofitted wood-frame prototypes, the first story exhibits the largest drift responses at the studied intensity levels due to the limited seismic force resisting system (SFRS). Although the original prototype is classified as a soft-story structure at all levels, the ground story is notably much softer than the upper stories because of larger openings which reduce the extent of timber lateral walls available to resist seismic loads. Additionally, when considering quantile values, the first-story peak drifts are more widely dispersed than those of the upper stories, which exhibit comparatively similar dispersions.
- The WSP-retrofitted prototype demonstrated enhanced seismic performance by effectively controlling drift and minimizing residual drift. Moreover, this method is practical, cost-

effective, and straightforward to implement, given that new plywood sheathing can be installed directly over the existing timber walls.

- While the WSP retrofitting method offers significant advantages for the upper stories due to the presence of existing walls at these levels, it is ineffective for the ground story. Consequently, alternative retrofitting techniques must be employed to reinforce the ground story as well.

7.2.2 Light Wood Framed Buildings Retrofitted with Self-Centering Viscoelastic Damper (SCVD) System on the Ground Story Only

Based on the findings from the nonlinear numerical analysis of the four-story wood framed soft-story prototype building retrofitted exclusively at the ground story using the self-centering viscoelastic damper (SCVD) system, the following conclusions can be drawn:

- Under the Far-field (FF) record set at the 0.45 DBE level, the SCVD-retrofitted prototype without TPAD exhibits an ensemble median of maximum IDR of less than 0.5%. At the same intensity level, the maximum residual IDR is below 0.25%. The aforementioned values for the case with TPAD are less than 0.45%, and 0.2%, respectively.

- In the SCVD-retrofitted prototype that does not incorporate a fuse plate, the peak IDR attains its maximum value at the roof level. While in the retrofitted case equipped with a fuse device, the highest peak IDR is observed at the second story. The minimum peak IDRs occur at the ground story for both cases. Moreover, peak drifts exhibit greater dispersion in the upper stories, whereas the ground story demonstrates a more limited range of dispersion.

- The SCVD retrofitting systems can be configured to retrofit the ground story only of a soft-story wood-frame building, thereby enhancing seismic performance under near frequent earthquake (FE) intensity levels. The retrofitted structure demonstrates favorable IDRs, improved recentering capability, and efficient energy dissipation. Moreover, this retrofit strategy is cost-effective and easy to employ, as it limits construction activities to the ground story without causing disruptions to the stories above.

7.2.3 Light Wood Framed Buildings Retrofitted with Y-type Braced Self-Centering Viscous Damper Eccentrically Braced Frame (Y-SCVD-EBF) System

The original wood framed prototype building was retrofitted with the proposed Y-type braced self-centering viscous damper eccentrically braced frame (Y-SCVD-EBF) modular system on all the four stories. The nonlinear seismic performance of the retrofitted prototype was investigated through static and dynamic analyses. The summarized results are as follows:

- The ensemble median of the maximum IDRs of the prototype building without the TPAD fuse device was 0.7% and 1.28% at the DBE and MCE_R levels, respectively. In the case with the fuse, these values were 0.63% and 0.78%, respectively. In both cases, the building was fully recentered.

- The integration of TPAD within the retrofitting system results in a reduction of the maximum IDR for the ground story by 0.12% at the DBE level. When TPAD is employed, the structure demonstrates an increased maximum base shear and more energy dissipated. Additionally, the incorporation of a fuse device within the viscoelastic damper effectively lowers the peak IDR in stories where the maximum IDR exceeds 0.5%.

- The implementation of TPAD results in a reduction of the median of maximum deformation ratio of the disc springs by 0.5% at the DBE level and by 5.3% at the MCE_R level, respectively. Additionally, TPAD effectively prevents the disc springs from experiencing flattening.

- The implementation of the TPAD fuse device reduces both the maximum inter-story drift ratio (IDR) and the deflection ratio of the disc springs particularly under more intense ground motions (GMs). The application of TPAD decreases the median of maximum IDR by 0.07%, and 0.5% at the design basis earthquake (DBE), and risk-targeted maximum considered earthquake (MCE_R) levels, respectively. Additionally, the use of the fuse device lowers the ensemble median of the maximum deflection ratio of the disc spring assemblies by 0.5% under DBE and by 5.3% under MCE_R, respectively.

- The retrofitted structure successfully met the design objectives, exhibiting satisfactory performance in drift control, recentering behavior, disc spring response, and the concentration of damage within the fuse.

- It was concluded that the wood-frame code-deficient prototype building retrofitted exclusively at the ground story with the SCVD system exhibits satisfactory performance up to nearly the frequent earthquake (FE) intensity level. In contrast, the counterpart entirely retrofitted with the Y-SCVD-EBF system demonstrates seismic efficiency at both design basis earthquake (DBE) and risk-targeted maximum considered earthquake (MCE_R) intensity levels. Thus, for owners with budgetary constraints who aim to retrofit existing structures to perform adequately under frequent earthquake intensities, ground-story-only retrofitting is recommended. However, for those without financial limitations, it is advisable to retrofit the entire building to ensure seismic adequacy up to the MCE_R

intensity level. Additionally, it is important to consider other distinctions between the two retrofitting approaches, including construction duration and the extent of area disruption during construction, which can affect residents across different floors of the building.

7.2.4 Regional Seismic Resilience Assessment of Multi-Family Residential Wood Framed Soft-Story Buildings Retrofitted with Self-Centering Viscous Damper Eccentrically Braced Frame (Y-SCVD-EBF) Modules

A model for intensity-based seismic resilience assessment of wood-framed soft-story residential buildings was used at a regional scale in Python software. This model employs several Python packages, including OpenSeesPy, Pelicun, and ArcPy, to perform response history analysis (RHA), conduct probabilistic assessments of seismic damage and loss, and visualize the outputs, respectively. FEMA P-58 method was employed for seismic damage and loss evaluations of the buildings. As a case study, over 2,000 multi-family residential buildings in the San Francisco Municipal Area were retrofitted with the proposed Y-SCVD-EBF modular system and were analyzed at nine different intensity measures (IMs). Finally, various graphical representations were utilized to present the outputs. The primary findings of the case study are summarized as follows:

- At the highest seismic intensity level (IM-9), the regional normalized mean repair cost (NRC) reaches 22.4%, with more than 95% of this expenditure linked to nonstructural component damages and less than 5% attributed to structural components. However, at the lowest intensity measure (IM-1), the NRC is roughly 5%, stemming almost exclusively from nonstructural component repairs.

- In this study, no irreparable damage occurs in any case due to the high restoring force and minimal plastic deformation afforded by preloaded disc springs. Furthermore, the investigated buildings, which are light wood-framed structures with high strength-to-weight ratios, were originally code-deficient but have been retrofitted with the novel retrofitting systems. This retrofit reduces seismic demands and prevents severe damage, thus eliminating the need for irreparable repairs or replacements. The interplay of robust restoring mechanisms and advantageous structural properties renders these retrofitted buildings highly resilient under seismic loading.

- Regional seismic losses predominantly stem from nonstructural components at all intensity levels. The fuse devices, integral to the proposed retrofitting system, do not contribute to overall losses because they require replacement only at very large inter-story drift ratios (IDRs) circumstances in which the building would typically be considered irreparable. Therefore, wood shear walls remain the sole structural elements contributing to losses, although their impact is relatively low.
- The contribution of individual building components to total seismic loss varies according to the level of seismic intensity.
- In high-performance self-centering systems, repair costs for structural components are relatively minor, whereas nonstructural elements dominate overall seismic losses. Because peak floor accelerations significantly influence nonstructural damage, the inclusion of viscous dampers as primary energy dissipation devices proves particularly effective, further minimizing acceleration responses and thus reducing the likelihood of nonstructural failures.

7.3 Future Research

In this section, identified research gaps are summarized which need to be addressed in future research work:

- It is recommended to conduct full-scale shake table experiments to further investigate the seismic response behavior of the proposed self-centering viscoelastic systems, thereby empirically evaluating their effectiveness.
- Using other self-centering elements such as post-tensioned (PT) cables in the retrofitting system would help investigating the effectiveness of the self-centering mechanism utilized and make a comparison between the two.
- The effects of using other viscous fluids on the seismic performance of the structure need to be investigated as this study investigated using one viscous fluid only.
- The effectiveness of employing the fuse device (TPAD) in the system can be further studied by using it considering zero gap separating it from the adjacent walls.
- It is recommended to perform a regional seismic resilience assessment for the code-deficient wood framed buildings retrofitted on their first story only with the proposed self-centering viscoelastic damper (SCVD) system discussed in Chapter 4 and compare the results with those of discussed in Chapter 6 of this dissertation. This helps decision-makers how the resilience metrics would be affected in both cases.
- The effect of the friction force between the vertical link beam and upper and lower connecting members due to the link beam relative movement would also contribute to the energy dissipation in the system. Investigating this effect is recommended to conduct in future research work.

Appendices

Appendix A: Specification of the Ground Motion Record Set

A set of Far-field (FF) ground motions from the FEMA P695 [94] database was employed in this study. This dataset comprises twenty-two pairs of horizontal ground motion components sourced from sites located at distances of ten kilometers or more from fault ruptures. In Chapters 3, 4, and 5, one ground motion from each component pair within this dataset was selected for response history analysis (RHA). Subsequently, in Chapter 6, to determine the engineering demand parameters (EDPs) for regional seismic damage and loss assessment in accordance with the FEMA P-58 methodology [8], RHA was performed using eleven component pairs from the same record set. The specifications of the ground motions in the Far-field (FF) record set, including event magnitude, year, name, and station, are detailed in Table A.1. Each ground motion comprises two components, designated as D-1 and D-2, with the corresponding chapters in which they are utilized specified in the table. Subsequently, the acceleration histories of the ground motions are illustrated [6].

Table A.1 Far-field ground motions according to FEMA P695

EQ ID	Earthquake			Recording Station	Used in Chapters	
	M	Year	Name	Name	D-1	D-2
GM-01	6.7	1994	Northridge	Beverly Hills	6	3,4,5,6
GM-02	6.7	1994	Northridge	Canyon Country	---	3,4,5
GM-03	7.1	1999	Duzce, Turkey	Bolu	3,4,5,6	6
GM-04	7.1	1999	Hector Mine	Hector	---	3,4,5
GM-05	6.5	1979	Imperial Valley	Delta	6	3,4,5,6
GM-06	6.5	1979	Imperial Valley	El Centro Array #11	3,4,5	---
GM-07	6.9	1995	Kobe, Japan	Nishi-Akashi	6	3,4,5,6
GM-08	6.9	1995	Kobe, Japan	Shin-Osaka	3,4,5	---
GM-09	7.5	1999	Kocaeli, Turkey	Duzce	3,4,5,6	6
GM-10	7.5	1999	Kocaeli, Turkey	Arcelik	---	3,4,5
GM-11	7.3	1992	Landers	Yermo Fire Station	6	3,4,5,6
GM-12	7.3	1992	Landers	Coolwater	3,4,5	---
GM-13	6.9	1989	Loma Prieta	Capitola	6	3,4,5,6
GM-14	6.9	1989	Loma Prieta	Gilroy Array #3	3,4,5	---
GM-15	7.4	1990	Manjil, Iran	Abbar	3,4,5,6	6
GM-16	6.5	1987	Superstition Hills	El Centro Imp. Co.	3,4,5,6	6
GM-17	6.5	1987	Superstition Hills	Poe Road (temp)	---	3,4,5
GM-18	7.0	1992	Cape Mendocino	Rio Dell Overpass	---	3,4,5
GM-19	7.6	1999	Chi-Chi, Taiwan	CHY101	3,4,5,6	6
GM-20	7.6	1999	Chi-Chi, Taiwan	TCU045	3,4,5	---
GM-21	6.6	1971	San Fernando	LA - Hollywood Stor	3,4,5,6	6
GM-22	6.5	1976	Friuli, Italy	Tolmezzo	---	3,4,5

Far-Field (FF) Ground Motions (GMs)

Earthquake: Northridge | Year: 1994 | Magnitude: 6.7

Station: Beverly Hills | Chapters: 6 | ID: GM-01

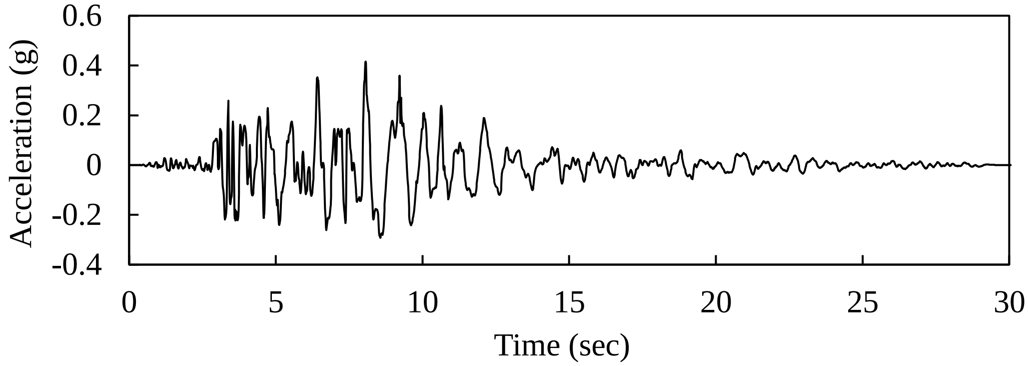

Earthquake: Northridge | Year: 1994 | Magnitude: 6.7

Station: Beverly Hills | Chapter: 3,4,5,6 | ID: GM-01

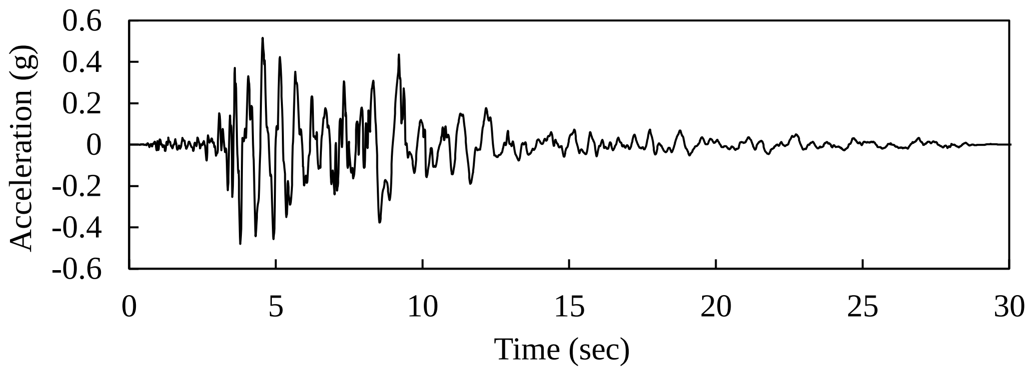

Earthquake: Northridge | Year: 1994 | Magnitude: 6.7

Station: Canyon Country | Chapters: 3,4,5 | ID: GM-02

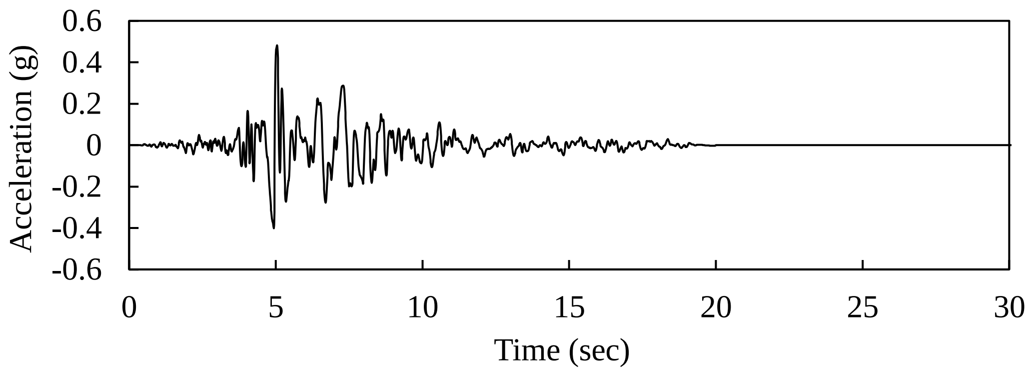

Earthquake: Duzce, Turkey	Year: 1999	Magnitude: 7.1
Station: Bolu	Chapters: 3,4,5,6	ID: GM-03

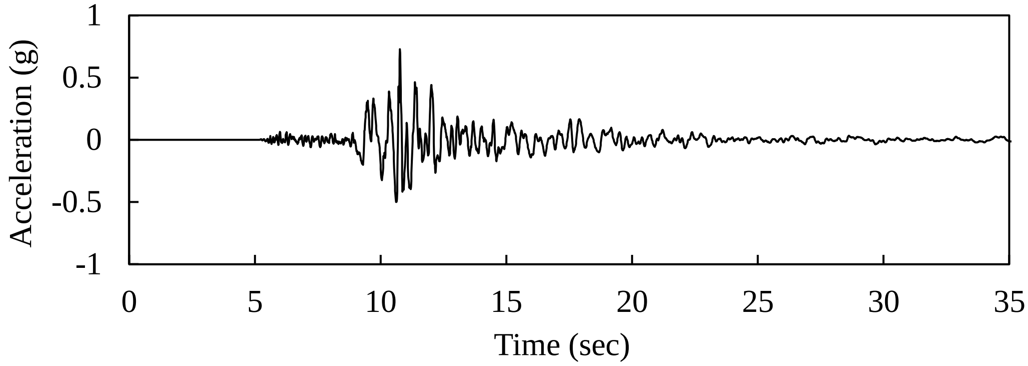

Earthquake: Duzce, Turkey	Year: 1999	Magnitude: 7.1
Station: Bolu	Chapter: 6	ID: GM-03

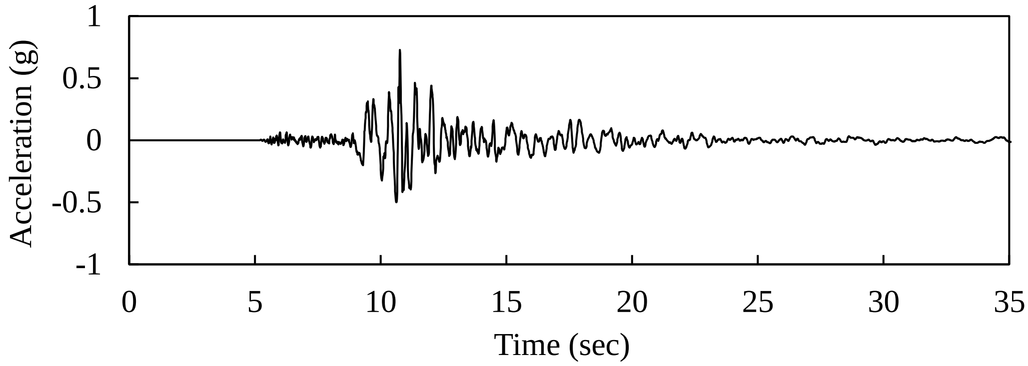

Earthquake: Hector Mine	Year: 1999	Magnitude: 7.1
Station: Hector	Chapters: 3,4,5	ID: GM-04

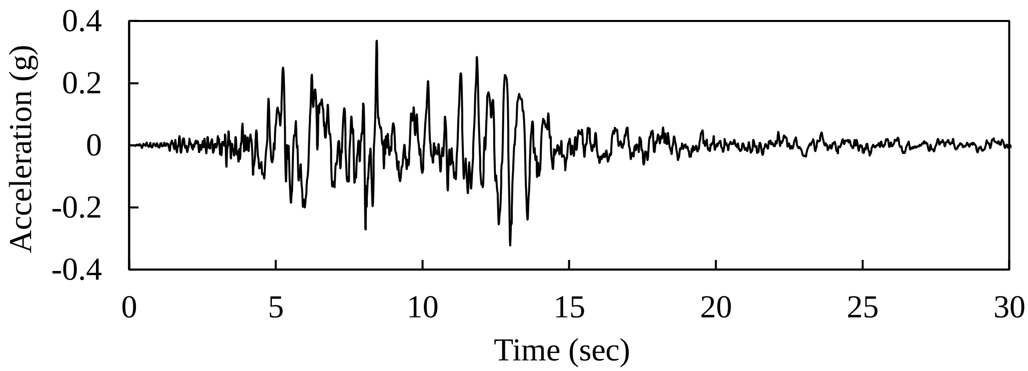

Earthquake: Imperial Valley	Year: 1979	Magnitude: 6.5
Station: Delta	Chapters: 6	ID: GM-05

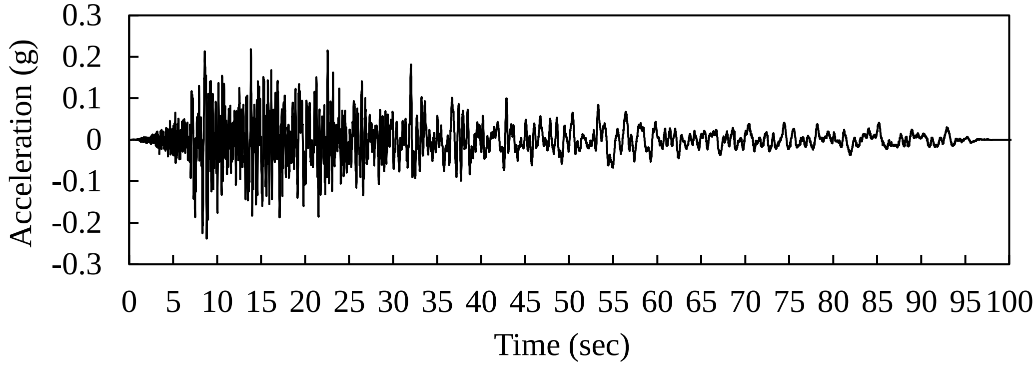

Earthquake: Imperial Valley	Year: 1979	Magnitude: 6.5
Station: Delta	Chapter: 3,4,5,6	ID: GM-05

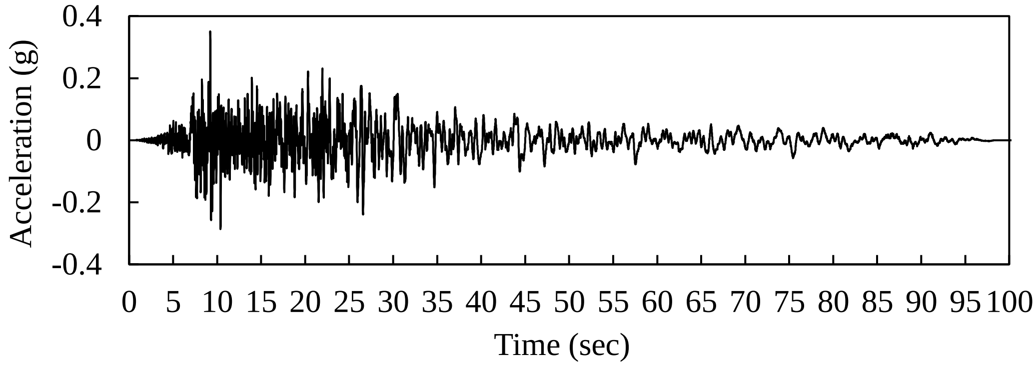

Earthquake: Imperial Valley	Year: 1979	Magnitude: 6.5
Station: El Centro Array #11	Chapters: 3,4,5	ID: GM-06

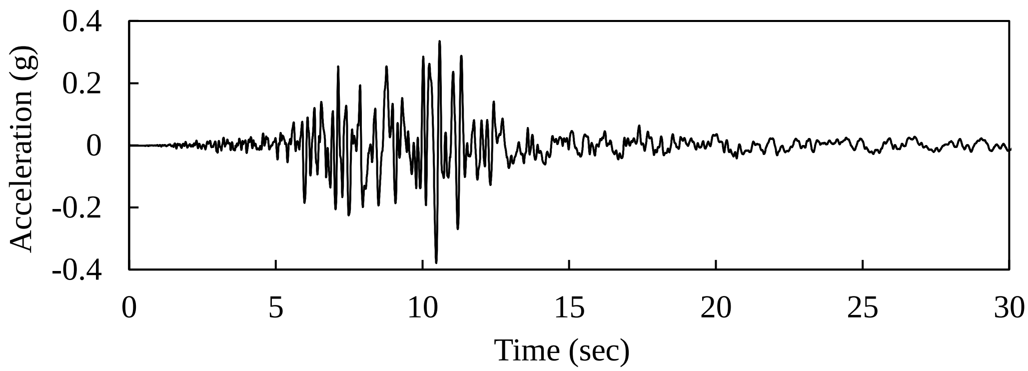

Earthquake: Kobe, Japan	Year: 1995	Magnitude: 6.9
Station: Nishi-Akashi	Chapters: 6	ID: GM-07

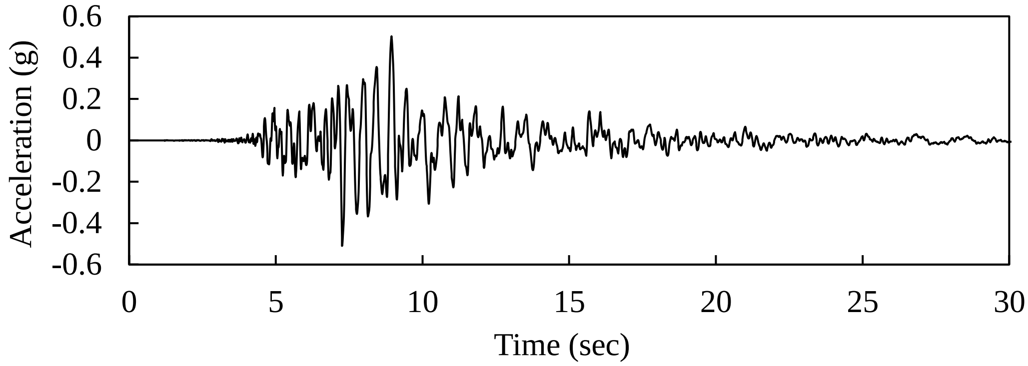

Earthquake: Kobe, Japan	Year: 1995	Magnitude: 6.9
Station: Nishi-Akashi	Chapter: 3,4,5,6	ID: GM-07

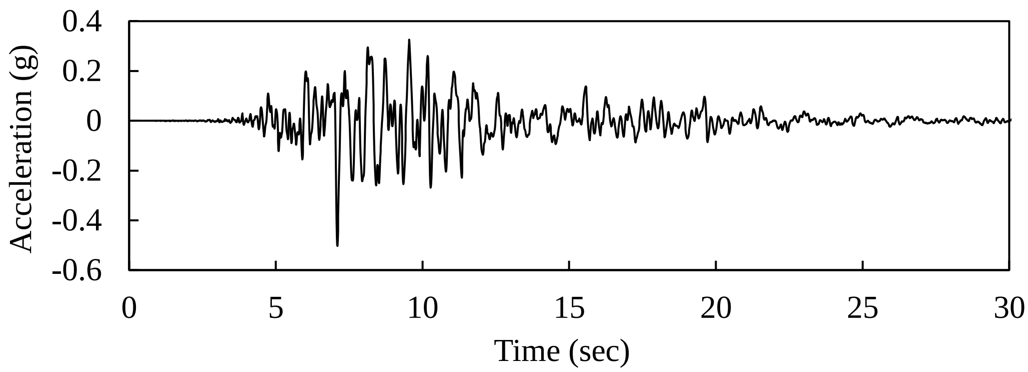

Earthquake: Kobe, Japan	Year: 1995	Magnitude: 6.9
Station: Shin-Osaka	Chapters: 3,4,5	ID: GM-08

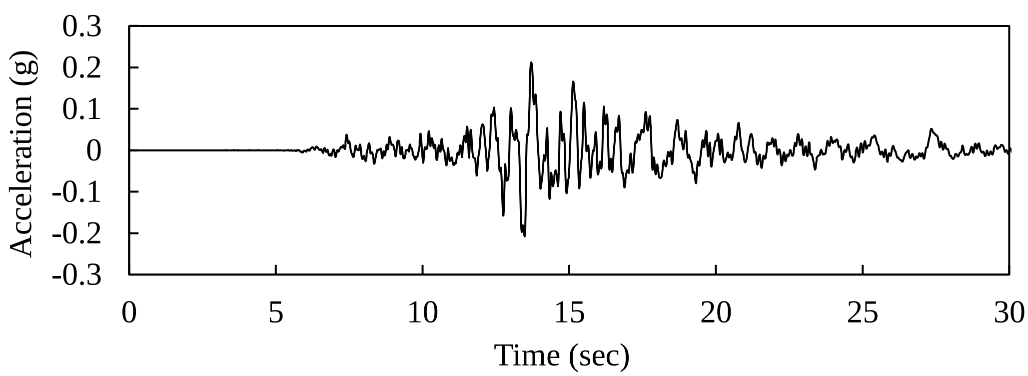

Earthquake: Kocaeli, Turkey	Year: 1999	Magnitude: 7.5
Station: Duzce	Chapters: 3,4,5,6	ID: GM-09

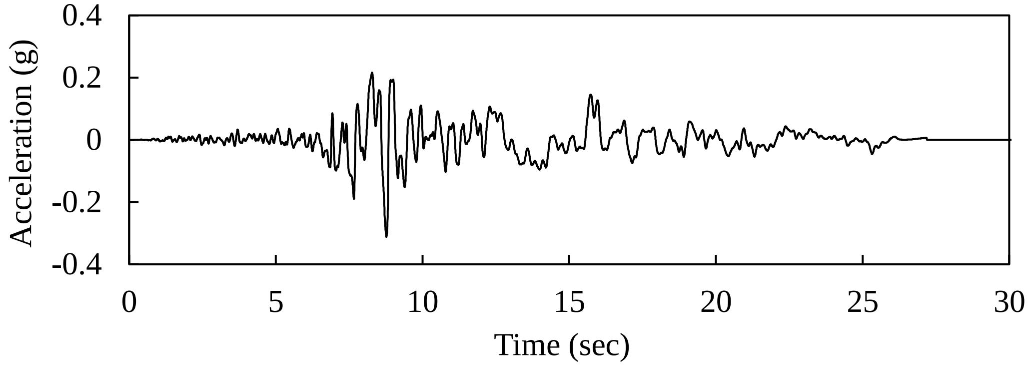

Earthquake: Kocaeli, Turkey	Year: 1999	Magnitude: 7.5
Station: Duzce	Chapter: 6	ID: GM-09

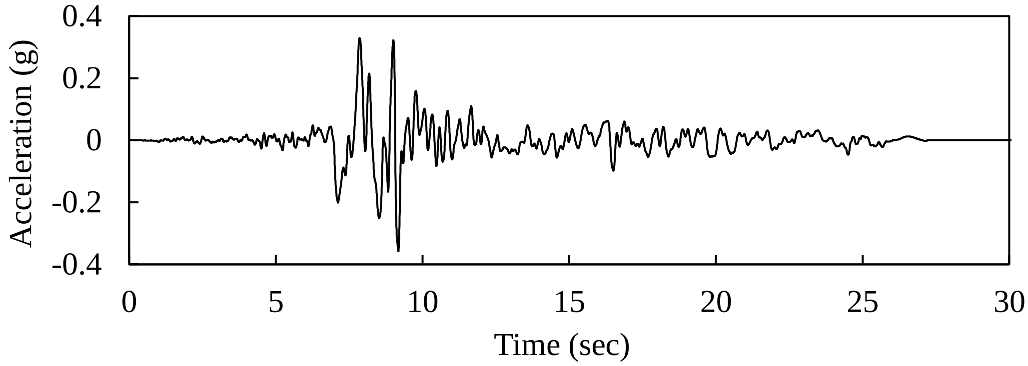

Earthquake: Kocaeli, Turkey	Year: 1999	Magnitude: 7.5
Station: Arcelik	Chapters: 3,4,5	ID: GM-10

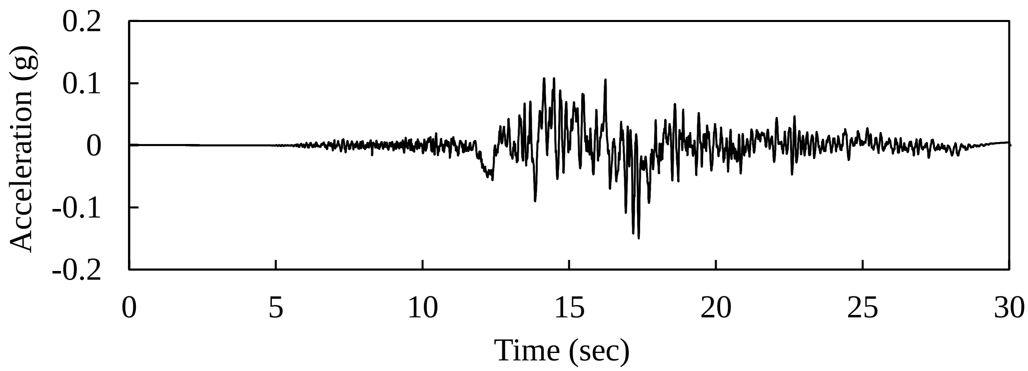

Earthquake: Landers | Year: 1992 | Magnitude: 7.3

Station: Yermo Fire Station | Chapters: 6 | ID: GM-11

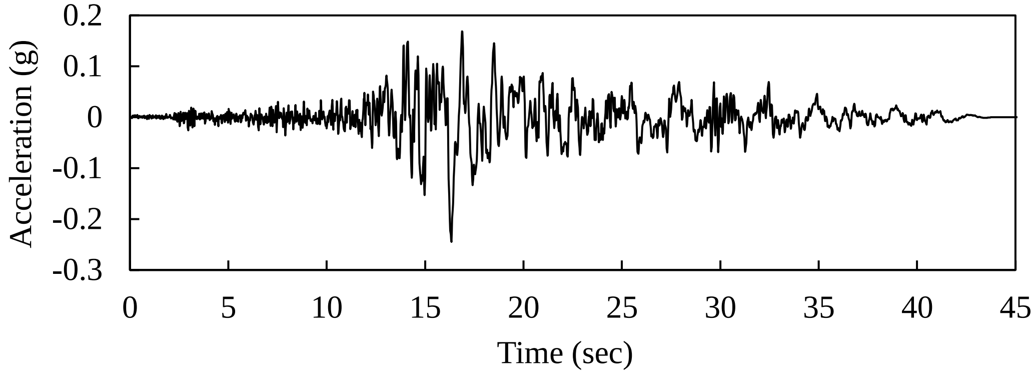

Earthquake: Landers | Year: 1992 | Magnitude: 7.3

Station: Yermo Fire Station | Chapter: 3,4,5,6 | ID: GM-11

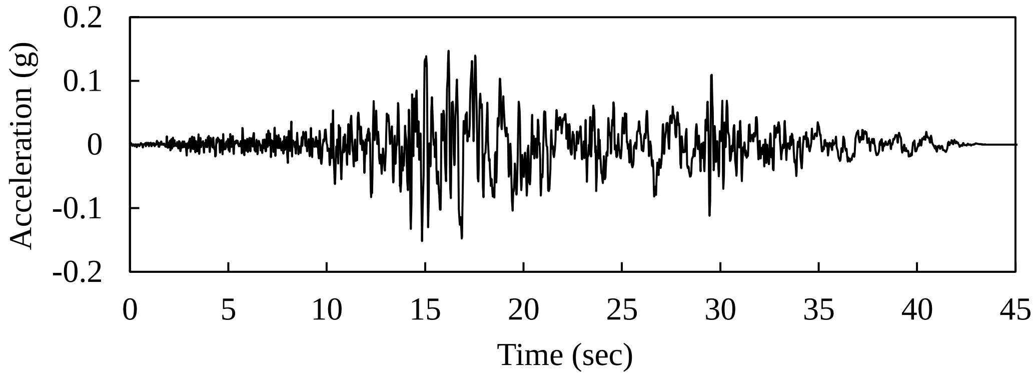

Earthquake: Landers | Year: 1992 | Magnitude: 7.3

Station: Coolwater | Chapters: 3,4,5 | ID: GM-12

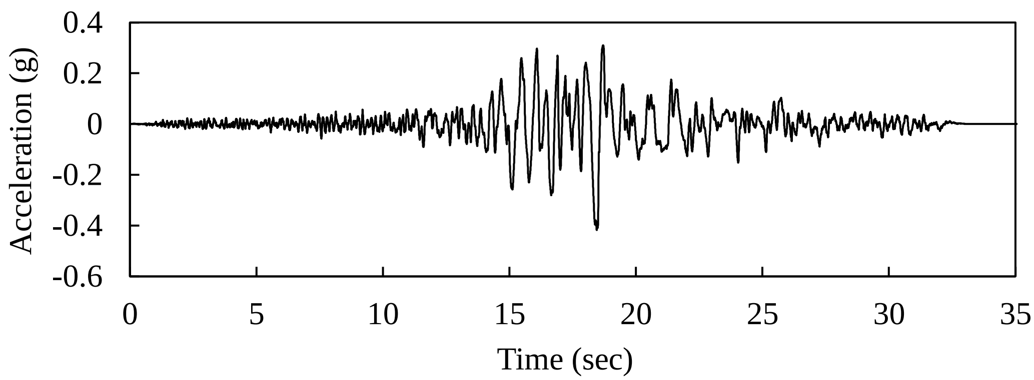

Earthquake: Loma Prieta Year: 1989 Magnitude: 6.9

Station: Capitola Chapters: 6 ID: GM-13

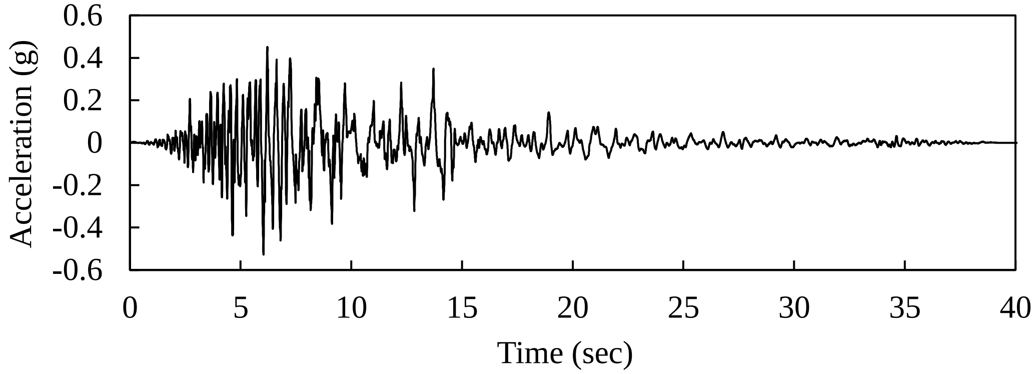

Earthquake: Loma Prieta Year: 1989 Magnitude: 6.9

Station: Capitola Chapter: 3,4,5,6 ID: GM-13

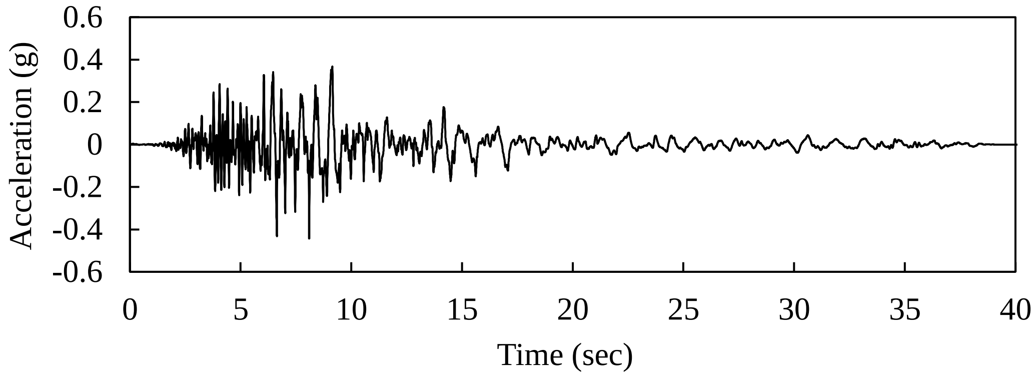

Earthquake: Loma Prieta Year: 1989 Magnitude: 6.9

Station: Gilroy Array #3 Chapters: 3,4,5 ID: GM-14

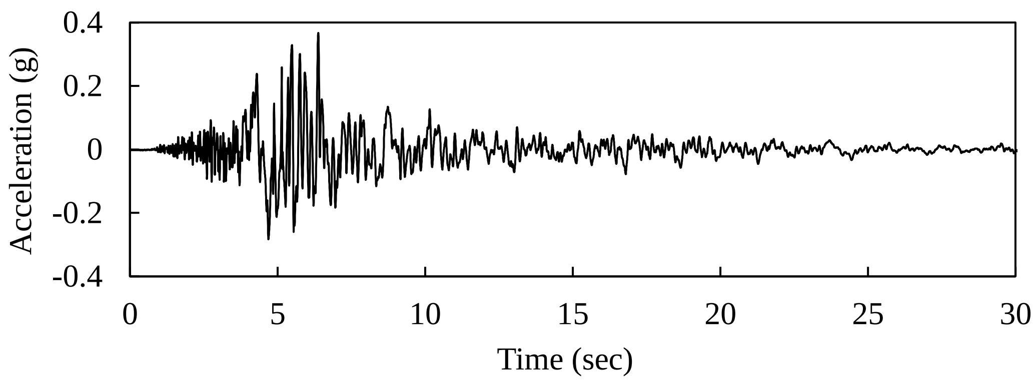

Earthquake: Manjil, Iran | Year: 1990 | Magnitude: 7.4

Station: Abbar | Chapters: 3,4,5,6 | ID: GM-15

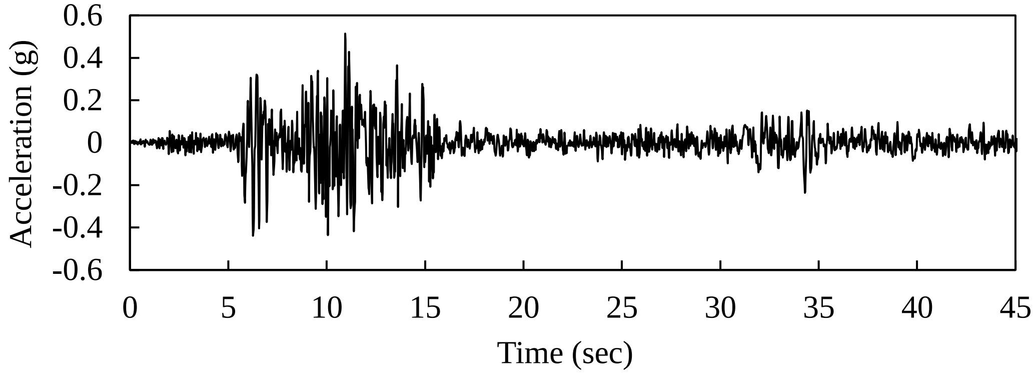

Earthquake: Manjil, Iran | Year: 1990 | Magnitude: 7.4

Station: Abbar | Chapter: 6 | ID: GM-15

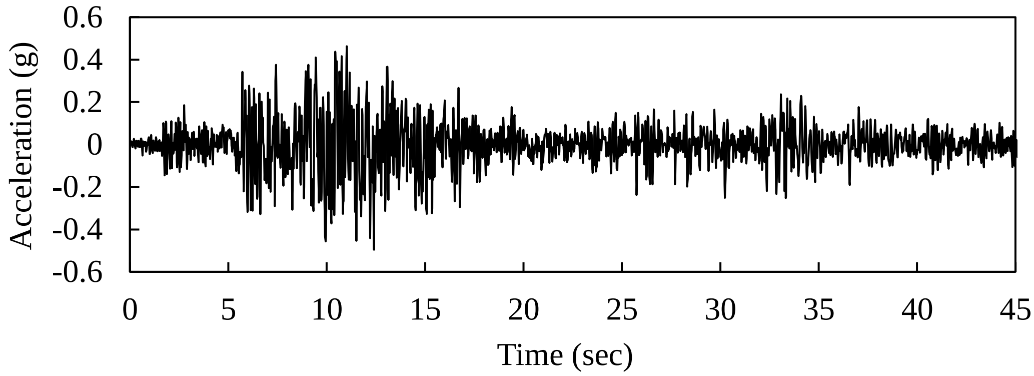

Earthquake: Superstition Hills | Year: 1987 | Magnitude: 6.5

Station: El Centro Imp. Co. | Chapter: 3,4,5,6 | ID: GM-16

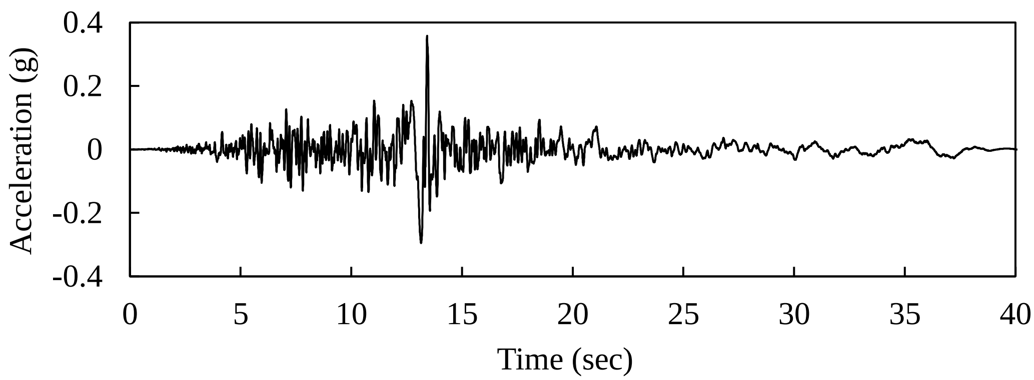

Earthquake: Superstition Hills Year: 1987 Magnitude: 6.5

Station: El Centro Imp. Co. Chapters: 6 ID: GM-16

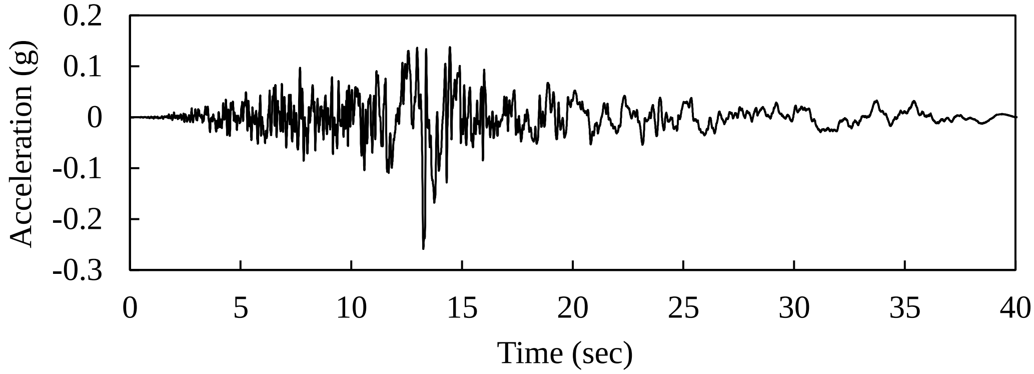

Earthquake: Superstition Hills Year: 1987 Magnitude: 6.5

Station: Poe Road (temp) Chapters: 3,4,5 ID: GM-17

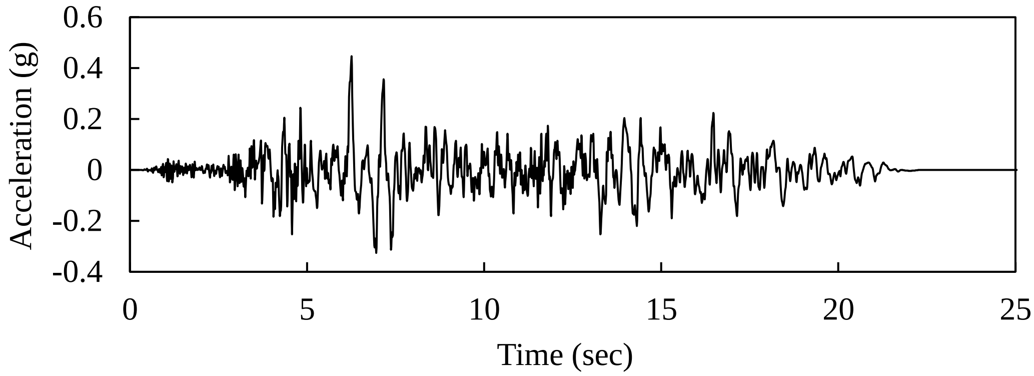

Earthquake: Cape Mendocino Year: 1992 Magnitude: 7.0

Station: Rio Dell Overpass Chapters: 3,4,5 ID: GM-18

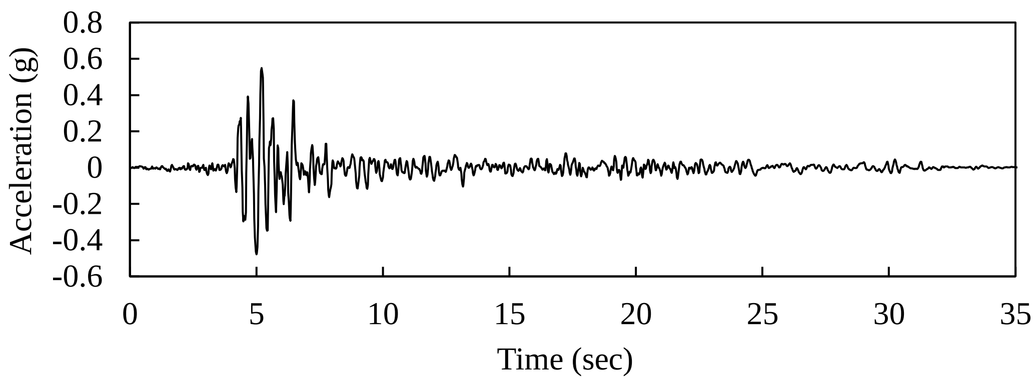

Earthquake: Chi-Chi, Taiwan | Year: 1999 | Magnitude: 7.6

Station: CHY101 | Chapters: 3,4,5,6 | ID: GM-19

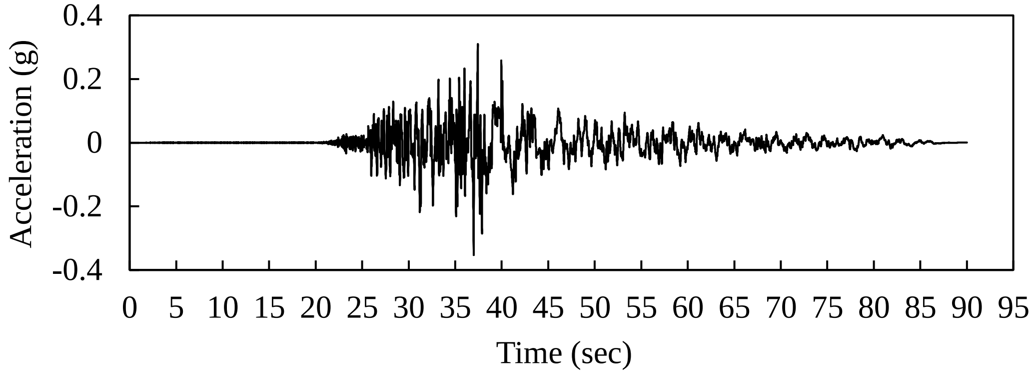

Earthquake: Chi-Chi, Taiwan | Year: 1999 | Magnitude: 7.6

Station: CHY101 | Chapter: 6 | ID: GM-19

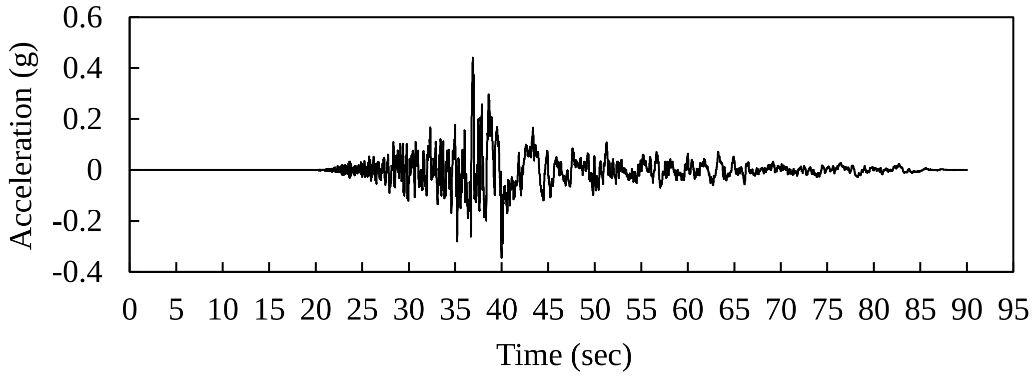

Earthquake: Chi-Chi, Taiwan | Year: 1999 | Magnitude: 7.6

Station: TCU045 | Chapters: 3,4,5 | ID: GM-20

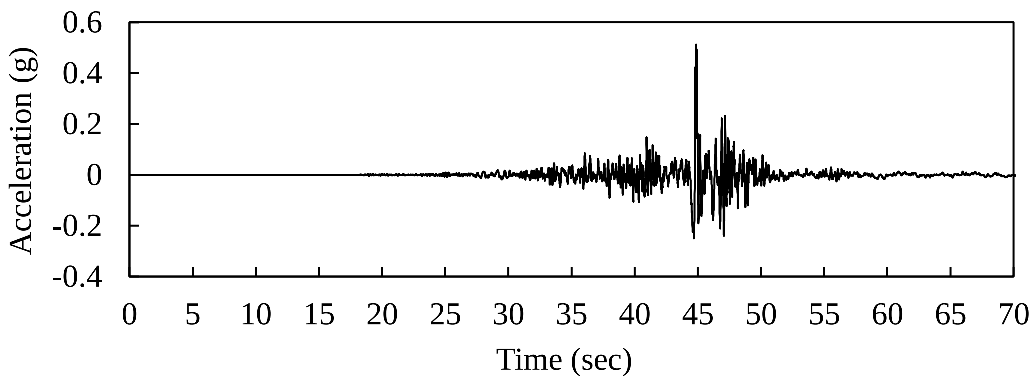

Earthquake: San Fernando | Year: 1971 | Magnitude: 6.6

Station: LA - Hollywood Stor | Chapterss: 3,4,5,6 | ID: GM-21

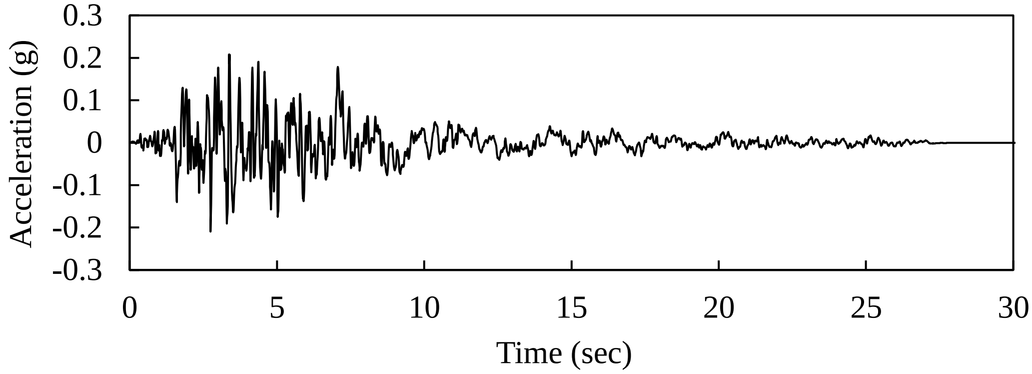

Earthquake: San Fernando | Year: 1971 | Magnitude: 6.6

Station: LA - Hollywood Stor | Chapters:6 | ID: GM-21

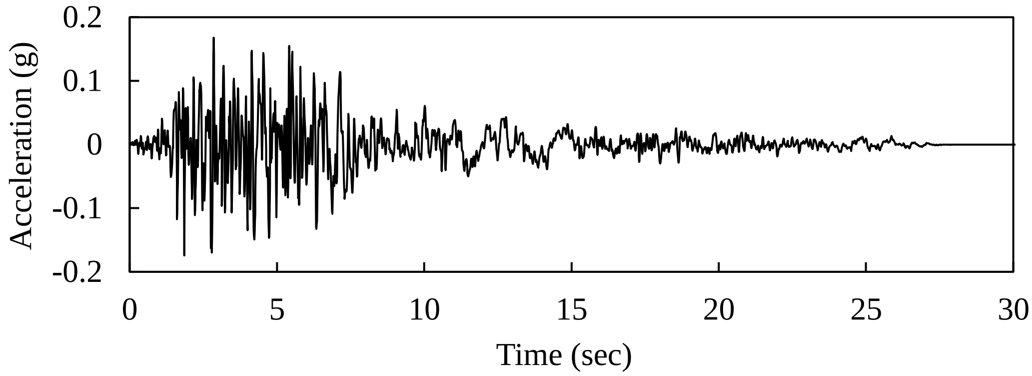

Earthquake: Friuli, Italy | Year: 1976 | Magnitude: 6.5

Station: Tolmezzo | Chapterss:3,4,5 | ID: GM-22

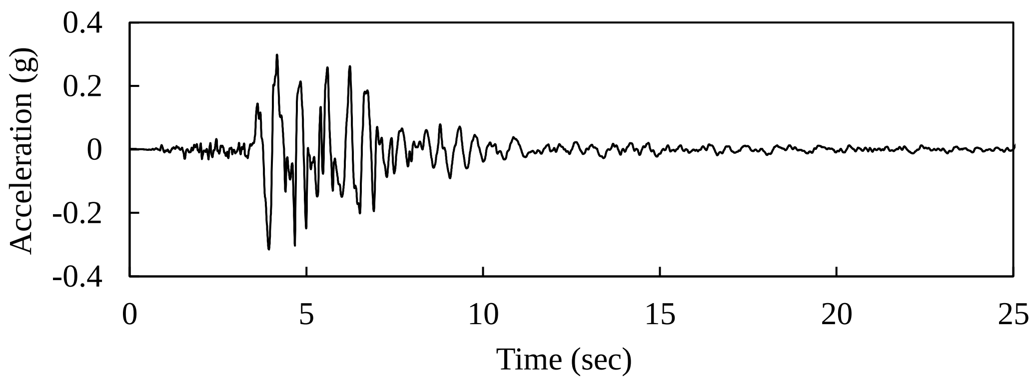

Appendix B: Stiffness and Strength of the Original and WSP-retrofitted Prototypes

In this appendix, the lateral stiffness and strength of the existing unretrofitted light wood framed prototype are presented first, and the stiffness and strength of the WSP-retrofitted counterpart are summarized afterwards which were both discussed in Chapter 3.

B.1 Original Wood-Frame Prototype

Floor	Stiffness S_0 (N/mm)		Strength F (N)	
	HWS	GWB	HWS	GWB
1	2183.65	2965.55	16929.7	16705.55
2	1256.3	7013.7	9740	39509.7
3	1256.3	7013.7	9740	39509.7
4	1256.3	7013.7	9740	39509.7

B.2 WSP-retrofitted Prototype

Floor	Stiffness S_0 (N/mm)				Strength F (N)			
	WSP (305/305)	WSP (153/305)	WSP (76/305)	WSP (51/305)	WSP (305/305)	WSP (153/305)	WSP (76/305)	WSP (51/305)
1	-	-	-	5834.4	-	-	-	78415.2
2	-	-	6092.8	13613.6	-	-	61535.6	182968.8
3	-	4132.8	13273.6	-	-	34898.1	134059.7	-
4	915.2	5962	-	-	7733	50344.8	-	-

Appendix C: Analytical Calculations of the Hysteretic Behavior of the Self-Centering Systems

This section presents comprehensive analytical calculations aimed at predicting the load–displacement behavior of the two self-centering systems investigated in this study: the self-centering viscoelastic damper modular frame (Chapter 4) and the Y-type braced self-centering viscous damper eccentrically braced frame module (Chapter 5).

C.1 Self-Centering Viscoelastic Damper (SCVD) System

Analytical Calculation Table					
SCVD (Chapter 4)					
1-Specifications					
Frame Geometry					
H	*Frame height*			3150	*mm*
W	*Bay width*			5830	*mm*
e	*Length of the Vertical link beam*			2915	*mm*
Section Dimensions					
Unit: mm	Type	depth	web thickness	flange width	flange thickness
Link Beam	W	700	6	320	12
Material Properties					
E	*Steel modulus of Elasticity*			2.00E+05	*Mpa*
G	*Steel Shear modulus*			7.69E+04	*Mpa*
F_y	*Steel yield stress*			345	*Mpa*
Section Properties					
I_{lb}	*Vertical link moment of inertia*			1.063E+09	*mm^4*
A_{lb}	*Vertical Link area*			11736	*mm^2*
A_{lb}^w	*Vertical Link web area*			4056	*mm^2*
S_{lb}	*Link beam elastic section modulus*			3.038E+06	*mm^3*
Z_{lb}	*Link beam plastic section modulus*			3.327E+06	*mm^3*
Self-Centering Damper Box Enclosure					
F_y	*Material yield stress*			690	*Mpa*
W_{SCVD}	*Height of the damper box*			300	*mm*
t_{SCVD}	*Thickness of the damper box*			35	*mm*
L_{SCVD}	*Length of the damper box*			1300	*mm*

TPAD Fuse Device Specification			
F_y	*Material yield stress*	225	*Mpa*
t	*Thickness of fuse plate*	25	*mm*
w_1	*Width of the fuse base*	360	*mm*
w_2	*Width of the fuse tongue*	120	*mm*
h_1	*Length of the trapezoid*	200	*mm*
h	*Total length of the fuse*	250	*mm*
gap	*Fuse gap to the adjacent walls*	6	*mm*
α_{sh}	*Strain hardening ratio*	0.003	
Disc Springs Specification			
E	*Young's modulus*	2.06E+05	*Mpa*
μ	*Poisson's ratio*	0.3	
D_e	*Outside Diameter*	250	*mm*
D_i	*Inside Diameter*	102	*mm*
l_0	*Free height of disc*	18	*mm*
t	*Thickness of disc*	10	*mm*
h_0	*Solid height(l_0-t)*	8	*mm*
t'	*Reduced thickness*	9.6	*mm*
h'_0	*l_0-t'*	8.4	*mm*
F_{PL}	*Total preload*	114.05	*kN*
n_p	*Number of discs in parallel*	3	
n_s	*Number of discs serial sets*	14	
δ	*Disc dimension ratio* (D_e/D_i)	2.45	
h_0/t	*Disc dimension ratio*	0.8	
D_e/t	*Disc dimension ratio*	25	
C_1	*Parameter*	7.11	
C_2	*Parameter*	8.84	
K_1	*Parameter*	0.76	
K_2	*Parameter*	1.32	
K_3	*Parameter*	1.55	
K_4	*Parameter*	1.04	
L	*Total length of the disc springs*	475.68	*mm*
F (s= h'_0)	*Force at the flat position*	153.62	*kN*
Viscous Damper Specification			
c_d	*Damping constant*	9290	*N.s/mm*
α	*Damping exponent*	0.5266	
2-Stiffness			
K_{lb}^f	*Link beam flexural stiffness*	25.8	*kN/mm*

K_{lb}^s	*Link beam shear stiffness*	107.03	*kN/mm*
K_{lb}	*Vertical link beam stiffness*	20.8	*kN/mm*
K_{DS}	*Preloaded disc springs stiffness*	4.15	*kN/mm*
K_{ED}	*Lateral stiffness due to TPAD*	12	*kN/mm*
3- Strength			
V_{GO}	*Gap-opening force*	*228.1*	*kN*
V_{ED}	*Strength provided by TPAD*	50.6	*kN*
V_{lb}	*Link Beam Yield Strength*	393.8	*kN*

C.2 Y-type Braced Self-Centering Viscous Damper Eccentrically Braced Frame (Y-SCVD-EBF) System

Analytical Calculation Table					
Y-SCVD-EBF (Chapter 5)					
1-Specifications					
Frame Geometry					
H	*Frame height*			3150	*mm*
W	*Bay width*			5830	*mm*
e	*Length of the Vertical link beam*			800	*mm*
L_{br}	*Length of the braces*			2830	*mm*
L_{sb}	*Length of the support beam*			2250	*mm*
Section Dimensions					
Unit: mm	Type	depth	web thickness	flange width	flange thickness
Column	W	180	14	300	20
Beam	W	400	14	300	20
Link Beam	W	410	20	240	30
Brace	W	300	14	200	15
Support beam	W	400	14	300	20
Material Properties					
E	*Steel modulus of Elasticity*			2.00E+05	*Mpa*
G	*Steel Shear modulus*			7.69E+04	*Mpa*
F_y	*Steel yield stress*			345	*Mpa*
Self-Centering Damper Box Enclosure					
F_y	*Material yield stress*			690	*Mpa*
W_{SCVD}	*Height of the damper box*			200	*mm*
t_{SCVD}	*Thickness of the damper box*			35	*mm*
L_{SCVD}	*Length of the damper box*			2300	*mm*

TPAD Fuse Device Specification				
F_y	*Material yield stress*		225	*Mpa*
t	*Thickness of fuse plate*		25	*mm*
w_1	*Width of the fuse base*		1080	*mm*
w_2	*Width of the fuse tongue*		360	*mm*
h_1	*Length of the trapezoid*		100	*mm*
h	*Total length of the fuse*		150	*mm*
gap	*Fuse gap to the adjacent walls*		16	*mm*
α_{sh}	*Strain hardening ratio*		0.003	
Disc Springs Specification				
E	*Young's modulus*		2.06E+05	*Mpa*
μ	*Poisson's ratio*		0.3	
D_e	*Outside Diameter*	*1^{st} Floor*	100	*mm*
		2^{nd} Floor	90	
		3^{rd} Floor	125	
		4^{th} Floor	125	
D_i	*Inside Diameter*	*1^{st} Floor*	41	*mm*
		2^{nd} Floor	46	
		3^{rd} Floor	51	
		4^{th} Floor	51	
l_0	*Free height of disc*	*1^{st} Floor*	7.75	*mm*
		2^{nd} Floor	7	
		3^{rd} Floor	9.4	
		4^{th} Floor	9.4	
t	*Thickness of disc*	*1^{st} Floor*	5	*mm*
		2^{nd} Floor	5	
		3^{rd} Floor	6	
		4^{th} Floor	6	
h_0	*Solid height(l_0-t)*	*1^{st} Floor*	2.75	*mm*
		2^{nd} Floor	2	
		3^{rd} Floor	3.4	
		4^{th} Floor	3.4	
t'	*Reduced thickness*	*1^{st} Floor*	4.7	*mm*
		2^{nd} Floor	4.7	
		3^{rd} Floor	5.64	
		4^{th} Floor	5.64	
h'_0	*l_0-t'*	*1^{st} Floor*	3.05	*mm*
		2^{nd} Floor	2.3	
		3^{rd} Floor	3.76	
		4^{th} Floor	3.76	
F_{PL}	*Total preload*	*1^{st} Floor*	35.88	*kN*
		2^{nd} Floor	32.99	
		3^{rd} Floor	24.75	
		4^{th} Floor	12.37	

n_p	*Number of discs in parallel*	*1st Floor*	4	
		2nd Floor	4	
		3rd Floor	2	
		4th Floor	1	
n_s	*Number of discs series sets*	*1st Floor*	37	
		2nd Floor	49	
		3rd Floor	30	
		4th Floor	30	
δ	*Disc dimension ratio* (D_e/D_i)	*1st Floor*	2.44	
		2nd Floor	1.96	
		3rd Floor	2.45	
		4th Floor	2.45	
h_0/t	*Disc dimension ratio*	*1st Floor*	0.55	
		2nd Floor	0.4	
		3rd Floor	0.57	
		4th Floor	0.57	
D_e/t	*Disc dimension ratio*	*1st Floor*	20	
		2nd Floor	18	
		3rd Floor	20.83	
		4th Floor	20.83	
C_1	*Parameter*	*1st Floor*	11.08	
		2nd Floor	17.81	
		3rd Floor	10.58	
		4th Floor	10.58	
C_2	*Parameter*	*1st Floor*	13.97	
		2nd Floor	21.98	
		3rd Floor	13.38	
		4th Floor	13.38	
K_1	*Parameter*	*1st Floor*	0.76	
		2nd Floor	0.69	
		3rd Floor	0.76	
		4th Floor	0.76	
K_2	*Parameter*	*1st Floor*	1.32	
		2nd Floor	1.21	
		3rd Floor	1.32	
		4th Floor	1.32	
K_3	*Parameter*	*1st Floor*	1.54	
		2nd Floor	1.36	
		3rd Floor	1.55	
		4th Floor	1.55	
K_4	*Parameter*	*1st Floor*	1.07	
		2nd Floor	1.08	
		3rd Floor	1.07	
		4th Floor	1.07	
F (s= h'_0)	*Force at the flat position*	*1st Floor*	43.38	*kN*
		2nd Floor	45.14	
		3rd Floor	58.97	
		4th Floor	58.97	

L	*Total length of the disc springs*	*1st Floor*	779.78	*mm*
		2nd Floor	1003.25	
		3rd Floor	428.03	
		4th Floor	261.26	
Viscous Damper Specification				
c_d	*Damping constant*		9290	*N.s/mm*
α	*Damping exponent*		0.5266	
2-Stiffness				
K_{DS}	*Preloaded disc springs stiffness*	*1st Floor*	1.56	*kN/mm*
		2nd Floor	1.62	
		3rd Floor	1.06	
		4th Floor	0.53	
3- Strength				
V_{GO}	*Gap-opening force*	*1st Floor*	*71.76*	*kN*
		2nd Floor	*65.98*	
		3rd Floor	*49.5*	
		4th Floor	*24.74*	

Bibliography

1. Benedetti, Franco & Jara-Cisterna, Alan & Grandon, Juan & Astroza, Nicool & Opazo-Vega, Alexander. (2022). Numerical Analysis of the Seismic Performance of Light-Frame Timber Buildings Using a Detailed Model. Buildings. 12. 981. 10.3390/buildings12070981.

2. Pang, Weichiang & Ziaei, Ershad & Filiatrault, Andre. (2012). A 3D model for collapse analysis of soft-story light-frame wood buildings. World Conference on Timber Engineering 2012, WCTE 2012. 2. 113-120.

3. Bahmani, Pouria & Lindt, John & Iqbal, Asif & Rammer, Douglas. (2017). Mass Timber Rocking Panel Retrofit of a Four-Story Soft-Story Building with Full-Scale Shake Table Validation. Buildings. 7. 48. 10.3390/buildings7020048.

4. Bahmani, P. Performance-Based Seismic Retrofit (PBSR) Methodology for Multi-Story Buildings with Full-Scale Experimental Validation. Ph.D. Thesis, Colorado State University, Fort Collins, CO, USA, May 2015.

5. CAPSS, (2010). “A Community Action Plan for Seismic Safety”, Applied Technology Council (ATC), Redwood City, California.

6. Rezvan, P. Nonlinear numerical simulation study and regional-scale seismic resilience assessment of self-centering systems with sliding rocking link beams. Ph.D. Thesis, University of Maryland, College Park, MD, USA, May 2023.

7. Ayyub B. Practical Resilience Metrics for Planning, Design, and Decision Making. ASCE-ASME Journal of Risk and Uncertainty in Engineering Systems, Part A: Civil Engineering 2015; 1: 04015008. DOI: 10.1061/AJRUA6.0000826.

8. Federal Emergency Management Agency (FEMA). Seismic performance assessment of buildings volume 1: Methodology. Technical Report. FEMA P-58-1 2018.

9. Kirkham, W.J.; Gupta, R.; Miller, T.H. State of the Art: Seismic Behavior of Wood-Frame Residential Structures. J. Struct. Eng. 2014, 140, 04013097.

10. Tomasi, R.; Sartori, T.; Casagrande, D.; Piazza, M. Shaking Table Testing of a Full-Scale Prefabricated Three-Story Timber-Frame Building. J. Earthq. Eng. 2015, 19, 505–534.

11. Casagrande, D.; Grossi, P.; Tomasi, R. Shake table test on a full-scale timber-frame building with gypsum fibre boards. Eur. J. Wood & Wood Prod. 2016, 74, 425–442.

12. Pilarska, D.; Maleska, T. Numerical Analysis of Steel Geodesic Dome under Seismic Excitations. Materials 2021, 14, 4493.

13. Fan, F.; Zhi, X.; Li, W. Analysis of the Acceleration Response Spectra of Single-Layer Spherical Reticulated Shell Structures. Appl. Sci. 2022, 12, 2116.

14. Ali, O.; Bigaud, D.; Riahi, H. Seismic performance of reinforced concrete frame structures strengthened with FRP laminates using a reliability-based advanced approach. Compos. B Eng. 2018, 139, 238–248.

15. Dolan, J.D. The Dynamic Response of Timber Shear Walls. Ph.D. Dissertation, University of British Columbia, Vancouver, BC, Canada, 1989.

16. Kasal, B.; Xu, H. A mathematical model of connections with nonlinear nonconservative hysteretic behavior. In Earthquake Performance and Safety of Timber Structures; Foliente, G.C., Ed.; Forest Products Society: Madison, WI, USA, 1997; pp. 105–107.

17. Folz, B.; Filiatrault, A. Seismic Analysis of Wood frame Structures. I: Model Formulation. J. Struct. Eng. 2004, 130, 1353–1360.

18. Folz, B.; Filiatrault, A. CASHEW: A Computer Program for the Cyclic Analysis of Shear Walls; Department of Structural Engineering, University of California: San Diego, CA, USA, 2000.

19. Folz, B.; Filiatrault, A. Seismic Analysis of Wood frame Structures. II: Model Implementation and Verification. J. Struct. Eng. 2004, 130, 1361–1370.

20. Pei, S.; van de Lindt, J.W. Coupled shear-bending formulation for seismic analysis of stacked wood shear wall systems. Earthq. Eng. Struct. 2009, 38, 1631–1647.

21. Pei, S.; van de Lindt, J.W. Seismic Numerical Modeling of a Six-Story Light-Frame Wood Building: Comparison with Experiments. J. Earthq. Eng. 2011, 15, 924–941.

22. Christovasilis, I.P.; Filiatrault, A. Two-dimensional seismic analysis of multi-story light-frame wood buildings. In Proceedings of the 9th US National & 10th Canadian Conference on Earthquake Engineering: Reaching Beyond Borders, Toronto, ON, Canada, 25–29 July 2010.

23. Pang, W.; Shirazi, M.H. Next generation numerical model for nonlinear in-plane analysis of wood-frame shear walls. In Proceedings of the 11th World Conference on Timber Engineering, Trentino, Italy, 22–24 June 2010.

24. Di Gangi, G.; Demartino, C.; Quaranta, G.; Monti, G. Dissipation in sheathing-to-framing connections of light-frame timber shear walls under seismic loads. Eng. Struct. 2020, 208, 110246.

25. Kuai, L.; Ormarsson, S.; Vessby, J.; Mahatjam, R. A numerical and experimental investigation of non-linear deformation bahaviors in light-frame timber walls. Eng. Struct. 2022, 252, 113599.

26. Estrella, X.; Guindos, P.; Almazán, J.L.; Malek, S. Efficient nonlinear modeling of strong Wood frame shear walls for mid-rise buildings. Eng. Struct. 2020, 215, 110670.

27. Orellana, P.; Santa María, H.; Almazán, J.L.; Estrella, X. Cyclic behavior of Wood-frame shear walls with vertical load and bending moment for mid-rise timber buildings. Eng. Struct. 2021, 240, 112298.

28. Filiatrault, A. Wood-Frame Project Testing and Analysis Literature Review; CUREECaltech Wood frame Project; CUREE W-03; Consortium of Universities for Research in Earthquake Engineering: Richmond, CA, USA, 2001.

29. Filiatrault, A.; Fischer, D.; Folz, B.; Uang, C.-M. Seismic Testing of a Two-Story Wood-frame House: Influence of Wall Finish Materials. ASCE J. Struct. Eng. 2002, 128, 1337–1345.

30. Filiatrault, A.; Christovasilis, I.; Wanitkorkul, A.; van de Lindt, J.W. Experimental Seismic Response of a Full-Scale Light-Frame Wood Building. ASCE J. Struct. Eng. 2010, 136, 246–254.

31. Uniform Building Code. International Conference of Building Officials; UBC: Whittier, CA, USA, 1988.

32. Pang, W.; Rosowsky, D.; van de Lindt, J.; Pei, S. Simplified Direct Displacement Design of Six-Story NEESWood Capstone Building and Pre-Test Seismic Performance Assessment; NEESWood Report NW-05; MCEER: Buffalo, NY, USA, 2009.

33. Mosalam, K.M.; Mahin, S.A. Seismic Evaluation and Retrofit of Asymmetric Multi-story Wood-frame Building. J. Earthq. Eng. 2007, 11, 968–986.

34. Seim, Werner & Kramar, Miha & Pazlar, Tomaž & Vogt, Tobias. (2015). OSB and GFB As Sheathing Materials for Timber-Framed Shear Walls: Comparative Study of Seismic Resistance. Journal of Structural Engineering. E4015004. 10.1061/(ASCE)ST.1943-541X.0001293.

35. Van de Lindt, J.; Bahmani, P.; Mochizuki, G.; Pryor, S.; Gershfeld, M.; Tian, J.; Symans, M.; Rammer, D. Experimental Seismic Behavior of a Full-Scale Four-Story Soft-Story Wood-Frame Building with Retrofits. II: Shake Table Test Results. ASCE J. Struct. Eng. 2014.

36. Bahmani, P.; van de Lindt, J.; Gershfeld, M.; Mochizuki, G.; Pryor, S.; Rammer, D. Experimental Seismic Behavior of a Full-Scale Four-Story Soft-Story Wood-Frame Building with Retrofits. I: Building Design, Retrofit Methodology, and Numerical Validation. ASCE J. Struct. Eng. 2014, 142.

37. FEMA P-807, Federal Emergency Management Agency. Seismic Evaluation and Retrofit of Multi-Unit Wood-Frame Buildings with Weak First Stories; FEMA: Washington, DC, USA, 2012.

38. Bahmani, P.; van de Lindt, J.; Dao, T. Displacement-Based Design of Buildings with Torsion: Theory and Verification. ASCE J. Struct. Eng. 2013.

39. Kurama Y, Pessiki S, Sause R, Lu LW. Seismic behavior and design of unbonded post-tensioned precast concrete walls. PCI Journal 1999; 44(3): 72–89. DOI: 10.15554/pcij.05011999.72.89.

40. Ricles JM, Sause R, Garlock MM, Zhao C. Posttensioned seismic-resistant connections for steel frames. Journal of Structural Engineering 2001; 127(2): 113–121. DOI: 10.1061/(ASCE)0733-9445(2001)127:2(113).

41. Christopoulos C, Filiatrault A, Uang CM, Folz B. Posttensioned energy dissipating connections for moment-resisting steel frames. Journal of Structural Engineering 2002; 128(9): 1111–1120. DOI: 10.1061/(ASCE)0733-9445(2002)128:9(1111).

42. Chou CC, Chen JH, Chen YC, Tsai KC. Evaluating performance of post-tensioned steel connections with strands and reduced flange plates. Earthquake Engineering & Structural Dynamics 2006; 35(9): 1167–1185. DOI: 10.1002/eqe.579.

43. Garlock MM, Sause R, Ricles JM. Behavior and Design of Posttensioned Steel Frame Systems. Journal of Structural Engineering 2007; 133(3): 389–399. DOI: 10.1061/(ASCE)0733-9445(2007)133:3(389).

44. Zhang Y, Zhu S. A shape memory alloy-based reusable hysteretic damper for seismic hazard mitigation. Smart Materials and Structures 2007; 16(5): 1603–1613. DOI: 10.1088/0964-1726/16/5/014.

45. Wang B, Nishiyama M, Zhu S, Tani M, Jiang H. Development of novel self-centering steel coupling beams without beam elongation for earthquake resilience. Engineering Structures 2021; 232: 111827. DOI: 10.1016/j.engstruct.2020.111827.

46. Wang W, Wang X. Tests, model, and applications for coned-disc-spring vertical isolation bearings. Bulletin of Earthquake Engineering 2020; 18(1): 357–398. DOI: 10.1007/s10518-019-00728-8.

47. Xu LH, Fan XW, Li ZX. Cyclic behavior and failure mechanism of self-centering energy dissipation braces with pre-pressed combination disc springs. Earthquake Engineering & Structural Dynamics 2017; 46(7): 1065–1080. DOI: 10.1002/eqe.2844.

48. Xu L, Xiao S, Li Z. Hysteretic behavior and parametric studies of a self-centering RC wall with disc spring devices. Soil Dynamics and Earthquake Engineering 2018; 115: 476–488. DOI: 10.1016/j.soildyn.2018.09.017.

49. Fang C, Wang W, Shen D. Development and Experimental Study of Disc Spring–Based Self-Centering Devices for Seismic Resilience. Journal of Structural Engineering 2021; 147(7): 04021094. DOI: 10.1061/(ASCE)ST.1943-541X.0003058.

50. Wang W, Fang C, Zhao Y, Sause R, Hu S, Ricles J. Self-centering friction spring dampers for seismic resilience. Earthquake Engineering & Structural Dynamics 2019; 48(9): 1045–1065. DOI: 10.1002/eqe.3174.

51. Hu S, Wang W, Qu B, Alam MS. Development and validation test of a novel Self-centering Energy-absorbing Dual Rocking Core (SEDRC) system for seismic resilience. Engineering Structures 2020; 211: 110424. DOI: 10.1016/j.engstruct.2020.110424.

52. Rezvan, Pooya & Zhang, Yunfeng. (2023). Seismic design and performance study of self-centering moment-resisting frames with sliding rocking beams and preloaded disc springs. Earthquake Engineering & Structural Dynamics. 10.1002/eqe.3859.

53. Fang C, Wang W, Shen D. Development and Experimental Study of Disc Spring – Based Self-Centering Devices for Seismic Resilience. J Struct Eng. 2021;147(7): 04021094. Doi: 10.1061/(ASCE)ST.1943-541X.0003058.

54. Wang W, Wang X. Tests, model, and applications for coned-disc-spring vertical isolation bearings. Bull Earthquake Eng. 2020; 18(1): 357-398. Doi: 10.1007/s10518-019-00728-8.

55. Cheng CT, Hsu CH, Lin K. Seismic Behavior of Self-centering Designed Eccentrically Braced Frames, 2012.

56. Tong, Lewei & Zhang, Yunfeng & Zhou, Xin & Keivan, Arshia & Li, Ruipeng. (2019). Experimental and Analytical Investigation of D-Type Self-Centering Steel Eccentrically Braced Frames with Replaceable Hysteretic Damping Devices. Journal of Structural Engineering. 145. 04018229. 10.1061/(ASCE)ST.1943-541X.0002235.

57. Keivan, Arshia & Zhang, Yunfeng. (2019). Nonlinear seismic performance of Y-type self-centering steel eccentrically braced frame buildings. Engineering Structures. 179. 448-459. 10.1016/j.engstruct.2018.11.002.

58. Keivan A, Zhang Y. Seismic performance evaluation of self-centering K-type and D-type eccentrically braced frame systems. *Engineering Structures* 2019; **184**: 301–317. DOI: 10.1016/j.engstruct.2019.01.087.

59. Rezvan P, Zhang Y. Nonlinear seismic performance study of D-type self-centering eccentric braced frames with sliding rocking link beams. Earthquake Engng Struct Dyn. 2022;51:875-895. https://doi.org/10.1002/eqe.3595.

60. Yan, Xin & Alam, M. Shahria & Shu, Ganping & Qin, Ying. (2023). A novel self-centering viscous damper for improving seismic resilience: Its development, experimentation, and system response. Engineering Structures. 279. 115632. 10.1016/j.engstruct.2023.115632.

61. Xu, Longhe & Fan, Xiaowei & Li, Zhongxian. (2017). Experimental behavior and analysis of self-centering steel brace with pre-pressed disc springs. Journal of Constructional Steel Research. 139. 363-373. 10.1016/j.jcsr.2017.09.021.

62. Fang C, Wang W, Shen D. Development and Experimental Study of Disc Spring–Based Self-Centering Devices for Seismic Resilience. J Struct Eng. 2021; 147(7):04021094. doi: 10.1061/(ASCE)ST.1943-541X.0003058.

63. Zhang, Hongmei & Quan, Liumeng & Lu, Xilin. (2022). Experimental Hysteretic Behavior and Application of an Assembled Self-Centering Buckling-Restrained Brace. Journal of Structural Engineering. 148. 10.1061/(ASCE)ST.1943-541X.0003287.

64. Xie, Qin & Zhou, Zhen & Meng, Shao-Ping. (2020). Experimental investigation of the hysteretic performance of self-centering buckling-restrained braces with friction fuses. Engineering Structures. 203. 109865. 10.1016/j.engstruct.2019.109865.

65. Qiu, Can-Xing & Zhu, Songye. (2016). High-mode effects on seismic performance of multi-story self-centering braced steel frames. Journal of Constructional Steel Research. 119. 133-143. 10.1016/j.jcsr.2015.12.008.

66. Tremblay, Robert & Lacerte, M. & Christopoulos, C.. (2008). Seismic Response of Multistory Buildings with Self-Centering Energy Dissipative Steel Braces. Journal of Structural Engineering-asce - J STRUCT ENG-ASCE. 134. 10.1061/(ASCE)0733-9445(2008)134:1(108).

67. Karavasilis, Theodore & Seo, Choungyeol. (2011). Seismic structural and non-structural performance evaluation of highly damped self-centering and conventional systems. Engineering Structures - ENG STRUCT. 33. 2248-2258. 10.1016/j.engstruct.2011.04.001.

68. Tang, Wenke & Lui, Eric. (2014). Hybrid Recentering Energy Dissipative Device for Seismic Protection. Journal of Structures. 2014. 1-17. 10.1155/2014/262409.

69. Eskandari Nasab, Mohammad & Kim, Jinkoo. (2020). Seismic Retrofit of Structures Using Hybrid Steel Slit–Viscoelastic Dampers. Journal of Structural Engineering. 146. 04020238. 10.1061/(ASCE)ST.1943-541X.0002816.

70. Canxing Qiu, Lizi Cheng, Xiuli Du, Seismic design of hybrid braced frames with self-centering braces and fluid viscous damping braces, Engineering Structures, Volume 280, 2023, 115728, ISSN 0141-0296, https://doi.org/10.1016/j.engstruct.2023.115728.

71. Dimopoulos AI, Tzimas AS, Karavasilis TL, Vamvatsikos D. Probabilistic economic seismic loss estimation in steel buildings using post-tensioned moment-resisting frames and viscous

dampers. Earthquake Engineering & Structural Dynamics 2016; 45(11): 1725–1741. DOI: 10.1002/eqe.2722.

72. Guan X, Burton H, Moradi S. Seismic performance of a self-centering steel moment frame building: From component-level modeling to economic loss assessment. Journal of Constructional Steel Research 2018; 150: 129–140. DOI: 10.1016/j.jcsr.2018.07.026.

73. Federal Emergency Management Agency (FEMA). Hazus 5.1- Earthquake Model Technical Manual 2022.

74. Federal Emergency Management Agency (FEMA). Hazus 5.1- Earthquake Model User Guidance 2022.

75. Federal Emergency Management Agency (FEMA). Hazus 4.2- Hazus Inventory Technical Manual 2021.

76. Schneider P, Schauer B. HAZUS-its development and its future. Natural Hazards Review 2006; 7. DOI: 10.1061/(ASCE)1527-6988(2006)7:2(40).

77. Kircher CA, Whitman RV, Holmes WT. HAZUS Earthquake Loss Estimation Methods. Natural Hazards Review 2006; 7(2).

78. Neighbors C, Cochran E, Caras Y, Noriega G. Sensitivity analysis of FEMA HAZUS earthquake model: Case study from King County, Washington. Natural Hazards Review 2013; 14: 134–146. DOI: 10.1061/(ASCE)NH.1527-6996.0000089.

79. Remo JWF, Pinter N. Hazus-MH earthquake modeling in the central USA. Natural Hazards 2012; 63(2): 1055–1081. DOI: 10.1007/s11069-012-0206-5.

80. Mangalathu S, Soleimani F, Jeon JS. Bridge classes for regional seismic risk assessment: Improving HAZUS models. Engineering Structures 2017; 148: 755–766. DOI: 10.1016/j.engstruct.2017.07.019.

81. Zeng X, Lu X, Yang TY, Xu Z. Application of the FEMA-P58 methodology for regional earthquake loss prediction. Natural Hazards 2016; 83(1): 177–192. DOI: 10.1007/s11069-016-2307-z.

82. Porter K. An Overview of PEER's Performance-Based Earthquake Engineering Methodology. Proc Ninth International Conference on Applications of Statistics and Probability in Civil Engineering (ICASP9) 2003.

83. Federal Emergency Management Agency (FEMA). Seismic performance assessment of buildings volume 2: Implementation guide. Technical Report. FEMA P-58-2 2018.

84. Federal Emergency Management Agency (FEMA). Seismic performance assessment of buildings volume 3: Supporting materials and background documentation. Technical Report. FEMA P-58-3 2018.

85. Lu X, Han B, Hori M, Xiong C, Xu Z. A coarse-grained parallel approach for seismic damage simulations of urban areas based on refined models and GPU/CPU cooperative computing. Advances in Engineering Software 2014; 70: 90–103. DOI: 10.1016/j.advengsoft.2014.01.010.

86. Deierlein, Gregory & Zsarnóczay, Ádám & Arduino, Pedro & Baker, Jack & Bray, Jonathan & Conte, Joel & Deodatis, George & Elhaddad, Wael & Gardner, Michael & Govindjee, Sanjay & Hu, Liang & Kareem, Ahsan & Kijewski-Correa, Tracy & Lynett, Patrick & Mckenna, Frank & Miura, Yuki & Motley, Michael & Taciroglu, Ertugrul & Taflanidis, Alexandros & Wang, Chaofeng. (2019). State-of-Art in Computational Simulation for Natural Hazards Engineering. 10.5281/zenodo.2579582.

87. Lu X, Guan H. Earthquake Disaster Simulation of Civil Infrastructures. Singapore: Springer; 2017. DOI: 10.1007/978-981-10-3087-1.

88. Lu X, McKenna F, Cheng Q, Xu Z, Zeng X, Mahin SA. An open-source framework for regional earthquake loss estimation using the city-scale nonlinear time history analysis. Earthquake Spectra 2020; 36(2): 806–831. DOI: 10.1177/8755293019891724.

89. Yi, Zhengxiang & Burton, Henry & Shokrabadi, Mehrdad & Issa, Omar. (2020). Multi-scale cost-benefit analysis of the Los Angeles Soft-Story Ordinance. Engineering Structures. 214. 10.1016/j.engstruct.2020.110652.

90. You, Tian & Teweldebrhan, Biniam & Wang, Wei & Tesfamariam, Solomon. (2023). Seismic loss and resilience assessment of tall-coupled cross-laminated timber wall building. Earthquake Spectra. 10.1177/87552930231152512.

91. Lu X, Tian Y, Guan H, Xiong C. Parametric sensitivity study on regional seismic damage prediction of reinforced masonry buildings based on time-history analysis. Bulletin of Earthquake Engineering 2017; 15(11): 4791–4820. DOI: 10.1007/s10518-017-0168-9.

92. Folz, B., and Filiatrault, A. (2000). “A computer program for cyclic analysis of wood shear walls.” CUREE Report W-08, Task 1.5.1, Consortium of Universities for Research in Earthquake Engineering, Richmond, Calif.

93. Mazzoni S, McKenna F, Scott MH, Fenves GL. OpenSees command language manual. Pacific Earthquake Engineering Research (PEER) Center 2006; 264.

94. FEMA P695. Quantification of Building Seismic Performance Factors. Washington, D.C.: Federal Emergency Management Agency; 2009.

95. DIN EN 16984 - Disc springs - Calculation (Tellerfedern - Berechnung), Beuth Verlag GmbH, Berlin 2017.

96. Wang W, Wang X. Tests, model, and applications for coned-disc-spring vertical isolation bearings. *Bulletin of Earthquake Engineering* 2020; **18**(1): 357–398. DOI: 10.1007/s10518-019-00728-8.

97. KEH-CHYUAN TSAI et al. “Design of Steel Triangular Plate Energy Absorbers for Seismic-Resistant Construction: Passive Energy Dissipation.” Earthquake spectra 9.3 (1993): 505–528.

98. N.S. Armouti, Effect of dampers on seismic demand of short period structures in deep cohesion less sites, Adv. Steel Construct. 7 (2) (2011) 192–205.

99. J.S. Hwang, Seismic Design of Structures with Viscous Dampers, International Training Programs for Seismic Design of Building Structures Hosted by National Center for Research on Earthquake Engineering Sponsored by Department of International Programs, National Science Council, January 21–25, Taipei, Taiwan, 2002.

100. American Society of Civil Engineers, editor. Minimum design loads and associated criteria for buildings and other structures. Reston, Virginia: American Society of Civil Engineers; 2022.

101. FEMA Geospatial Resource Center. https://gis-fema.hub.arcgis.com.

102. The National Map - Data Delivery | U.S. Geological Survey. https://www.usgs.gov/the-national-map-data-delivery.

103. ArcGIS Pro 3.4.0.

104. Seismic Design Web Service Documentation. https://earthquake.usgs.gov/ws/designmaps.

105. Zhu M, McKenna F, Scott MH. OpenSeesPy: Python library for the OpenSees finite element framework. *SoftwareX* 2018; **7**: 6–11. DOI: 10.1016/j.softx.2017.10.009.

106. Zsarnóczay A, Deierlein GG. PELICUN – A COMPUTATIONAL FRAMEWORK FOR ESTIMATING DAMAGE, LOSS AND COMMUNITY RESILIENCE 2020: 12.